University of Nottingham

School of Mathematical Sciences

The Dynamics of Neural Fields and Applications to Vision

Abigail Cocks

A thesis submitted to the University of Nottingham for the degree of
Doctor of Philosophy

January 2023

For Gramps

ABSTRACT

Explorations of visual hallucinations, and in particular those of Billock and Tsou [V. A. Billock and B. H. Tsou, Proceedings of the National Academy of Sciences USA, 104 (2007), pp. 8490–8495], show that annular rings with a background flicker can induce visual hallucinations in humans that take the form of radial fan shapes. The well-known retinocortical map tells us that the corresponding patterns of neural activity in the primary visual cortex for rings and arms in the retina are orthogonal stripe patterns. The implication is that cortical forcing by spatially periodic input can excite orthogonal modes of neural activity. Here we show that a simple scalar neural field model of primary visual cortex with state-dependent spatial forcing is capable of modelling this phenomenon. Moreover, we show that this occurs most robustly when the spatial forcing has a 2:1 resonance with modes that would otherwise be excited by a Turing instability. By utilising a weakly nonlinear multiple-scales analysis we determine the relevant amplitude equations for uncovering the parameter regimes which favour the excitation of patterns orthogonal to sensory drive. In combination with direct numerical simulations we use this approach to shed further light on the original psychophysical observations of Billock and Tsou.

Homogeneous connectivity profiles are commonly used as standard in neural field models. However, connectivity is known to be patchy and organised by a roughly hexagonal periodicity. We use a periodically modulated connectivity profile in the neural field model to explore this patchiness. Turing analysis and direct numerical simulations allow us to determine the consequences of this on pattern formation. The orientation preference map in primary visual cortex also has roughly periodic structure organised around pinwheels. We show that a multi-layered neural field model with patchy connectivity is capable of generating a realistic orientation preference map.

ACKNOWLEDGEMENTS

Firstly, I would like to thank my supervisors, Prof. Stephen Coombes and Dr. Rachel Nicks; you have been so supportive and helpful throughout the years. I have really enjoyed working with you and couldn't have asked for better supervisors. Thank you to Prof. Alan Johnston for helping us with the psychology aspects of my work and sitting through numerous meetings which were heavily maths-based. Also, I would like to thank Dr. Daniele Avitabile for your supervision and support during my first two years.

I would like to thank all my friends from my time in Nottingham. I am very grateful to numerous people in the Maths department, there are too many to name here. Thank you to Sunil, James, Mustafa, and Michael for all our conversations about neural fields and for all the fun we had at conferences. A special thank you to my housemates, Sarah, Lorna, and Shelly and my almost-housemates, James and Daniel; you were all a constant support inside and outside the department. Finally, thank you to Sammy for being (literally) by my side since the first day of the PhD, we got through many highs and lows, and I will forever be grateful for your friendship.

I would like to thank Zoë for being such an amazing friend for over a decade. Our teenage selves would be so proud of what we have achieved.

To Paul, thank you for constantly inspiring and motivating me to work harder, especially throughout the pandemic and the final year.

Finally, thank you to my family for all your love and support and always being there no matter what. To Chloe and Elliot, thank you for

being so great at everything you do and constantly pushing me to be better. Thank you to my Mum for believing in me even when I didn’t and making me the person that I am today. To Gramps, thank you for being so very proud of everything I have achieved, I wish you could be here to see this.

Publications

R. Nicks, A. Cocks, D. Avitabile, A. Johnston, and S. Coombes. Understanding Sensory Induced Hallucinations : From Neural Fields to Amplitude Equations. SIAM Journal on Applied Dynamical Systems, 20(4):1683–1714, 2021.

CONTENTS

1

INTRODUCTION

Despite the large amount of study involving the brain, the most complex organ in the body, there is still so much about the brain that is not understood. The complexity and ethical implications of performing experiments on the human brain emphasises the need for mathematical neuroscience for understanding the brain at microscopic, mesoscopic and macroscopic levels and to provide insight into mechanisms underlying natural computation. With the rapid growth of technology and computing power, we are able to collect vast quantities of data and also analyse and simulate brain activity in such a way that was not an option before. Close collaboration between the many fields that involve neuroscience, both theoretical and experimental, will allow further groundbreaking discoveries to be made.

The story of spontaneous pattern formation in models of visual cortex is one that has attracted much attention since it was developed in the 1970s by Ermentrout and Cowan to explain drug induced geometric visual hallucinations [38]. These often take the form of lattice (a.k.a. honeycomb, grating, or chessboard), cobweb-like, tunnel (a.k.a. funnel, cone, or vessel), and spiral patterns, as described in the experiments of Klüver [67] in which participants were given mescaline. When transformed from the retinocentric coordinates of the eye to the coordinates of the primary visual cortex (V1), these so-called Klüver form constants manifest as simple geometric planforms such as rolls, hexagons, squares, etc. [106].

Neural field models are used to represent the activity in the brain at the tissue level and we will use these to model activity in V1. They are formulated as a type of continuum neural mass model that use spatial-temporal coarse grained scales to model population activity. Neural field models are either activity or voltage based and we will be focusing on the latter. Neural fields are essentially descriptions of cortical neural activity described by integro-differential equations. They are specified by a set of nonlocal spatial interaction kernels and nonlinear firing rate functions to describe the coarse-grained activity of interacting excitatory and inhibitory neuronal populations.

It was the great insight of Ermentrout and Cowan that some of the geometries of the Klüver form constants could be generated via a Turing instability in a simple neural field model of V1. Despite the difference in their mathematical form from many other pattern forming systems that arise in the modelling of physical systems, and in particular partial differential equations of reaction-diffusion type, they can be analysed using many of the same techniques. For example, a weakly nonlinear analysis can be used to derive the amplitude equations for patterns emerging beyond the point of a Turing instability [37, 116]. Cells in V1 are selective to certain features for example orientation, meaning they respond strongly to a particular orientation. More recently, an extension of the original work by Ermentrout and Cowan was developed by Bressloff et al. [21] to describe the dynamics of orientation selective cells. This more biologically realistic neural field model includes anisotropic lateral connections that only connect distal elements with the same orientation selectivity along the direction of their (common) orientation preference. Interestingly this model can generate representations of all the Klüver form constants. Nevertheless, both this and the original model of Ermentrout and Cowan have a focus on spontaneous pattern formation that is induced by changes of parameters intrinsic to the models, rather than by external drive. However, it is particularly important to address this when trying to understand the mechanisms of sensory induced illusions and hallucinations in response to the presentation of either static or dynamic visual input.

The focus of the theoretical study presented in the first part of this thesis, is on the type of visual hallucinations reported in the work of Billock and Tsou [10]. These authors tried to induce certain geometric hallucinations by biasing them with appropriate visual stimuli from a flickering monitor. For example, a set of centrally presented concentric rings was expected to induce a hallucination of circle in the surround. Instead, and to their surprise, they found that fan-shaped patterns were perceived in the surround (and a complementary pattern of concentric ring circles in the surround for radial patterns in the center). The retinocortical map, mentioned above, tells us that the corresponding patterns of neural activity in the primary visual cortex for rings and arms in the retina are orthogonal stripe patterns. The implication of the psychophysical experiments of Billock and Tsou is that cortical forcing by spatially periodic input can excite orthogonal modes of neural activity. By using a neural field model with spatial forcing, we can use analysis techniques such as Turing analysis and deriving amplitude equations find parameter regimes for the model to simulate these psychophysical experiments.

Standard neural field models have focused on using connectivity profiles that are homogeneous and isotropic; however,this is a significant simplification of complex biological details. The focus of this work in the second half of the thesis is to explore neural field models incorporating the patchy connectivity that is observed biologically in visual cortex. Furthermore, this is now known to be approximately hexagonal in nature [42, 129], and can be incorporated into the model using modulation by a hexagonal lattice, as a first approximation. Again, by performing Turing analysis on the model, the system can be positioned past bifurcation to allow for spontaneous pattern formation to observe the resultant neural activity patterns when patchy connections with a hexagonal geometry are imposed. The cells in V1 have an orientation selectivity, that is, they respond strongly to lines or edges of a particular orientation, and the layout of orientation preference is described by an orientation preference map (OPM). The OPM has a pinwheel structure where all orientations converge and linear regions in which orientations are parallel to each other. The same structure of the patchy connections is seen in the orientation preference map in visual cortex, with the pinwheel structure and linear regions of orientation appearing in a similar manner. By using the patchy connectivity in a multi-layer model with different orientations we show that this can create an orientation preference map. The work of Rankin and Chavane in [96] on a multi-layered model including orientation preference is used as a starting point for a multi-layered neural field model. It also provides methods for converting layers of neural activity into one optical imaging signal to obtain the orientation preference map.

The structure of the thesis is as follows. We start by covering the background of the visual system and neural field models including a literature review in chapter 2. This gives an overview of the biology of vision and the mechanisms and mappings required for the first section of the visual pathway, from the eye to primary visual cortex. Also, neural field models will be introduced and explained to show how these fit into modelling activity in V1.

Chapter 3, 4 and 5 focus on modelling the visual hallucinations described by Billock and Tsou [10]. Firstly in chapter 3, the psychophysical experiments that we are interested in modelling are introduced. Next, there is an overview of other pattern-forming dynamical systems that have similar properties to the ones that we desire, to aid us in developing a model. We then explore the linear stability of the neural field model using Turing analysis. In chapter 4, we then explore the neural field model with spatial forcing to derive amplitude equations using weakly nonlinear analysis to give parameters for pattern formation. Details of the calculations are provided in Appendix A. Simulations for the model are computed giving stationary results of neural activity showing the desired pattern formation in two dimensions for the Billock and Tsou hallucinations. Then, a model with adaptation to allow for the development of travelling waves and time varying percepts is analysed in chapter 5, thus giving us the ability to model the spatial phase changes with time in the hallucinations. Firstly, the model with adaption is introduced in one dimension and the linear stability of the new model is explored. Amplitude equations for this model are derived and parameter regimes for the existence and stability of time varying percepts are found. Again, further details of the calculations are provided in Appendix B. The theoretical work highlights patterns of activity which occur due to global forcing. The numerical simulations confirm that the phenomena of orthogonal response to forcing and movement of patterns also occur when forcing is applied on the cortical half space, more closely matching the experiments of Billock and Tsou who provided stimulation on only part of the visual field. Details on coding tools required for the simulations can be found in Appendix C.

Chapter 6 investigates the presence of patchy connectivity in the visual cortex as reported from biological studies. Whilst many current standard connectivity models are homogeneous and isotropic, incorporating patchiness requires this homogeneity to be abandoned. A new model of connectivity is introduced; firstly, to help introduce and develop the relevant methodology, we implement a square lattice model of patchy connections and perform Turing analysis to find the conditions for spontaneous pattern formation. Next, due to the patchy connections actually being hexagonal in nature [42, 129], we alter the lattice to hexagonal instead of square. Turing analysis is performed and numerical simulations are provided that are shown to agree well with the theory. Finally, we introduce a new parameter, ϵ, to control the strength of the patchy connections and again perform Turing analysis and provide simulations for this revised model. The code required to compute all of the simulations in this chapter is provided in Appendix D.

Finally, the focus of chapter 7 is to define a simple connectivity rule that can lead to spontaneous pattern formation of a realistic orientation preference map via a Turing instability. The work of chapter 6 underpins the development of the patchy connectivity model. This is developed and merged with the work of Rankin and Chavane [96] to create the required model and resultant orientation preference map. This chapter starts with a brief overview of the models and techniques explored in [96]. Further details of the model are provided in Appendix E. Next, a multi-layered model with patchy connectivity is explored and Turing analysis presented. Simulations of this model with different parameters are performed to find the best options to create a realistic OPM. Finally, orientation preference maps are computed from the network model, and shown to be robust with parameter variation. The code to create these simulations is provided in Appendix F.

We end this thesis with a summary of the main results provided in chapter 8. Then, we provide a discussion of the ways in which the work can be extended in the future.

2

BACKGROUND

2.1 THE VISUAL WORLD - BIOLOGICAL BACKGROUND

The brain is the most complex organ in the body. Despite the extent to which it has been studied by scientist for years, there are still many parts of the brain whose function and purpose are not yet understood. Due to the nature of how the brain has evolved, there appears to be a purpose for every area. The brain has around $10^{14} - 10^{15}$ highly organised synaptic connections [53]. Every area of the brain is connected to other specific areas of the brain, whether this is by short or long range connections. This means that activity in one area of the brain can affect any other region of the brain it is connected to. However, particular areas that perform certain tasks are more connected than others such as the visual cortex and auditory cortex.

There are areas of the brain that are more studied than others due to their interesting features and complexity, with the visual system being the most highly studied. This is aided by the first part of the visual system being located close to the surface of the brain and therefore making it easier to access. Yet there is still a vast amount to learn in this area and most of the knowledge is limited to the first visual processing areas. Vision is a complicated phenomena and the process of how it works is only partially understood; therefore, there is still a lot about how we see that is not known. In this chapter, we will focus on the visual pathway from the retina to the primary visual cortex, the first part of the visual system.

2.1.1 *Neurons*

The brain is composed of approximately 10^{12} neurons and every neuron has roughly 10^4 synapses [53]. These receive signals from sensory inputs to the brain, in our case the retina, and also signals from the intra-cortical connections between neurons. The neuron is a nerve cell that is comprised of an axon, a cell body and dendrites, which are all encased in a membrane, shown in Fig. 1. The cell body and dendrites receive electric impulses from other cells. The axon is able to transmit impulses to other neurons, a spike train of activity, to send a signal through the brain. Dendrites are on a micrometre scale, however, axons can range from <1 mm to 1 m [33]. The axon splits into many branches at its end, telodendria, to be able to reach other neurons to transmit this information to. Short axons are more efficient as the signal can be sent in less time; this is why cells that need to be more interconnected are grouped together. The axon is positioned close to, but doesn't touch, the cell bodies or dendrites of other neurons, this junction is called a neuronal synapse.

Information is sent from the presynaptic cell, the neuron transmitting the impulse, to the postsynaptic cell, the neuron receiving the impulse unidirectionally. A synapse has a membrane voltage potential that can be modified by activity from an input. Before the input it is at a dynamic equilibrium or resting potential which is approximately -65mV. The input causes the release of a neurotransmitter that causes the ion channels to open. The presynaptic and postsynaptic neurons then have different concentrations of ions that causes a difference in voltage. If the membrane voltage potential of a neuron at the cell body exceeds a threshold then an action potential is produced and this in turn then propagates along its

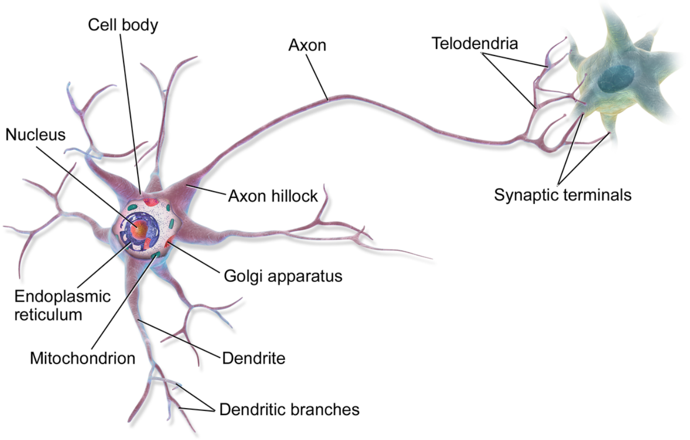

Figure 1.: A representation of a neuron, showing the cell body, axon and dendrites and how these synapse onto other neurons. Image reproduced from *Wikipedia*, Neuron.

axon to induce synaptic activity at sites across the entire brain. An action potential has a typical duration of approximately 1 ms [5], and after this the neuron is typically refractory, (cannot fire again), for another few ms.

2.1.2 *The Visual System*

The visual system is an extremely important part of the brain and allows us to process light signals to give a representation of our surroundings in the form of vision. It is also responsible for non-image producing processes such as circadian rhythms and pupilary light reflex. Humans have around 30 visual areas in the brain and approximately 50% of the surface area of the brain processes visual information [47].

Light rays are reflected off of an object and enter the eyes, refracted through the cornea, the pupil (which is controlled by the iris) and then the lens. A diagram of the parts of the eye is shown in Fig. 2. The refraction of the light results in an inverted image of the visual field being projected onto the retina, the back of the eye. The retina is comprised of photoreceptor cells which contain light sensitive proteins called opsins; in humans these are either rod opsins or cone opsins for visual processing. Rod opsins are used in low-level light and are mostly in the periphery of the retina. Cone opsins are used in normal light levels and distinguish colour by absorbing different wavelengths of light. The centre of the retina, the fovea, is solely comprised of cones. The fovea is only 1% of the retina, around half a millimetre in diameter, however it is densely packed and responsible for sharp, focused visual acuity [53]. It is the only area of the retina that is able to distinguish fine detail and can have 20/20 vision, a standard measure of normal vision describing the ability to seen an object clearly from 20 feet away. The rest of the retina is responsible for peripheral vision.

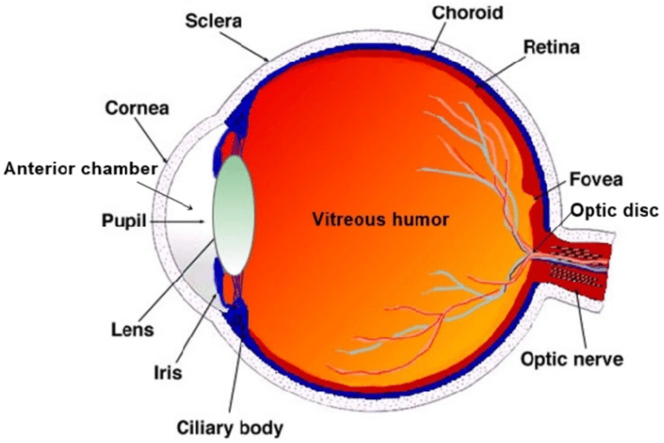

Figure 2.: A diagram of the parts of the eye. Image reproduced from [4].

The photoreceptor cells, rods and cones, form a synapse onto ganglion cells and then the axons of the ganglion cells form the optic nerve and can conduct spike trains to the next area of the visual system. There are approximately 130 million photoreceptors, yet around 1.2 million axons of ganglion cells that transmit signals from the retina to the brain [61]. The ratio of photoreceptors to ganglion cells is not uniform across the retina, at the fovea there is a 1:1 ratio whereas the edge of the retina has hundreds if not thousands of photoreceptors to one ganglion cell, meaning the information is not as highly retained. The point at which the optic nerve joins the eye is a natural blind spot as it is not possible to have photoreceptor cells there.

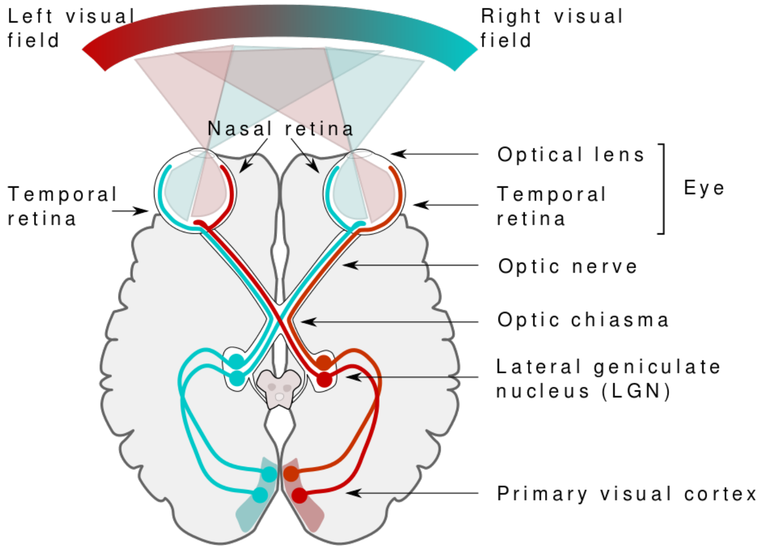

Figure 3.: A diagram of the initial part of the Visual System showing the pathway of the connections from the eye to the primary visual cortex (V1). Image reproduced from *Wikipedia, Magnocellular Cell*.

The signals from the left and right retina pass through their respective optic nerve's fibres to join together at the optic chasm, as shown in Fig. 3. The nerves sending information from the left visual field from both eyes are sent to the right side of the brain and vice versa. Thus, the visual fields are mapped onto the contralateral visual hemisphere of the brain. These signals then arrives at the lateral geniculate nucleus (LGN), this is a relay centre that splits the information received from the retina into different layers. The LGN is topographically organised, with a systematic mapping where the information of neighbouring cells on the retina are also neighbouring in the LGN. Organisation of cells by location provides the ability for cells to be connected to their neighbours with a lot of short range connections. Finally, the LGN is connected to the primary visual cortex (V1) by the optic radiation. The topological structure of the LGN is inherited in V1.

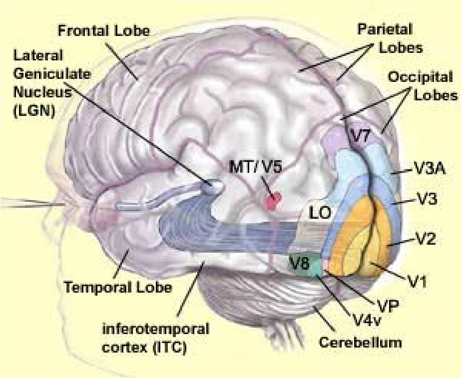

Figure 4.: A diagram of the brain showing the locations of the visual processing areas in the brain. Image reproduced from [39].

Signals from the retina to the visual cortex take approximately 40-60 ms to be transmitted. In humans, the visual cortex varies between 2-4 mm in thickness with surface area of around 200 cm^2 and the average number of neurons being 5 billion [123]. This is a lot more than the number of photoreceptors and ganglion cells, therefore the information is divided up and different parts are analysed together, this is discussed further in section 2.1.3. We will focus on V1, a large part of which is located at the back of the brain, see Fig. 4, in the calcarine fissure. The calcarine fissure is located at the back of the brain in the middle of the occipital lobe and divides the visual cortex, the location of which is shown in Fig. 5. V1 is composed of 100 million neurons and in comparison the input from the optical nerve only consists of 1 million fibres.

V1 is the first visual processing system in the brain and is one of the most studied. V1 has two very unique mappings that we will study, the retinocortical map and the orientation preference map. The retinocortical map is a well defined map of the position of stimuli on the retina to the position in V1. The orientation preference map shows which neurons in the cortex respond to certain orientations in the visual field. V1 is

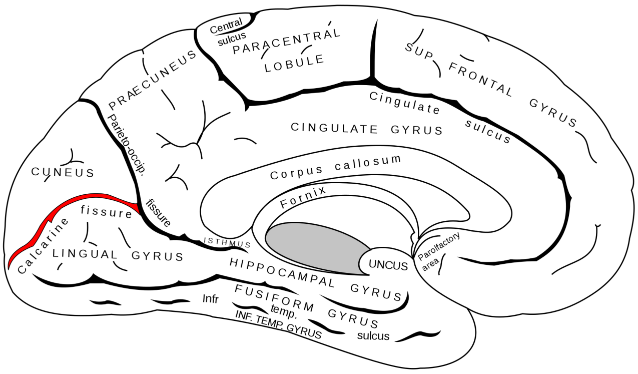

Figure 5.: A diagram of the parts of the brain, showing the location of the calcarine fissure (red). Image reproduced from *Wikipedia*, Calcarine Sulcus.

incredibly important in visual processing and does not just involve bottom up processes, only processing the information it is receiving [74]; but rather also top down processes that involve perception and filling in of images using past experiences. Furthermore, it is not limited to only basic visual processing, and is for example, involved in highly specific processes such as fine resolution of images. There are two types of connections in the primary visual cortex, retino-geniculo-cortical (vertical) connections and cortico-cortical (horizontal) connections; we will be focusing on the former when looking at activity in the tissue. The vertical connections are within the layers of V1 and the horizontal connections are between to the layers of V1, due to the hypercolumn structure between the layers, which will be outlined in section 2.1.4. V1 of a Macaque monkey is 50% of the surface area of its brain, so from that and their close genetic relation to humans is why they are predominately used in vision studies.

The visual system then continues after V1, with signals being sent onto V2, V3, V4 etc. seen in Fig. 4. Secondary visual cortex (V2) is the second area in the visual cortex. It receives strong feed forward signals from V1 but also sends strong feedback connections to V1. It has more attention modulation than V1 and its response is more complex. Following on from V2 is the third visual cortex, which includes V3; controversy still exists regarding the exact extent of area V3. The top of V3 receives input from V1 and V2; whereas, the lower regions have weaker connections to V1. Visual area V4 receives strong feed forward input from V2. V4 is known as the colour centre of the brain. However, no one has defined a full parametric description of V4 and all of these higher visual areas have lots of unknowns. Also these areas send information directly to a multitude of other areas in the brain to assist with both visual and non-visual specific tasks.

2.1.3 *Retinocortical Mapping*

We will use multiple coordinate systems throughout this work. The position of the stimulus in the real world is modelled by a 2D vector as only position, not depth, is required,

$$\mathbf{r_w} = (x_w, y_w). \tag{1}$$

This position is then transformed to a 2D position vector on the retina,

$$\mathbf{r_r} = (x_r, y_r). \tag{2}$$

The most interesting mapping for this work is the one from the retina to the visual cortex, the retinocortical mapping. The coordinate system for the visual cortex is denoted by,

$$\mathbf{r_c} = (x_c, y_c). \tag{3}$$

The transformation of the retinal coordinate system to the cortical coordinate system, $\Psi : \mathbf{r_r} \to \mathbf{r_c}$, is nonlinear. A representation of the human visual cortex, Fig. 6, shows that the distribution of cells are not arranged linearly and a large portion of the visual cortex is comprised of the first few degrees of the visual field. The reconstruction of the human V1 using fMRI recordings has been completed in [34, 104, 123]; before these fMRI reconstructions there had only been reconstructions of macaque visual cortex [119]. The retina has fovea to periphery gradients horizontally and vertically from the lower vertical meridian (LVM) to the upper vertical meridian (UVM). However, the fovea to periphery gradient in the primary visual cortex is nonlinear and there is a huge magnification of input from the fovea. This nonlinearity is extremely important in visual processing and for us, how hallucinations occur.

One of the main structures of the visual cortex is this retinotopy structure, a neurophysiological projection of the retina to the visual cortex, a mapping in a mathematical sense. The complex-log mapping [107] is the most common representation of the mapping of points from the retina to the visual cortex. The cross section of the right visual field is mapped to the left visual cortex. The visual fields are contralaterally projected onto the opposite primary visual cortex's. These are both identical; therefore, we only need to consider one of the visual fields as the other one is identically translated to the other hemisphere of the brain. The fovea is only 1% of the area of the retina; however, is magnified to be responsible for 50% of the area of V1.

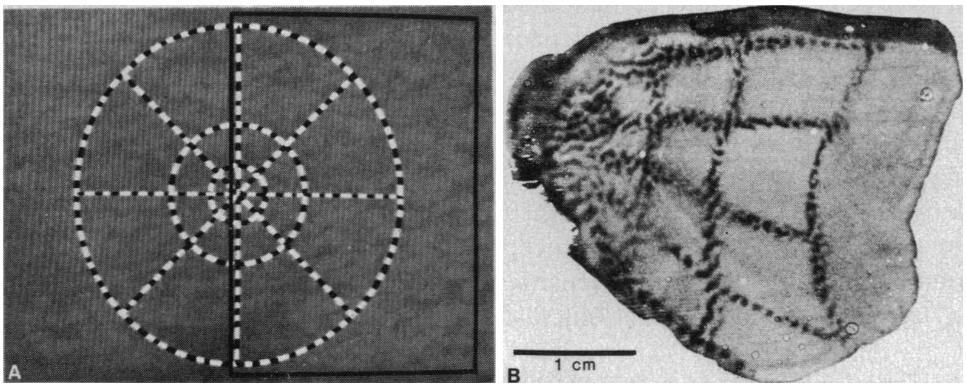

(a) Visual Field (b) Actual right V1

Figure 6.: Retinocortical mapping reproduced from [118]. The visual field (a) is mapped to primary visual cortex in a complex logarithmic like manner (b).

The first retinocortical mapping, proposed by Schwartz in 1980 [107], was the monopole mapping,

$$\Psi(z) = \log(z + a), \qquad z, a \in \mathbb{C}, \tag{4}$$

where z is the position on the retina represented as a complex number, $z = \rho e^{i\theta}$, and $a < Re(z)$ gives a linear mapping and for larger z this is closer to a logarithmic mapping. This was then extended to the dipole model [104],

$$\Psi(z) = k \log \frac{z + a}{z + b}, \qquad a, b, k, z \in \mathbb{C}, \tag{5}$$

with b helping shape the boundary for periphery vision and k being a scaling constant. There are many different versions of this model that can be found in the literature as this is the most widely accepted model for the retinotopical mapping. By using the different values for a and b given in [3], [92] and [104], this gives generic models for the retinocortical map; examples of which can be seen in Fig. 7. The fovea massively expanded and is mapped to around half of the left side of these models and then the right side is the mapping of the rest of the retina. These are simplistic mathematical models of Fig. 6, with (b) being a more realistic looking model.

However, these basic dipole models are not a good representation of the visual cortex, especially at the fovea [104]. This is due to neither of them showing topographical anisotropy, shear, at the vertical meridians, which represent peripheral vision. In [12] results show that there is indeed a diminution at the vertical edges of V1 and therefore, this has to be included in the model. A new model is proposed in [104], the Double-Sech model, which introduces a shear term f_γ, $\gamma \in \{a, b\}$;

$$\Psi(z(\rho, \theta)) = k \log \frac{\rho e^{i\theta f_a} + a}{\rho e^{i\theta f_b} + b}, \qquad a, b, k \in \mathbb{C}, \tag{6}$$

where $\rho = |z|,\ z \in \mathbb{C}$, and $\theta = \arg z,\ z \in \mathbb{C}$, and

$$f_\gamma = \text{sech}(\theta)^{0.1821 \text{sech}(0.76 \log(\rho/\gamma))}. \tag{7}$$

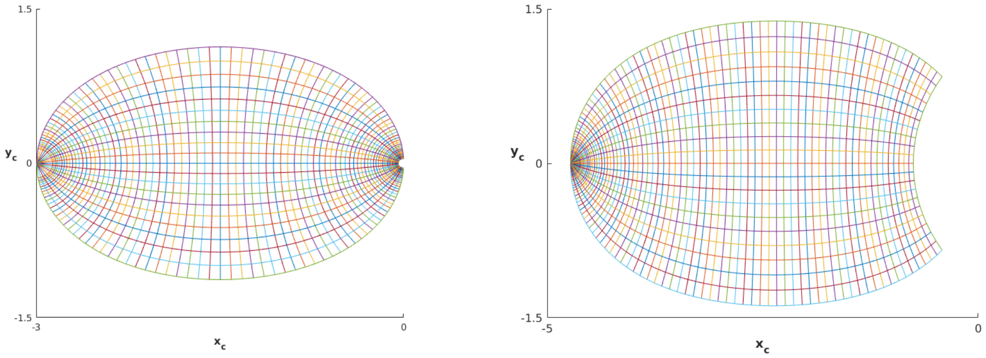

(a) The dipole model from (5) with $a = 0.333$, $b = 6.66$ and $k = 1$.

(b) The dipole model from (5) with $a = 1.5$, $b = 170$ and $k = 1$.

Figure 7.: Two models of the dipole mapping redrawn from [92] and [3] respectively.

However, whilst this is an entirely new geometric principle, the model is not a lot more computationally expensive. The Double-Sech model shows that the mapping is no longer as uniformly curved, this can be seen in Fig. 8.

Comparing the actual visual cortex, Fig. 6, to these models that have been presented, Fig. 7 and 8; whilst these are the standard mappings used, none of these retinocortical mappings are a completely accurate representation of the visual cortex. The Double-Sech model perhaps being the closest to the true shape. Some more complex models of the retinocortical mapping have also been proposed, such as [59, 60], using a spatial density model and fitting it to magnification data.

2.1.4 *Orientation Preference Map*

There are three types of structures that occur in V1; these are the layered, retinotopic and hypercolumn structures. Firstly, the layered structure is comprised of approximately the depth of V1, 1.8 mm, and is constructed of six horizontal layers parallel to the surface of the cortex. Most of the

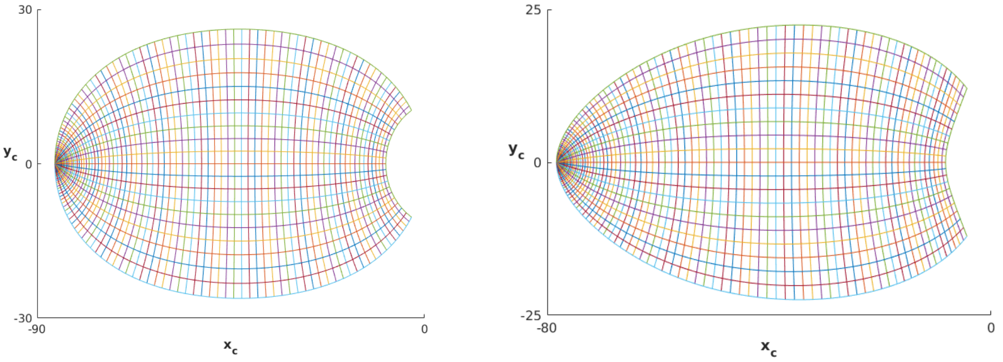

(a) The dipole model from (5) where $a = 1.05$, $b = 90$ and $k = 19.3$.

(b) The Double-Sech model from (6) with $a = 0.96$, $b = 90$ and $k = 17.6$.

Figure 8.: A comparison of the dipole and Double-Sech model from [104], emphasising the shear at the top and bottom edges in the Double Sech model.

input from the LGN arrives at layer 4, specifically to the sub-layer 4C. This then relays input to layers 2 and 3 and projects to layer 5, layer 6, the spinal cord and thalamus respectively. Secondly, the retinotopic structure means that input from the retina is globally mapped to layer 4C of the visual cortex to preserve the retinal topography. There is a local mapping of the retinotopical mapping to the other layers of the visual cortex from layer 4C that is also topologically preserving.

Finally, the hypercolumn structure is the splitting of V1 into columns that are perpendicular to the surface of the cortex. This also keeps the retinal position and orientation preference roughly constant. V1 is comprised of simple neurons which are sensitive to orientation, ocular dominance and colour. Orientation columns are approximately 20μm apart and are a horizontal grouping of columns whose input are from retinal cells with a preferred orientation varying from 0 to π. These three types of structure allows the brain to process images at a higher resolution than just receiving this information from a single neuron. This early orientation selectivity is crucial for all higher forms of visual processing and is a fundamental part of the visual cortex [6]. A representation of this structure can be seen in Fig. 9.

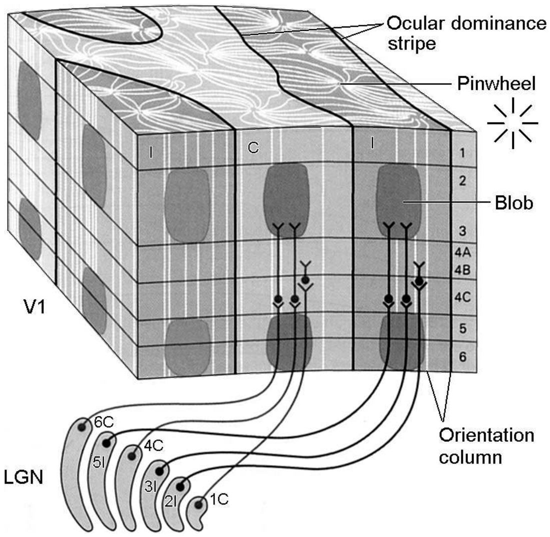

Figure 9.: Hypercolumn in primary visual cortex showing the orientation columns arranged in pinwheels and how the ocular dominance stripes from the ipsilateral (I) and the contralateral (C) eye alternate. The connections between the layers of the cortex 1-6 are shown and how this corresponds to the input received from the lateral geniculate nucleus (LGN). Reproduced from [7].

The variation of orientations of the hypercolumns across V1 is not monotonic and it was not until the 1990s when *in vivo* optical imaging determined the structure of this orientation preference map (OPM) [14]. The orientation preferences rotate over V1 and approximately every 300 μm the same orientation preference reappears. The orientation of the stimuli is represented as its acute angle; therefore, only range from 0 to π. The work of [54, 55, 56] and then [13, 46] showed that the OPM has a pinwheel structure. The OPM is covered in singular points, where all the orientations converge, which are approximately 600μm apart in primates. These are then connected with all of the orientations from 0 to π to make a global map. These pinwheel structures are bounded by areas of linear zones, see Fig. 10. Therefore, the OPM is comprised of three main structures; regular lines that are approximately parallel to each other, singular points at the centre of the pinwheels where the orientations converge and saddle points where bifurcations of orientations occur, two orientations leave one pinwheel and diverge to two separate pinwheels. These features can be seen in Fig. 10b, with the linear areas and pinwheels being shown specifically.

The map is globally homogeneous; however, at the pinwheels it appears to be inhomogeneous. This is due to the perception of the colours representing the different orientations, see Fig. 10, at the pinwheel. When a pinwheel occurs, all the colours converge which results in a colour wheel. When a continuous colour wheel is used this causes the primary colours to dominate and the secondary colours appear to not be as prominent. This makes some orientations appear to occur more than others when in fact they are all equally distributed. When the orientation preference map is discretised, the work of [53, 56] shows that the neurons responding to a certain orientation preference changed every 10 degrees on average, therefore, ideally would be modelled as roughly 18 different orientations. When discretised, the colour map will look homogeneous as the colour wheel will show a higher contrast between colours.

We can synthetically model the orientation preference map, θ, using a random field model adapted from [91];

$$T(x_c, y_c) = \sum_{k=1}^{k=N} c_k \mathrm{e}^{2i\pi\left(x_c \cos\left(\frac{2\pi k}{N}\right) + y_c \sin\left(\frac{2\pi k}{N}\right)\right)}, \tag{8}$$

$$\theta(x_c, y_c) = \frac{1}{2}\left(\tan^{-1}\left(\mathrm{Re}(T(x_c, y_c)), \mathrm{Im}(T(x_c, y_c))\right) + \pi\right), \tag{9}$$

where c_k are random complex coefficients, with the real and imaginary parts of each c_k variable being generated separately using a normal distribution of $\mu = 0$ and $\sigma = 2$. The choice of μ and σ gives a sufficient distribution of coefficients to give arctan values from $\pm\pi$ which is then shifted to the domain $[0,\ \pi]$. N is a parameter chosen here to be 2^8 following [91]. An illustration of this model, Fig 10a, in comparison to a real OPM is shown in Fig. 10.

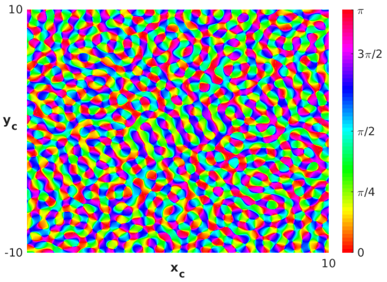

(a) A synthetic orientation preference map computed using (9).

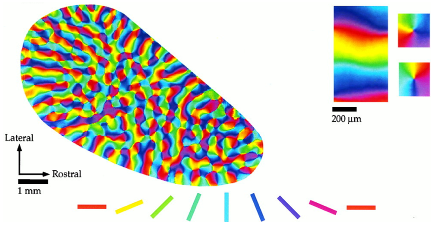

(b) Modified figure reproduced from [15] of a tree shrew's visual cortex with the colour coded orientations shown below. Sections of the orientation preference map have been highlighted, the left showing linear areas and the right showing two examples of pinwheel structures.

Figure 10.: A comparison of a synthetic OPM model from equation (9) and real data.

Neurons in the visual cortex have intra-cortical connections which are both local and long range. These are recurrent connections and the synaptically connected neurons constantly encode the changes in their firing pattern as the visual input changes. When a neuron fires due to a stimulus in the visual field, it also induces activity in nearby neurons, this is caused by the local connections. The local connections are independent of orientation and so, on average homogeneous. Activity is induced in neurons of a similar orientation preference all over the cortex via the long range connections. These long range connections are patchy [122] and are not homogeneous; they can link neurons of similar orientation preferences up to ±30 degrees difference in orientation.

2.1.5 *Hallucinations*

In the 1990s, mathematical neuroscientists such as Jean Petitot [91, 92] first developed the concept of 'neurogeometry of vision'. Originally this referred to the geometrical models of functional architecture of primary visual areas [25]. It is the internal and inherent geometric algorithms present in our visual system that allow the brain to build the external and transcendent geometry of our surrounding world [92]. The complicated structure and functions of the visual system are what we can use to explain why and how we perceive visual stimuli.

There are two aspects to neurogeometry, firstly the geometry of perception, the psychology of vision that has been researched for centuries by philosophers, psychophysicists and psychologists. This is known as perceptual geometry and it was only in the 1960s that mathematics was first used to understand this. Secondly, the stricter definition of neurogeometry is in fact the mathematical models for these neural algorithms that process perceptual geometry [25]. The mathematical models are geometric, yet in a completely different way to the perceptual geometry. Hallucinations are the result of differences between stimuli and visual perception. For example, the Kanizsa triangles in Fig. 11 are a type of sensory induced hallucination. They have been studied on a perceptual geometry level for centuries by psychophysicists, however they have only been modelled on a neurogeometry level in recent decades. These hallucinations are a result of the functional architecture of V1, the retinocortical mapping and OPM.

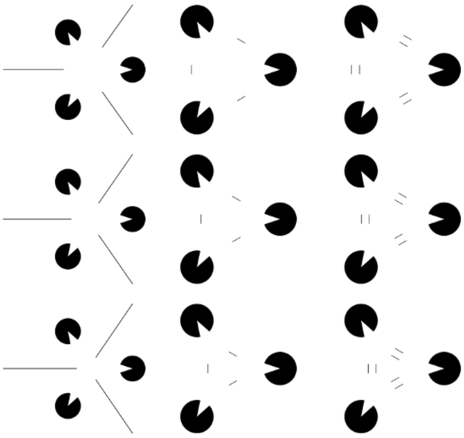

Figure 11.: Examples of curved Kanizsa triangles, with three ways of determining the position of the illusory curve. The most effective is the single lines parallel to the 'edges' of the triangle as seen in the middle. Reproduced from [25].

Geometric visual hallucinations can occur due to many different types of stimulations, this includes, flickering lights [49, 95, 110], administering certain types of anaesthetics [127], just before or after sleep [35], applying deep binocular pressure onto the eyeballs [121] and drug induced [88, 108]. Hallucinations have even been shown to be seen by blind subjects and also subjects in sealed dark rooms [70]. Furthermore, they are difficult to precisely locate in space and move with respect to eye movement, yet the actual position of the hallucinations relative to each other remains the same [67]. These behaviours have lead to the conclusion that hallucinations are not generated in the eye but in the way the brain processes this information.

It has been proposed that the first areas of the visual cortex, V1 and V2, are where hallucinations occur, especially if the stimuli requires precise inspection for the hallucination to be observed [68]. The topological representation of V1 has been suggested to support the occurrence of these hallucinations. The hallucinatory images are generated in V1 and then the mechanisms of V2 stabilise the image with respect to eye movements.

There are feedback mechanisms between the V1 and V2, so the image stabilising information is fed back to V1 [74].

2.1.6 *Summary of Vision and its Application*

This section has introduced how the visual system works from the eye to the visual cortex and the mechanisms present in V1 for how the stimuli is mapped from the eye to V1 and orientation is processed. V1 is an important part of the visual system and is responsible for many aspects of vision. The retinocortical mapping is vital for us to be able to understand the activity in V1, due to its unintuitive nature and nonlinearity. It allows us to see how stimuli are mapped to neurons in V1 and how that can affect visual perception. The retinocortical mapping underpins how and what hallucinations can occur. The OPM is an extremely sophisticated aspect of V1. In the next section we will introduce neural field models and how these can be used to model V1 at the tissue level.

2.2 NEURAL FIELD MODELS

Before the 1900s very little was known about activity in the brain. The first EEG recording was done by Hans Berger in 1924 [103]. This sparked interest in developing models on how this activity could be generated. The earliest work on neural fields was by Beurle [9] in the 1950s. Beurle's model was a continuum approximation, instead of looking at a single neuron, he modelled the active neurons over the entire tissue per unit time. However, his work only took into consideration the neurons that were exactly at the firing rate threshold and these models really needed to incorporate all neurons that are at or above the threshold excitation. Furthermore, there were no inhibitory neurons in this model. There were also single neuron models developed around this time. However, these consider brain activity at the microscopic scale, whereas we wish to model macroscopic dynamics which requires models of neuronal tissue and therefore, a population of neurons.

The modern incarnation of neural field models were first published by Wilson and Cowan [125, 126], Nunez [86] and Amari [1] in the 1970s. Wilson and Cowan constructed an activity based neural field model that distinguishes between excitatory and inhibitory sub-populations. Their equations can be written in continuum or network form and are mean field equations. Nunez and Amari focused their single population voltage-based models on local excitation and distal inhibition. All neural field models represent a continuous network of interacting populations across the cortex at the tissue level. Furthermore, neuronal densities are considered to create spikes of activity per unit time, modelled by a mean firing rate. The spatial distribution of neuronal connections is modelled using an anatomical weight kernel.

The predominant model for voltage-based neural fields is the Amari equation, for a position $\mathbf{r}$ in the domain Ω,

$$\frac{\partial u(\mathbf{r},t)}{\partial t} = -u(\mathbf{r},t) + \int_{\Omega} w(\mathbf{r},\mathbf{r}') f(u(\mathbf{r}'),t)\; \mathrm{d}\mathbf{r}', \tag{10}$$

where $u(\mathbf{r},t)$ is the activity of the cortex at position $\mathbf{r} = (x,y)$, evolving over time t. The kernel w represents the connection between neurons and can include excitatory interactions as positive values and inhibitory interactions as negative values. The firing rate of the neurons is represented by f and this is modelled using a sigmoidal function.

The kernel, or weight function, is often represented by a function of the distance between neurons, so that it is translationally invariant,

$$w(\mathbf{r},\mathbf{r}') = w(|\mathbf{r}-\mathbf{r}'|). \tag{11}$$

This can then be used to write the integral as a spatial convolution. When this is combined with Fourier transforms, the model is easy to computationally simulate in the case where $\Omega = \mathbb{R}^2$. One of the simplest choices for w is the decaying exponential function,

$$w(\mathbf{r}) = \frac{e^{-|\mathbf{r}|}}{2}. \tag{12}$$

However, this is only a representation of short range excitatory connections and has no inhibition. Therefore, usually a second exponential is added to give a Wizard-hat shaped connectivity model, examples of these include

$$w(\mathbf{r}) = e^{-|\mathbf{r}|} - \frac{e^{-|\mathbf{r}|/2}}{2}, \tag{13}$$

$$w(\mathbf{r}) = (1 - |\mathbf{r}|)e^{-|\mathbf{r}|}, \tag{14}$$

and

$$w(\mathbf{r}) = Ae^{-\mathbf{r}/\sigma} - e^{-\mathbf{r}}, \qquad A > 1,\ \sigma < 1. \tag{15}$$

Sometimes it is useful to work with a 'balanced' kernel with the property $\int_{\mathbb{R}^2} w(\mathbf{r})d\mathbf{r} = 0$. For equation (15) this is achieved in two-dimensions when,

$$A = 1/\sigma^2. \tag{16}$$

Equation (15) is a good representation of typical cortical connections which includes the excitation and inhibition. A Mexican-Hat shape is also often chosen, this is a difference of Gaussians,

$$w(\mathbf{r}) = e^{-|\mathbf{r}|^2} - \frac{e^{-|\mathbf{r}|^2/2}}{2}, \tag{17}$$

which is similar to the Wizard-hat formula (13) but the square allows it to be differentiable at the origin which may be useful in analysis. An example of a mathematical connectivity kernel can be seen in Fig. 12.

The simplest model of the firing rate is the Heaviside function,

$$f(u) = H(u - h) \tag{18}$$

where H is the Heaviside step-function, a piecewise function,

$$H(x) = \begin{cases} 1 & x > 0, \\ 0 & x \leq 0, \end{cases} \tag{19}$$

and $h \in \mathbb{R}$ is a threshold parameter to move the step of the function. This is often used in analysis due its tractability. In this work, we shall take another commonly used sigmoidal function for the firing rate,

$$f(u) = \frac{1}{1 + \mathrm{e}^{-\mu(u-h)}}, \tag{20}$$

where $\mu \in \mathbb{R}^+$ is used to control the steepness of the sigmoid around the threshold value $h \in \mathbb{R}$ [27]. This tends to the Heaviside function as $\mu \to \infty$. An example of this can be seen in Fig. 12

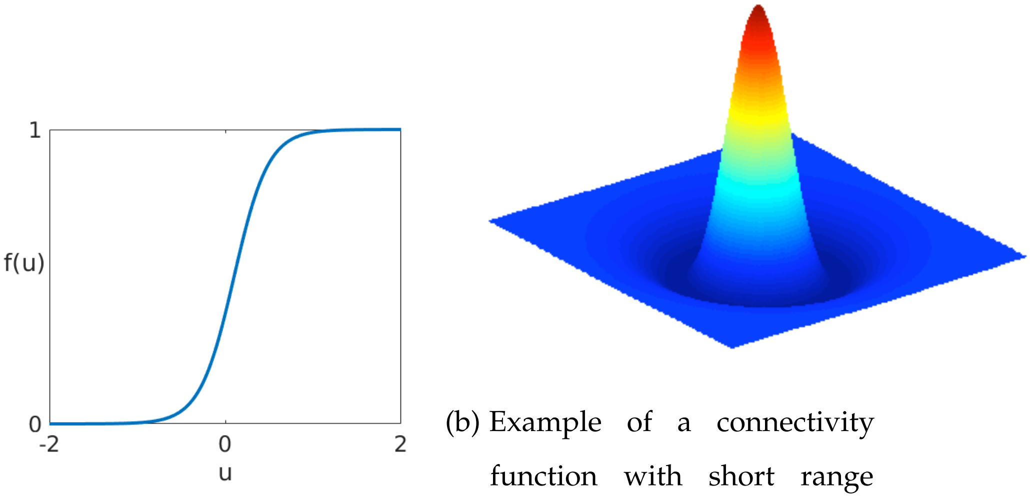

(a) Example of sigmoidal firing rate.

(b) Example of a connectivity function with short range excitation and long range inhibition.

Figure 12.: Examples of the functions used in the neural field equation to model neuronal activity across a tissue.

Obviously, there are both advantages and disadvantages to using any of these models as they are only approximate representations of brain activity. The neural field models have the advantage of having fewer parameters than spiking neural networks and do not resolve single neurons. Therefore, they are lower dimensional than other models. However, this is only the most simplistic version of this model, as then it can also be extended in multiple different ways; this can be by adding more populations, external activity or orientation preference to name just a few examples.

2.3 EXTENDING THE NEURAL FIELD MODEL

The model (10) is the basic neural field models that can initially be built upon to incorporate other factors that need to be included such as input and adaptation. Input can be added as an extra term,

$$\frac{\partial u(\mathbf{r},t)}{\partial t} = -u(\mathbf{r},t) + \int_{\Omega} w(\mathbf{r},\mathbf{r}')f(u(\mathbf{r}'),t)\,\mathrm{d}\mathbf{r}' + I(\mathbf{r},t), \tag{21}$$

with $I(\mathbf{r},t)$ representing an external input. If the input I is set to zero then the system is unforced. However, adding this forcing term can lead to different types of pattern formation. The input can incorporate both time and space. It can also be used as a bifurcation parameter of the system [126]. Furthermore, the input can be inhomogeneous [22, 40]. The forcing term can represent interaction between neurons but also external stimuli that the brain receives. It is an adaptable term that can help model many of the brain's intricacies.

The neural field model can also be extended by adding the concept of negative feedback, often referred to as spike-frequency adaptation, that the spiking rate of neurons drops after sustained activation due to the high metabolic demand of spiking activity [94]. This implementation aims to capture this effect at the population level. From the biological description of a neuron in section 2.1.1, it is known that a neuron must require a certain level of activity for it to spike, which is implemented by the firing rate. However, it also must return back to the resting potential after periods of high activity and this makes it harder for the neuron to fire again. This model is based on work by Hansel and Sompolinsky [48], where they consider a network in which the excitatory cells are given spike-frequency adaptation. Spike frequency adaptation was then extended by several authors such as [32, 94] to be often modelled with the use of a negative feedback term that couples to a field a with dynamics of a simple linear form,

$$\frac{1}{\tau}\frac{\partial u(\mathbf{r},t)}{\partial t} = -u(\mathbf{r},t) + \int_{\Omega} w(\mathbf{r},\mathbf{r}')f(u(\mathbf{r}'),t)\ \mathrm{d}\mathbf{r}' - ga(\mathbf{r},t), \tag{22}$$

$$\frac{\partial a(\mathbf{r},t)}{\partial t} = u(\mathbf{r},t) - a(\mathbf{r},t), \tag{23}$$

where $a(\mathbf{r},t)$ is a field that describes the local feedback mechanisms that modulate synaptic currents in the tissue. The parameter $g \in \mathbb{R}$ the strength of the negative feedback and $\tau > 0$ sets the relative time scale of the two processes. Adaptation can be used with only excitatory kernels to include inhibition in the model as seen in [22, 40]; more uses of adaptation are seen in [26].

More extensions of the neural field model can be including two populations, one of excitatory neurons and one of inhibitory to have more control over the types of connections in the model for interesting pattern formation [125, 126]. Also, delays can be added to the model as the transfer of activity across the cortex is not instantaneous especially for longer range connections and these have an affect on neural activity [26, 57, 58].

2.3.1 *Neural Field Models for Vision*

'. . . the hallucination is . . . not a static process but a dynamic process, the instability of which reflects an instability in its conditions of origin' [67, 21].

Many neurobiological phenomena have been modelled using integro-differential neural field equations such as: wave propagation in cortical slices [94, 98], *in vivo* experiments of spiral waves in rat neocortex [52], EEG rhythms [77, 87, 99, 113], geometric visual hallucinations [21, 38], orientation tuning in V1 [8, 20, 111], short term working memory [24, 73], control of head direction [131], motion perception [43], binocular rivalry [23, 124] and the aperture effect in motion vision [97].

The first mathematical theory of visual hallucinations appeared in 1979 by Ermentrout and Cowan [38], developing a possible mechanism for spontaneous patterns of neural activity for hallucinations from hallucinogenic drugs. This was modelled using the Wilson and Cowan equations; a model of excitatory and inhibitory populations of neurons on a two-dimensional cortical sheet. The spatially periodic activity patterns occurred because of a bifurcation from a homogeneous low activity state due to a Turing-like instability [120]. Their model was also able to support hexagon and square patterns.

This was then explored further by Bressloff *et al* in 2001 [21], where they studied the relationship between geometric visual hallucinations and the functional architecture of the striate cortex. The large-scale dynamics of spatially structured networks of neurons required to model the hallucinatory activity on the cortex is easy to see using such models. However, this only works providing that the firing rate incorporates short-range excitation and long-range inhibition interactions. These models can exhibit a considerable number of spatiotemporal dynamical properties, such as travelling fronts, pulses, spiral waves and Turing patterns [19, 26, 37].

2.3.2 *Orientation Preference Models*

Using standard neural field models is an oversimplification of the cortex and is just a projection of the activity on the retina. For more complex hallucinations other than stripes and squares, the OPM needs to be incorporated. The OPM being included in the neural field model is seen in the work done by Bressloff in [21]. Thus, by writing the connectivity kernel as,

$$w(\mathbf{r},\mathbf{r}') = W(|\theta(\mathbf{r}) - \theta(\mathbf{r}')|), \tag{24}$$

where, as well as having $\mathbf{r}$, (the position on the cortex), $\theta(\mathbf{r})$, (the orientation preference of a neuron at position $\mathbf{r}$), is also incorporated,. Here $W(|\theta(\mathbf{r}) - \theta(\mathbf{r}')|)$ is the weight of the connections between neurons at position $\mathbf{r}$ tuned to the orientation θ and $\mathbf{r}'$ tuned to the orientation θ'. Due to features of the OPM now being incorporated into the model, we can no longer treat the anatomical connectivity w in the neural field equation as homogeneous.

The model can also be adapted to incorporate other features of the functional architecture of V1 such as ocular dominance and spatial frequency [18, 100]. Furthermore, Bressloff also looks at working on planar Cartesian lattices in 2D to be able to produce all of the pattern types and there are a range of planforms in [21], that are able to achieve spirals, hexagons, rhombus' etc.

2.3.3 *Summary of Neural Field Models*

This section has introduced neural field equations and how they are used to model brain activity. In particular, we have discussed the Amari model (10), a nonlinear single population integro-differential equation, and how it can be extended. We use the connectivity kernel to model short range excitation and long range inhibition across the cortical tissue. This is a basic model that can then be adapted to incorporate more complex aspects of brain activity. This is the standard model used in a wide range of recent research, especially in visual neuroscience modelling. The rest of this thesis will use neural field equations to model neural activity in V1.

3

UNDERSTANDING SENSORY INDUCED HALLUCINATIONS

The aim of the next three chapters is to be able to use mathematical neuroscience to explain the visual hallucinatory phenomena shown by Billock and Tsou in [10]. There is little known about the interactions between sensory driven and self organised cortical activity. Therefore, we are going to use mathematical models to help understand more about the hallucinations presented in [10], first discussed in chapter 1 and expanded on later in this chapter. A standard way to model brain activity is to use neural field equations to model activity in the brain at a tissue level, see discussion in chapter 2. We will use such models and analyse them to understand the types of pattern formation that can occur in response to spatially structured visual drive. Pattern formation can occur when a dynamical system is driven past the point of a Turing bifurcation and a spatially homogeneous steady state becomes unstable, for example. Thus small perturbations can grow exponentially to create patterns of activity. Amplitude equations are a quantitative description of patterns that evolve in time and space after a bifurcation. We can use these to analyse the type of pattern formation that arise and to understand how sensory induced hallucinations occur. The same properties that govern natural vision are also expected to govern natural self-organised hallucinations. Therefore, we can also use the retinocortical mapping and other know aspects of visual processing to model hallucinations.

Recall from chapter 1 that, the implication of the psychophysical experiments of Billock and Tsou is that cortical forcing by spatially periodic input can excite orthogonal modes. For instance, cortical forcing with spatially periodic vertical stripes can result in an emergent activity pattern of horizontal stripes, orthogonal to the stimulus. Thus, a natural question arises as to whether there is a minimal model of visual cortex with external drive capable of supporting this observed orthogonal response and whether it requires a departure from existing neural field models. In short the answer is that standard neural field models with a state-dependent drive are sufficient and we will demonstrate this in this chapter and the next. Although the orthogonal response property may seem somewhat surprising from an experimental perspective, relatively recent theoretical studies of the spatially forced Swift-Hohenberg equation have shown that under certain mild conditions orthogonal responses are robust [81]. Here we adapt and develop the techniques originally used for analyzing spatially forced partial differential equation models to nonlocal neural fields and use these to uncover the parameter windows that robustly reproduce orthogonal responses to spatially periodic forcing. In doing so we highlight the potential mechanisms that can underpin the original psychophysical observations of Billock and Tsou.

Firstly, in section 3.1 we will introduce the psychological experiments of Billock and Tsou that we are interested in modelling. Next, in section 3.2 we give an overview of the work on the spatially forced Swift-Hohenberg equation [81] which revealed a mechanism by which orthogonal response to forcing can be achieved. This will aid us in developing and describing the analytical methodology for our extension of this work to nonlocal systems. The key mechanism for the success of the model is the combination of a Turing instability and a 2:1 resonance arising between the spatial scale of the periodic forcing and that of the emergent Turing pattern. An important parameter of the model is then the spatial frequency mismatch between these two scales. In section 3.3, Turing analysis of the standard neural field model is explored. Next in chapter 4 we introduce the neural field model with spatial forcing in one and two dimensions. For both of these models, we develop a weakly nonlinear analysis, valid for weak forcing in the neighborhood of a Turing instability, and derive equations governing the amplitude of emergent planforms. This is concluded with the simulations produced from this stationary two-dimensional model using parameters obtained from the analysis to explain the psychophysics. This work will then be extended again in chapter 5 to included the movement present in the hallucinations reported by Billock and Tsou [10]. This work is published in [85].

3.1 PSYCHOPHYSICAL OBSERVATIONS

The first mathematical theory of visual hallucinations appeared in 1979 by Ermentrout and Cowan [38], developing a possible mechanism for spontaneous patterns of neural activity for hallucinations from hallucinogenic drugs. This was then explored further by Bressloff *et al* in 2001 [21]. They investigated geometric visual hallucinations and the functional architecture of the striate cortex using orientation preference of the neuron in the neural field model. Geometric hallucinations, most commonly lattices, spirals, circles and fan shapes, are thought to occur from autonomous activity in the visual cortex. These hallucinations are seen as spontaneous states of activity as they arise due to the natural organisation of the visual cortex and can even occur without any presented stimuli on the retina. The hallucinations are governed by the orientation preference map and the retinocortical mapping as these are the key components of how the visual cortex processes information. In humans, hallucinations have been seen to arise from migraines, drug intoxication, and empty-field flicker [102].

Surprisingly little is known about the interactions between sensory-driven and self-organized cortical activity. Billock and Tsou have worked to address this deficit by probing the link between natural visual perception and the geometric hallucinations that can be induced by the presentation of certain regular spatio-temporal patterns. In [10], Billock and Tsou investigate whether these sensory induced patterns arise in humans (as they had previously only been seen in animal studies such as [64]) and if these interact with the neural activity to alter perception of a physical stimuli. They proposed a study where annular and radial patterns were used as a physical stimuli to create flicker induced hallucinations. These shapes are used as they can arise without any visual stimulation and are self organised by the visual cortex, in the sense that annular rings and radial arms are percepts on the retina corresponding to patterns of activity that arise through spontaneous pattern formation in visual cortex. It was expected that introducing these physical stimuli would evoke hallucinations of the same type as the stimuli. For example, concentric circles in the centre of the visual field would cause a bias to hallucinate more concentric circles. Yet it was radial fan arms that were hallucinated instead. This is considered an orthogonal response since the corresponding patterns of activity in V1 are stripes of activity oriented at right angles to each other. This latter result stems from the well-known retinocortical map that maps radial arms in the visual field to horizontal stripes of activity in V1, and concentric rings to vertical stripes (with respect to a ventral-dorsal axis). To a first approximation this map (away from the fovea) is often approximated by a quasi-conformal dipole map [3] as discussed in section 2.1.3 that would map spiral arms in retinal coordinates to oblique stripes in cortical coordinates, as illustrated in Fig. 13. The cortical map can also be thought of as a spherical map in the eye stretched along the optical axis and viewed from the side [59]. One might say that if the image of a circle opposed by a radial arm is considered on the retina, then it is locally orthogonal, whereas if the corresponding cortical activity is considered, then it is globally orthogonal.

Billock and Tsou also reported similar orthogonal responses in three other scenarios: (i) if the area around a circular pattern is flickered, an illusory rotating fan shape is perceived (and if the circles are flickering too, the rotating fan shape extends through the physical circles), (ii) if a biasing pattern of peripheral radial arms is presented, then central (tightly packed) rings are perceived, and (iii) a rotating petal-like pattern often appears in the flickering central area in response to a peripheral set of biasing concentric rings. These types of hallucinatory percepts are all illustrated in Fig. 14. In all cases of perceived rotation (typically between 0.75 and 1.3 revolutions per second) the direction of rotation is arbitrary and subject to reversal.

The experiment was conducted using the principles of MacKay's effect [80]. The physical stimuli are presented on a white background and a strobe is used to back-illuminate this. The best results were seen when the flicker was 10-15 Hz, the experiment was completed in a dark room and the stimuli was 1/10th to 1/3rd of the flickered area. Empty-field flicker-induced patterns are not usually seen very quickly and generally can take up to 30 seconds to appear; however, these stimuli driven hallucinations are more stable and appear within a few seconds. The experiment showed that it was easier to see hallucinatory fans than circles.

All participants had orthogonal induced hallucinations to both the centre and surround stimuli. The physical image is seen on the flash of the flicker and the hallucination is seen on the off phase, similar to a negative after image, this is consistent with the MacKay effect. The radial fan patterns induce illusory circle patterns and similarly, the circle patterns

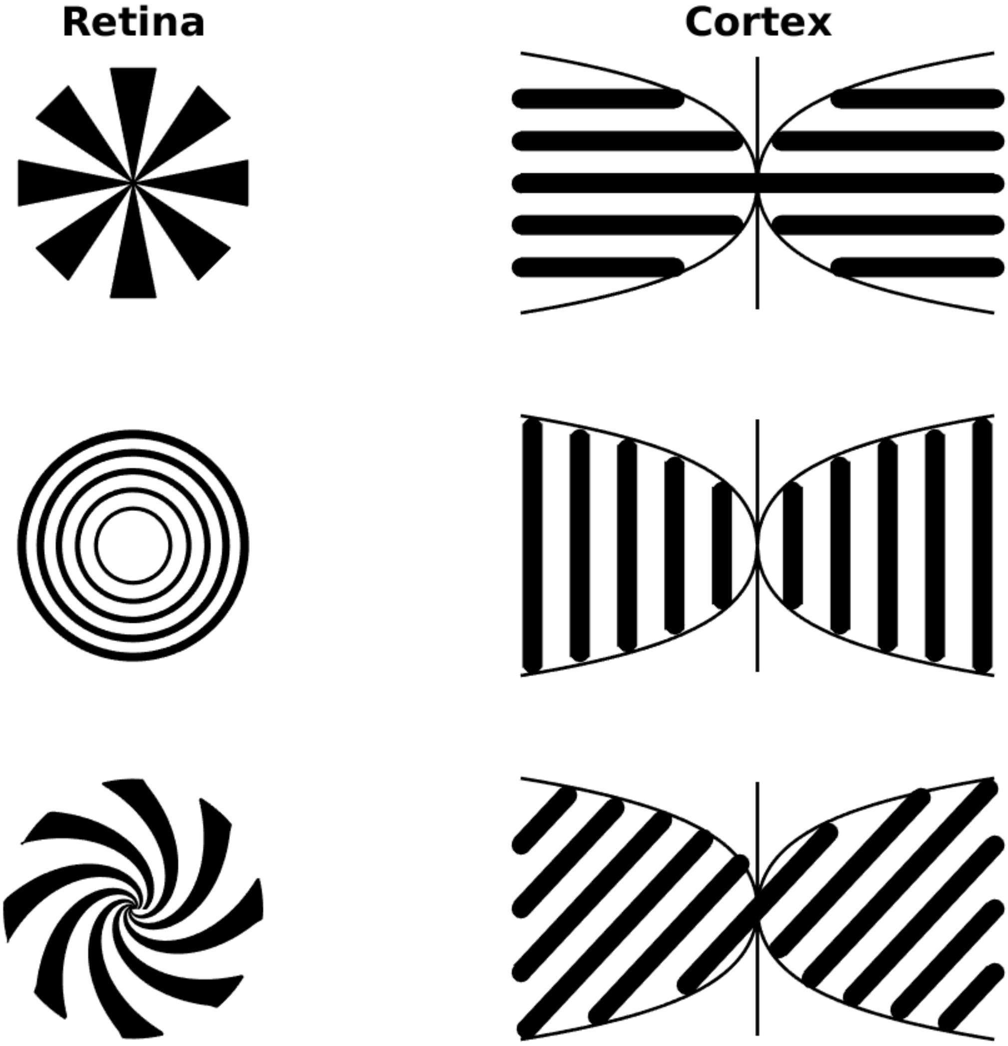

Figure 13.: An illustration of the retinocortical map that takes points of stimuli on the retina to points in V1 (left and right primary visual cortex), showing how radial arms, rings, and spirals on the retina transform to oriented stripes on V1.

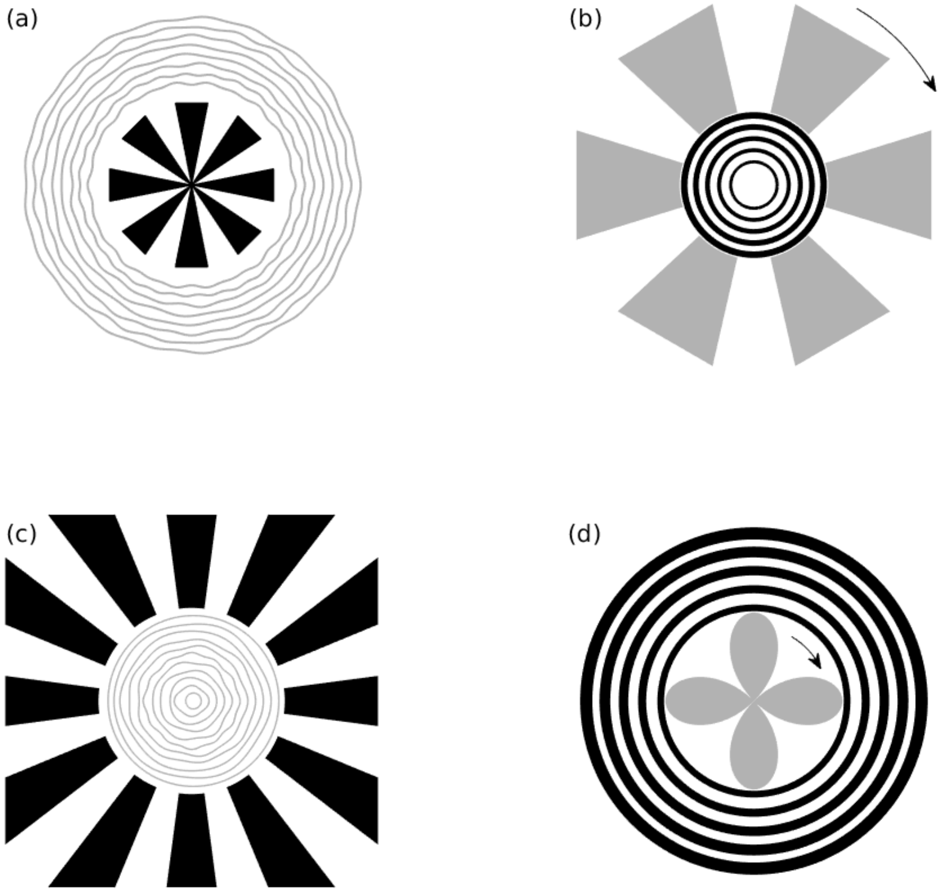

Figure 14.: An illustration of the biasing stimuli (black) and hallucinatory percepts (grey) as reported by Billock and Tsou and redrawn from [10]. (a) If the area around a small fan shape is flickered, subjects report seeing illusory circular patterns, (b) if the area around a circular pattern is flickered, an illusory rotating fan shape is perceived, (c) if a biasing pattern of peripheral radial arms is presented then central rings are perceived, and (d) a rotating petal-like pattern often appears in the flickering central area in response to a peripheral set of biasing concentric rings. The arrows indicate perceived rotation.

induce illusory radial fan patterns. Furthermore, the concentric circle hallucinations are seen to pulse or wobble and the illusory fan shapes are seen to rotate.

We now turn to the perception of patterns of activity in V1. One of the main structures of the visual cortex is that of retinotopy, a neurophysiological projection of the retina to the visual cortex. The log-polar mapping (seen in chapter 2) is perhaps the most common representation of the mapping of points from the retina to the visual cortex and see Fig. 13. The action of the retinocortical map turns a circle of radius r in the visual field into a vertical stripe at $x = \ln(r)$ in the cortex, and also turns a ray emanating from the origin with an angle θ into a horizontal stripe at $y = \theta$. Simply put, if a point on the visual field is described by (r, θ) in polar coordinates, the corresponding point in V1 has Cartesian coordinates $(x, y) = (\ln(r), \theta)$. Thus to answer how a pattern would be perceived we need only apply the inverse (conformal) log-polar mapping.

A major conclusion of Billock and Tsou is that the pattern of sensory induced hallucinations in their psychophysical experiments reflects the same cortical properties, including local connectivity and lateral inhibition within a retinotopic map in V1, that shape routine visual processing. Given the success of neural field models in describing drug induced (spontaneous) hallucinations in V1, it is thus natural to see if they are also capable of explaining the orthogonal response in these flicker induced visual phenomena. To this end we will consider a minimal model of V1 with the inclusion of a forcing term to mimic sensory input to the system. From a biological perspective cells in V1 would be driven by synaptic currents, and these in turn would be mediated by conductance changes arising from afferent inputs. These currents have a simple ohmic form that multiplies the voltage of the postsynaptic neuron with that of the conductance change. Thus the input signal is mixed with the state of the neuron. We shall be careful to carry this important effect over into our phenomenological model of drive.

3.2 PATTERN FORMATION IN SPATIALLY FORCED SYSTEMS

Patterns are found in a wide range of natural contexts, for example a zebra's stripes, spots on a leopard, ripples in sand. The pioneering work of Turing on morphogenesis [120] spurred on extensive research into explaining the appearance and evolution of spontaneous patterns in biological and physical systems [31, 84]. This was considered in a neural context in [125] and in a visual context for orientation tuning [8, 20, 111], hallucinations [17, 38, 117] and developmental models of cortical maps [115].

Pattern formation via a Turing instability starts with a stable steady state of the system that is driven past the point of a bifurcation. The system then becomes unstable due to the exponential growth of small perturbations, thus causing patterns, in time, space, or both. We can use linear stability analysis to find the characteristic length and time scales of these emergent solutions near bifurcation. This is the analytical approach to predicting the types of pattern formation that we will use here. This can then be tested by computing numerical simulations of the system in different parameter regimes and also to probe the behaviour of the system away from bifurcation.

Pattern forming systems can be controlled and new patterns can be found by adding a periodic forcing term to the system. It is possible, perhaps unintuitively, for forcing in planar systems to be applied in the x-direction to generate patterns in the y-direction, thus evoking an orthogonal response as seen in the psychophysical observations. This can be done by using frequency and wavenumber locking following the approach and parameterisation from [81]. A frequency being of the scale

$n : 1$ means that the forcing frequency, k_f, is n times larger than the emergent frequency of the unforced system, k_0. We assume that the wave number k_f is approximately a multiple of k_0, wavenumber locking,

$$k_f \approx nk_0, \quad n \in \mathbb{Z}. \tag{25}$$

At the Turing instability all wavevectors $\mathbf{k} = (k_x, k_y)$ of magnitude $|\mathbf{k}| = k_0$ are excited. We investigate solutions which are locked to the forcing wavevector $\mathbf{k} = (k_f, 0)$. Here, $n : 1$ resonant solutions have

$$k_x = \frac{k_f}{n} + \nu_1 = k_0 - \nu_2 \tag{26}$$

(see Fig. 15), where the mismatch parameters ν_1, ν_2 satisfy $|\nu_1 + k_f/n| \leq k_0$ and equivalently $0 \leq \nu_2 \leq 2k_0$. When working in one spatial dimension, for example in sections 4.1 and 5.2, we set $\nu_2 = 0$. In two dimensions, we can set $\nu_1 = 0$ (as in [81]), as it is not needed because all of the information about frequency mismatch can be carried by ν_2 by fixing k_x. Fig. 15 visualises this relationship between the mismatch, wavenumber and wavenumber locking parameters.

Plotting the regions of existence between parameters at different resonances is useful to visualize them. This is described as Arnol'd tongues, a representation of the phase-locked region around integer values in a driven system [16]. The resonance $n = 2$ most commonly has the widest Arnol'd tongue, as seen from the one dimensional Swift-Hohenberg model [82] and our model in one dimension, see Fig. 22. Therefore, this is usually the region in which parameters are chosen [82]. In the analysis, when $k_f = 2k_x$, this allows additional terms to appear in the amplitude equations that are not present for other resonances. Note, when working in one dimension we set $k_x = k_0$.

For pattern forming dynamical systems, we can look for two dimensional solutions of the type,

$$u(x, y, t) \cong a(x, y, t)\mathrm{e}^{i(k_x x + k_y y)} + b(x, y, t)\mathrm{e}^{i(k_x x - k_y y)} + c.c., \tag{27}$$

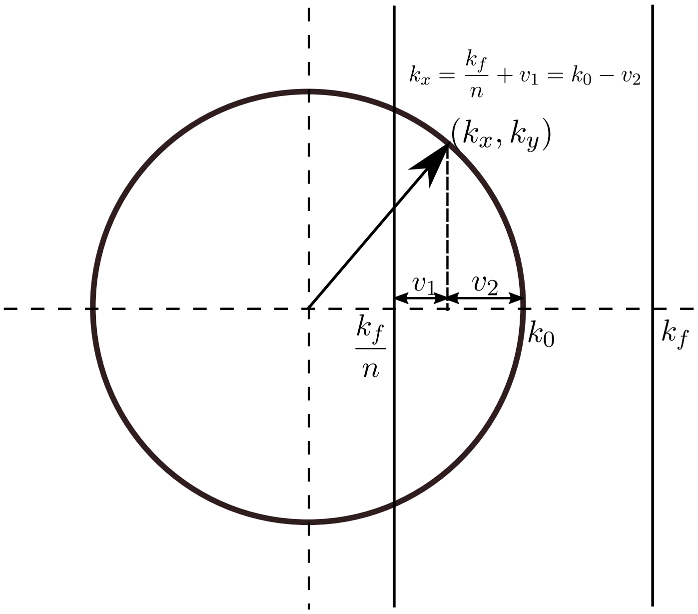

Figure 15.: The circle indicates the ring of fastest growing wavenumbers with critical value $|\mathbf{k}| = k_0$, for $\mathbf{k} = (k_x, k_y)$. The forcing wavevector is $\mathbf{k_f} = (k_f, 0)$. We take $k_x = k_f/n + \nu_1 = k_0 - \nu_2$ for mismatch parameters ν_1 and ν_2, with $n \in \mathbb{Z}$. The wavevector component k_y satisfies $k_y^2 = k_0^2 - k_x^2$ to achieve the total wavenumber k_0. The unforced system can support a spatially periodic Turing pattern with $|\mathbf{k}| = k_0$. With the introduction of forcing there are wide regions in parameter space that support a resonance with $n = 2$ leading to the formation of rectangular and oblique solutions.

where a and b are complex valued two-dimensional amplitudes. When $a = b$ and $k_x = k_y$ the system produces rectangular patterns and when $a \neq b$ and $k_x \neq k_y$ then oblique patterns emerge, this can be seen graphically in Fig. 16. The spatial structure of the two-dimensional patterns that form are, to leading order, a superposition of the modes $\exp(ik_x x \pm ik_y y)$, which can lead to rectangular (equal amplitude) and oblique (unequal amplitude) patterns. These are $n : 1$ resonant patterns that respond to the spatial forcing by locking the wavevector components in the forcing direction $k_x = k_f/n$ and creating a wavevector component in the orthogonal direction, k_y, to compensate for the unfavorable forcing wave number, so that $k_y = \sqrt{k_0^2 - k_x^2}$ to achieve the total wavenumber k_0 .

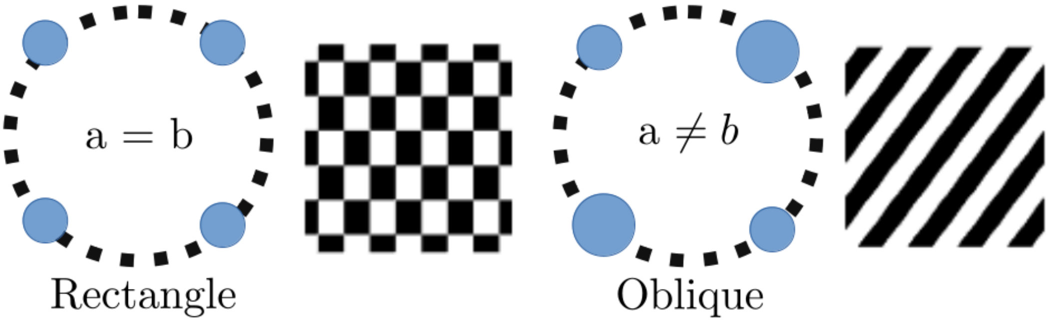

Figure 16.: Changing the relationship between k_x and k_y alters the type of pattern formation. With $a = b$ and $k_x = k_y$ giving rectangular patterns (left) and $a \neq b$ and $k_x \neq k_y$ giving oblique patterns (right).

3.2.1 *Amplitude Equations*

Amplitude equations can be derived for a dynamical system, they describe the emerging patterns that occur after the bifurcation point. They define the normal form of the bifurcation, contain the systems resonant terms and show how the system develops near the instability of a steady state. The growth of a mode, different types of pattern formation, can be expressed in terms of a complex-valued amplitude. They are a method that allows us to describe spatial and temporal distortions of a steady state close to bifurcation, this is very useful when looking at hallucinations as these are not the standard visual pattern that occurs but a distortion of reality. They are widely used in pattern formation and dynamics in nonequilibrium systems [45].

The theory for ordinary differential equation (ODE) dynamical systems was developed in the early 1900s; however, for partial differential equations

(PDE) and integro-differential equations, such as our model, these equations are more complex and there are less generic methods to solve them. We use weakly non-linear analysis with multiple scale perturbation theory to derive them. By deriving them close to the instability, we can use expansion techniques to treat the evolution of perturbations in time and space. We use this to show the existence and stability of solutions. This can help us predict what parameters are needed to control the system to produce the patterns we are looking for. This analysis is valid only close to the bifurcation and for small amplitudes. Far away from bifurcation, pattern states are best studied numerically. All amplitude equations are broadly composed of the same three components: the growth of the perturbation after the spatially uniform state, the saturation of this growth due to the non-linearity and the effect of spatial distortions.

3.2.2 *Pattern Formation in the Spatially Periodically Forced Swift-Hohenberg Model*

The Swift-Hohenberg equation is a PDE that was derived from the equations for thermal convection and is known for its pattern forming behaviour. It was named after Jack B. Swift and Pierre Hohenburg [114]. The work of Meron *et al* [81] derives the amplitude equations for the driven Swift-Hohenberg equation, which we will review before adapting and extending the theory for the neural field model. In [81], the authors use the Swift-Hohenberg equation to examine systems that undergo stationary finite wave-number instability to stripe patterns and they do this by subjecting the system to time independent, spatial periodic forcing in one dimension. Without the forcing, the solutions are non-oscillatory in space and time. The instability can create a stationary orthogonal stripe pattern solution; similar to what we want to see across the visual cortex for the hallucinatory patterns.

The Swift-Hohenberg equation is

$$u_t = \epsilon u - (\nabla^2 + k_0^2)^2 u - u^3, \qquad u = u(x, y, t), \tag{28}$$

where ϵ is the distance from the pattern-forming instability of the steady state, $u = 0$, of the unforced system. The wave number of the first mode to grow past the instability is k_0, this is found using the following Turing analysis. By linearising about this state $u + \delta v$ for a small δ. Then v satisfies the linearised equation,

$$v_t = \epsilon v - (\nabla^2 + k_0^2)^2 v. \tag{29}$$

Assuming that $v(\mathbf{r}, t) \sim \mathrm{e}^{\mathrm{i}\mathbf{k}\cdot\mathbf{r}} \mathrm{e}^{\lambda t}$. Then by writing $\mathbf{r} = (x, y)$ and $\mathbf{k} = (k_x, k_y)$, we obtain

$$\lambda \mathrm{e}^{\mathrm{i}\mathbf{k}\cdot\mathbf{r}} = \epsilon \mathrm{e}^{\mathrm{i}\mathbf{k}\cdot\mathbf{r}} - \left(\frac{\partial^2}{\partial x^2} + \frac{\partial^2}{\partial y^2} + k_0^2 \right)^2 \mathrm{e}^{\mathrm{i}(k_x x + k_y y)} \tag{30}$$

Expanding (30) and writing $\mathbf{k} = |k|$ and $k^2 = k_x^2 + k_y^2$, gives

$$\lambda(k) = \epsilon - (k^2 - k_0^2)^2 \tag{31}$$

Therefore, a Turing instability occurs when $\epsilon = 0$ and beyond the instability there is a band of growing wavenumbers around k_0. The growing wavenumbers are k with $k_1 < k < k_2$ where $k_1 < k_2$ are the roots of $\lambda(k) = 0$ which occurs when $k = \sqrt{k_0^2 \pm \sqrt{\epsilon}}$. If the band of wavenumbers is narrow, when $k \sim k_0$, then $k - k_0 \approx \pm\sqrt{\epsilon}/2k_0$. All wavenumbers (k_x, k_y) of magnitude k_0 are excited beyond the instability.

Now we turn to the work of the Swift-Hohenberg equation with [81] including forcing. The forced Swift-Hohenberg equation is,

$$u_t = \epsilon u - (\nabla^2 + k_0^2)^2 u - u^3 + \gamma u \cos(k_f x), \qquad u = u(x, y, t). \tag{32}$$

The forcing is added with strength γ and wave number k_f in the x-direction. The relationship between k_0 and k_f is vital to the type of pattern formation after the instability, as seen earlier in Fig. 15.

Meron *et al* [81] investigate resonance with these locked to the forcing wavevector $(k_f, 0)$ in a $2:1$ resonance with $k_x = k_f/2 = k_0 + \nu$ (where $\nu = \nu_2$ from (26) and $\nu_1 = 0$) where $-2k_0 < \nu < 0$ and $k_y = \sqrt{k_0^2 - k_x^2}$. Using weakly nonlinear analysis the equations are computed governing the dynamics of the amplitudes $a(x, y, t)$ and $b(x, y, t)$, where,

$$u = \epsilon \left(a(x, y, t)\mathrm{e}^{\mathrm{i}(k_x x + k_y y)} + b(x, y, t)\mathrm{e}^{\mathrm{i}(k_x x - k_y y)} + \text{c.c.} \right). \tag{33}$$

The Swift-Hohenberg amplitude equations are derived to be,

$$a_t = \epsilon a + (k_x \partial_x + k_y \partial_y)^2 a + \frac{\gamma}{2} b^* - (|a|^2 a + 2|b|^2 a), \tag{34}$$

$$b_t = \epsilon b + (k_x \partial_x + k_y \partial_y)^2 b + \frac{\gamma}{2} a^* - (|b|^2 b + 2|a|^2 b). \tag{35}$$

A full derivation can be seen in [81]. Note that the mismatch ν enters only through the spatially dependent terms and therefore, when we consider spatially homogeneous solutions, their existence and stability do not depend on ν beyond requiring $-2k_0 < \nu < 0$. However, ν does determine the planform of the patterned state (i.e. aspect ratio of rectangles and angle of obliques to horizontal). Then bifurcation analysis is completed to find the parameter regimes for oblique and rectangular patterns. Stationary homogeneous solutions of the amplitude equations are derived, by looking for solutions using the polar form,

$$a = \rho_a \exp(i\alpha), \quad b = \rho_b \exp(i\beta). \tag{36}$$

For rectangular patterns, there is a constant solution when $\rho_a = \rho_b = \rho_0$, where

$$\rho_0 = \sqrt{\frac{\epsilon + \gamma/2}{3}}. \tag{37}$$

Thus, this gives a one-parameter family of solutions,

$$\alpha_0 = \rho_0 \mathrm{e}^{\mathrm{i}\alpha}, \quad \beta_0 = \rho_0 \mathrm{e}^{-\mathrm{i}\alpha}. \tag{38}$$

This solution exists for $\epsilon > -\gamma/2$ and $-2k_0 < \nu < 0$.

For oblique patterns, there is a constant solution when $\rho_a = \rho_\pm$ and $\rho_b = \rho_\mp$, where

$$\rho_\pm = \sqrt{\frac{\epsilon \pm \sqrt{\epsilon^2 - \gamma^2}}{2}}. \tag{39}$$

Thus, this gives a one-parameter family of solutions,

$$\alpha_\pm = \rho_\pm e^{i\alpha}, \quad \beta_\mp = \rho_\mp e^{-i\alpha}. \tag{40}$$

This solution exists for $\epsilon > \gamma$ and $-2k_0 < \nu < 0$.

The linear stability of these solutions are then examined to uniform perturbations It was found that linearising around the constant solution $\rho_a = \rho_{a0}$ and $\rho_b = \rho_{b0}$ gives the eigenvalues to be,

$$\Lambda_\pm = \epsilon - \frac{5}{2}\left(\rho_{a0}^2 + \rho_{b0}^2\right) \pm \sqrt{\frac{1}{4}\left(\rho_{a0}^2 - \rho_{b0}^2\right)^2 + \left(\frac{\gamma}{2} - 4\rho_{a0}\rho_{b0}\right)^2}. \tag{41}$$

The stability of the rectangular and oblique patterns can be found from these. The bifurcation diagram using (37) & (39) can be seen in Fig. 17. The phase diagram to show the parameter regimes for obliques and rectangles for a given γ, is shown in Fig. 18, using the derived existence regimes.

The planforms to the equation showing how the variation in v and ϵ affects the type of pattern formation are seen in Fig. 19. This shows how horizontal or vertical stripes of activity can be forced to orthogonal stripes of activity by varying v, either through oblique or rectangular patterns by changing the value of ϵ. This is exactly the forcing of patterns that we will replicate in our model. We want to model the vertical stripes of activity in V1 that, after applying the retinocortical map, represent circle patterns that force horizontal stripes of activity in the remainder of V1 to induced fan shape hallucinations.

3.2.3 *Summary*

The work of Meron *et al* in [81] on the driven Swift-Hohenberg equation will play a large part in helping us model the sensory induced hallucinations. From right to left in Fig. 19, it is shown that patterns in the same direction of the drive are forced to oblique or rectangular patterns until they become orthogonal to the drive. This is what we desire to represent for the psycho-physical observations. In the next section, we will show how we performed similar calculations for our integro-differential forced neural field model.

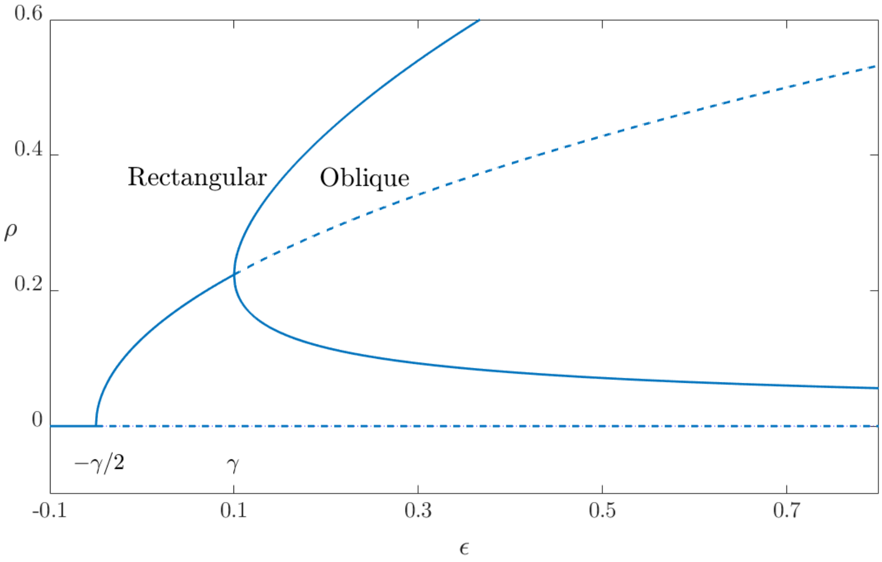

Figure 17.: Bifurcation diagram for the solutions for the amplitude equations for the forced Swift-Hohenberg equation with $\gamma = 0.1$. Rectangular patterns (ρ_0) appear at $\epsilon = -\gamma/2$ and become unstable to oblique patterns $(\rho_\pm)$ at $\epsilon = \gamma$. Solutions exist for $-2k_0 < \nu < 0$.

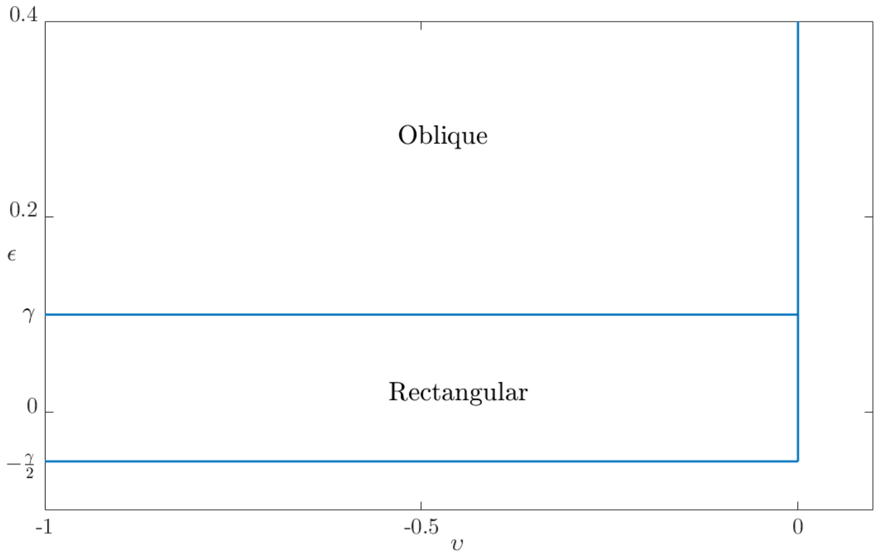

Figure 18.: Phase diagram for the amplitude equations for the forced Swift-Hohenberg equation in the $v - \epsilon$ parameter plane showing the regions of stable resonant patterns with $\gamma = 0.1$ and $k_0 = 1$.

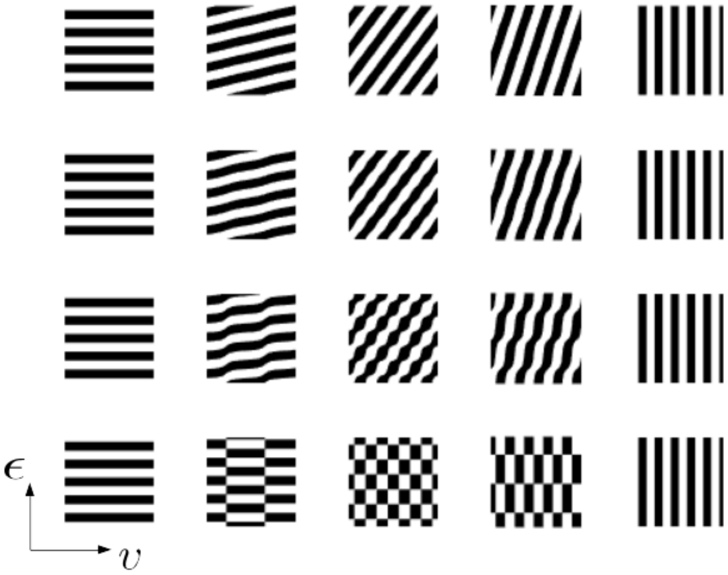

Figure 19.: The analytical planforms for the spatially forced Swift Hohenberg Equation, showing oblique, rectangular and stripe patterns as v is increased from -k_0 to 0 (left to right) and as ϵ is increased from less than γ to more than γ. The left column shows patterns orthogonal to the drive. Redrawn from [81].

3.3 NEURAL FIELD MODEL

In this section and continuing in chapter 4, we adapt the analysis used for the forced Swift-Hohenberg equation in section 3.2 to a simple neural field model with spatial forcing. The predominant model for voltage-based neural fields is the Amari equation [1], for a position $\mathbf{r}$ in the domain Ω,

$$\frac{\partial u(\mathbf{r},t)}{\partial t} = -u(\mathbf{r},t) + \int_{\Omega} w(\mathbf{r},\mathbf{r}')f(u(\mathbf{r}'),t)\,\mathrm{d}\mathbf{r}', \tag{42}$$

where $u(\mathbf{r},t)$ is the activity of the cortex at position $\mathbf{r}$ evolving over time t, w is an anatomical kernel representing the connection between neurons and can include excitatory and inhibitory interactions. As discussed in section 2.2, this is often represented by a Mexican or Wizard hat function as this is a good representation of typical cortical connections as it includes short range excitation and long range inhibition. The firing rate of the neurons is represented by f and this is modelled using a sigmoidal function. We use the standard sigmoidal firing rate function,

$$f(u) = \frac{1}{1+\mathrm{e}^{-\mu(u-h)}}, \tag{43}$$

and note that

$$f'(u) = \mu f(u)(1-f(u)). \tag{44}$$

We use a rotationally symmetric kernel, with $w(\mathbf{r},\mathbf{r}') = w(|\mathbf{r_c} - \mathbf{r}'_\mathbf{c}|)$, that is the difference of two exponentials to model the short and long range connectivity,

$$w(\mathbf{r}) = A\mathrm{e}^{-\mathbf{r}/\sigma} - \mathrm{e}^{-\mathbf{r}}. \tag{45}$$

For computational simplicity, we use a balanced kernel, as defined by (16). We used the balanced kernel to control the steady state of the system, as a balanced kernel gives a steady state of (42) at zero, $u_0 = 0$.

3.3.1 *Linear Stability Analysis*

By defining the steady state of the system as $\bar{u} = u(x,t)$,

$$0 = -\bar{u} + f(\bar{u}) \int_{\Omega} w(\mathbf{r})\ \mathrm{d}\mathbf{r}. \tag{46}$$

where Ω is the two-dimensional cortical domain. This gives,

$$\bar{u} = \widehat{w}(0) f(\bar{u}). \tag{47}$$

where $\widehat{w}(\mathbf{k}) = \int_{\Omega} w(\mathbf{r})\mathrm{e}^{-i\mathbf{k}\cdot\mathbf{r}}\mathrm{d}\mathbf{r}$ is the Fourier transform of the connectivity kernel.

The stability of the steady state can be found by writing $u(\mathbf{r},t)$ as the steady state $\bar{u}$ plus a perturbation,

$$u(\mathbf{r},t) = \bar{u} + q(\mathbf{r},t). \tag{48}$$

This gives,

$$\frac{\partial q(\mathbf{r},t)}{\partial t} = -q(\mathbf{r},t) + f'(\bar{u}) \int_{\Omega} w(|\mathbf{r}-\mathbf{r}'|) q(\mathbf{r}',t)\ \mathrm{d}\mathbf{r}'. \tag{49}$$

We look for solutions of the form $q(\mathbf{r},t) = \mathrm{e}^{\lambda t}\mathrm{e}^{i\mathbf{k}\cdot\mathbf{r}}$. Therefore the spectrum of the Turing instability is, defined by $E(\lambda,\mathbf{k}) = 0$, where

$$E(\lambda,\mathbf{k}) = \lambda + 1 - f'(\bar{u})\widehat{w}(\mathbf{k}). \tag{50}$$

Note that all roots of $E(\lambda,k) = 0$ are real. Given $\lambda = -1 + f'(\bar{u})\widehat{w}(\mathbf{k})$, since $f'(\bar{u})$ and $\widehat{w}(\mathbf{k})$ are real then λ is real. However, $\widehat{w}(\mathbf{k})$ is only real if w is even, which is the case for all of our choices. Therefore, we have a static Turing instability.

3.3.2 *Fourier Transform of Kernel*

For our choice of connectivity kernel, $w(\mathbf{r}) = A\mathrm{e}^{-|\mathbf{r}|/\sigma} - \mathrm{e}^{-|\mathbf{r}|}$, as in (45), since $w(|\mathbf{r}|)$, the Fourier transform $\widehat{w}(\mathbf{k}) = \widehat{w}(k)$ where $k = |\mathbf{k}|$. The Fourier transform can be calculated as,

$$\begin{aligned}
\widehat{w}(k) &= \int_{-\infty}^{\infty}\int_{-\infty}^{\infty} A\mathrm{e}^{-|\mathbf{r}|/\sigma}\mathrm{e}^{-i\mathbf{k}\cdot\mathbf{r}}\mathrm{d}\mathbf{r} - \int_{-\infty}^{\infty}\int_{-\infty}^{\infty} \mathrm{e}^{-|\mathbf{r}|}\mathrm{e}^{-i\mathbf{k}\cdot\mathbf{r}}\mathrm{d}\mathbf{r}, \\
&= \left[\int_0^{2\pi}\int_0^{\infty} A\mathrm{e}^{-Sr}\mathrm{e}^{-ikr\cos\theta} r\mathrm{d}r\mathrm{d}\theta - \int_0^{2\pi}\int_0^{\infty} \mathrm{e}^{-r}\mathrm{e}^{-ikr\cos\theta} r\mathrm{d}r\mathrm{d}\theta,\right]\Bigg|_{S=1/\sigma} \\
&= \left[\frac{\partial}{\partial S}\int_0^{2\pi} \frac{A}{S + ik\cos\theta}\mathrm{d}\theta - \frac{\partial}{\partial S}\int_0^{2\pi} \frac{1}{1 + ik\cos\theta}\mathrm{d}\theta\right]\Bigg|_{S=1/\sigma} \\
&= 2\pi\left[\frac{AS}{(S^2 + k^2)^{3/2}} - \frac{1}{(1 + k^2)^{3/2}}\right]\Bigg|_{S=1/\sigma}. \qquad (51)
\end{aligned}$$

Therefore, the formula for $\widehat{w}(k)$ is,

$$\widehat{w}(k) = 2\pi\left[\frac{A}{\sigma(\sigma^{-2} + k^2)^{3/2}} - \frac{1}{(1 + k^2)^{3/2}}\right]. \qquad (52)$$

The maximum of this occurs at k_0 (which depends on the value of σ), as shown in Fig. 20.

The homogeneous steady state u_0 becomes unstable to patterns with wavenumber k_0 for values of μ beyond the bifurcation which occurs when (from (50)) $\mu = \mu_c$ where

$$f'(u_0) = \frac{1}{\widehat{w}(k_0)} \implies \mu_c f(u_0)(1 - f(u_0)) = \frac{1}{\widehat{w}(k_0)}. \qquad (53)$$

Since we have $u_0 = 0$, the bifurcation condition is,

$$\mu_c f(0)(1 - f(0)) = \frac{1}{\widehat{w}(k_0)}, \qquad (54)$$

where from (50) $f(0) = 1/(1 + \mathrm{e}^{\mu_c h})$. Equation (54) can typically be solved (e.g. using Matlab *fsolve*) to determine the value of μ_c for a given choice of h. In the particular case that $h = 0$, $f(0) = 1/2$ and therefore,

$$\mu_c = \frac{4}{\widehat{w}(k_0)}. \qquad (55)$$

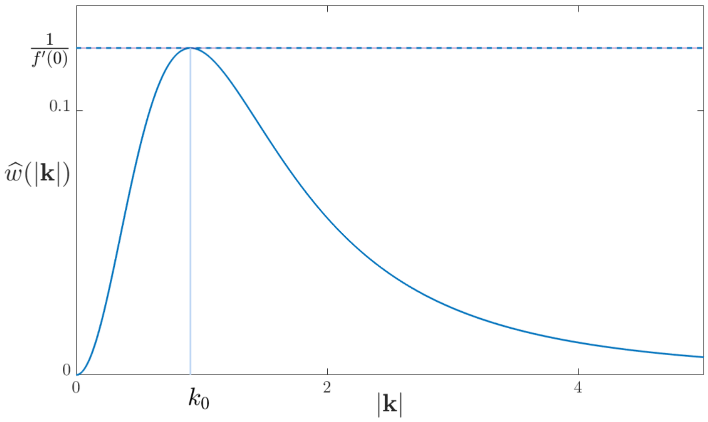

Figure 20.: The Fourier transform of $\widehat{w}(k)$ from (52) showing the relationship between k_0 and $1/f'(0)$ using $\sigma = 0.8$.

3.3.3 *Simulations*

The neural field equation (42) produces patterns for certain parameters after the bifurcation point at $\mu = \mu_c$ without any forcing required. We carried out simulations and this produces spots of activity across the cortex, shown in Fig. 21. Brief details of the numerical methods used to implement the model are presented in Appendix C.

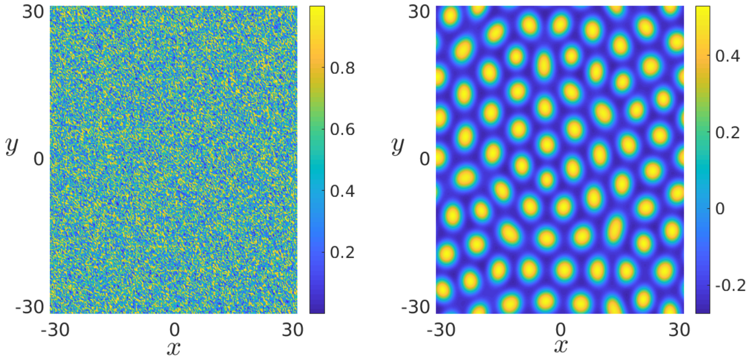

Figure 21.: Simulations of the neural field model (42) with random initial conditions (left) giving spots (right) with firing rate (43) and connectivity (45) with $\sigma = 0.8$, $h = 0.1$ and using (55) to calculate μ past the bifurcation point. Plotted using 256×256 mesh points on the domain $[-10\pi, 10\pi] \times [-10\pi, 10\pi]$.

3.4 SUMMARY

In this chapter, we have introduced the psychophysical phenomena presented by Billock and Tsou in [10] and the underlying neural phenomena that occurs for these hallucinations to occur in V1 once the activity has been mapped to the cortex using the retinocortical mapping. We presented the work of Manor *et al* [81] on the spatially forced Swift-Hohenburg equation, the derivation of amplitude equations for the 2:1 resonance leads to parameter regimes to be found to force vertical stripes to horizontal stripes by adding a spatial drive term to the model. Finally, we also performed Turing analysis on the standard neural field model as background for further Turing analysis we will perform within this thesis, and to determine the wavenumber k_0 of the spontaneous patterned solutions of (42) beyond the static Turing instability. In the next chapter, we will add the spatial forcing term to the neural field model (42) to uncover our own parameter regimes in which we can force stripes of activity in the orthogonal direction.

4

NEURAL FIELD MODEL WITH SPATIAL FORCING

After introducing the work of Billock and Tsou in the previous chapter and then exploring a driven PDE system that produced an orthogonal response like the one we want to model, we will now turn to adding a similar spatial forcing term to the neural field equation (42). This will enable us to find parameter regimes in which we can replicate the neural activity occurring during the psychophysical phenomena. In section 4.1 we introduce the neural field model with spatial forcing in one dimension. This is extended in section 4.2 to two dimensions to drive hallucinations. In these sections, we develop a weakly nonlinear analysis, valid for weak forcing in the neighborhood of a Turing instability, and derive equations governing the amplitude of emergent planforms. These in turn are analysed using bifurcation theory to uncover appropriate parameter choices (in the strength of forcing, the frequency mismatch, and shape of the nonlinear firing rate) to generate an orthogonal response. This is concluded in section 4.3 with simulations of the stationary patterns produced from this two-dimensional model using parameters obtained from the analysis to explain the psychophysics. In chapter 5, we will complete the story by introducing adaptation to the neural field model to invoke parameter regimes that allow for travelling waves to form and thus, creating the movement that occurs in the hallucinations.

4.1 NEURAL FIELD MODEL IN ONE DIMENSION WITH SPATIAL FORCING

Since we are primarily interested in the mechanisms that underlie an orthogonal response, we shall develop theory for the case that this is a simple spatial pattern of stripes in the x-direction with a spatial forcing wavenumber k_f. Our interest is in the development of striped patterns in neural activity along the y-direction requiring analysis of the model in two spatial dimensions. For the PDE case (Swift-Hohenberg), Manor *et al* [81] showed that resonances (and in particular a 2:1 resonance) between the wavenumber k_0 of the spontaneous patterns and forcing wavenumber are required for the observation of orthogonal response to forcing. We first investigate whether resonances arise naturally in a neural field model with forcing and note that this question does not require a treatment in two spatial dimensions. We therefore begin by exploring resonances in the neural field model (42) posed on the real line. As seen for the Swift-Hohenburg equation [81], the $2 : 1$ resonance is the most dominant and whilst we predict this is the same for our model, we first show this with the one dimensional model. We can apply similar spatial forcing used in the Swift-Hohenberg equation (32) [81] to our neural field model (42),

$$\frac{\partial u(x,t)}{\partial t} = -u(x,t) + \int_\Omega w(|x-x'|) f(u(x'),t)\,\mathrm{d}x' + \gamma u(x,t)\cos(k_f x), \quad (56)$$

where the forcing is added with strength γ and wave number k_f in the x-direction and we allow for a simple form of mixing by including a multiplication with the state u. The wave number of the first mode to grow past the instability is again denoted k_0. However, now the value of k_0 is determined by the Turing bifurcation condition $f'(u_0, \mu_c) = 1/\widehat{w}(k_0)$ where in one dimension the Fourier transform of the kernel (45) is given by,

$$\widehat{w}(k) = 2\int_0^\infty w(x)\mathrm{e}^{-\mathrm{i}kx}\,\mathrm{d}x = 2\left[\frac{1}{1+\sigma^2k^2} - \frac{1}{1+k^2}\right]. \tag{57}$$

and for balance we take $A = 1/\sigma$. This ensures the homogeneous steady state remains at u_0. The relationship between k_0 and k_f determines the type of pattern formation after the instability.

From a biological perspective cells in V1 would be driven by synaptic currents, and these in turn would be mediated by conductance changes arising from afferent inputs. These currents have a simple ohmic form that multiplies the voltage of the postsynaptic neuron with that of the conductance change. Thus the input signal is mixed with the state of the neuron. Hence in the forcing term $\gamma u(x,t)\cos(k_f x)$, the u term represents this state dependence, the $\cos(k_f x)$ term represents the sensory input pattern and γ controls the strength of this forcing (always very small to ensure weak forcing). The sensory input patterns are lines of activity which have been represented here by a cos wave, other trigonometric functions or sums of exponential functions that give similar waves of activity could be used; however, this is the most simplistic whilst being realistic which will help when deriving the equations.

4.1.1 *Multiple Scale Analysis*

We also look for solutions of the type,

$$u \cong A(\chi,\tau)\mathrm{e}^{i(k_0x)} + A^*(\chi,\tau)\mathrm{e}^{-i(k_0x)}, \tag{58}$$

where A is a complex valued amplitude that has been extended in one spatial dimension, $\chi = \epsilon x$ and once in time, $\tau = \epsilon^2 t$. Using multiple scale analysis, we consider weak forcing $\gamma \ll 1$ near the instability $\epsilon \ll 1$. The equations which describe the dynamics of the amplitude $A(\chi, \tau)$ can be derived using the following methods.

4.1.2 *Hierarchy of Equations*

From now on we will assume that the forcing wavenumber k_f is approximately a multiple of k_0, so that $k_f \approx nk_0$, $n \in \mathbb{Z}$ and introduce the mismatch parameter ν_1

$$\nu = k_0 - k_f/n, \tag{59}$$

by taking $\nu = \nu_1$ from (26). The value of n can be used to describe an n:1 *resonance*. If the system is poised at a static Turing instability to a pattern with wavenumber k_0 and the forcing is weak ($|\gamma| \ll 1$) then it is natural to consider a multiple-scales analysis to understand the response properties of the driven system. We assume that the small detuning can be scaled as $\nu = \epsilon c$ for a small parameter ϵ where $c \approx O(1)$. We consider power series expansions for u and γ as

$$u = u_0 + \epsilon u_1 + \epsilon^2 u_2 + \epsilon^3 u_3 + \dots, \tag{60}$$

$$\gamma = \epsilon\gamma_1 + \epsilon^2\gamma_2 + \epsilon^3\gamma_3 + \dots, \tag{61}$$

with, as yet, unknown functions $u_\alpha = u_\alpha(x, t, \chi, \tau)$, $\alpha = 1, 2, 3, \dots$. Further, we substitute the firing rate function f by its Taylor series expansion $f(u) = f(u_0) + \beta_1(u - u_0) + \beta_2(u - u_0)^2 + \beta_3(u - u_0)^3 + \dots,$ where $\beta_2 = f''(u_0)/2$, $\beta_3 = f'''(u_0)/6$, and we treat β_1 as a bifurcation parameter and write $\beta_1 = \beta_c + \epsilon^2\delta$ where $\beta_c = f'(u_0)$ subject to $\beta_c = 1/\widehat{w}(k_0)$ (the static Turing bifurcation condition). This choice of scaling was following the work of [81, 82, 85]. This can be justified by balancing the dispersion relation $\lambda = -1 + f'(\bar{u})\widehat{w}(\mathbf{k})$. All of the scaling is set by the choice $\nu = \epsilon^a c$. We need $\nu x = cX$ and so take $X = \epsilon^a x$ and then $T = \epsilon^{2a} t$ to balance terms in the dispersion relation. If we want $\beta_1 = \beta_c + \epsilon^2\delta$ then we must have a=1.

This gives, the expansion of the left hand side of (56) as,

$$\frac{\partial(\epsilon^2 u_0 + \epsilon^3 u_1 + \epsilon^4 u_2 + \epsilon^5 u_3 + \dots)}{\partial\tau}. \tag{62}$$

Therefore, the expansion of the right hand side is,

$$\begin{aligned} &-(u_0 + \epsilon u_1 + \epsilon^2 u_2 + \epsilon^3 u_3 + \dots) + w \otimes [f(u_0) + (\beta_c + \epsilon^2\delta)(\epsilon u_1 + \epsilon^2 u_2 \\ &\quad + \epsilon^3 u_3 + \dots) + \beta_2(\epsilon u_1 + \epsilon^2 u_2 + \epsilon^3 u_3 + \dots)^2 + \beta_3(\epsilon u_1 + \epsilon^2 u_2 + \epsilon^3 u_3 \\ &\quad + \dots)^3 + \dots] + (\epsilon\gamma_1 + \epsilon^2\gamma_2 + \epsilon^3\gamma_3 + \dots)(u_0 + \epsilon u_1 + \epsilon^2 u_2 + \epsilon^3 u_3 \\ &\quad + \dots)\cos k_f x. \end{aligned} \tag{63}$$

A further Taylor series expansion of the functions u_α as

$$\begin{aligned} u_\alpha(x', t', \epsilon x', \epsilon^2 t') &= u_\alpha(x', t', \chi + \epsilon(x' - x), \epsilon^2 t') \\ &\simeq u_\alpha(x', t', \chi, \tau) + \epsilon(x' - x)\frac{\partial}{\partial\chi}u_\alpha(x', t', \chi, \tau) \\ &+ \frac{1}{2}\epsilon^2(x' - x)^2\frac{\partial^2}{\partial\chi^2}u_\alpha(x', t', \chi, \tau) + O(\epsilon^3), \end{aligned} \tag{64}$$

facilitates an evaluation of the spatial convolution in (56).

By using the multiscale expansion of u (58) that has been extended in one spatial dimensions, χ, and once in time, τ, and using the multiple scale expansion (62) and (63), this gives the fully expanded model. Taking the terms for each order of epsilon gives,

$$u_0 = M_0(f(u_0)) \tag{65}$$

$$u_1 = M_0(\beta_c u_1) + \gamma_1 u_0 \cos(k_f x) \tag{66}$$

$$u_2 = M_0(\beta_c u_2 + \beta_2 u_1^2) + M_1(\beta_c u_1) + (\gamma_1 u_1 + \gamma_2 u_0)\cos(k_f x), \tag{67}$$

$$\begin{aligned} \frac{\partial u_1}{\partial\tau} + u_3 &= M_0(\beta_c u_3 + \delta u_1 + 2\beta_2 u_1 u_2 + \beta_3 u_1^3) + M_1(\beta_c u_2 + 2\beta_2 u_1^2) \\ &+ M_2(\beta_c u_1) + (\gamma_1 u_2 + \gamma_2 u_1 + \gamma_3 u_0)\cos k_f x, \end{aligned} \tag{68}$$

where the linear operators M_α are given by

$$M_0 = w\otimes, \tag{69}$$

$$M_1 = W^x \otimes \partial_\chi, \tag{70}$$

$$M_2 = \frac{1}{2}W^{xx} \otimes \partial_{\chi\chi}, \tag{71}$$

and the symbol $\otimes$ denotes spatial convolution,

$$[w \otimes u](x) = \int_{-\infty}^{\infty} w(|x - x'|)u(x')\mathrm{d}x'. \tag{72}$$

Furthermore, here we have introduced the new kernels,

$$W^x = -w(|x|)x \tag{73}$$

and

$$W^{xx} = w(|x|)x^2. \tag{74}$$

However, we note that,

$$\begin{aligned}\widehat{W}^x(k) &= -\int_{-\infty}^{\infty} xw(|x|)\mathrm{e}^{ikx}\,\mathrm{d}x \\ &= -i\frac{\partial}{\partial k}\widehat{w}(k).\end{aligned} \tag{75}$$

Therefore, note as $\widehat{w}(k_0)$ is a maximum, its derivative is zero and this can be to eliminate terms further on in our derivation; $\widehat{W}^x(k_0) = 0$.

4.1.3 *Solving the equations*

One can see that each equation in the hierarchy (65-68) above contains terms of the asymptotic expansion of u only of the same order or lower. This means that we can start from the first equation and systematically solve for u_α. In fact, if we set $\mathcal{L} = -1 + \beta_c w\otimes$ the system (66)-(68) has the general form $\mathcal{L}u_\alpha = g_\alpha(u_1, u_2, \dots, u_{\alpha-1})$ and the right-hand side g_α will always contain known quantities.

The first equation (65) in the hierarchy fixes the steady state u_0. By choosing a balanced kernel we have $u_0 = 0$. The second equation (66) is linear with solutions $u_1 = A(\chi,\tau)\mathrm{e}^{ik_0x} + \text{c.c.}$ (where k_0 is the critical wavenumber at the static bifurcation). A dynamical equation for the complex amplitude $A(\chi,\tau)$ can be obtained by deriving solvability conditions for the higher-order equations, a method known as the Fredholm alternative [41, 51]. The inner product of two periodic functions, with periodicity $2\pi/k_0$ is defined as,

$$\langle U, V\rangle = \frac{k_0}{2\pi}\int_0^{\frac{2\pi}{k_0}} U^*(x)V(x)\,\mathrm{d}x. \tag{76}$$

For all $u \in \ker \mathscr{L}^\dagger$ then,

$$\langle u, g_\alpha\rangle = \langle u, \mathscr{L}u_\alpha\rangle = \langle \mathscr{L}^\dagger u, u_\alpha\rangle = 0, \tag{77}$$

where $\mathscr{L}^\dagger$ is the adjoint of $\mathscr{L}$. It is easy to establish that $\mathscr{L}$ is self-adjoint so that the set of solvability conditions is $\langle e^{\pm \mathrm{i}k_0x}, g_\alpha\rangle = 0$. To evaluate the solvability condition at $\alpha = 2$ we note the useful results

$$\langle \mathrm{e}^{ik_0x}, \mathcal{L}u_2\rangle = 0, \quad \langle \mathrm{e}^{ik_0x}, \beta_2 w \otimes u_1^2\rangle = 0, \quad \langle \mathrm{e}^{ik_0x}, \beta_c W^x \otimes \partial_\chi u_1\rangle = 0, \tag{78}$$
$$\langle \mathrm{e}^{ik_0x}, \gamma_1 u_1 \cos k_f x\rangle = \begin{cases} 0 & n \neq 2 \\ \frac{\gamma_1}{2}A^*\mathrm{e}^{-2ivx} & n = 2 \end{cases}.$$

Hence to avoid secular terms we must set $\gamma_1 = 0$ for the 2:1 resonance (with the solvability condition automatically guaranteed for all $n \neq 2$). We write $\gamma_1 = (1-\delta_{n,2})\overline{\gamma_1}$. A particular solution of u_2 can be found by assuming that it is a linear combination of terms involving $\mathrm{e}^{i(\pm k_f \pm k_0)}$ and terms present in u_1^2. Substitution into (67) and balancing terms gives, for our balanced kernel ($\widehat{w}(0) = 0$),

$$u_2 = d_0A^2\mathrm{e}^{2ik_0x} + (1-\delta_{n,2})\frac{\overline{\gamma_1}}{2}\left[d_+A\mathrm{e}^{i(k_f+k_0)x} + d_-A^*\mathrm{e}^{i(k_f-k_0)x}\right] + \text{c.c.}, \tag{79}$$

where

$$d_0 = \frac{\beta_2\widehat{w}(2k_0)}{1-\beta_c\widehat{w}(2k_0)}, \quad d_\pm = \frac{1}{1-\beta_c\widehat{w}(k_f \pm k_0)}. \tag{80}$$

4.1.4 *Amplitude Equations*

A similar analysis of the solvability condition at $\alpha = 3$, and using the results in Appendix A.1, gives the evolution of the amplitude A as

$$\begin{aligned}\frac{\partial A}{\partial \tau} &= \delta\widehat{w}(k_0)A + [2\beta_2\widehat{w}(k_0)d_0 + 3\beta_3\widehat{w}(k_0)]\, A|A|^2 - \frac{1}{2}\beta_c\widehat{w}''(k_0)\frac{\partial^2 A}{\partial \chi^2} \\ &+ \frac{\gamma_2}{2}A^*\mathrm{e}^{-2ic\chi}\delta_{n,2} + (1-\delta_{n,2})\left(\frac{\overline{\gamma_1}}{2}\right)^2\left[(d_+ + d_-)A + A^* d_- \mathrm{e}^{-2ic\chi}\delta_{n,1}\right]. \end{aligned} \tag{81}$$

If we now introduce the amplitude variable $a = \epsilon\mathrm{e}^{ic\chi}A$ then to leading order the solution for u is of the form

$$u - u_0 \simeq a\mathrm{e}^{ik_f x/n} + \text{c.c.}. \tag{82}$$

After rescaling back to the original time and space variables the amplitude a evolves according to

$$\begin{aligned}\beta_c\frac{\partial a}{\partial t} &= \epsilon^2\delta a - \Phi|a|^2 a + \frac{1}{2}\widehat{w}''(k_0)[\beta_c(\nu + i\partial_x)]^2 a + \delta_{n,2}\frac{\epsilon^2\gamma_2}{2}\beta_c a^* \\ &+ (1-\delta_{n,2})\beta_c\left(\frac{\epsilon\overline{\gamma_1}}{2}\right)^2[(d_+ + d_-)a + a^* d_- \delta_{n,1}]. \end{aligned} \tag{83}$$

where $\Phi = -3\beta_3 - 2\beta_2 d_0$. Thus, from the solution form of (82), constant solutions of the amplitude equation (83) generate n:1 resonant stationary stripe patterns. We next investigate the existence of such solutions for different values of n.

4.1.5 *Existence of Solutions*

Using the derived equation (83), we consider the case $n \neq 2$ and $n = 2$. For $n \neq 2$, this becomes,

$$\begin{aligned}\beta_c\frac{\partial a}{\partial t} &= \epsilon^2\delta a - \Phi a|a|^2 + \frac{1}{2}\widehat{w}''(k_0)\left[\beta_c(\nu + i\partial_x)\right]^2 a \\ &+ \beta_c\left(\frac{\gamma}{2}\right)^2\left[(d_+ + d_-)\,a + d_1 a^* \delta_{n,1}\right], \end{aligned} \tag{84}$$

where $\gamma = \epsilon\overline{\gamma_1}$. This has solutions of the form,

$$a = \rho_n e^{i\phi}, \quad \rho_n = \sqrt{\frac{4\epsilon^2\delta + 2\widehat{w}''(k_0)(\beta_c\nu)^2 + \beta_c\gamma^2[d_+ + d_-(1+\delta_{n,1})]}{4\Phi}}. \tag{85}$$

For $\Phi > 0$, resonant stripe solutions exist for

$$\gamma > \sqrt{\frac{-2\widehat{w}''(k_0)(\beta_c\nu)^2 - 4\epsilon^2\delta}{\beta_c[d_+ + d_-(1+\delta_{n,1})]}}. \tag{86}$$

For $n = 2$ for the rich diversity of pattern formation, (83) becomes,

$$\beta_c\frac{\partial a}{\partial t} = \epsilon^2\delta a - \Phi a|a|^2 + \frac{1}{2}\widehat{w}''(k_0)\left[\beta_c(\nu + i\partial_x)\right]^2 a + \frac{\epsilon^2\gamma_2}{2}\beta_c a^*. \tag{87}$$

This has constant solutions of the form $a = \rho_2 e^{i\phi}$ where,

$$\rho_2 = \sqrt{\frac{2\epsilon^2\delta + \widehat{w}''(k_0)(\beta_c\nu)^2 + (-1)^m\gamma\beta_c}{2\Phi}}, \quad \phi = \frac{m\pi}{2}, \quad m \in \mathbb{Z}, \tag{88}$$

where $\gamma = \epsilon^2\gamma_2$. The solutions with m odd are unstable, so do not need to be considered any further. Assuming that m is even and also that $\Phi > 0$, the resonant stripe solutions exist for

$$\gamma > -\widehat{w}''(k_0)\beta_c\nu^2 - 2\epsilon^2\frac{\delta}{\beta_c}. \tag{89}$$

The tongue shaped existence ranges for n:1 resonant stripe patterns for $n = 1, \ldots 4$ are shown in Figure 22. The parameter values are such that $\Phi > 0$. We take $\epsilon^2\delta > 0$ so that we are beyond the pattern forming instability. Notice that in this case the existence regions have finite width, even at $\gamma = 0$ so the unforced system also supports bands of stripe solutions beyond the pattern forming instability.

The 2:1 resonance tongue is noticeably wider than those for other resonances and we also note that narrow bands of the tongues for the n:1 resonance patterns exists around $k_f/k_0 = 2$ for all values of $n \neq 2$. This is due to the fact that the tongue for $n = 2$ has a different form to those for other values of n. For $n = 2$, the forcing strength coefficient γ

appears linearly in the amplitude equation and therefore forcing has a stronger effect in this case than when $n \neq 2$ where γ appears squared. This difference in the power to which γ is raised in the amplitude equation occurs as a direct result of the forcing function being applied to a linear term in u in (56). If for instance we were to add forcing via a cubic order term in u we would expect to see a prominent 4:1 resonance.

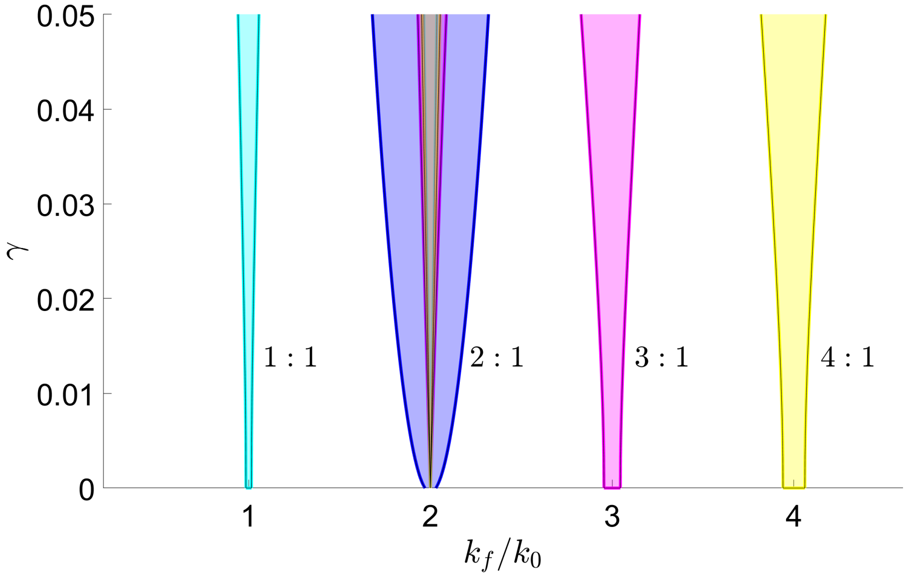

Figure 22.: Existence tongues for resonant stripe patterns in a one-dimensional neural field model with spatially periodic forcing. The kernel is chosen as in (45) with $\sigma = 0.8$. Other parameters are $h = 0$ and $\epsilon^2\delta = 10^{-4}$. The tongue with a 2:1 resonance is dominant.

4.2 NEURAL FIELD MODEL WITH SPATIAL FORCING IN TWO DIMENSIONS

Next, we calculate the amplitude equations and pattern formation regions for (56) in two dimensions; therefore this time with $\mathbf{r} = (x, y)$,

$$\frac{\partial u(\mathbf{r},t)}{\partial t} = -u(\mathbf{r},t) + \int_\Omega w(|\mathbf{r}-\mathbf{r}'|) f(u(\mathbf{r}'),t)\, \mathrm{d}\mathbf{r}' + \gamma u(x,t)\cos(k_f x), \quad (90)$$

We are modelling V1 using a tissue level model and thus require two dimensions for a complete model of the hallucinations.

4.2.1 *Multiple Scale Analysis*

Using multiple scale analysis, again we consider weak forcing $\gamma \ll 1$ near the instability $\epsilon \ll 1$. Now in two dimensions, we look for solutions of the type,

$$u \cong A(\chi, Y, \tau)e^{i(k_x x + k_y y)} + B(\chi, Y, \tau)e^{i(k_x x - k_y y)} + \text{c.c.}, \tag{91}$$

where A and B are complex valued amplitudes that have been extending in two spatial dimensions, $\chi = \epsilon x$ and $Y = \epsilon y$ and once in time, $\tau = \epsilon^2 t$. These amplitudes can be derived using the following methods.

In two dimensions, a further Taylor series expansion of the function u_α as

$$\begin{aligned} u_\alpha(x', y', t', \epsilon x', \epsilon y', \epsilon^2 t') &= u_\alpha(x', y', t', \chi + \epsilon(x' - x), Y + \epsilon(y' - y), \epsilon^2 t') \\ &\simeq u_\alpha(x', y', t', \chi, Y, \tau) + \epsilon \left[(x' - x)\frac{\partial}{\partial \chi} + (y' - y)\frac{\partial}{\partial Y} \right] u_\alpha(x', y', t', \chi, Y, \tau) \\ &+ \frac{1}{2}\epsilon^2 \left[(x' - x)\frac{\partial}{\partial \chi} + (y' - y)\frac{\partial}{\partial Y} \right]^2 u_\alpha(x', y', t', \chi, Y, \tau) + O(\epsilon^3), \end{aligned} \tag{92}$$

facilitates an evaluation of the spatial convolution of (90).

Note that since we are now working in two spatial dimensions we use wavenumber mismatch parameter $\nu_2 = k_0 - k_x$ where $k_x = k_f/2 + \nu_1$ and $k_y = \sqrt{k_0^2 - k_x^2}$ to compensate for the unfavorable forcing wavenumber and achieve the total wavenumber k_0. For the calculations we retain ν_1, however we can later set $\nu_1 = 0$ without loss of generality.

4.2.2 *Hierarchy of Equations*

The expansion of (90) in two dimensions is the same as before (62 - 63) as the space was defined as u without defining the dimension. By using the multiscale expansion of u (92) this is now extended in two spatial dimensions, χ and Y and in once in time, τ, and using the multiple scale expansion (62) and (63), this gives the fully expanded model. Taking the terms for each order of epsilon gives the same as before (65 - 68), whereas now we have two dimensional operators,

$$M_0 = w\otimes, \tag{93}$$

$$M_1 = W^x \otimes \partial_\chi + W^y \otimes \partial_\mathrm{Y}, \tag{94}$$

$$M_2 = \frac{1}{2}\left[W^{xx} \otimes \partial_{\chi\chi} + W^{yy} \otimes \partial_{\mathrm{YY}} + 2W^{xy} \otimes \partial_{\chi\mathrm{Y}}\right]. \tag{95}$$

where we now introduce the two dimensional kernels as $W^x(\mathbf{r}) = -w(|\mathbf{r}|)x$ and $W^{xy}(\mathbf{r}) = w(|\mathbf{r}|)xy$ analogously to the scalar case (73-74). Similarly to the one dimensional case, the two dimensional Fourier transforms of these kernels satisfy $\widehat{W}^{xy}(\mathbf{k}) = \widehat{W}^{xx}(\mathbf{k}) = \widehat{W}^{yy}(\mathbf{k}) = -\widehat{w}''(k)$ where $k = |\mathbf{k}|$ and also $\widehat{W}^x(\mathbf{k}) = \widehat{W}^y(\mathbf{k}) = -\mathrm{i}\widehat{w}'(k)$ and so $\widehat{W}^x(k_0) = \widehat{W}^y(k_0) = 0$.

4.2.3 *Solving the equations*

Once again, we can see that each equation in the hierarchy above contains terms of the asymptotic expansion of u only of the same order or lower. This means that we can start from the first equation and systematically solve for u_α. The first equation (65) in the hierarchy again fixes the steady state u_0. By choosing a balanced kernel we have $u_0 = 0$.

The null space of the linear operator $\mathcal{L}$ is spanned by $\left\{\mathrm{e}^{\pm i(k_x x \pm k_y y)}\right\}$ where $k_x^2 + k_y^2 = k_0^2$ and therefore u_1 has solution

$$u_1 = A(\chi, \mathrm{Y}, \tau)\mathrm{e}^{i(k_x x + k_y y)} + B(\chi, \mathrm{Y}, \tau)\mathrm{e}^{i(k_x x - k_y y)} + \text{c.c.}, \tag{96}$$

4.2.4 *Amplitude Equations*

By using the Fredholm Alternative, we find a particular solution to (67) and use a solvability condition for (68) to derive the evolution of the amplitudes $A(\chi, Y, \tau)$ and $B(\chi, Y, \tau)$. The calculations of these can be found in Appendix. A.2 and the resulting amplitude equations, rescaled back to the original time and space variables, are

$$\begin{aligned}\beta_c \frac{\partial a}{\partial t} &= \epsilon^2 \delta a - \Phi_1 |a|^2 a - \Phi_2 |b|^2 a + \frac{\beta_c^2}{2} \widehat{w}''(k_0) \left((i\partial_x + v_1)^2 - \partial_{yy} \right) a \\ &\quad + \frac{\epsilon^2 \gamma_2}{2} b^* \delta_{n,2} + \left(\frac{\epsilon \overline{\gamma}_1}{2} \right)^2 (1 - \delta_{n,2}) \left[(z_+ + z_-) a + z_- b^* \delta_{n,1} \right], \qquad (97) \\ \beta_c \frac{\partial b}{\partial t} &= \epsilon^2 \delta b - \Phi_1 |b|^2 b - \Phi_2 |a|^2 b + \frac{\beta_c^2}{2} \widehat{w}''(k_0) \left((i\partial_x + v_1)^2 - \partial_{yy} \right) b \\ &\quad + \frac{\epsilon^2 \gamma_2}{2} a^* \delta_{n,2} + \left(\frac{\epsilon \overline{\gamma}_1}{2} \right)^2 (1 - \delta_{n,2}) \left[(z_+ + z_-) b + z_- a^* \delta_{n,1} \right], \qquad (98)\end{aligned}$$

All new parameters created in this derivation are defined as they arise in Appendix A.2.

4.2.5 *Existence of Solutions*

Using the derived equations (97 - 98), for $n = 2$ for the rich diversity of pattern formation, we have,

$$\beta_c \frac{\partial a}{\partial t} = \epsilon^2 \delta a - \Phi_1 |a|^2 a - \Phi_2 |b|^2 a + \frac{\beta_c^2}{2} \widehat{w}''(k_0) \left((i\partial_x + v_1)^2 - \partial_{yy} \right) a + \frac{\gamma}{2} b^* \qquad (99)$$

$$\beta_c \frac{\partial a}{\partial t} = \epsilon^2 \delta b - \Phi_1 |b|^2 b - \Phi_2 |a|^2 a + \frac{\beta_c^2}{2} \widehat{w}''(k_0) \left((i\partial_x + v_1)^2 - \partial_{yy} \right) b + \frac{\gamma}{2} a^*. \qquad (100)$$

where $\gamma = \epsilon^2 \gamma_2$. We look for stationary homogeneous solutions of (99 - 100). We also choose to set $\nu_1 = 0$ so that $k_x = k_f/2 = k_0 - \nu_2$ and dependence on the mismatch between k_f and k_0 enters the amplitude equations through

k_x and k_y, noting that Φ_2 depends on these parameters. By looking for solutions using the polar form,

$$a = \rho_a \exp(i\alpha), \quad b = \rho_b \exp(i\beta). \tag{101}$$

By substituting (101) into (99 & 100), we obtain,

$$\beta_c \left[\rho_a \mathrm{e}^{i\alpha} \left(i \frac{\partial \alpha}{\partial t} \right) + \frac{\partial \rho_a}{\partial t} \mathrm{e}^{i\alpha} \right] = \epsilon^2 \delta \rho_a \mathrm{e}^{i\alpha} - \left(\Phi_1 \rho_a^2 + \Phi_2 \rho_b^2 \right) \rho_a \mathrm{e}^{i\alpha} + \frac{\gamma}{2} \beta_c \rho_b \mathrm{e}^{-i\beta}, \tag{102}$$

$$\beta_c \left[\rho_b \mathrm{e}^{i\beta} \left(i \frac{\partial \beta}{\partial t} \right) + \frac{\partial \rho_b}{\partial t} \mathrm{e}^{i\beta} \right] = \epsilon^2 \delta \rho_b \mathrm{e}^{i\beta} - \left(\Phi_1 \rho_b^2 + \Phi_2 \rho_a^2 \right) \rho_b \mathrm{e}^{i\beta} + \frac{\gamma}{2} \beta_c \rho_a \mathrm{e}^{-i\alpha}. \tag{103}$$

By balancing the real and imaginary parts of these equations and manipulating them, we derive the equations for space independent solutions,

$$\beta_c \rho_{a_t} = \delta \epsilon^2 \rho_a - \left(\Phi_1 \rho_a^2 + \Phi_2 \rho_b^2 \right) \rho_a + \frac{\gamma}{2} \beta_c \rho_b \cos(\phi), \tag{104}$$

$$\beta_c \rho_{b_t} = \delta \epsilon^2 \rho_b - \left(\Phi_1 \rho_b^2 + \Phi_2 \rho_a^2 \right) \rho_b + \frac{\gamma}{2} \beta_c \rho_a \cos(\phi), \tag{105}$$

$$\phi_t = -\frac{\gamma}{2} \left(\frac{\rho_b}{\rho_a} + \frac{\rho_a}{\rho_b} \right) \sin(\phi), \tag{106}$$

$$\psi_t = -\frac{\gamma}{2} \left(\frac{\rho_b}{\rho_a} - \frac{\rho_a}{\rho_b} \right) \sin(\phi), \tag{107}$$

where $\phi = \alpha + \beta$ and $\psi = \alpha - \beta$.

Therefore the steady states are,

$$0 = \delta \epsilon^2 \rho_a - \left(\Phi_1 \rho_a^2 + \Phi_2 \rho_b^2 \right) \rho_a + \frac{\gamma}{2} \beta_c \rho_b \cos(\phi), \tag{108}$$

$$0 = \delta \epsilon^2 \rho_b - \left(\Phi_1 \rho_b^2 + \Phi_2 \rho_a^2 \right) \rho_b + \frac{\gamma}{2} \beta_c \rho_a \cos(\phi), \tag{109}$$

$$0 = -\frac{\gamma}{2} \left(\frac{\rho_b}{\rho_a} + \frac{\rho_a}{\rho_b} \right) \sin(\phi), \tag{110}$$

$$0 = -\frac{\gamma}{2} \left(\frac{\rho_b}{\rho_a} - \frac{\rho_a}{\rho_b} \right) \sin(\phi), \tag{111}$$

By looking at (111 & 110) we either have the trivial solution $\rho_a = \rho_b = 0$ or constant solutions of the form,

$$\rho_a = \rho_{a0}, \quad \rho_b = \rho_{b0}, \quad \phi = n\pi, \quad n = 0, 1.$$

By linearising (106) around this solution we obtain,

$$\begin{aligned}\frac{\partial}{\partial t}\left[\phi_0+\Delta\phi\right] =& -\frac{\gamma}{2}\left(\frac{\rho_{b0}+\Delta\rho_b}{\rho_{a0}+\Delta\rho_a}+\frac{\rho_{a0}+\Delta\rho_a}{\rho_{b0}+\Delta\rho_b}\right)\sin(\phi_0+\Delta\phi)\\ =& -\frac{\gamma}{2}\left(\frac{\rho_{b0}+\Delta\rho_b}{\rho_{a0}\left(1+\Delta\rho_a/\rho_{a0}\right)}+\frac{\rho_{a0}+\Delta\rho_a}{\rho_{b0}\left(1+\Delta\rho_b/\rho_{b0}\right)}\right)\sin(\phi_0)\\ &+\cos(\phi_0)\Delta\phi\\ =& -\frac{\gamma}{2}\left(\frac{\left(\rho_{b0}+\Delta\rho_b\right)\left(1-\Delta\rho_a/\rho_{a0}\right)}{\rho_{a0}}\right.\\ &\left.+\frac{\left(\rho_{a0}+\Delta\rho_a\right)\left(1-\Delta\rho_b/\rho_{b0}\right)}{\rho_{b0}}\right)\sin(\phi_0)+\cos(\phi_0)\Delta\phi,\\ \frac{\partial\psi_0}{\partial t} =& (-1)^{n+1}\frac{\gamma}{2}\left(\frac{\rho_{b0}}{\rho_{a0}}+\frac{\rho_{a0}}{\rho_{b0}}\right)\Delta\phi_0.\end{aligned}$$

When $n=1$, $\phi=\pi$ which is unstable, therefore we will not consider this. When $n=0$, $\phi=0$, ψ is constant and therefore we have α and $\beta=-\alpha$ being independent of time, Thus,

$$\beta_c\rho_{a_t} = \delta\epsilon^2\rho_a-\left(\Phi_1\rho_a^2+\Phi_2\rho_b^2\right)\rho_a+\frac{\gamma}{2}\beta_c\rho_b, \tag{112}$$

$$\beta_c\rho_{b_t} = \delta\epsilon^2\rho_b-\left(\Phi_1\rho_b^2+\Phi_2\rho_a^2\right)\rho_b+\frac{\gamma}{2}\beta_c\rho_a, \tag{113}$$

is now a three-dimensional dynamical system for (ρ_a,ρ_b,ψ).

4.2.6 *Existence of Patterns*

From (112 & 113), we look for a constant solution of the form, $\rho_a=\rho_b=\rho_0$. This gives,

$$0 = \delta\epsilon^2\rho_0-\left(\Phi_1\rho_0^2+\Phi_2\rho_0^2\right)\rho_0+\frac{\gamma}{2}\beta_c\rho_0, \tag{114}$$

$$= \rho_0\left(\delta\epsilon^2-\left(\Phi_1+\Phi_2\right)\rho_0^2+\frac{\gamma}{2}\beta_c\right), \tag{115}$$

which has roots $\rho_0=0$ (the trivial solution again) or

$$\rho_0=\sqrt{\frac{\delta\epsilon^2+\frac{\gamma}{2}\beta_c}{\Phi_1+\Phi_2}}. \tag{116}$$

These are constant rectangular patterns

$$\begin{aligned}u(x,y,t) &= \rho_0 e^{ik_f x/2}\left(e^{i(k_y y+\phi_a)}+e^{-i(k_y y+\phi_a)}\right)+\text{c.c.}\\ &= 4\rho_0\cos(k_f x/2)\cos(k_y y+\phi_a),\end{aligned} \tag{117}$$

where $k_y = \sqrt{k_0^2 - k_x^2}$, $k_x = k_f/2 = k_0 - v_2$. The undetermined phase ϕ_a arises due to the continuous translational symmetry in the y-direction which is not broken by the forcing. These solutions exist for $0 < v_2 < 2k_0$ (to ensure that $k_y \in \mathbb{R}$) and where also $2\epsilon^2\delta + \gamma\beta_c$ and $\Phi_1 + \Phi_2$ have the same sign, noting that $\Phi_2 = \Phi_2(v_2)$.

From (112 & 113), we can also look for a constant solution of the form, $\rho_a = \rho_\pm, \quad \rho_b = \rho_\mp$. We can manipulate the steady states of (112 & 113) to give,

$$\delta\epsilon^2 = \Phi_1(\rho_a^2 + \rho_b^2), \tag{118}$$

$$\frac{\gamma\beta_c}{2} = -\rho_a\rho_b(\Phi_1 - \Phi_2). \tag{119}$$

Thus, giving,

$$\rho_\pm = \sqrt{\frac{\delta\epsilon^2}{2\Phi_1} \pm \sqrt{\frac{\delta^2\epsilon^4}{4\Phi_1^2} - \frac{\beta_c\gamma^2}{4(\Phi_1 - \Phi_2)^2}}}. \tag{120}$$

Hence, this gives a one-parameter family of solutions,

$$a_\pm = \rho_\pm \exp(i\alpha), \quad b_\mp = \rho_\mp \exp(-i\alpha). \tag{121}$$

These are constant oblique patterns

$$\begin{aligned} u(x,y,t) &= e^{ik_f x/2}\left(\rho_\pm e^{i(k_y y + \phi_a)} + \rho_\mp e^{-i(k_y y + \phi_a)}\right) + \text{c.c.} \\ &= 2\rho_\pm \cos(k_f x/2 + k_y y + \phi_a) + 2\rho_\mp \cos(k_f x/2 - k_y y - \phi_a), \end{aligned} \tag{122}$$

where ϕ_a is again undetermined and $k_y = \sqrt{k_0^2 - k_x^2}$, $k_x = k_f/2 = k_0 - v_2$. These solutions exist for $0 < v_2 < 2k_0$ (to ensure that $k_y \in$ R) and where also

$$\frac{\epsilon^2\delta}{2\Phi_1} > 0 \qquad \text{and} \qquad |\gamma| < \frac{\epsilon^2\delta}{\beta_c\Phi_1}\left|\Phi_1 - \Phi_2\right|.$$

The values of v_2 and γ for which resonant rectangle and oblique patterns exist depend on the values of σ (the spatial scale of interaction) and h (the firing rate threshold).

The existence regions for a range of values of h for $\sigma = 0.5$ are illustrated in Fig. 23. Regions where rectangle patterns exist are shaded blue, while red shading indicates existence of oblique patterns under the additional assumption that $\epsilon^2\delta/\Phi_1 > 0$. Outside of these regions, solutions do not exist so were not considered. For $h = 0$ we observe similar existence regions for these patterned states as observed in [81] for the Swift-Hohenberg equation under periodic spatial forcing. For nonzero choices of h we observe more complex existence regions. We note that the existence regions for $-h$ are identical to those for h. This is due to the fact that $f'(u_0)$ is an even function of h. The values of β_2 and β_3 depend on μ where μ is fixed once h and σ are specified. Since for given a given value of h, μ satisfies $\beta_c = 1/\widehat{w}(k_0) = f'(u_0)$, then $-h$ gives the same values of μ as h.

4.2.7 *Linear Stability of Patterns*

We can also consider the linear stability of the two-dimensional constant resonance patterns to uniform perturbations. Making perturbations $\Delta\rho_a$ and $\Delta\rho_b$ to the constant solution ρ_a, ρ_b and linearising we find that the perturbations satisfy

$$\frac{\partial}{\partial t}\begin{pmatrix} \Delta\rho_a \\ \Delta\rho_b \end{pmatrix} = \frac{1}{\beta_c}\begin{pmatrix} \epsilon^2\delta - 3\Phi_1\rho_a^2 - \Phi_2\rho_b^2 & -2\Phi_2\rho_a\rho_b + \frac{\gamma\beta_c}{2} \\ -2\Phi_2\rho_a\rho_b + \frac{\gamma\beta_c}{2} & \epsilon^2\delta - 3\Phi_1\rho_b^2 - \Phi_2\rho_a^2 \end{pmatrix}\begin{pmatrix} \Delta\rho_a \\ \Delta\rho_b \end{pmatrix}. \tag{123}$$

The Jacobian, J, in (123) has eigenvalues

$$\lambda_\pm = \frac{\mathrm{Tr}(J)}{2} \pm \frac{1}{2}\sqrt{(\mathrm{Tr}(J))^2 - 4\mathrm{Det}(J)}.$$

The zero state ($\rho_a = \rho_b = 0$) has eigenvalues $(\epsilon^2\delta/\beta_c) \pm \gamma/2$ and is therefore stable for $2\epsilon^2\delta \pm \gamma\beta_c < 0$ since $\beta_c > 0$. Rectangular patterns have $\rho_a = \rho_b = \rho_0$ and eigenvalues

$$\lambda_+ = -2\left(\frac{\epsilon^2\delta}{\beta_c} + \frac{\gamma}{2}\right), \quad \lambda_- = \frac{-2(\Phi_1 - \Phi_2)\epsilon^2\delta - 2\Phi_1\gamma\beta_c}{\beta_c(\Phi_1 + \Phi_2)}.$$

Therefore rectangles are stable when $2\epsilon^2\delta + \gamma\beta_c > 0$ (and we need $\Phi_1 + \Phi_2 > 0$ so that the solutions exist here) and also $(\Phi_1 - \Phi_2)\epsilon^2\delta + \Phi_1\gamma\beta_c > 0$.

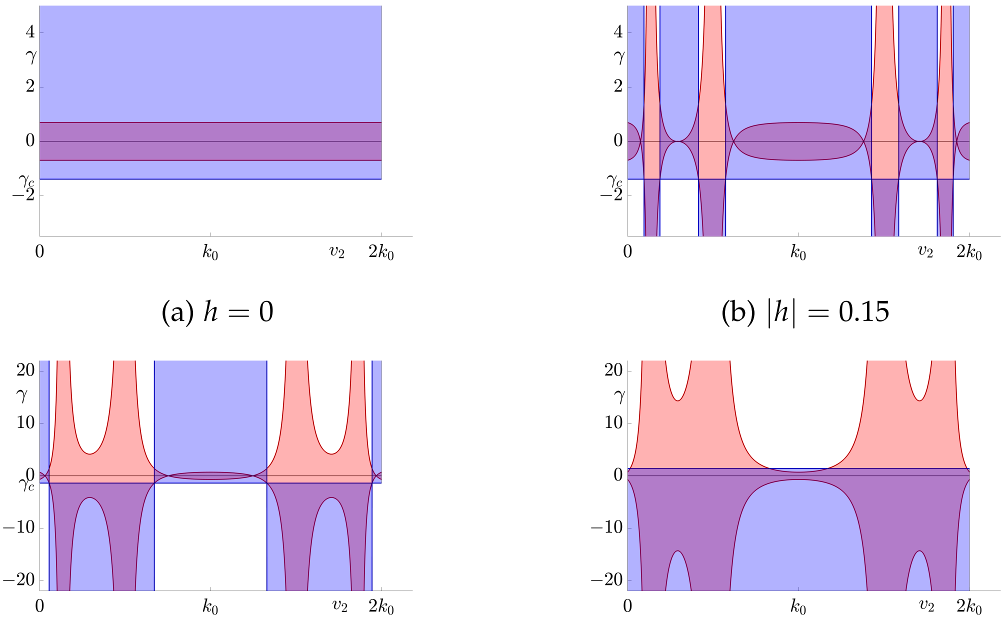

(a) $h = 0$ (b) $|h| = 0.15$

(c) $|h| = 0.3$ (d) $|h| = 0.5$

Figure 23.: Existence regions for patterned states in a two-dimensional neural field model with spatially periodic forcing. Blue shaded regions indicate where stationary rectangle patterns exist and red shading indicates existence of oblique patterns. The kernel is chosen as in (45) with $\sigma = 0.5$ and the firing rate is given by (43) with (a) $h = 0$, (b) $|h| = 0.15$, (c) $|h| = 0.3$, (d) $|h| = 0.5$. Other parameters are $\epsilon^2\delta = 0.3$ for (a)–(c) and $\epsilon^2\delta = -0.3$ for (d). Note that existence of oblique patterns also requires that $\epsilon^2\delta/\Phi_1 > 0$. Here $\gamma_c = -2\epsilon^2\delta/\beta_c$.

For oblique patterns, where $\rho_a \neq \rho_b$, we note from (116) that the constant solutions satisfy

$$\epsilon^2\delta = \Phi_1(\rho_a^2 + \rho_b^2) \quad \text{and} \quad \gamma\beta_c = -2\rho_a\rho_b(\Phi_1 - \Phi_2),$$

and therefore the Jacobian matrix J in (123) has

$$\mathrm{Tr}(J) = -(\Phi_1 + \Phi_2)\frac{\epsilon^2\delta}{\beta_c\Phi_1}, \tag{124}$$

$$\mathrm{Det}(J) = -2\left(\frac{\epsilon^2\delta}{\beta_c\Phi_1}\right)^2 \Phi_1(\Phi_1 - \Phi_2) + \left(\frac{3\Phi_1 - \Phi_2}{\Phi_1 - \Phi_2}\right)^2 \left(\frac{\gamma}{2}\right)^2. \tag{125}$$

The oblique patterns are stable when $\mathrm{Tr}(J) < 0$ and $\mathrm{Det}(J) > 0$. The first of these conditions is satisfied when the patterns exist and $\Phi_1 + \Phi_2 > 0$. Note then that all stable constant resonant two-dimensional patterns exist within the upper blue shaded regions in Figure 23a–23d. Stability regions in the (v_2, γ) plane are indicated for rectangle and oblique patterns in Figure 24 for $\epsilon^2\delta = 0.3$ and $|h| = 0.15$. Stability results for $|h| = 0.15$ are illustrated in the bifurcation diagrams in Figure 25. There is a change in stability between rectangles and obliques at $\gamma = \gamma_c = (\Phi_2 - \Phi_1)\epsilon^2\delta/(\Phi_1\beta_c)$ for fixed $\epsilon^2\delta$ or at $(\epsilon^2\delta)_c = \gamma\Phi_1\beta_c/(\Phi_2 - \Phi_1)$ for fixed γ.

The stable two-dimensional leading order pattern for values of v_2 increasing from 0 to k_0 (corresponding to k_x decreasing from k_0 to 0) and a range of values of forcing strength γ are shown in Figure 26. Here we choose $h = 0$ so that stable two-dimensional leading order patterns exist for all values of v_2. As v_2 is increased from 0 to k_0 the pattern changes from vertical stripes to rectangles (when $\gamma > \gamma_c$) or oblique patterns (when $\gamma < \gamma_c$) to horizontal stripes which are orthogonal to the forcing. At $v_2 = k_0/4$ the rectangular patterns are square and the oblique patterns are precisely diagonal. Direct numerical simulations confirm that using the mismatch parameter v_2 to control the forcing can indeed lead to stripe patterns along the x-direction changing to stripe patterns along the y-direction. Thus, a simple neural field model can support an orthogonal response to patterned input.

The two-dimensional resonant patterns exist and are stable for a range of values of the detuning v_2 and these lie in 1, 3 or 5 bands whose widths depend on the value of the firing rate threshold h. The width of these bands does not depend on γ and hence the resonant patterns exist even in the limit of weak forcing $\gamma \to 0$. We also note in particular that a band of stable resonant orthogonal response patterns exists around $v_2 = k_0$ for all $|h| < h_c$ where $h_c \approx 0.4196$ for $\sigma = 0.5$.

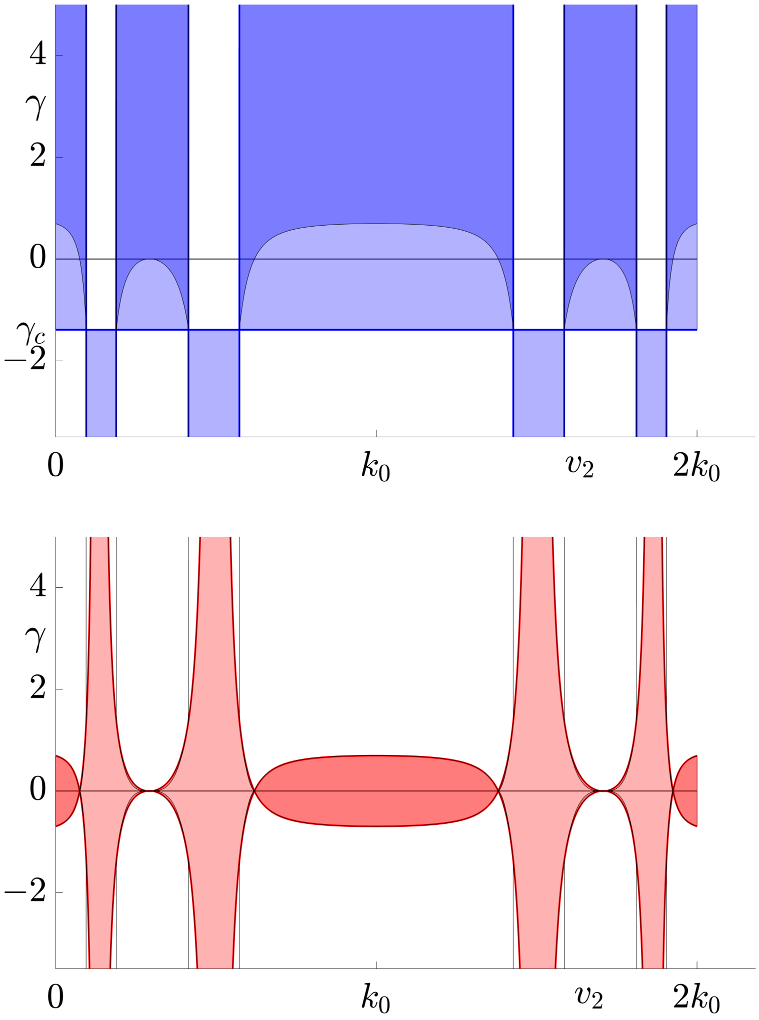

Figure 24.: Stability tongues for constant two-dimensional 2:1 resonant solution patterns for the forced neural field equation (90). The top (bottom) diagram show the existence and stability tongues for rectangles (obliques). Darker shading indicates where the pattern is stable. Here $\sigma = 0.5$, $|h| = 0.15$, $\epsilon^2\delta = 0.3$ and $\gamma_c = -2\epsilon^2\delta/\beta_c$.

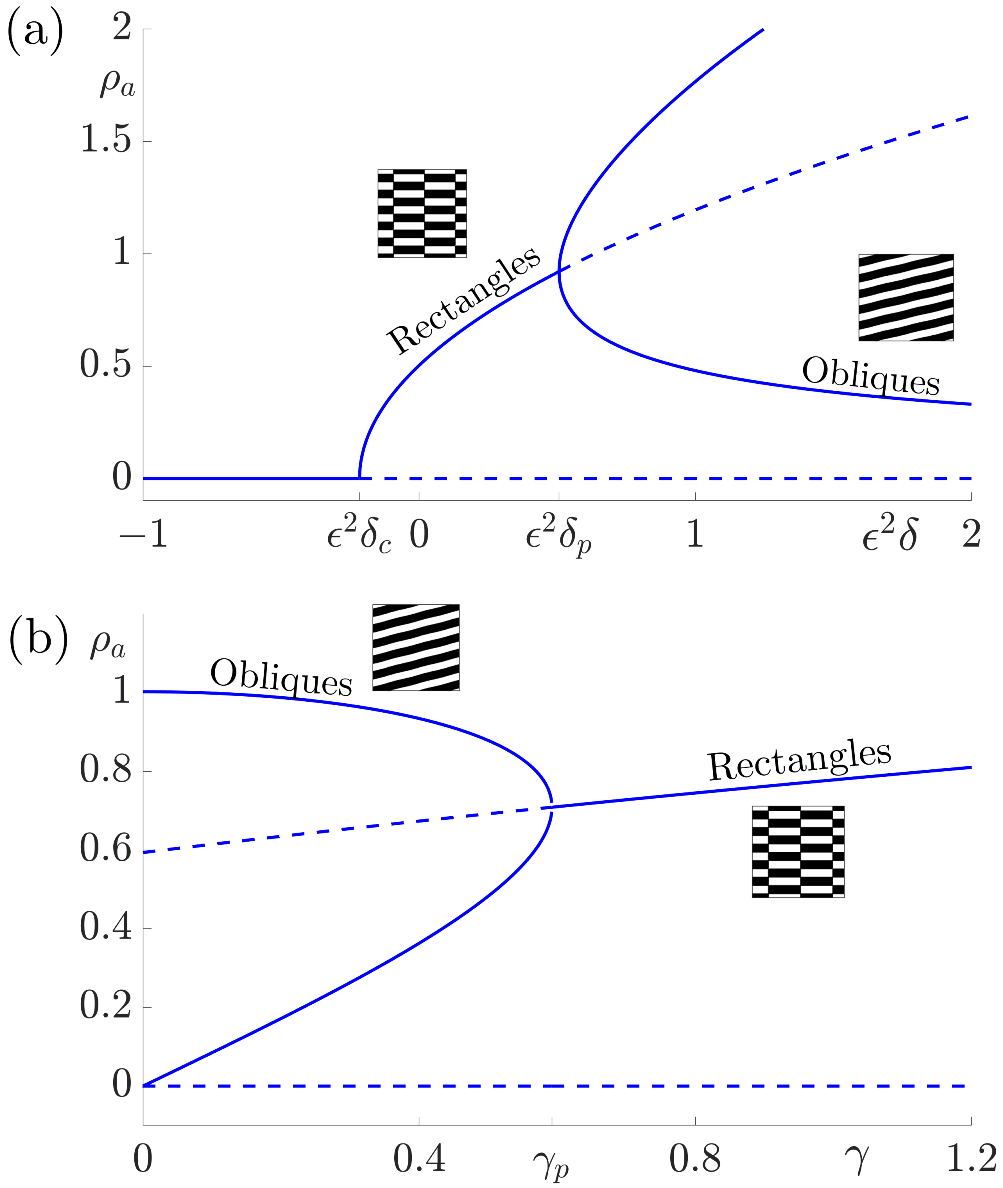

Figure 25.: Bifurcation diagrams for constant two-dimensional pattern solutions for the forced neural field equation (90). Solid lines indicate stable states while dotted lines indicate unstable solutions. In both diagrams parameter values are $\sigma = 0.5$, $|h| = 0.15$ and $v_2 = 0.75k_0$. In diagram (a) we fix forcing strength $\gamma = 1$ and range over values of $\epsilon^2\delta$. Here the Turing bifurcation occurs at $\epsilon^2\delta_c = -\gamma\beta_c/2$ and the bifurcation of rectangles to stable obliques occurs at $\epsilon^2\delta_p = \gamma\beta_c\Phi_1/(\Phi_2 - \Phi_1)$. In diagram (b) we hold the distance from Turing instability, $\epsilon^2\delta = 0.3$, and range over values of γ with the bifurcation between patterned states at $\gamma_p = (\Phi_2 - \Phi_1)\epsilon^2\delta/(\beta_c\Phi_1)$.

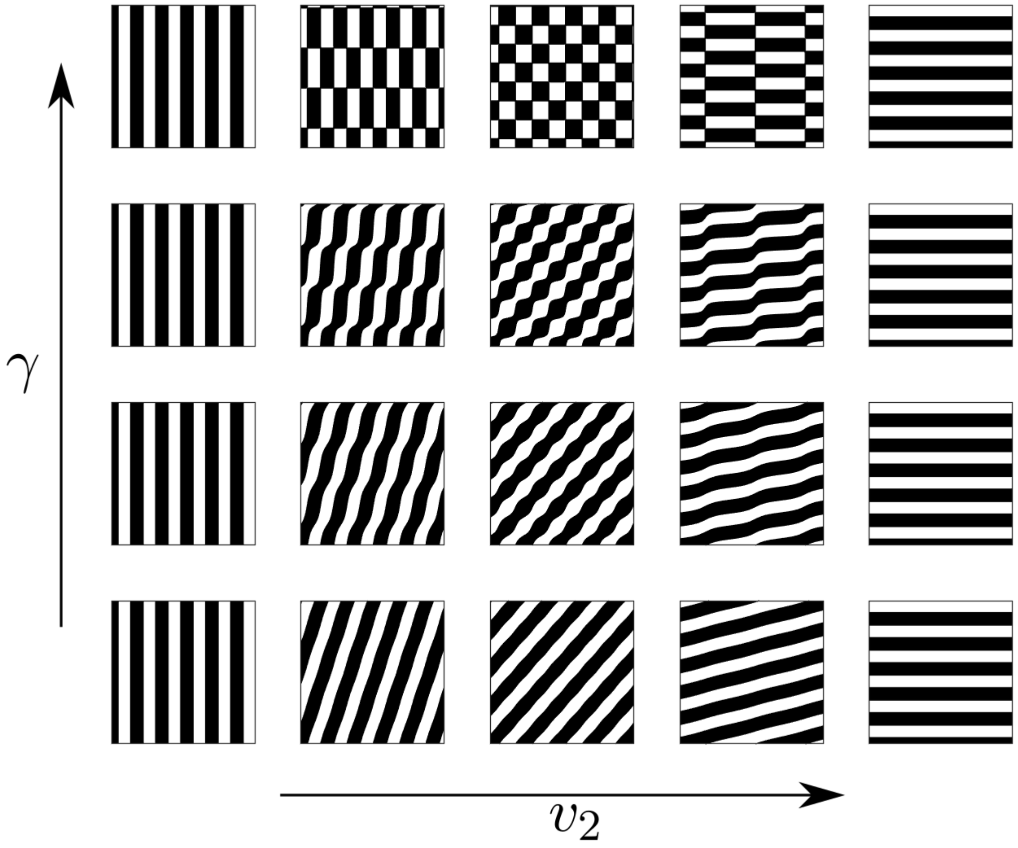

Figure 26.: Planforms of the stable leading order solution demonstrating pattern diversity and orthogonal response. Choosing $h = 0$ (so that existence and stability of solutions does not depend on v_2) we see that as v_2 is increased from 0 to k_0 the pattern changes from vertical stripes to rectangles (when $\gamma > \gamma_c$) or oblique patterns (when $\gamma < \gamma_c$) to horizontal stripes which are orthogonal to the forcing. This corresponds to varying k_x from k_0 (with a response in the direction of forcing) to 0 (with a response orthogonal to the direction of forcing). Note that if we choose h differently then for some values of v_2 these leading order solution patterns do not exist. Other parameter values are $\sigma = 0.5$, $\epsilon^2\delta = 0.3$, $v_2 = [0, 0.05, 0.25, 0.75, 1]k_0$, $\gamma = [0.1, 0.4, 0.65, 1.1]$. Planforms are plotted for $x, y \in [0, 10\pi]$.

4.3 SIMULATIONS

The analytical work in previous sections has established that an orthogonal response to global spatially periodic forcing can be robustly supported in a standard neural field model. If the conditions for a resonant response are met, then a visual stimulus in the form of a set of concentric rings may give rise to a percept of a set of radial arms (one for each ring). Similarly, a visual stimulus in the form of a set of radial arms may give rise to a percept of a set of concentric rings. This is consistent with the observations of Billock and Tsou described in section 3.1, albeit these are more accurately described by drive on the cortical half-space (since the stimuli do not cover the whole visual field). To complement our results for forcing on the whole cortical space we now turn to direct numerical simulations. By forcing with striped patterns on the cortical half-space we recover the two dimensional stationary features reported in Fig. 14, once the inverse retinocortical map is applied. We show the corresponding plots for cortical activity in Fig. 27 and the cortical activity mapped to the retina in Fig. 28.

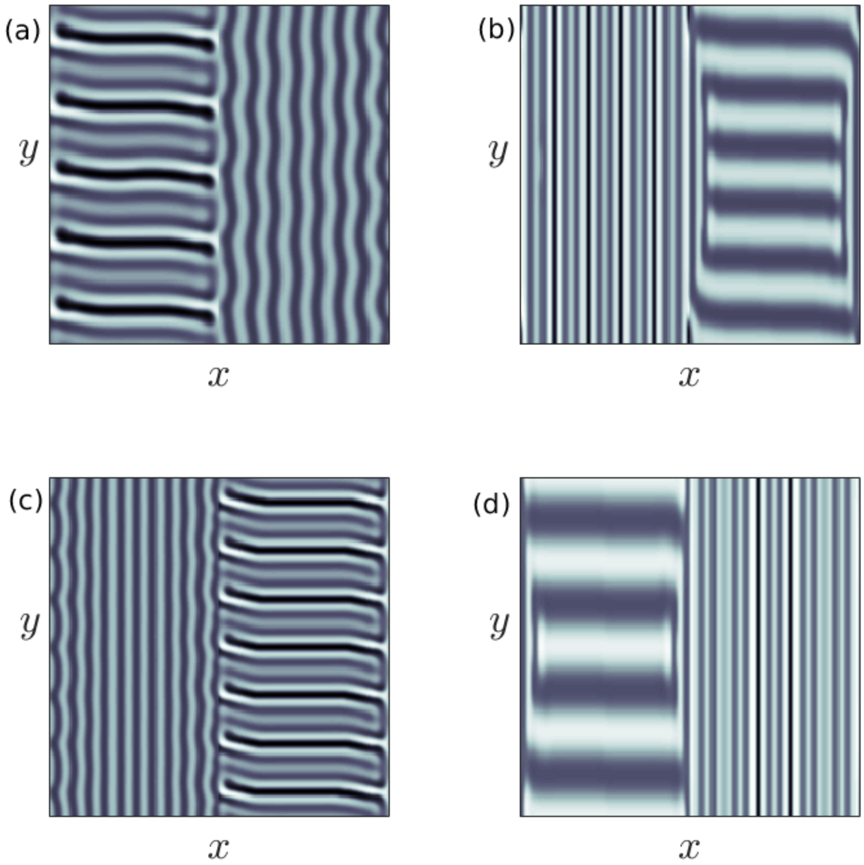

Figure 27.: Simulation results from a neural field model with spatially periodic striped forcing on the half-space. (a) Horizontal stripes forcing the left half-space give rise to stationary vertical stripes on the right. (b) Vertical stripes forcing the left half-space give rise to stationary horizontal stripes on the right. (c) Horizontal stripes forcing the right half-space give rise to stationary vertical stripes on the left. (d) Vertical stripes forcing the right half-space give rise to stationary horizontal stripes on the left. Parameter values are $\sigma = 0.8, \mu = 7.1974, h = 0, \gamma = 0.05$ and $\nu_2 = 0$ for (a) and (c) and $\nu_2 = k_0$ for (b) and (d). The plots are on the domain $x, y \in [0, 10\pi]$ with periodic boundary conditions.

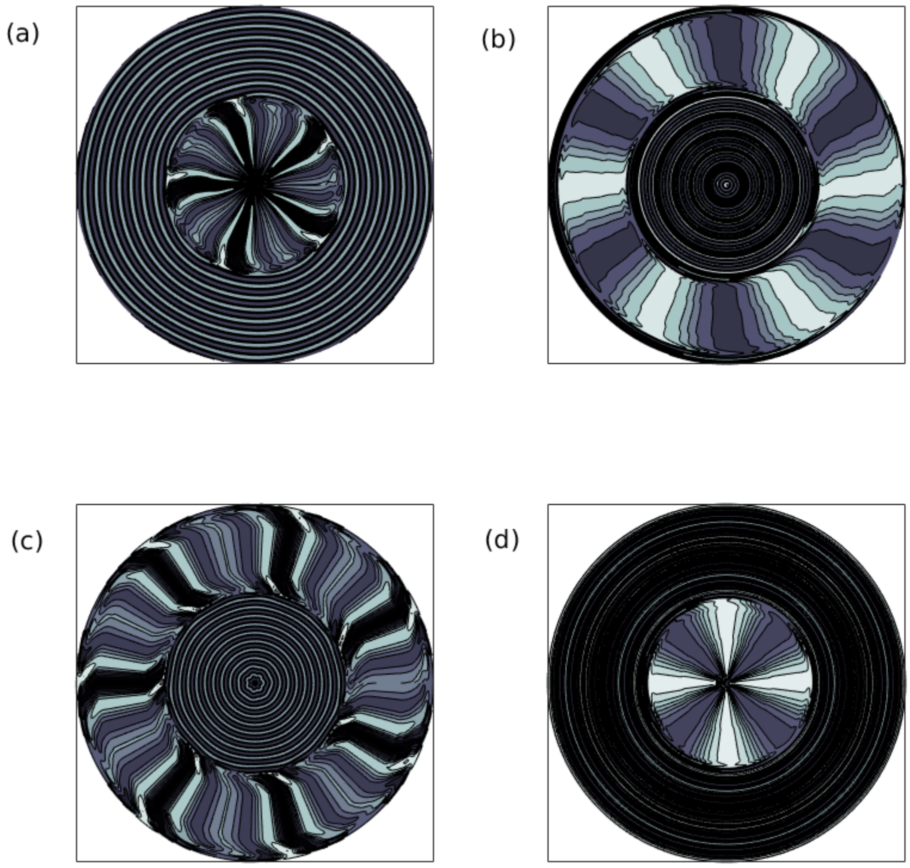

Figure 28.: Simulation results from a neural field model with spatially periodic striped forcing on the half-space mapped back onto the retina using a simple log mapping. (a) Horizontal stripes forcing the left half-space give rise to stationary vertical stripes on the right. (b) Vertical stripes forcing the left half-space give rise to stationary horizontal stripes on the right. (c) Horizontal stripes forcing the right half-space give rise to stationary vertical stripes on the left. (d) Vertical stripes forcing the right half-space give rise to stationary horizontal stripes on the left. Parameter values are $\sigma = 0.8, \mu = 7.1974, h = 0, \gamma = 0.05$ and $\nu_2 = 0$ for (a) and (c) and $\nu_2 = k_0$ for (b) and (d). The plots are on the cortical domain $x, y \in [0, 10\pi]$ with periodic boundary conditions.

4.4 SUMMARY

In summary, in this chapter, we were able to derive the amplitude equations for the neural field model with spatial forcing and conduct analysis for the existence and stability of solutions to find parameter regimes for spatially periodic patterns in both one and two dimensions. Direct numerical simulations were produced to show the resultant activity of the model in chosen parameter regimes to replicate the neural activity of interest in the hallucination context. By mapping this cortical activity back to the retina using an inverse log mapping, we showed that these simulation were in fact a good likeness for the hallucinations that occurred in the work of Billock and Tsou, albeit stationary. In the next chapter, we extend this work to treat a form of of spike frequency adaptation that can underlie pattern movement to introduce travelling waves and hence, the movement in the hallucinations. In conclusion, we have all of the underlying analytical work to be able to find parameter regimes for interesting pattern formation in numerical simulations relevant to the psychophysical observations with movement.

5

ADAPTATION MODEL

The simulations of the two dimensional neural field model with spatial forcing paint a picture showing how to recreate the Billock and Tsou hallucinations in Fig. 14. The patterns of activity in Fig. 27 are stationary corresponding to the stationary hallucination patterns. However, the hallucinations reported by Billock and Tsou [10] also include rotational movement so a mechanism for the creation of patterns which move (i.e. travelling or standing wave patterns) now needs to be incorporated into our model. The inclusion of adaptation means that the model is more realistic, in the sense that this gives a phenomenological description of metabolic processes that lead to fatigue. It also provides a well-known route to dynamic instabilities leading to the formation of travelling periodic waves. The latter are expected to be a key requirement for illusory motion.

5.1 ADAPTION MODEL

The neural field model can be extended to the adaptation model, introduced by [94] and analysed in [28, 65], this includes negative feedback of the firing of neurons,

$$\frac{\partial u(\mathbf{r},t)}{\partial t} = -u(\mathbf{r},t) + \int_{\mathbb{R}} w(\mathbf{r},\mathbf{r}')f(u(\mathbf{r}',t))\ \mathrm{d}\mathbf{r}' - ga(\mathbf{r},t), \tag{126}$$

$$\tau_a \frac{\partial a(\mathbf{r},t)}{\partial t} = u(\mathbf{r},t) - a(\mathbf{r},t). \tag{127}$$

Here a is a scalar field that represents a negative feedback adaptation variable that describes the local feedback mechanisms that modulate synaptic currents in the tissue. Also, the parameter $g > 0 \in \mathbb{R}$ controls the strength of the negative feedback and τ_a determines the relative time-scale. In this chapter, we will first consider $\mathbf{r} = x \in \mathbb{R}$ and then $\mathbf{r} = (x, y) \in \mathbb{R}^2$, both with $t > 0$. Again, we will work with the rotationally symmetric Wizard hat function (45) and firing rate function (43) from chapter 4.

5.1.1 *Change of Formula*

All of the previous work in chapter 4 was completed on one nonlinear equation and this is useful for performing analysis. The adaption model has been stated in (126-127) as two equations; however, these can be combined to give the model as one equation. As (127) is linear we can solve this equation and therefore condense (126 & 127) into one equation,

$$\tau_a \frac{\partial a(\mathbf{r},t)}{\partial t} = -a(\mathbf{r},t) + u(\mathbf{r},t), \tag{128}$$

$$\frac{\partial}{\partial t}[a\mathrm{e}^{t/\tau_a}] = \frac{u}{\tau_a}\mathrm{e}^{t/\tau_a}, \tag{129}$$

$$a\mathrm{e}^{s/\tau_a}\bigg|_0^t = \frac{1}{\tau_a}\int_0^t \mathrm{e}^{s/\tau_a} u(\cdot, s)\mathrm{d}s, \tag{130}$$

$$a(t) = \int_0^t \eta(t-s)u(\cdot, s)\mathrm{d}s, \tag{131}$$

assuming $a(0) = 0$, where

$$\eta(t) = \begin{cases} \frac{1}{\tau_a}\mathrm{e}^{-t/\tau_a} & \text{if} \quad t \geq 0 \\ 0 & \text{if} \quad t < 0. \end{cases} \tag{132}$$

Furthermore, (131) can be written as,

$$a(t) = \int_{-\infty}^t \eta(t-s)u(\cdot, s)\mathrm{d}s, \tag{133}$$

$$= \int_0^{\infty} \eta(s)u(\cdot, t-s)\mathrm{d}s \equiv \eta * u. \tag{134}$$

Therefore, the adaptation model can be written as one equation,

$$\frac{\partial u(\mathbf{r},t)}{\partial t} = -u(\mathbf{r},t) + w \otimes f(u(\mathbf{r},t)) - g\eta * u(\mathbf{r},t). \tag{135}$$

where $\otimes$ denotes a spatial convolution and $*$ a temporal convolution.

5.1.2 *Linear Stability Analysis*

Note that the Laplace transform of η is given by,

$$\widetilde{\eta}(\lambda) = \int_0^\infty \eta(t) \mathrm{e}^{-\lambda t} \mathrm{d}t = \frac{1}{1 + \lambda \tau_a}. \tag{136}$$

The homogeneous steady state $(u(\mathbf{r}, t), a(\mathbf{r}, t)) = (u_0, a_0)$ of the neural field model is then given by $a_0 = u_0$ with

$$u_0 = \widehat{w}(0) f(u_0)/(1 + g\widetilde{\eta}(0)). \tag{137}$$

For a balanced kernel $\widehat{w}(0) = 0$ and we have that $(u_0, a_0) = (0, 0)$ for all model parameter choices. Linearising around the homogeneous steady state by writing

$$u(\mathbf{r}, t) = u_0 + \epsilon \delta u(\mathbf{r}, t), \tag{138}$$

for some small amplitude $|\epsilon| \ll 1$, and expanding to first order gives the evolution for the perturbations as

$$\frac{\partial}{\partial t} \delta u = -\delta u + f'(u_0) w \otimes \delta u - g\eta * \delta u. \tag{139}$$

Equation (139) has separable solutions of the form $\delta u(\mathbf{r}, t) = \mathrm{e}^{\lambda t} \mathrm{e}^{i\mathbf{k} \cdot \mathbf{r}}$ where the dispersion relation between λ and $|\mathbf{k}|$ can be written implicitly in the form $\mathcal{E}(\lambda, k) = 0$ with

$$\mathcal{E}(\lambda, k) = 1 + \lambda + g\widetilde{\eta}(\lambda) - f'(u_0)\widehat{w}(k). \tag{140}$$

To obtain the above we have used the result that $w \otimes \mathrm{e}^{i\mathbf{k} \cdot \mathbf{r}} = \widehat{w}(\mathbf{k}) \mathrm{e}^{i\mathbf{k} \cdot \mathbf{r}}$ and $\eta * \mathrm{e}^{\lambda t} = \widetilde{\eta}(\lambda) \mathrm{e}^{\lambda t}$. When $g = 0$, we observed in section 3.3.1 that all roots of 140 are real. However, in general the values of λ in $\mathcal{E}(\lambda, k) = 0$ are complex. After decomposing $\lambda = \nu + i\omega$, and then equating real and imaginary parts of (140) it can be shown that the spectrum lies on the curve given by

$$\tau_a^2(\nu^2 + \omega^2) + 2\tau_a \nu = \tau_a g - 1, \tag{141}$$

and to the left of the line,

$$\nu = \frac{-(1+\tau_a - \tau_a f'(u_0)\widehat{w}(k_0))}{2\tau_a}. \tag{142}$$

Thus for $g > 0$ a Turing instability to a dynamic (time-dependent) pattern ($\omega \neq 0$) will occur when $\nu = 0$ to give,

$$\widehat{w}(k_0) = (1+\tau_a)/(\tau_a f'(u_0)), \tag{143}$$

for $\tau_a g > 1$ and

$$g > f'(u_0)\widehat{w}(k_0) - 1, \tag{144}$$

which excludes the possibility of a static bifurcation. The emergent frequency of oscillation is

$$\omega_c = \sqrt{\tau_a g - 1}/\tau_a. \tag{145}$$

We note that the conditions for static and dynamic Turing instabilities given here agree with those in [32] since the model equations only differ in the placement of the nonlinear firing rate.

5.2 ADAPTATION MODEL WITH SPATIAL FORCING IN ONE DIMENSION

We next take the adaptation model (135) and as in Chapter 4, add the same spatial forcing term from [81],

$$\frac{\partial u(x,t)}{\partial t} = -u(x,t) + w \otimes f(u(y,t)) - g\eta * u(x,t) + \gamma u(x,t)\cos k_f x, \tag{146}$$

We look for travelling wave and standing solutions near the dynamic Turing instability using multiple scale analysis. We carry out the analysis in one spatial dimension since out aim is to demonstrate for the model with adaptation (135) that spatial forcing of dynamic patterns can give dynamic resonant patterns which travel; this does not require analysis in two dimensions. Note that the amplitude equations for (135) in two spatial dimensions are developed in [85], but due to their high dimension (four complex amplitudes), they are reduced to one spatial dimension equations which we will find in this section for analysis of the travelling and standing wave solutions. Since we again work in one spatial dimension, the mismatch parameter ν_2 of (26) is set to zero and the Fourier transform of the connectivity kernel is given by (57).

5.2.1 *Hierarchy of Equations*

Using multiple scale analysis, we consider weak forcing $\gamma \ll 1$ near the instability $\epsilon \ll 1$. The multiple scale perturbation theory is shown in Appendix B.1, using the same multiple scale expansion from Section 4.1.2. Now $\beta_c = f'(u_0)$ subject to

$$\beta_c = \begin{cases} \dfrac{1+g}{\widehat{w}(k_0)} & \text{at a static Turing bifurcation,} \\ \dfrac{\tau_a + 1}{\tau_a \widehat{w}(k_0)} & \text{at a dynamic Turing instability.} \end{cases} \tag{147}$$

Furthermore, the expansion of the right hand side is,

$$\begin{aligned} &-(u_0 + \epsilon u_1 + \epsilon^2 u_2 + \epsilon^3 u_3 + \dots) + w \otimes [f(\bar{u}) + (\beta_c + \epsilon^2 \delta)(\epsilon u_1 + \epsilon^2 u_2 \\ &+ \epsilon^3 u_3 + \dots) + \beta_2(\epsilon u_1 + \epsilon^2 u_2 + \epsilon^3 u_3 + \dots)^2 + \beta_3(\epsilon u_1 + \epsilon^2 u_2 + \epsilon^3 u_3 + \dots)^3 \\ &+ \dots] - g\eta * (u_0 + \epsilon u_1 + \epsilon^2 u_2 + \epsilon^3 u_3 + \dots) \\ &+ (\epsilon\gamma_1 + \epsilon^2 \gamma_2 + \epsilon^3 \gamma_3 + \dots)(u_0 + \epsilon u_1 + \epsilon^2 u_2 + \epsilon^3 u_3 + \dots) \cos k_f x. \end{aligned} \tag{148}$$

To fully expand the convolution $w \otimes f(u)$ this time, we need to expand u_α in one spatial and one temporal direction to include the other terms from this. The Taylor expansion of the spatial convolution in one dimension is given by (64) and the temporal convolution is,

$$\begin{aligned} u_\alpha(x', t', \epsilon x', \epsilon^2 t') &= u_\alpha(x', t', \epsilon x', \tau + \epsilon^2(t' - t)) \\ &\simeq u_\alpha(x', t', \chi, \tau) + \epsilon^2 (t' - t) \frac{\partial}{\partial \tau} u_\alpha(x', t', \chi, \tau) + O(\epsilon^4). \end{aligned} \tag{149}$$

Balancing the $O(1)$ terms in (146) fixes the steady state $u_0 = 0$ since we again choose the kernel as in (45) with $A = \sigma^{-1}$ which is balanced in one spatial dimension and has Fourier transform (52). By using the multiscale expansion of u (149) and using the expansion of the right hand side (148), this gives the fully expanded model. Taking the terms for each order of epsilon gives,

$$\mathscr{L}_g u_1 = 0, \tag{150}$$

$$\mathscr{L}_g u_2 = - M_0(\beta_2 u_1^2) - M_1(\beta_c u_1) - \gamma_1 u_1 \cos(k_f x), \tag{151}$$

$$\mathscr{L}_g u_3 = \frac{\partial u_1}{\partial \tau} - M_0(\delta u_1 + 2\beta_2 u_1 u_2 + \beta_3 u_1^3) - M_1(\beta_c u_2 + \beta_2 u_1^2) \tag{152}$$

$$- M_2\left(\beta_c u_1\right) + N_1(g u_1) - (\gamma_2 u_1 + \gamma_1 u_2)\cos k_f x, \tag{153}$$

where

$$\mathscr{L}_g = -1 - \frac{\partial}{\partial t} + \beta_c w \otimes - g\eta *,$$

M_0, M_1 and M_2 are defined by (69 - 71), and

$$N_1 = \eta^t * \partial_\tau. \tag{154}$$

Note that $\mathscr{L}_g^\dagger \neq \mathscr{L}_g$ so $\mathscr{L}$ is not self adjoint, but $\mathrm{Ker}(\mathscr{L}_g^\dagger) = \mathrm{Ker}(\mathscr{L}_g)$. The null space of the linear operator $\mathcal{L}_g$ is spanned by $\left\{ \mathrm{e}^{\pm i(k_0 x \pm \omega_c t)} \right\}$ where $\omega_c = \sqrt{\tau_a g - 1}/\tau_a$, and therefore (150) has solution of the form

$$u_1 = A(\chi,\tau)\mathrm{e}^{i(k_0 x + \omega_c t)} + B(\chi,\tau)\mathrm{e}^{i(k_0 x - \omega_c t)} + \text{c.c.}. \tag{155}$$

5.2.2 *Amplitude Equations*

Using the Fredholm alternative, we find a particular solution to (151) and use a solvability condition for (153) to derive amplitude equations for the evolution of the complex amplitudes $A(\chi, Y, \tau)$ and $B(\chi, Y, \tau)$. Details of these calculations can be found in Appendix B.1, and the resulting amplitude equations, rescaled back to the original time and space variables, are

$$\begin{aligned}(1 + g\widetilde{\eta}'(i\omega_c))\frac{\partial a}{\partial t} =& \widehat{w}(k_0)\delta\epsilon^2 a - \widehat{w}(k_0)\left[\Phi_1|a|^2 + \Phi_2|b|^2\right] a \\ &+ \frac{1}{2}\beta_c \widehat{w}''(k_0)(i\partial_x + \nu_1)^2 a + \frac{\epsilon^2\gamma_2}{2} b^* \delta_{n,2} \\ &+ \left(\frac{\epsilon\overline{\gamma_1}}{2}\right)^2 (1 - \delta_{n,2})\left[(\zeta_4 + \zeta_5)a + \zeta_5 b^* \delta_{n,1}\right],\end{aligned} \tag{156}$$

and similarly,

$$\begin{aligned}(1+g\widetilde{\eta}'(-i\omega_c))\frac{\partial b}{\partial t} =&\widehat{w}(k_0)\delta\epsilon^2 b - \widehat{w}(k_0)\left[\Phi_1^*|b|^2+\Phi_2^*|a|^2\right]b\\ &+\frac{1}{2}\beta_c\widehat{w}''(k_0)(i\partial_x+\nu_1)^2 b+\frac{\epsilon^2\gamma_2}{2}a^*\delta_{n,2}\\ &+\left(\frac{\epsilon\overline{\gamma_1}}{2}\right)^2(1-\delta_{n,2})\left[(\zeta_4^*+\zeta_5^*)b+\zeta_5 a^*\delta_{n,1}\right], \qquad (157)\end{aligned}$$

where all new parameters are defined in Appendix B.1. Note that $\Phi_1 \in \mathbb{C}$, $\Phi_2 \in \mathbb{R}$ and $\zeta_4, \zeta_5 \in \mathbb{C}$.

5.2.3 *Existence of Solutions*

We now consider the 2:1 resonance patterns that exist in the model with adaptation (146) with $g \neq 0$, as shown in Fig. 22 to be the widest existence tongue, so we take $n = 2$. Here, beyond the dynamic Turing instability at $\beta_c = (\tau_a+1)/(\tau_a\widehat{w}(k_0))$, the unforced system, $\gamma = 0$, supports periodic travelling waves. We then have the following amplitude equations:

$$(1+g\widetilde{\eta}'(i\omega_c))\frac{\partial a}{\partial t} = \Lambda a - \widehat{w}(k_0)\left(\Phi_1|a|^2+\Phi_2|b|^2\right)a+\frac{\gamma}{2}b^*, \qquad (158)$$

$$(1+g\widetilde{\eta}'(-i\omega_c))\frac{\partial b}{\partial t} = \Lambda b - \widehat{w}(k_0)\left(\Phi_1^*|b|^2+\Phi_2^*|a|^2\right)b+\frac{\gamma}{2}a^*, \qquad (159)$$

where $\Lambda = \widehat{w}(k_0)\epsilon^2\delta + \beta_c\widehat{w}''(k_0)\left(i\partial_x+v_1\right)^2/2$ and $\gamma = \epsilon^2\gamma_2$. Using the definition of $\widetilde{\eta}$ as in (136), and also the relationship between g, τ_a and the emergent frequency, ω_c, of the dynamic pattern, the amplitude equations can be written in the form

$$\frac{\partial a}{\partial t} = \frac{1}{2}\left(1-\frac{i}{\tau_a\omega_c}\right)\left(\Lambda a - \widehat{w}(k_0)\left(\Phi_1|a|^2+\Phi_2|b|^2\right)a+\frac{\gamma}{2}b^*\right), \qquad (160)$$

$$\frac{\partial b}{\partial t} = \frac{1}{2}\left(1+\frac{i}{\tau_a\omega_c}\right)\left(\Lambda b - \widehat{w}(k_0)\left(\Phi_1^*|b|^2+\Phi_2|a|^2\right)b+\frac{\gamma}{2}a^*\right). \qquad (161)$$

We now look for spatially homogeneous solutions of (160)–(161), so take $\Lambda = \widehat{w}(k_0)\epsilon^2\delta + \beta_c\widehat{w}''(k_0)v_1^2/2$ which is now real-valued. Writing $a = \rho_a e^{i\phi_a}$ and $b = \rho_b e^{i\phi_b}$ we find that the phases and amplitudes satisfy

$$\begin{aligned}\frac{\partial\rho_a}{\partial t} &= \frac{1}{2}\left(\Lambda\rho_a - \widehat{w}(k_0)\rho_a\left(\Phi_1^r\rho_a^2 + \Phi_2\rho_b^2\right) + \frac{\gamma}{2}\rho_b\cos(\psi)\right)\\ &\quad - \frac{1}{2\tau_a\omega_c}\left(\frac{\gamma}{2}\rho_b\sin(\psi) + \widehat{w}(k_0)\Phi_1^i\rho_a^3\right),\end{aligned} \tag{162}$$

$$\begin{aligned}\frac{\partial\rho_b}{\partial t} &= \frac{1}{2}\left(\Lambda\rho_b - \widehat{w}(k_0)\rho_b\left(\Phi_1^r\rho_b^2 + \Phi_2\rho_a^2\right) + \frac{\gamma}{2}\rho_a\cos(\psi)\right)\\ &\quad + \frac{1}{2\tau_a\omega_c}\left(\frac{\gamma}{2}\rho_a\sin(\psi) - \widehat{w}(k_0)\Phi_1^i\rho_b^3\right),\end{aligned} \tag{163}$$

$$\begin{aligned}\frac{\partial\psi}{\partial t} &= -\frac{1}{2\tau_a\omega_c}\left(\frac{\gamma}{2}\cos(\psi)\left(\frac{\rho_b}{\rho_a} - \frac{\rho_a}{\rho_b}\right) - \widehat{w}(k_0)(\rho_a^2 - \rho_b^2)(\Phi_1^r - \Phi_2)\right)\\ &\quad - \frac{\gamma}{4}\sin(\psi)\left(\frac{\rho_b}{\rho_a} + \frac{\rho_a}{\rho_b}\right) - \frac{1}{2}\widehat{w}(k_0)\Phi_1^i(\rho_a^2 - \rho_b^2),\end{aligned} \tag{164}$$

$$\begin{aligned}\frac{\partial\theta}{\partial t} &= -\frac{1}{2\tau_a\omega_c}\left(2\Lambda + \frac{\gamma}{2}\cos(\psi)\left(\frac{\rho_b}{\rho_a} + \frac{\rho_a}{\rho_b}\right) - \widehat{w}(k_0)(\rho_a^2 + \rho_b^2)(\Phi_1^r + \Phi_2)\right)\\ &\quad - \frac{\gamma}{4}\sin(\psi)\left(\frac{\rho_b}{\rho_a} - \frac{\rho_a}{\rho_b}\right) - \frac{1}{2}\widehat{w}(k_0)\Phi_1^i(\rho_a^2 + \rho_b^2),\end{aligned} \tag{165}$$

where $\psi = \phi_a + \phi_b$, $\theta = \phi_a - \phi_b$ and Φ_1^r, Φ_1^i denote the real and imaginary parts of Φ_1 respectively.

Looking for solutions with constant and equal amplitudes $\rho_a = \rho_b = \rho_0$ we see that ψ is constant when it takes the values $\psi = m\pi$ for $m = 0, 1$. Then

$$\rho_0 = \sqrt{\frac{\tau_a\omega_c\left(2\Lambda + (-1)^m\gamma\right)}{2\widehat{w}(k_0)(\tau_a\omega_c\left(\Phi_1^r + \Phi_2\right) + \Phi_1^i)}}, \tag{166}$$

and we observe that

$$\begin{aligned}\frac{\partial\theta}{\partial t} &= -\frac{1}{2\tau_a\omega_c}\left(2\Lambda + (-1)^m\gamma - 2\widehat{w}(k_0)\left(\Phi_1^r + \Phi_2 - \tau_a\omega_c\Phi_1^i\right)\rho_0^2\right)\\ &= -\frac{1}{2\tau_a\omega_c}\left(2\Lambda + (-1)^m\gamma\right)\left(1 + \tau_a^2\omega_c^2\right)\Phi_1^i.\end{aligned} \tag{167}$$

Therefore θ is constant when $\Phi_1^i = 0$ corresponding to periodic standing wave solutions, and otherwise θ is a linear function of time, corresponding to amplitude modulated standing waves. Assuming that $\tau_a\omega_c\left(\Phi_1^r + \Phi_2\right) +$

$\Phi_1^i > 0$, the solution with $m = 0$ exists when $\gamma > -2\Lambda$ and the solution with $m = 1$ exists for $\gamma < 2\Lambda$. Linear stability analysis shows that the solution with $\psi = m\pi$ is stable when

$$(-1)^m\gamma > \max\left\{0, \frac{-2\Lambda\tau_a\omega_c(\Phi_1^r - \Phi_2)}{2\tau_a\omega_c\Phi_1^r + \Phi_1^i}, \frac{-2\Lambda(\tau_a\omega(\Phi_1^r - \Phi_2) + \Phi_1^i)}{\tau_a\omega_c(3\Phi_1^r + \Phi_2) + 3\Phi_1^i}\right\}.$$

We note that $\Phi_1^i = 0$ only when $h = 0$ so that $\beta_2 = 0$ and in this case $\Phi_2 = 2\Phi_1^r$. Therefore, in the case where $\Phi_1^i = 0$, the solution with $\psi = m\pi$ is stable for $(-1)^m\gamma > 2\Lambda$.

We can also find stable solutions of (162)–(165) with unequal constant amplitudes. Suppose that ψ takes the constant values $m\pi$ for $m = 0, 1$. Then from (164) we observe that either $\rho_a = \rho_b$ or

$$\rho_a\rho_b = \frac{(-1)^m\gamma}{2\widehat{w}(k_0)(\tau_a\omega_c\Phi_1^i - \Phi_1^r + \Phi_2)} := P_m.$$

In the latter case, substitution into (162) multiplied by ρ_a reveals that the constant amplitudes have values $\rho_a = \rho_\pm$, $\rho_b = \rho_\mp$ where $(\rho_\pm)^2$ are the two roots of

$$\widehat{w}(k_0)\Phi_1^r\rho^4 - \left(\Lambda - \frac{\widehat{w}(k_0)\Phi_1^i P_m}{\tau_a\omega_c}\right)\rho^2 - P_m\left(\frac{(-1)^m\gamma}{2} - \widehat{w}(k_0)\Phi_2 P_m\right) = 0.$$

Such solutions exist when the roots are real and positive. When $\Phi_1^i = 0$ the solutions have constant $\theta = 2\phi_a - m\pi$ and therefore the solutions are periodic travelling waves. They exist when $\Lambda\Phi_1^r > 0$ and for $|\gamma| < |\Lambda|$ and can also be shown to be stable in this parameter range (see Fig. 29(a)). When $\Phi_1^i \neq 0$ the solutions have $\theta(t) = 2\phi_a(t) - m\pi$ and correspond to resonant amplitude modulated travelling waves. Numerical investigation with XPPAUT [36] for the parameter choices as in Fig. 29(a) indicates that the solutions are stable wherever they exist. The stability region covers the range of values of forcing strength γ where the modulated standing waves are unstable and there are also regions of bistability of the modulated standing and travelling waves. These solutions are indicated in Fig. 29(b) in red ($m = 0$) and magenta ($m = 1$). We also find stable modulated travelling waves with constant $\rho_a \neq \rho_b$ and constant $\psi \neq 0$ as indicated in green in Fig. 29(b). Fig. 29 summarises the solution branches and their stability for $\Phi_1^i = 0$ and $\Phi_1^i \neq 0$ respectively where other parameter values are as given in the caption. This indicates that travelling waves dominate for weak forcing, and there is an exchange of stability to standing waves for stronger forcing γ.

The significant outcome of this investigation is that when adaptation is included, there are stable 2:1 resonant solutions which travel. Investigating the fully two-dimensional model with adaptation numerically reveals the same qualitative behaviour as predicted in the one dimensional model. Moreover, when the unforced system supports traveling waves, resonant rectangular patterns remain stationary but oblique patterns travel in an orthogonal direction, namely along the axis for which the continuous translational symmetry is not broken by the forcing. Thus, if spatial forcing is by a striped pattern along the x-direction then the tissue response could be a striped pattern in the orthogonal y-direction. Moreover, the presence of adaptation would allow for a dynamic instability so that this could propagate as a plane wave. Although the theory above has only been developed with spatially periodic forcing over the whole space, it has uncovered a mechanism for the generation of orthogonal responses that we expect to hold in the presence of more structured forcing. We explore this further in section 5.3 and provide support for this claim using direct numerical simulations of forcing on the half-space relevant to the psychophysical experiments of Billock and Tsou [10].

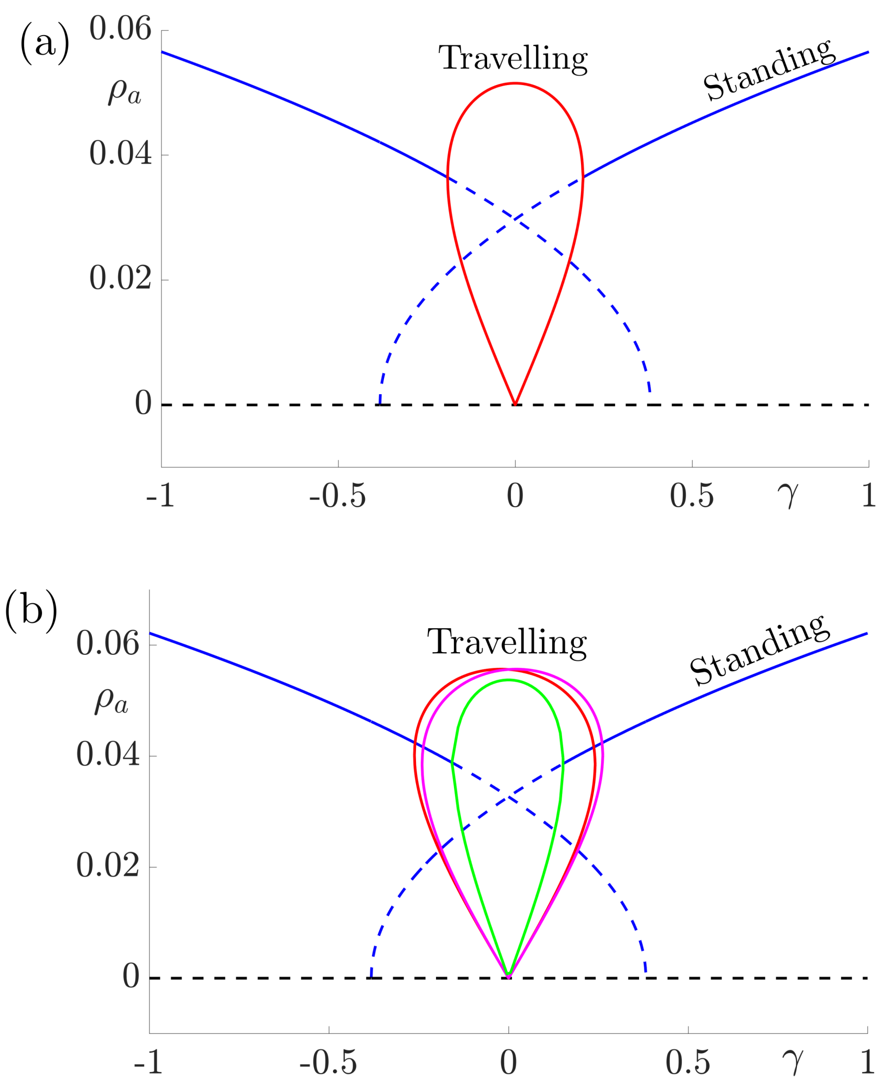

Figure 29.: Bifurcation diagrams for resonant stripe pattern solutions for the forced neural field equation (146) in one spatial dimension with adaptation ($g \neq 0$) under variation of the forcing strength γ. In (a) we take the threshold for the firing rate $h = 0$ which gives $\Phi_1^i = 0$ and therefore we observe periodic standing waves (blue) and travelling waves (red). Dashed lines indicate unstable solutions while solid lines indicate stable waves. In (b) we choose $|h| = 0.05$ and therefore $\Phi_1^i \neq 0$ and we observe modulated (quasiperiodic) standing (blue) and various travelling (red, magenta and green) waves. Other parameter values for both diagrams are $\sigma = 0.5$, $\tau_a = 1$, $g = 5$. These give $\beta_c = 3$, $\widehat{w}(k_0) = 2/3$ and $\widehat{w}''(k_0) = -16/27$ and here we take $\epsilon^2\delta = 0.3$ and $v_1 = 0.1$ so that $\Lambda = \widehat{w}(k_0)\epsilon^2\delta + \beta_c\widehat{w}''(k_0)v_1^2/2 = 43/225$.

5.3 SIMULATIONS

By forcing with striped patterns on the cortical half-space we recover all of the features reported in Fig. 14, once the inverse retinocortical map is applied. We show the corresponding plots for cortical activity in Fig. 30. The presence of the adaptation current allows the formation of travelling striped patterns, and these correspond to rotating waves in the retinal space with *blinking* versions associated to standing waves. Although the psychophysical experiments of Billock and Tsou involve a component of temporal flicker we have found that it is not strictly necessary to include this within the model to generate results consistent with their observations. Nonetheless, direct numerical simulations with flicker do show that the phenomenon is robust to this inclusion. We posit that in the psychophysical experiments the background flicker helps put the primary visual cortex in a state conducive to a 2:1 resonance, whereas in our model we tune intrinsic parameters to reach this condition.

Brief details of the numerical methods used to implement the model are presented in appendix C.

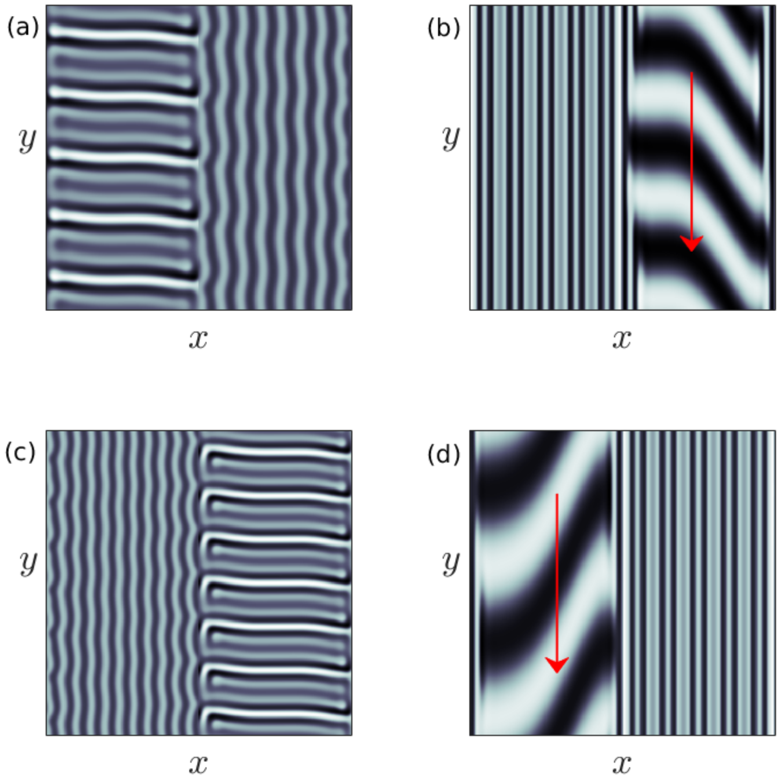

Figure 30.: Simulation results from a neural field model with spatially periodic striped forcing on the half-space. (a) Horizontal stripes forcing the left half-space give rise to stationary vertical stripes on the right. (b) Vertical stripes forcing the left half-space give rise to travelling horizontal stripes on the right. (c) Horizontal stripes forcing the right half-space give rise to stationary vertical stripes on the left. (d) Vertical stripes forcing the right half-space give rise to travelling horizontal stripes on the left. An application of the inverse retinocortical map to (a), …, (d) generates patterns consistent with (a), …, (d) shown in Fig. 14. Parameter values are $\sigma = 0.8$, $\mu = 2$, $h = 0.05$, $\gamma = 0.5$ and for b) and d) $\tau_a = 10$, $g = 0.14$. The domain sizes are a) $[-16.53, 16.53] \times [-15.71, 15.71]$, b) $[-31.42, 31.42] \times [-3.10, 3.10]$, c) $[-22.73, 22.73] \times [-22.00, 22.00]$ and d) $[-31.42, 31.42] \times [-2.07, 2.07]$ with periodic boundary conditions. Movies available in Supplementary Materials of [85].

5.4 SUMMARY

In this chapter we have shown that the psychophysical observations of Billock and Tsou [10] can be explained with a parsimonious neural field model that does not require any exotic extension compared to standard approaches. It was originally suggested in [10, Supporting Information] that a neural field with some form of anisotropic coupling would be necessary to explain the observed spatial opponency between rings and radial arms. Rather we find, perhaps non-intuitively, that the pattern forming properties of a spatially forced isotropic model with a 2:1 resonance provide a sufficient mechanism for the observed phenomena. Importantly, when the unforced model is poised near a Turing instability, we have shown that there are reasonably large windows of parameter space that allow for such a resonance between a spatial Turing pattern and a spatially periodic pattern of forcing. To establish this we have made use of perturbation arguments valid only for weak forcing. Nonetheless, this *amplitude equation* approach has proven especially useful for gaining insight into the main control parameters that can encourage an orthogonal response to the forcing of a two-dimensional neural field with a simple periodic stripe pattern. A key parameter in this regard is the deviation between k_0, the spatial frequency excited by the Turing instability, and $k_f/2$, where k_f is the spatial frequency of the forcing. An orthogonal response is promoted as this deviation becomes closer to k_0. As well as using mathematical arguments, strictly only valid for global periodic forcing, we have used direct numerical simulations to show that the model responds similarly when patterns are presented only on the half-space (which is more consistent with the psychophysical experiments). Moreover, we have shown that some form of negative feedback or adaptation is useful for promoting travelling Turing patterns, which (via the inverse retinocortical map) generate rotating percepts. These would also be expected in a more refined two-population neural field model without adaptation that distinguishes between excitatory and inhibitory sub-populations [38, 116]. We have opted for the study of an effective single population model with adaptation solely to keep the mathematical analysis manageable.

6

PATCHY CONNECTIONS

6.1 INTRODUCTION

Neural connectivity in neocortex, including the visual cortex, has a crystalline microstructure [75] that has a length scale of millimetres. In primary visual cortex (V1) there are long range lateral connections of several millimetres in length which link neurons that have common functional properties, such as orientation preference. The neural field model considered so far has been based on the assumption that interactions between neurons are homogeneous, isotropic and invariant. Exploiting Euclidean symmetry, the author in [37] used equivariant bifurcation theory to predict the type of patterns that may form beyond Turing instabilities for homogeneous models [38, 125]. Amplitude equations have been used to determine pattern formation [21, 38] in neural field models along the lines described in chapters 3, 4 and 5. However, in V1 the crystalline structure is approximately periodic and organises patchy long range connections that break continuous rotational symmetry (isotropy), though not necessarily continuous translational symmetry (homogeneity). Therefore, our previous neural field models that have used isotropic connectivity should be adapted to incorporate this. We model these patchy connections by taking a homogeneous and isotropic neural field model and modulating it by a spatially periodic function to reflect this underlying microstructure.

A crystalline structure is demonstrated by both the pinwheel structure of the orientation preference map (OPM) and also cytochrome oxidase (CO) blobs in the primary visual cortex of cats and primates. Pinwheels are areas of high rates of change of orientation preference and are separated by approximately linear regions of orientation. The linear regions are perpendicular to the ocular dominance region borders but the pinwheels align with the centre of ocular dominance stripes. The CO blobs are approximately 0.2 mm in diameter and 0.6 mm apart and they align with cells that are very metabolically active when responding to visual stimuli [50]. This distribution shows correlation with visual sites of high functionality such as the OPM, spatial frequency and ocular dominance [78, 109]. These features and the relationship between them can be seen in Fig. 31. CO blobs are aligned with approximately half of pinwheel structures [18]. It has been shown in [130] that some neurons halfway between two CO blobs have no or little horizontal connections; therefore, the location of CO blobs correlates with the strength and range of horizontal connections. We believe that as the patchy connection structure is underpinned by the same principles as the OPM structure, we can exploit this to use neural activity with patchy connections to create an orientation preference map. This will provide the basis for the work completed in the next chapter.

6.2 PATCHY MODEL

We start with the standard two-dimensional scalar neural field model, as previously described in chapter 3,

$$\frac{\partial u(\mathbf{r},t)}{\partial t} = -u(\mathbf{r},t) + \int_{\mathbb{R}^2} w(\mathbf{r},\mathbf{r}')f(u(\mathbf{r}',t))\mathrm{d}\mathbf{r}. \tag{168}$$

In general $w(\mathbf{r},\mathbf{r}')$ is inhomogeneous. However, to be able to mathematically analyse the model, there are usually two special cases that are considered. When $w(\mathbf{r},\mathbf{r}') = w(|\mathbf{r}-\mathbf{r}'|)$, this is homogeneous (translationally invariant),

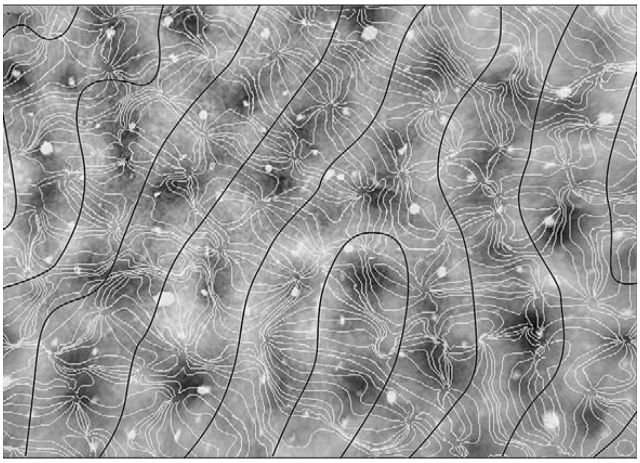

Figure 31.: Example of iso-orientation contours (light grey lines) and ocular dominance boundaries (black lines) in relation to CO blob regions (light shaded areas) of a macaque primary visual cortex, figure adapted from [18] which was redrawn from [11].

and isotropic (rotationally invariant). Secondly, when $w(\mathbf{r}, \mathbf{r}') = w(\mathbf{r} - \mathbf{r}')$, this is homogeneous but not isotropic.

We now introduce the periodically modulated spatial connectivity required to model the patchy connections, this is homogeneous but not isotropic and denoted $w^p(\mathbf{r}, \mathbf{r}')$, where

$$w^p(\mathbf{r}, \mathbf{r}') = w(|\mathbf{r} - \mathbf{r}'|)M(\mathbf{r} - \mathbf{r}'). \tag{169}$$

Here $w(|\mathbf{r} - \mathbf{r}'|)$ is a standard kernel, for example a Mexican hat or Wizard hat function, and $M(\mathbf{r} - \mathbf{r}')$ is a periodic function that we will use to model patchy connectivity. M is a simple model of patchiness, we require this to be of the (approximate) periodicity seen in OPMs with a spatial scale d.

6.3 TWO DIMENSIONAL MODEL WITH SQUARE LATTICE

Firstly, we will consider a regular square lattice $\mathscr{L}$ with generators $\mathbf{l}_1 = d(0,1)$ and $\mathbf{l}_2 = d(1,0)$ as basis vectors, an example shown in Fig. 32. This has reciprocal lattice $\mathscr{L}^\dagger$ with reciprocal lattice generators,

$$\mathbf{q}_1 = \frac{2\pi}{d}(1,0), \quad \mathbf{q}_2 = \frac{2\pi}{d}(0,1), \tag{170}$$

satisfying $\mathbf{q}_i \cdot \mathbf{l}_j = 2\pi\delta_{ij}$.

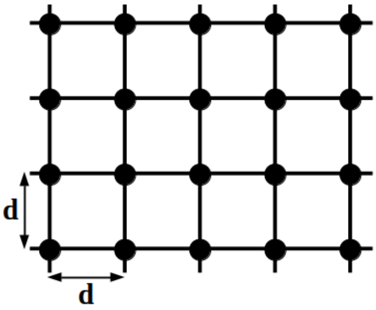

Figure 32.: An example of a regular square lattice with distance d between grid points

We will model the patchy connections via the function, M. This is chosen to vary periodically with respect to the regular planar lattice $\mathscr{L}$, and can be represented in the form of,

$$M(\mathbf{r}) = \sum_{\mathbf{q}\in\mathscr{L}^\dagger} M_{\mathbf{q}} \mathrm{e}^{i\mathbf{q}\cdot\mathbf{r}}, \quad \mathscr{L}^\dagger = \{m\mathbf{q}_1 + p\mathbf{q}_2 : m, p \in \mathbb{Z}\}. \tag{171}$$

Since $M \in \mathbb{R}$ then $M_{\mathbf{q}} = (M_{-\mathbf{q}})^*$ where * is the complex conjugate. We can exploit the periodicity of M to represent it as a Fourier series. $M_{\mathbf{q}}$ are Fourier coefficients given by

$$M_{\mathbf{q}} = \frac{1}{(2\pi)^2} \int_{\mathbb{R}^2} M(\mathbf{r}) \mathrm{e}^{-i\mathbf{q}\cdot\mathbf{r}} \mathrm{d}\mathbf{r}. \tag{172}$$

6.3.1 *Turing Analysis of the Patchy Two Dimensional Model with a Square Lattice*

Following standard Turing Analysis, see section 3.3.1, we take the homogeneous steady state represented by $u(\mathbf{r}, t) = u_0$ as,

$$u_0 = (f \circ u_0) \int_{\mathbb{R}^2} w(|\mathbf{r}|) M(\mathbf{r}) \mathrm{d}\mathbf{r}. \tag{173}$$

Introducing the two dimensional Fourier transform of the kernel,

$$\widehat{W}(\mathbf{k}) = \int_{\mathbb{R}^2} w(|\mathbf{r}|) M(\mathbf{r}) \mathrm{e}^{-i\mathbf{k}\cdot\mathbf{r}} \mathrm{d}\mathbf{r}, \tag{174}$$

then the steady state can be written as,

$$u_0 = \widehat{W}(\mathbf{k} = 0)(f \circ u_0). \tag{175}$$

The Fourier transform (174) with our choice of M is,

$$\widehat{W}(\mathbf{k}) = \sum_{\mathbf{q}} M_{\mathbf{q}} \int_{\mathbb{R}^2} w(|\mathbf{r}|) \mathrm{e}^{-i(\mathbf{k}-\mathbf{q})\cdot\mathbf{r}} \mathrm{d}\mathbf{r} = \sum_{\mathbf{q}} M_{\mathbf{q}} \widehat{w}(\mathbf{k} - \mathbf{q}), \tag{176}$$

where

$$\widehat{w}(\mathbf{k}) = \int_{\mathbb{R}^2} w(|\mathbf{r}|) \mathrm{e}^{-\mathrm{i}\mathbf{k}\cdot\mathbf{r}} \, \mathrm{d}\mathbf{r}. \tag{177}$$

Now as $\widehat{w}(\mathbf{k}) = \widehat{w}(|\mathbf{k}|)$, we have that,

$$\widehat{W}(\mathbf{k}) = \sum_{\mathbf{q}} M_{\mathbf{q}} \widehat{w}(|\mathbf{k} - \mathbf{q}|). \tag{178}$$

Taking the steady state with a small perturbation $u = u_0 + \epsilon \mathrm{e}^{\lambda t} \mathrm{e}^{i\mathbf{k}\cdot\mathbf{r}}$, for $\epsilon \ll 1$, gives the characteristic equation,

$$\begin{aligned} \lambda(\mathbf{k}) &= -1 + f'(u_0) \widehat{W}(\mathbf{k}), \\ &= -1 + f'(u_0) \sum_{\mathbf{q}} M_{\mathbf{q}} \widehat{w}(|\mathbf{k} - \mathbf{q}|). \end{aligned} \tag{179}$$

We will consider the choice of periodic model of patchiness to be,

$$M(\mathbf{r}) = \frac{1}{2} \left[\cos(\mathbf{q}_1 \cdot \mathbf{r}) + \cos(\mathbf{q}_2 \cdot \mathbf{r}) \right], \tag{180}$$

which has Fourier coefficients,

$$M_{\mathbf{q}} = \frac{1}{(2\pi)^2} \int_{\mathbb{R}^2} \frac{1}{2} \left[\frac{e^{i\mathbf{q}_1\cdot\mathbf{r}} + e^{-i\mathbf{q}_1\cdot\mathbf{r}}}{2} + \frac{e^{i\mathbf{q}_2\cdot\mathbf{r}} + e^{-i\mathbf{q}_2\cdot\mathbf{r}}}{2} \right] e^{-i\mathbf{q}\cdot\mathbf{r}} d\mathbf{r}. \tag{181}$$

After noting,

$$\frac{1}{(2\pi)^2} \int_{\mathbb{R}^2} e^{-i(\mathbf{q}-\mathbf{k})\cdot\mathbf{r}} d\mathbf{r} = \delta_{\mathbf{q},\mathbf{k}}, \tag{182}$$

this gives the Fourier coefficients as,

$$M_{\mathbf{q}} = \frac{1}{4} \left[\delta_{\mathbf{q},\mathbf{q}_1} + \delta_{\mathbf{q},-\mathbf{q}_1} + \delta_{\mathbf{q},\mathbf{q}_2} + \delta_{\mathbf{q},-\mathbf{q}_2} \right]. \tag{183}$$

Therefore, using this definition of the Fourier coefficients (183), the eigenvalues of the square lattice system (179) can be written as,

$$\begin{aligned} \lambda(\mathbf{k}) = -1 + \frac{1}{4} f'(u_0) \left[\widehat{w}(|\mathbf{k} - \mathbf{q}_1|) + \widehat{w}(|\mathbf{k} + \mathbf{q}_1|) \right. \\ \left. + \widehat{w}(|\mathbf{k} - \mathbf{q}_2|) + \widehat{w}(|\mathbf{k} + \mathbf{q}_2|) \right]. \end{aligned} \tag{184}$$

The steady state u_0 is stable when $\mathrm{Re}(\lambda(\mathbf{k})) < 0$ for all $\mathbf{k}$. For our model of patchy connections, the eigenvalues $\lambda(\mathbf{k})$ depend on the direction of $\mathbf{k}$ as well as its magnitude. Previously, when considering the neural field model in the isotropic case, as considered in section 3.3.1, $\lambda = \lambda(|\mathbf{k}|)$ is only dependent on the magnitude of $\mathbf{k}$.

The steady state was defined earlier in (175); now with our choice of M the Fourier transform at $\mathbf{k} = 0$ is,

$$\widehat{W}(\mathbf{k} = 0) = \frac{1}{2} \left[\widehat{w}(|\mathbf{q}_1|) + \widehat{w}(|\mathbf{q}_2|) \right].$$

For a square lattice, $|\mathbf{q}_1| = |\mathbf{q}_2| = 2\pi/d$,

$$\widehat{W}(\mathbf{k} = 0) = \widehat{w}(2\pi/d).$$

Therefore, to find the steady state, we need to solve, $G(u_0) = 0$ where,

$$G(u) = u - f(u)\widehat{w}(2\pi/d). \tag{185}$$

This can be achieved numerically using Matlab's inbuilt function *fsolve*.

6.3.2 *Simulations of the Patchy Model with a Square Lattice*

To complete the theory, we will show computational examples to highlight the effects of the patchy connectivity on a square lattice using M as given by (180). We choose the kernel to again be a Wizard hat function,

$$w(\mathbf{r}) = Ae^{-\mathbf{r}/\sigma} - e^{-\mathbf{r}}, \tag{186}$$

with $\sigma = 0.6$ and $A = 1/\sigma^2$ to give a balanced kernel. We also make the choice of firing rate as,

$$f(u, \mu, h) = \frac{1}{1 + e^{-\mu(u-h)}}. \tag{187}$$

where μ is the steepness of the slope and has threshold h. Fig. 33 shows the patchy connections kernel $w^p(\mathbf{r}, \mathbf{r}')$ for the square periodic patchiness with this Wizard hat kernel.

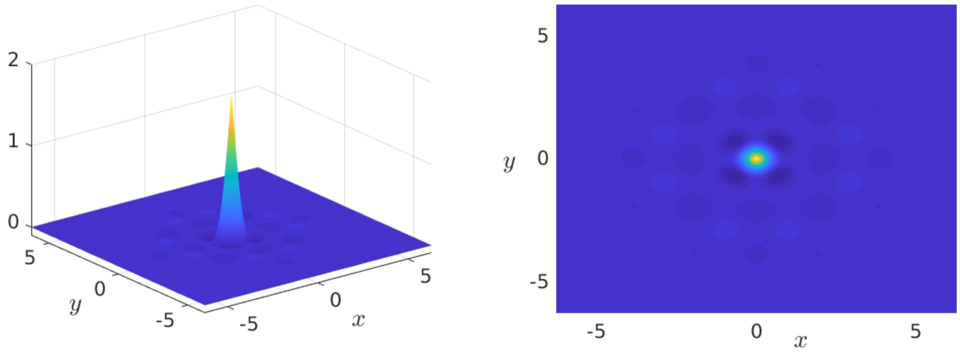

Figure 33.: The patchy connections kernel $w^p(\mathbf{r}, \mathbf{r}') = w(|\mathbf{r} - \mathbf{r}'|)M(\mathbf{r} - \mathbf{r}')$ where the standard kernel $w(\mathbf{r})$ is defined by (186) and the square periodic patchiness $M(\mathbf{r})$ by (180). Here, $\mu = 11$ and $d = 2$, plotted on the domain $[-2\pi, 2\pi] \times [-2\pi, 2\pi]$.

To calculate the critical wave vector $\mathbf{k}_c$ at bifurcation, we need to find the maximum of $\widehat{W}(\mathbf{k})$. Namely, for the square lattice we need to calculate

$$\frac{\partial \widehat{w}}{\partial k_\alpha}(|\mathbf{k} \pm \mathbf{q}_\beta|) \text{ for } \alpha = 1, 2 \text{ with } \beta = 1, 2 \text{ and } \mathbf{k} = (k_1, k_2). \tag{188}$$

We have,

$$\frac{\partial \widehat{w}}{\partial k_\alpha}(|\mathbf{k} \pm \mathbf{q}_\beta|) = \widehat{w}'(|\mathbf{k} \pm \mathbf{q}_\beta|). \tag{189}$$

Now,

$$|\mathbf{k} \pm \mathbf{q}_\beta| = \left[\left(k_1 \pm q_\beta^1\right)^2 + \left(k_2 \pm q_\beta^2\right)^2\right]^{\frac{1}{2}} \tag{190}$$

where $\mathbf{q}_\beta = (q_\beta^1, q_\beta^2)$. Hence,

$$\begin{aligned}\frac{\partial}{\partial k_\alpha}(|\mathbf{k} \pm \mathbf{q}_\beta|) =& \frac{1}{2}\left[\left(k_1 \pm q_\beta^x\right)^2 + \left(k_2 \pm q_\beta^y\right)^2\right]^{-\frac{1}{2}} \Big(2(k_1 \pm q_\beta^x)\delta_{1,\alpha} \\ &+2(k_2 \pm q_\beta^y)\delta_{2,\alpha}\Big) \\ =& \frac{1}{|\mathbf{k} \pm \mathbf{q}_\beta|}\left((k_1 \pm q_\beta^x)\delta_{1,\alpha} + (k_2 \pm q_\beta^y)\delta_{2,\alpha}\right).\end{aligned} \tag{191}$$

Therefore, we have,

$$\begin{aligned}&\frac{\partial}{\partial k_1}\left[\widehat{w}(|\mathbf{k} - \mathbf{q}_1|) + \widehat{w}(|\mathbf{k} + \mathbf{q}_1|) + \widehat{w}(|\mathbf{k} - \mathbf{q}_2|) + \widehat{w}(|\mathbf{k} + \mathbf{q}_2|)\right] \\ &= \widehat{w}'(|\mathbf{k} - \mathbf{q}_1|)\frac{1}{|\mathbf{k} - \mathbf{q}_1|}\left(k_1 - \frac{2\pi}{d}\right) + \widehat{w}'(|\mathbf{k} + \mathbf{q}_1|)\frac{1}{|\mathbf{k} + \mathbf{q}_1|}\left(k_1 + \frac{2\pi}{d}\right) \\ &\quad + \widehat{w}'(|\mathbf{k} - \mathbf{q}_2|)\frac{1}{|\mathbf{k} - \mathbf{q}_2|}(k_1) + \widehat{w}'(|\mathbf{k} + \mathbf{q}_2|)\frac{1}{|\mathbf{k} + \mathbf{q}_2|}(k_1),\end{aligned} \tag{192}$$

and

$$\begin{aligned}&\frac{\partial}{\partial k_2}\left[\widehat{w}(|\mathbf{k} - \mathbf{q}_1|) + \widehat{w}(|\mathbf{k} + \mathbf{q}_1|) + \widehat{w}(|\mathbf{k} - \mathbf{q}_2|) + \widehat{w}(|\mathbf{k} + \mathbf{q}_2|)\right] \\ &\quad = \widehat{w}'(|\mathbf{k} - \mathbf{q}_1|)\frac{1}{|\mathbf{k} - \mathbf{q}_1|}(k_2) + \widehat{w}'(|\mathbf{k} + \mathbf{q}_1|)\frac{1}{|\mathbf{k} + \mathbf{q}_1|}(k_2) \\ &+ \widehat{w}'(|\mathbf{k} - \mathbf{q}_2|)\frac{1}{|\mathbf{k} - \mathbf{q}_2|}\left(k_2 - \frac{2\pi}{d}\right) + \widehat{w}'(|\mathbf{k} + \mathbf{q}_2|)\frac{1}{|\mathbf{k} + \mathbf{q}_2|}\left(k_2 + \frac{2\pi}{d}\right).\end{aligned} \tag{193}$$

Hence, by acquiring the maximum critical wave vector value of the connectivity portion of the eigenvalue equation, the bifurcation condition can be solved. This occurs when $\lambda(\mathbf{k}) = 0$ and therefore, is determined by $\partial\widehat{w}/\partial k_\alpha = 0$ and the discriminant being greater than zero. Now, to find the bifurcation point, we need to solve $H(u_0) = 0$ where,

$$H(u) = -1 + f'(u)\widehat{W}(\mathbf{k}_c). \tag{194}$$

Again this can be computed using *fsolve* in MATLAB. Therefore, by setting the value of μ, the steady state condition and the bifurcation condition can be used to find the critical values of u_0 and h_c for the system. For $\mu = 11$, the values of u_0 and h_c are calculated as 0.0829 and 0.2233 respectively, as shown by the highlighted point in Fig. 34. Two steady state points are found. We consider the highlighted point with the smaller values of u_0 and h. Similar analysis could be applied to the other steady state. However, these values for u_0 and h_c are right at the point of bifurcation and therefore to push the system into the pattern formation regime, we alter the value of h to be $0.95h_c$ to be able to readily observe the activity away from the stable state. The Fourier transform of the patchy connection kernel $\widehat{W}$ is shown in Fig. 35 after writing $\mathbf{k} = (k_1, k_2)$, with one of the four degenerate maximum points, $\widehat{W}(\mathbf{k}_c)$ highlighted; furthermore, the plane of $4/f'(u_0, \mu, h)$ is emphasised to show where it intercepts the Fourier transform using $h = 0.95h_c$. This shows that the system is close to but past the bifurcation point and that there are four maximum points, occurring from the structure of the square lattice. In consequence, we expect to excite patterns with wave-vectors determined by the four maxima.

An example of the cortical activity from using the two dimensional neural field model with a patchy square lattice applied to the connectivity can be seen in Fig. 36. This shows horizontal and vertical lines of excitatory and inhibitory cortical activity. This is expected since the four directions in $\mathbf{k}$-space predicted to be unstable are at right-angles to each other. Thus predicting the excitation of patterns (stripes) that are orthogonal. The simulations are started at the steady state u_0 with random noise added and due to being unstable past bifurcation, this results in different patterns of activity with every simulation. This is reproducible for different values of μ, with Fig. 37 showing another example of the cortical activity with patchy connections on a square lattice with $\mu = 9$. The MATLAB code to produce these simulations is provided in Appendix D.

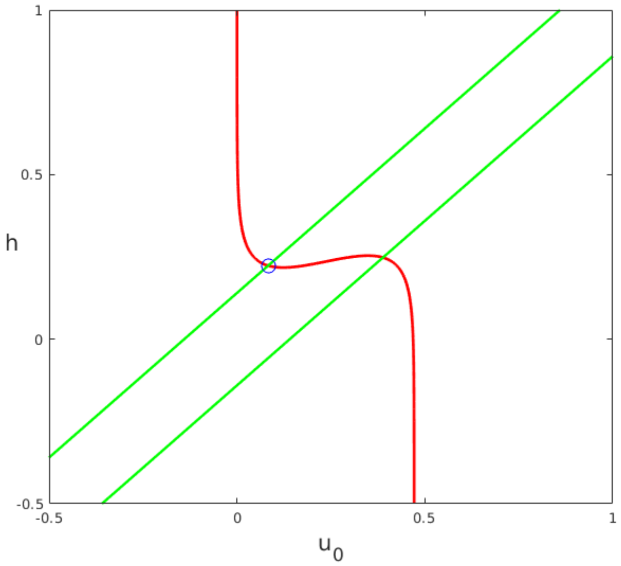

Figure 34.: The steady state condition of the square lattice system (red) and the bifurcation condition (green) plotted for a range of values for u_0 and h to show the values at which the conditions are satisfied, circled in blue. For the example here where $\mu = 11$, the conditions are met at $u_0 = 0.0829$ and $h = 0.2233$.

6.4 TWO DIMENSIONAL MODEL WITH HEXAGONAL LATTICE

Studies have shown that the excitatory connections in the primary visual cortex are hexagonal in nature [42, 129]. Therefore, as we are modelling these patchy connections in V1, we now want to extend this model from a square lattice to a hexagonal one. Now we will introduce a hexagonal lattice that is generated by lattice vectors,

$$\mathbf{l}_1 = d\left(\frac{\sqrt{3}}{2}, \frac{1}{2}\right), \quad \mathbf{l}_2 = d(0,1). \tag{195}$$

The dual (or reciprocal) hexagonal lattice is generated by the vectors

$$\mathbf{q}_1, \mathbf{q}_2 \text{ where } \mathbf{q}_i \cdot \mathbf{l}_j = 2\pi\delta_{ij}. \tag{196}$$

Therefore, we have

$$\mathbf{q}_1 = \frac{4\pi}{\sqrt{3}d}(1,0), \quad \mathbf{q}_2 = R_{\frac{2\pi}{3}}\mathbf{q}_1 = \frac{4\pi}{\sqrt{3}d}\left(-\frac{1}{2}, \frac{\sqrt{3}}{2}\right) \tag{197}$$

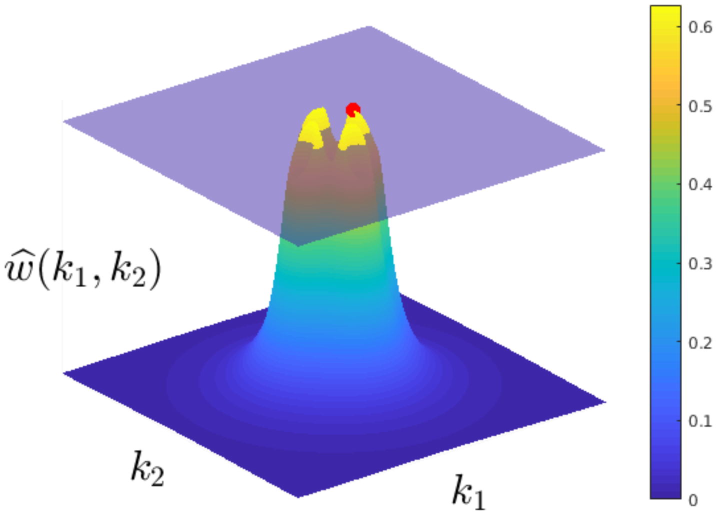

Figure 35.: The Fourier transform of the patchy connections kernel $w^p(\mathbf{r}, \mathbf{r}') = w(|\mathbf{r} - \mathbf{r}'|)M(\mathbf{r} - \mathbf{r}')$ where the standard kernel $w(\mathbf{r})$ is defined by (186) and the square periodic patchiness $M(\mathbf{r})$ by (180). The red dot shows one of the four maximum points of the Fourier transform. This is used to position the system at bifurcation, namely where the plane $4/f'(u_0, \mu, h)$ tangentially touches it. The plane used in the simulation is with $h = 0.95h_c$ to enable pattern formation past the bifurcation point, this is highlighted in blue. Here, $\mu = 11$ and $d = 2$, plotted on the domain $[-5\pi, 5\pi] \times [-5\pi, 5\pi]$.

and

$$\mathbf{q}_3 = -\mathbf{q}_1 - \mathbf{q}_2 = R_{\frac{4\pi}{3}}\mathbf{q}_1 = \frac{4\pi}{\sqrt{3}d}\left(-\frac{1}{2}, -\frac{\sqrt{3}}{2}\right), \tag{198}$$

where R_θ is the rotation matrix,

$$\mathbf{R}_\theta = \begin{pmatrix} \cos\theta & -\sin\theta \\ \sin\theta & \cos\theta \end{pmatrix}. \tag{199}$$

Another useful results is that the magnitude of these hexagonal lattice vectors is

$$|\mathbf{q}| = \frac{4\pi}{\sqrt{3}d}. \tag{200}$$

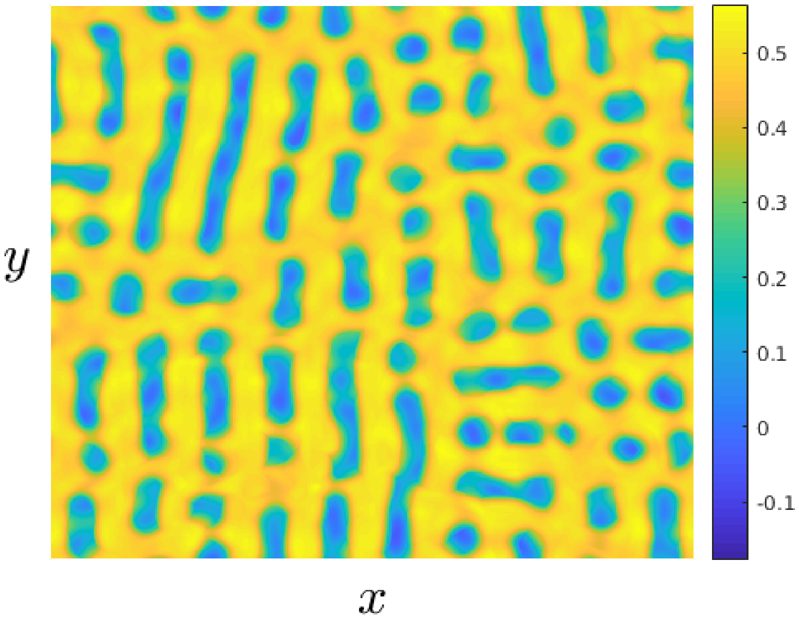

Figure 36.: An example of cortical activity for the two dimensional regular square lattice model defined by the neural field model (168), with kernel $w^p(\mathbf{r},\mathbf{r}') = w(|\mathbf{r}-\mathbf{r}'|)M(\mathbf{r}-\mathbf{r}')$ where the standard kernel $w(\mathbf{r})$ is defined by (186), the periodic patchiness $M(\mathbf{r})$ by (180) and the firing rate f by (187). This example is using $\mu = 11$, $d = 2$, plotted on the domain $[-5\pi, 5\pi] \times [-5\pi, 5\pi]$.

We will introduce the patchy connections for a hexagonal lattice, M, to vary periodically with respect to the regular hexagonal planar lattice $\mathscr{L}$ in the form of,

$$M^h(\mathbf{r}) = \sum_{\mathbf{q}\in\mathscr{L}^\dagger} M^h_{\mathbf{q}} \mathrm{e}^{-i\mathbf{q}\cdot\mathbf{r}}, \quad \mathscr{L}^\dagger = \{m\mathbf{q}_1 + p\mathbf{q}_2 + s\mathbf{q}_3 : m, p, s \in \mathbb{Z}\}.$$

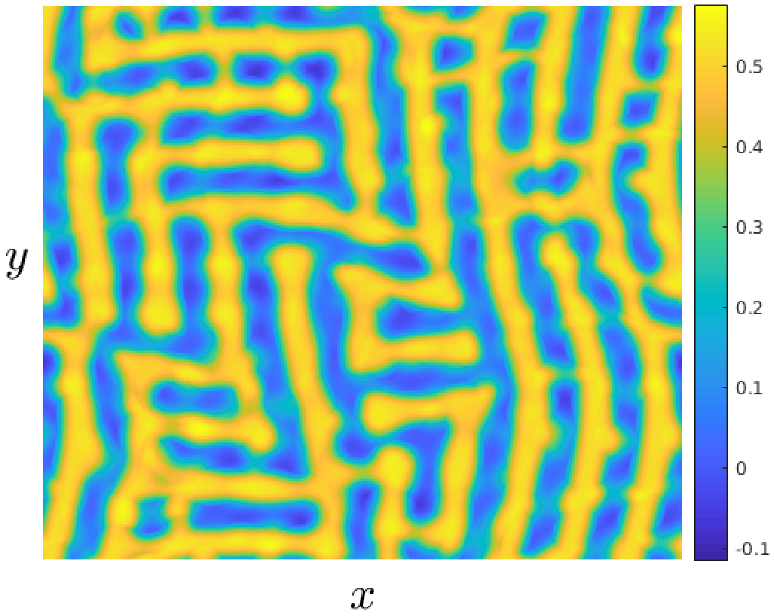

Figure 37.: Another example of cortical activity for the two dimensional regular square lattice model defined by the neural field model (168), with kernel $w^p(\mathbf{r},\mathbf{r}') = w(|\mathbf{r}-\mathbf{r}'|)M(\mathbf{r}-\mathbf{r}')$ where the standard kernel $w(\mathbf{r})$ is defined by (186), the periodic patchiness $M(\mathbf{r})$ by (180) and the firing rate f by (187). This example is using $\mu = 9$, $d = 2$, plotted on the domain $[-5\pi, 5\pi] \times [-5\pi, 5\pi]$.

6.4.1 *Turing Analysis of 2D Model with Hexagonal Lattice*

The analysis for the hexagonal lattice follows along closely with similar analysis to the square lattice in the previous section. Now, we consider the choice of periodic model of patchiness for the hexagonal lattice to be,

$$M^h(\mathbf{r}) = \frac{1}{3}\left[\cos(\mathbf{q}_1\cdot\mathbf{r}) + \cos(\mathbf{q}_2\cdot\mathbf{r}) + \cos(\mathbf{q}_3\cdot\mathbf{r})\right], \tag{201}$$

this has Fourier coefficients,

$$M^h_{\mathbf{q}} = \frac{1}{(2\pi)^2}\int_{\mathbb{R}^2}\frac{1}{3}\left[\frac{e^{i\mathbf{q}_1\cdot\mathbf{r}}+e^{-i\mathbf{q}_1\cdot\mathbf{r}}}{2} + \frac{e^{i\mathbf{q}_2\cdot\mathbf{r}}+e^{-i\mathbf{q}_2\cdot\mathbf{r}}}{2} + \frac{e^{i\mathbf{q}_3\cdot\mathbf{r}}+e^{-i\mathbf{q}_3\cdot\mathbf{r}}}{2}\right]e^{-i\mathbf{q}\cdot\mathbf{r}}d\mathbf{r}. \tag{202}$$

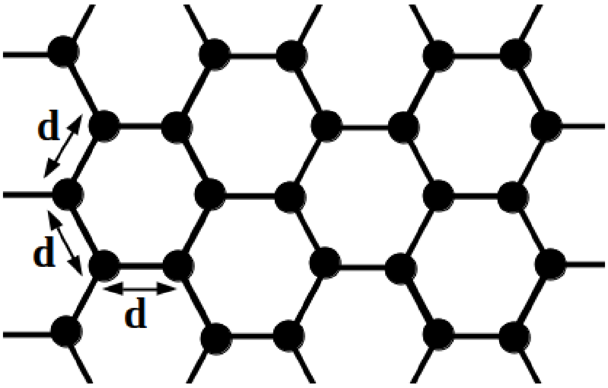

Figure 38.: An example of a regular hexagonal lattice with distance d between grid points.

Again by using the orthogonality (182), this gives the Fourier coefficients as,

$$M^h_{\mathbf{q}} = \frac{1}{6}\left[\delta_{\mathbf{q},\mathbf{q}_1} + \delta_{\mathbf{q},-\mathbf{q}_1} + \delta_{\mathbf{q},\mathbf{q}_2} + \delta_{\mathbf{q},-\mathbf{q}_2} + \delta_{\mathbf{q},\mathbf{q}_3} + \delta_{\mathbf{q},-\mathbf{q}_3}\right]. \tag{203}$$

Therefore, using this definition of the Fourier coefficients (203), the eigenvalues of the hexagonal lattice system (179) can be written as,

$$\lambda(\mathbf{k}) = -1 + \frac{1}{6}f'(u_0)\left[\widehat{w}(|\mathbf{k}-\mathbf{q}_1|) + \widehat{w}(|\mathbf{k}+\mathbf{q}_1|) + \widehat{w}(|\mathbf{k}-\mathbf{q}_2|) \right.$$
$$\left. + \widehat{w}(|\mathbf{k}+\mathbf{q}_2|) + \widehat{w}(|\mathbf{k}-\mathbf{q}_3|) + \widehat{w}(|\mathbf{k}+\mathbf{q}_3|)\right].$$

The steady state of the model was defined earlier as (175). Now, the hexagonal lattice has a steady state at

$$\widehat{W}(\mathbf{k}=0) = \frac{1}{3}\left[\widehat{w}(|\mathbf{q}_1|) + \widehat{w}(|\mathbf{q}_2|) + \widehat{w}(|\mathbf{q}_3|)\right]$$

Therefore,

$$\widehat{W}(\mathbf{k}=0) = \widehat{w}\left(\frac{4\pi}{\sqrt{3}d}\right).$$

So again to find the steady state, we need to solve, $G(u_0) = 0$ where this time,

$$G(u) = u - f(u)\widehat{w}\left(\frac{4\pi}{\sqrt{3}d}\right). \tag{204}$$

6.4.2 *Simulations of the Patchy Model with a Hexagonal Lattice*

To complete the theory, a computational example will be shown again, this to highlight the effects of patchy connections on a hexagonal lattice using M^h as given by (201). The choice of formula for the connectivity kernel $w(\mathbf{r})$ and firing rate $f(u, \mu, h)$ are the same as the square lattice example, (186) and (187) respectively.Fig. 39 shows the patchy connections kernel $w^p(\mathbf{r}, \mathbf{r}')$ for the hexagonal periodic patchiness with this Wizard hat kernel.

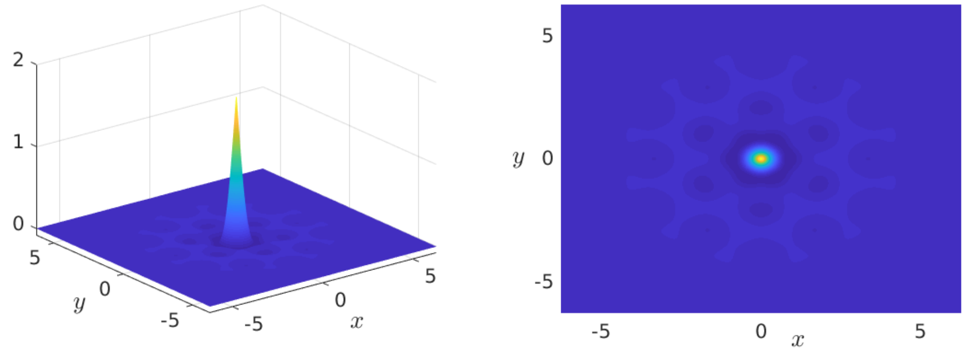

Figure 39.: The patchy connections kernel $w^p(\mathbf{r}, \mathbf{r}') = w(|\mathbf{r} - \mathbf{r}'|)M^h(\mathbf{r} - \mathbf{r}')$ where the standard kernel $w(\mathbf{r})$ is defined by (186) and the hexagonal periodic patchiness $M^h(\mathbf{r})$ by (201). Here, $\mu = 15$ and $d = 2$, plotted on the domain $[-2\pi, 2\pi] \times [-2\pi, 2\pi]$.

To calculate the critical wave vector $\mathbf{k}_c$ at bifurcation, we now need to find the maximum of $\widehat{w}(\mathbf{k})$ for the hexagonal lattice. The derivative of $\widehat{W}(\mathbf{k})$ is very similar to the square lattice with the extra basis vector $\mathbf{q}_3$; namely, we need to calculate,

$$\frac{\partial \widehat{w}}{\partial k_\alpha}(|\mathbf{k} \pm \mathbf{q}_\beta|) \text{ for } \alpha = 1, 2 \text{ with } \beta = 1, 2, 3 \text{ and } \mathbf{k} = (k_1, k_2). \tag{205}$$

which can be expanded using,

$$\frac{\partial \widehat{w}}{\partial k_\alpha}(|\mathbf{k} \pm \mathbf{q}_\beta|) = \widehat{w}(|\mathbf{k} \pm \mathbf{q}_\beta|)\frac{1}{|\mathbf{k} \pm \mathbf{q}_\beta|}\left((k_1 \pm q_\beta^x)\delta_{1,\alpha} + (k_2 \pm q_\beta^y)\delta_{2,\alpha}\right). \tag{206}$$

Therefore, by setting the value of μ, the steady state condition and the

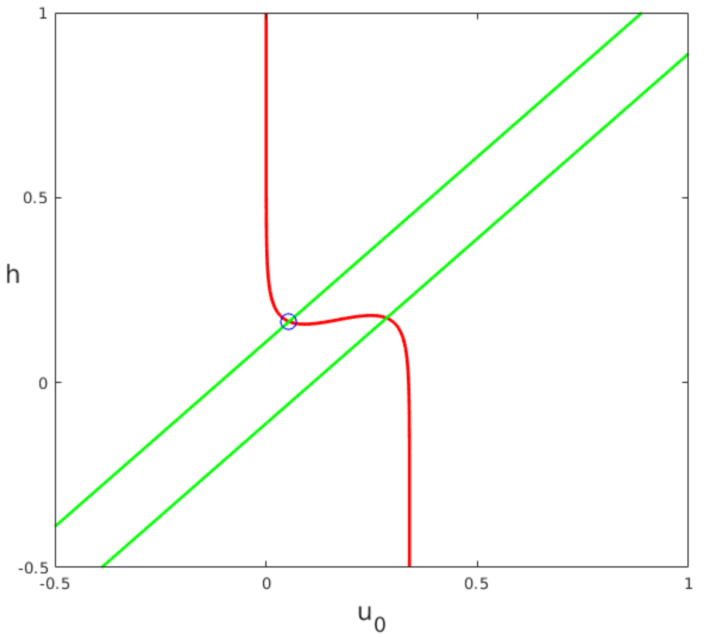

Figure 40.: The steady state condition of the hexagonal patchy connections system (red) and the bifurcation condition (green) plotted for a range of values for u_0 and h to show when the values at which the conditions are satisfied, circled in blue. For the example here where $\mu = 15$, the conditions are met at $u_0 = 0.0543$ and $h = 0.1648$.

bifurcation condition can be used to find the critical values of u_0 and h_c for the hexagonal system. For $\mu = 15$, the values of u_0 and h_c are calculated as 0.0543 and 0.1648 respectively, as shown by the highlighted point in Fig. 40. Again, we choose to focus on the stability of one of the steady states and anticipate similar behaviour for the other. The Fourier transform of the hexagonal patchy connection kernel $\widehat{W}$ is shown in Fig. 41, with one of the six maximum points, $\widehat{W}(\mathbf{k}_c)$ highlighted; again, the plane of $6/f'(u_0, \mu, h)$ is emphasised to show where it intercepts the Fourier transform using $h = 0.95h_c$. This shows that the system is close to but past the bifurcation point and that there are six maximum points, created from the structure of the hexagonal lattice. Thus, patterns orientated along three different

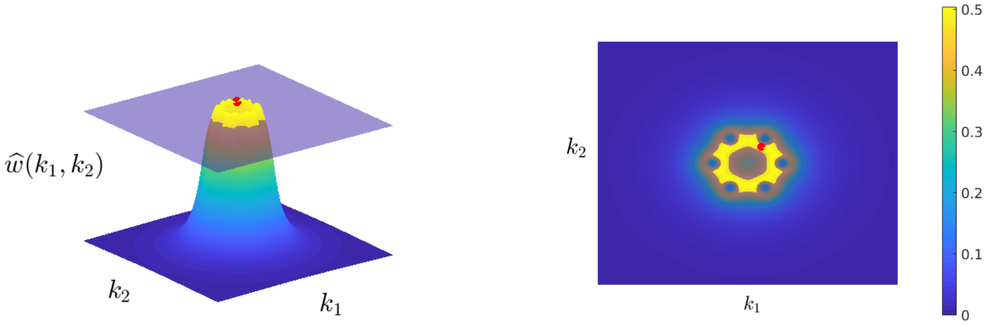

Figure 41.: The Fourier transform of the patchy connections kernel $w^p(\mathbf{r},\mathbf{r}') = w(|\mathbf{r}-\mathbf{r}'|)M^h(\mathbf{r}-\mathbf{r}')$ where the standard kernel $w(\mathbf{r})$ is defined by (186) and the hexagonal periodic patchiness $M^h(\mathbf{r})$ by (201). The red dot shows one of the six maximum points of the Fourier transform. This is used to position the system at bifurcation, namely where the plane $6/f'(u_0,\mu,h)$ tangentially touches it. The plane used in the simulation is with $h = 0.95h_c$ to enable pattern formation past the bifurcation point, this is highlighted in blue. On the right plot, the 6 maximum points of the Fourier transform for the hexagonal lattice can be clearly identified. Here, $\mu = 15$ and $d = 2$, plotted on the domain $[-5\pi, 5\pi] \times [-5\pi, 5\pi]$.

directions can be simultaneously excited at bifurcation.

An example of the cortical activity from using the two dimensional neural field model with a patchy hexagonal lattice applied to the connectivity can be seen in Fig. 42. This shows stripes of excitatory and inhibitory cortical activity with similar angles to hexagons, horizontal lines and lines at approximately 60° and 120°. This is expected since the six directions in $\mathbf{k}$-space predicted to be unstable are hexagonal in nature. The simulations are started at the steady state u_0 with random noise added and due to being unstable past bifurcation, this results in different patterns of activity with every simulation. This is reproducible for different values of μ, with Fig. 43

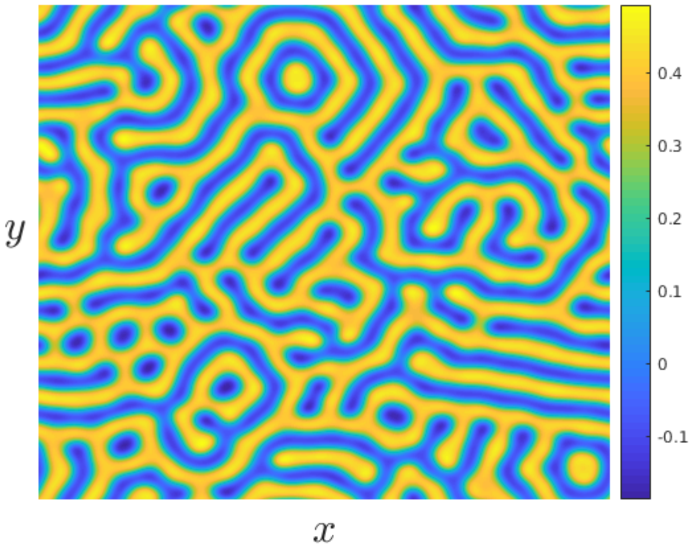

Figure 42.: An example of cortical activity for the two dimensional regular hexagonal lattice model defined by the neural field model (168), with kernel $w^p(\mathbf{r},\mathbf{r}') = w(|\mathbf{r}-\mathbf{r}'|)M^h(\mathbf{r}-\mathbf{r}')$ where the standard kernel $w(\mathbf{r})$ is defined by (186), the periodic patchiness $M^h(\mathbf{r})$ by (201) and the firing rate f by (187). This example is using $\mu = 15$, $d = 2$, plotted on the domain $[-5\pi, 5\pi] \times [-5\pi, 5\pi]$.

showing another example of the cortical activity with patchy connections on a hexagonal lattice with $\mu = 12$. The hexagonal patterns are a lot closer to what is expected of the patchy neural connections. The MATLAB code to produce these simulations is similar to the code provided in Appendix D but with the equations adapted to the hexagonal equivalents, more of which is also provided in the Appendix F for the next chapter.

6.5 MODEL WITH HEXAGONAL LATTICE: INTRODUCING ϵ

Now we will slightly adjust the patchy formula to include the parameter ϵ to modulate the strength of the patchiness with the hexagonal lattice. This is useful as it enables us to have more control over the strength of the patchy connections. Furthermore, the isotropic model is recoverable as $\epsilon \to 0$,

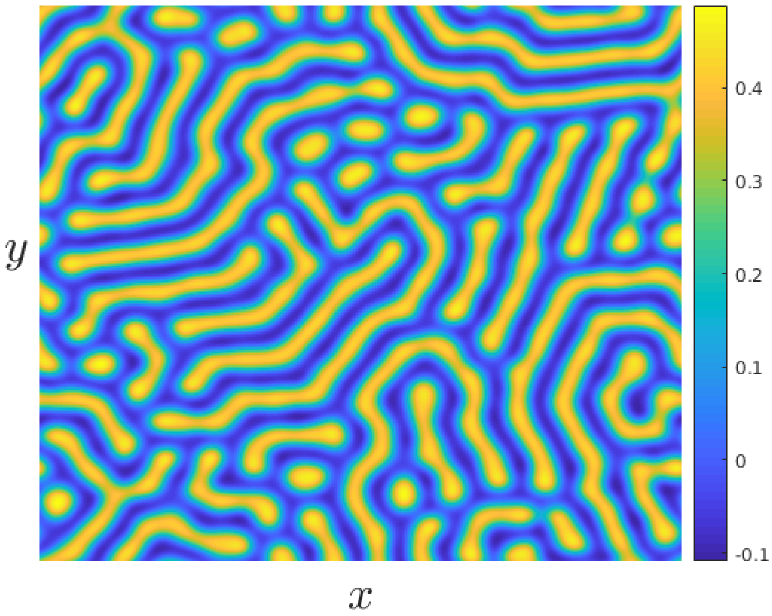

Figure 43.: Another example of cortical activity for the two dimensional regular hexagonal lattice model defined by the neural field model (168), with kernel $w^p(\mathbf{r},\mathbf{r}') = w(|\mathbf{r}-\mathbf{r}'|)M^h(\mathbf{r}-\mathbf{r}')$ where the standard kernel $w(\mathbf{r})$ is defined by (186), the periodic patchiness $M^h(\mathbf{r})$ by (201) and the firing rate f by (187). This example is using $\mu = 12$, $d = 2$, plotted on the domain $[-5\pi, 5\pi] \times [-5\pi, 5\pi]$.

hence this can be used to validate the analysis and compare against the standard neural field model. Therefore, we will now consider the formula of patchiness and the lattice to be,

$$M^{\epsilon}(\mathbf{r}) = 1 + \epsilon \left[\sum_{\mathbf{q} \in \mathscr{L}^{\dagger}} M^{\epsilon}_{\mathbf{q}} e^{-i\mathbf{q}\cdot\mathbf{r}} \right], \quad \mathscr{L}^{\dagger} = \{m\mathbf{q}_1 + p\mathbf{q}_2 + s\mathbf{q}_3 : m, p, s \in \mathbb{Z}\}. \tag{207}$$

using the same hexagonal generational vectors as previously, given by (197)-(198).

6.5.1 *Turing Analysis of Model with Hexagonal Lattice introducing ϵ*

The hexagonal lattice is used again with this model and so the analysis follows from previously in section 6.4.1. Hence, we now consider the choice of periodic model of patchiness to be similarly,

$$M^{\epsilon}(\mathbf{r}) = 1 + \epsilon \left[\frac{1}{3} \left[\cos(\mathbf{q}_1 \cdot \mathbf{r}) + \cos(\mathbf{q}_2 \cdot \mathbf{r}) + \cos(\mathbf{q}_3 \cdot \mathbf{r}) \right] \right], \tag{208}$$

The eigenvalues of this model are,

$$\lambda(\mathbf{k}) = -1 + f'(u_0) \Big[\widehat{w}(|\mathbf{k}|) + \frac{\epsilon}{6} \big[\widehat{w}(|\mathbf{k} - \mathbf{q}_1|) + \widehat{w}(|\mathbf{k} + \mathbf{q}_1|) + \widehat{w}(|\mathbf{k} - \mathbf{q}_2|) + \widehat{w}(|\mathbf{k} + \mathbf{q}_2|) + \widehat{w}(|\mathbf{k} - \mathbf{q}_3|) + \widehat{w}(|\mathbf{k} + \mathbf{q}_3|) \big] \Big].$$

The steady state of the model was defined earlier as (175). Now, the hexagonal lattice including the parameter ϵ has a steady state at

$$\widehat{W}(\mathbf{k} = 0) = \widehat{w}(0) + \frac{\epsilon}{3} \left[\widehat{w}(|\mathbf{q}_1|) + \widehat{w}(|\mathbf{q}_2|) + \widehat{w}(|\mathbf{q}_3|) \right].$$

So again to find the steady state, we need to solve, $G(u_0) = 0$, where this time, in the case where the kernel is balanced, ($\widehat{w}(0) = 0$),

$$G(u) = u - f(u) \epsilon \widehat{w} \left(\frac{4\pi}{\sqrt{3}d} \right). \tag{209}$$

6.5.2 *Computational Example*

To complete the theory, a computational example will be given to show the effects of varying the strength of an isotropic connectivity kernel with a hexagonal lattice using M^{ϵ} as given by (208). Again, the choice of formula for the connectivity kernel $w(\mathbf{r})$ and firing rate $f(u, \mu, h)$ for this example are (186) and (187) respectively. Fig. 44 shows the patchy connections kernel $w^p(\mathbf{r}, \mathbf{r}')$ for the hexagonal periodic patchiness with epsilon with this Wizard hat kernel.

To calculate the critical wave vector $\mathbf{k}_c$ at bifurcation, we now need to

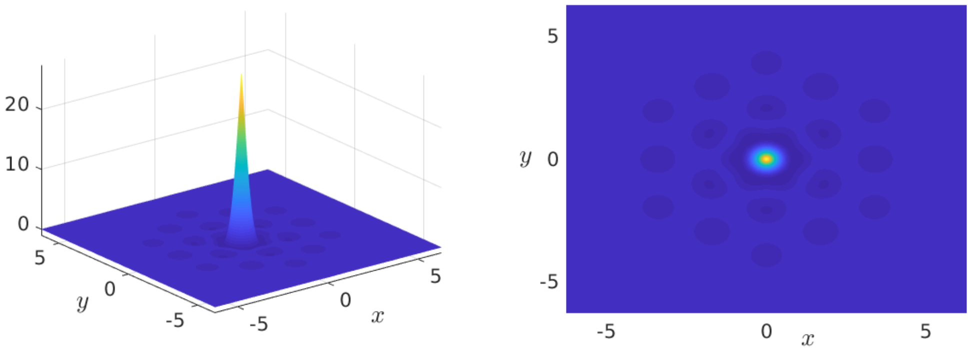

Figure 44.: The patchy connections kernel $w^p(\mathbf{r},\mathbf{r}') = w(|\mathbf{r}-\mathbf{r}'|)M(\mathbf{r}-\mathbf{r}')$ where the standard kernel $w(\mathbf{r})$ is defined by (186) and the hexagonal periodic patchiness $M^\epsilon(\mathbf{r})$ by (208). Here, $\mu = 1.1$, $\epsilon = 15$ and $d = 2$, plotted on the domain $[-2\pi, 2\pi] \times [-2\pi, 2\pi]$.

find the maximum of $\widehat{w}(\mathbf{k})$ for the hexagonal lattice with ϵ. Following equations (188-191) we have,

$$\begin{aligned}
\frac{\partial}{\partial k_1}\Bigg[\widehat{w}(|\mathbf{k}|) + \frac{\epsilon}{6}\Big[\widehat{w}(|\mathbf{k}-\mathbf{q}_1|) + \widehat{w}(|\mathbf{k}+\mathbf{q}_1|) + \widehat{w}(|\mathbf{k}-\mathbf{q}_2|) \\
+ \widehat{w}(|\mathbf{k}+\mathbf{q}_2|) + \widehat{w}(|\mathbf{k}-\mathbf{q}_3|) + \widehat{w}(|\mathbf{k}+\mathbf{q}_3|)\Big]\Bigg] \\
= \widehat{w}'(|\mathbf{k}|)\frac{k_1}{|\mathbf{k}|} + \frac{\epsilon}{6}\Bigg[\widehat{w}'(|\mathbf{k}-\mathbf{q}_1|)\frac{1}{|\mathbf{k}-\mathbf{q}_1|}\left(k_1 - \frac{4\pi}{\sqrt{3}d}\right) \\
+ \widehat{w}'(|\mathbf{k}+\mathbf{q}_1|)\frac{1}{|\mathbf{k}+\mathbf{q}_1|}\left(k_1 + \frac{4\pi}{\sqrt{3}d}\right) + \widehat{w}'(|\mathbf{k}-\mathbf{q}_2|)\frac{1}{|\mathbf{k}-\mathbf{q}_2|}\left(k_1 + \frac{2\pi}{\sqrt{3}d}\right) \\
+ \widehat{w}'(|\mathbf{k}+\mathbf{q}_2|)\frac{1}{|\mathbf{k}+\mathbf{q}_2|}\left(k_1 - \frac{2\pi}{\sqrt{3}d}\right) + \widehat{w}'(|\mathbf{k}-\mathbf{q}_3|)\frac{1}{|\mathbf{k}-\mathbf{q}_3|}\left(k_1 + \frac{2\pi}{\sqrt{3}d}\right) \\
+ \widehat{w}'(|\mathbf{k}+\mathbf{q}_3|)\frac{1}{|\mathbf{k}+\mathbf{q}_3|}\left(k_1 - \frac{2\pi}{\sqrt{3}d}\right)\Bigg]
\end{aligned} \tag{210}$$

and

$$\begin{aligned}
&\frac{\partial}{\partial k_2}\Big[\widehat{w}(|\mathbf{k}|)+\frac{\epsilon}{6}\big[\widehat{w}(|\mathbf{k}-\mathbf{q}_1|)+\widehat{w}(|\mathbf{k}+\mathbf{q}_1|)+\widehat{w}(|\mathbf{k}-\mathbf{q}_2|)\\
&\qquad\qquad +\widehat{w}(|\mathbf{k}+\mathbf{q}_2|)+\widehat{w}(|\mathbf{k}-\mathbf{q}_3|)+\widehat{w}(|\mathbf{k}+\mathbf{q}_3|)\big]\Big]\\
&=\widehat{w}'(|\mathbf{k}|)\frac{k_2}{|\mathbf{k}|}+\frac{\epsilon}{6}\Big[\widehat{w}'(|\mathbf{k}-\mathbf{q}_1|)\frac{1}{|\mathbf{k}-\mathbf{q}_1|}(k_2)+\widehat{w}'(|\mathbf{k}+\mathbf{q}_1|)\frac{1}{|\mathbf{k}+\mathbf{q}_1|}(k_2)\\
&+\widehat{w}'(|\mathbf{k}-\mathbf{q}_2|)\frac{1}{|\mathbf{k}-\mathbf{q}_2|}\left(k_2-\frac{2\pi}{d}\right)+\widehat{w}'(|\mathbf{k}+\mathbf{q}_2|)\frac{1}{|\mathbf{k}+\mathbf{q}_2|}\left(k_2+\frac{2\pi}{d}\right)\\
&+\widehat{w}'(|\mathbf{k}-\mathbf{q}_3|)\frac{1}{|\mathbf{k}-\mathbf{q}_3|}\left(k_2+\frac{2\pi}{d}\right)+\widehat{w}'(|\mathbf{k}+\mathbf{q}_3|)\frac{1}{|\mathbf{k}+\mathbf{q}_3|}\left(k_2-\frac{2\pi}{d}\right)\Big]
\end{aligned} \tag{211}$$

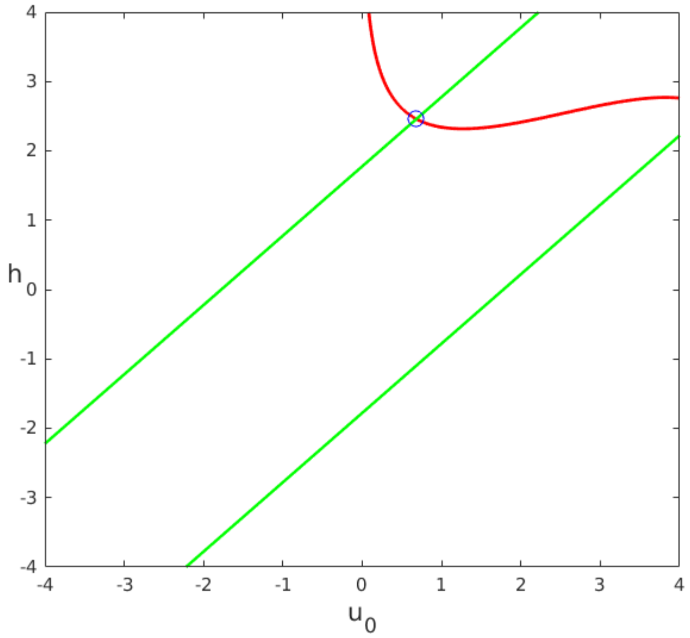

Figure 45.: The steady state condition of the hexagonal patchy connections system (red) and the bifurcation condition (green) plotted for a range of values for u_0 and h to show when the values at which the conditions are satisfied, circled in blue. For the example here where $\mu = 1.1$ and $\epsilon = 15$, the conditions are met at $u_0 = 0.6453$ and $h = 2.3995$.

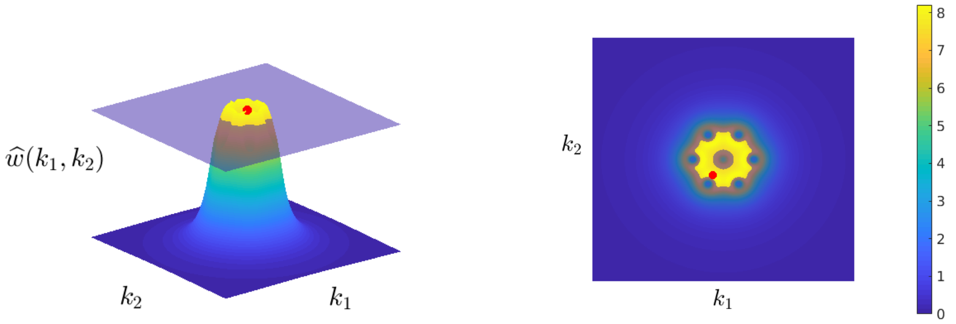

Figure 46.: The Fourier transform of the patchy connections kernel $w^p(\mathbf{r}, \mathbf{r}') = w(|\mathbf{r} - \mathbf{r}'|)M^\epsilon(\mathbf{r} - \mathbf{r}')$ where the standard kernel $w(\mathbf{r})$ is defined by (186) and the hexagonal periodic patchiness $M^\epsilon(\mathbf{r})$ by (208) and the strength of the patchiness is controlled by ϵ. The red dot shows one of the six maximum points of the Fourier transform. This is used to position the system at bifurcation, namely where the plane $6/f'(u_0, \mu, h)$ tangentially touches it. The plane used in the simulation is with $h = 0.95h_c$ to enable pattern formation past the bifurcation point, this is highlighted in blue. On the right plot, the 6 maximum points of the Fourier transform for the hexagonal lattice can be clearly identified. Here, $\mu = 1.1$, $\epsilon = 15$ and $d = 2$, plotted on the domain $[-5\pi, 5\pi] \times [-5\pi, 5\pi]$.

Therefore, by setting the value of μ, the steady state condition and the bifurcation condition can be used to find the critical values of u_0 and h_c for the hexagonal lattice controlled by ϵ. For $\mu = 1.1$ and $\epsilon = 15$, the values of u_0 and h_c are calculated as 0.6453 and 2.3995 respectively, as shown by the highlighted point in Fig. 45. Again, there is another steady state just outside the domain of the diagram which we do not consider, but for which we anticipate similar stability results and pattern forming behaviour. The Fourier transform of the hexagonal patchy connection kernel $\widehat{W}$ with ϵ is shown in Fig. 46, with one of the six maximum points, $\widehat{W}(\mathbf{k}_c)$ highlighted; again, the plane of $6/f'(u_0, \mu, h)$ is emphasised to show where it intercepts

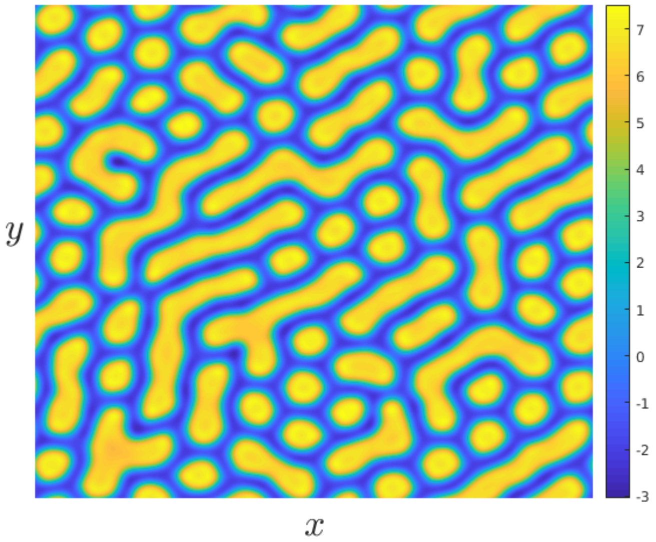

Figure 47.: An example of cortical activity for the two dimensional regular hexagonal lattice model defined by the neural field model (168), with kernel $w^p(\mathbf{r},\mathbf{r}') = w(|\mathbf{r}-\mathbf{r}'|)M^{\epsilon}(\mathbf{r}-\mathbf{r}')$ where the standard kernel $w(\mathbf{r})$ is defined by (186), the periodic patchiness $M^{\epsilon}(\mathbf{r})$ by (208) and the strength of the patchiness is controlled by ϵ, and the firing rate f by (187). This example is using $\mu = 1.1$, $\epsilon = 15$ and $d = 2$, plotted on the domain $[-5\pi, 5\pi] \times [-5\pi, 5\pi]$.

the Fourier transform using $h = 0.95h_c$. This shows that the system is close to but past the bifurcation point and that there are six maximum points, occurring from the structure of the hexagonal lattice.

An example of the cortical activity from using the two dimensional neural field model with a patchy hexagonal lattice controlled by ϵ applied to the connectivity can be seen in Fig. 47. This again shows lines of excitatory and inhibitory cortical activity with similar angles to hexagons, horizontal lines and lines at approximately 60° and 120° due to the six directions in $\mathbf{k}$-space predicted to be unstable are hexagonal in nature. The simulations are started at the steady state u_0 with random noise added and due to being unstable past bifurcation, this results in different patterns of activity with every simulation. The model with ϵ results in patchier connections than without, the lines are not as connected. The MATLAB code to produce these simulations is similar to the code provided in Appendix D but with the equations adapted to the equivalent ones for the hexagonal model with ϵ.

6.6 SUMMARY

In this chapter, we set out to incorporate the long range patchy connections that are seen in the crystalline microstructure of V1 cortex. The standard connectivity model that we have previously used (186) included short range inhibition and long range excitation; however, this was homogeneous and isotropic, the same across the cortex. To model the patchiness in the connectivity, we included modulation by a periodic function $M(\mathbf{r} - \mathbf{r}')$. This was firstly shown using a square lattice. However, it has been shown that the connections in V1 are approximately hexagonal in structure. Consequently, we used a hexagonal lattice. Finally, we added the ϵ coefficient to be able to control the strength of the patchiness. In conclusion, the hexagonal patchy model is a better representation of the neuronal connections in V1 as it is more realistic of the activity than the previous standard neural field models. Furthermore, we have managed to augment standard Turing analysis in neural fields to incorporate a form of patchy connections in a model that is consistent with the microstructure of V1.

We believe that the relationship between the microstructure of patchy connectivity and orientation preference will allow us to create a model of the orientation preference by using the patchy connections to help create the pinwheel and linear structure. This will be explored in the next chapter, using a multi-layered neural field model.

7

USING PATCHY CONNECTIONS TO GENERATE AN ORIENTATION PREFERENCE MAP

7.1 INTRODUCTION

The aim of this chapter is to explore how patchy connections between neurons in primary visual cortex can allow us to create an orientation preference map (OPM). Primary visual cortex has a lattice-like pattern of connectivity that is similar to the OPM, with short range connections between the orientations, similar to the pinwheel structure of the OPM, as well as long range connections to the same orientation, the linear regions of the OPM. First, we will review the layered neural field model of Rankin and Chavane in [96] that generates orientation preference. Their work on this model looks at replicating voltage sensitive dye (VSD) experiments that show a stable orientation selective response in activity to local, orientated visual stimuli in V1. They present a layered model of four sub-populations incorporating orientation preference to model these voltage-sensitive dye experiments; with connectivity that is split into inhibition, and long and short range excitation, along with an input term to replicate the stimulus driven input in the experiments. The orientation preference weights used in their model were generated using spatial Hebbian-like learning. Orientation preference has previously been added to neural field models before in the work of Bressloff in [21], discussed in Chapter 2. Techniques used in the layered model from [96] to combine multi-layer activity into one signal and also computing the orientation preference of the activity will then allow us to build our own layered model with patchy connections for OPM generation. We start with the patchy connections model from Chapter 6, the homogeneous and isotropic neural field model that is modulated by a spatially periodic function. Turing analysis of our layered model with linear coupling between the state variables in each layer allows us to find the bifurcation point at which pattern formation occurs and then in turn will use this in our studies of OPM generation.

The artificial generation of orientation preference maps have been modelled in a variety of different ways previously. The work in [2], investigates how the crystalline microstructure can be used to model spatial hallucinations and how it affects long range connections such as orientation. This work develops this by creating an orientation preference map from the properties of the crystalline microstructure. In [96], the OPM is created using a spatial Hebbian-like learning rule. A Hebbian learning method using adaptation and normalisation is also investigated by [112]. In [128], long range connections are shown to be important for creating key map features having quasi-periodic repetition. Orientation preference maps that are normalised by the regular length scale can give a constant pinwheel density, shown by [62, 63, 105]. The receptive fields of ganglion cells is used to model an OPM in [89] and also investigates the hexagonal symmetry of OPMs. In [93], the relationship between specialised glial cells and orientation preference is explored to create a computational OPM.

7.2 LAYERED NEURAL FIELD MODEL WITH LEARNED ORIENTATION PREFERENCE

In [96], Rankin and Chavane use a a planar neural field model to describe neural activity in V1. Average membrane potential $u_i(x,y,t)$, which represents the neural activity, is split into four orientation sub-populations,

$i = \{0°, 45°, 90°, 135°\}$. This results in a dynamical model giving a coarse grained evolution of the average membrane potential on a continuous domain in two-dimensional cortical space with a discrete representation of the orientations. Unlike the standard neural field model by [1] and [86], this model splits the connectivity profile into inhibition, local excitation and lateral excitation. This allows more control over the effects of the different types of connections in the model. There are far more parameters and intricacies to the model than the standard neural field model. Furthermore, a lot of the parameters and parameter ranges were chosen to be consistent with anatomical data.

7.2.1 *Description of the Rankin-Chavane Model*

The Rankin-Chavane neural field equation model calculates the neural activity on a mesoscopic scale on a continuous two-dimensional plane (x, y). It consists of four interacting layers, each representing the average membrane potential coding for a quantised orientation. An integro-differential equation models the dynamics of each subpopulation as,

$$\begin{aligned}
\tau \frac{\partial}{\partial t} u_i(x,y,t) = & -\sum_j \rho_{ij} u_j(x,y,t) && (212)\\
& + \sum_j k_{ij} I_j(x,y)(1 + \beta_{\text{inp}} J_j(x,y)) && (213)\\
& + S(u_i(x,y,t)) \otimes \left[g_{\text{ex}} w_{\text{E}}^{\text{loc}}(x,y) - g_{\text{in}} w_{\text{I}}(x,y) \right] && (214)\\
& + (1 + \beta_{\text{rec}} J_i(x,y)) S(u_i(x,y,t)) \otimes g_{\text{ex}} w_{\text{E}}^{\text{lat}}(x,y). && (215)
\end{aligned}$$

with timescale $\tau = 10\text{ms}$ and the symbol $\otimes$ denotes a spatial convolution.

Term (212) is the decay of the population activity to resting potential and the sub-population decay term coefficient is,

$$\rho_{ij} = \delta_{ij} + 0.1(1 - \delta_{ij}) \tag{216}$$

giving local, linear cross inhibition. Term (213) being the stimulus driven input, I_j and the sub-population active orientations are weighted by k_{ij}, where

$$k_{ij} = k_2(1 + \delta_{ij}). \tag{217}$$

The orientation input $J_j(x, y)$ is learned in this model and modulated by β_{inp} and this is given strength $\beta_{\text{inp}} = 0.25$. Term (214) is the local excitation and inhibition connectivity convolved with a sigmoidal firing rate functions. The orientation selective excitatory connections are modulated by β_{rec} and this is a free parameter in $[0, 1]$. Furthermore, term (215) models the orientation-selective interactions of the excitatory lateral connections. The formula for connectivity, firing rate, conversion to VSD signal and parameters used are described in Appendix E and are all taken from [96].

7.2.2 *Orientation Preference Map*

In [96], the weights J_i were learned using a spatial Hebbian-like learning method for connections. A spatial Hebbian-like rule was applied using the converged model output $u_{i,n}^{\text{fin}}$ computed using a series of localised inputs I_i with random orientations and at random locations. In more detail, this learning rule takes the form,

$$J_{i,n+1} = J_{i,n} + H_a I_i (1 - \langle |J_{i,n}| \star G \rangle_{[0,1]}) u_{i,n}^{\text{fin}} \tag{218}$$

$$J_{i,n+1} = \langle |J_{i,n+1}| \rangle_{[-1,1]}, \tag{219}$$

where H_a is the learning rate, G is a smoothing kernel. The density of pinwheels stabilised after 1600 steps of learning; however, the simulation carried on for 6400 steps. The result of this is shown in Fig. 48. In the paper, they suggest that maps J obtained experimentally or synthetically could also be used to replicate the results as long as the same pinwheel structures and the quasi-periodic organisation is preserved.

The von Mises distribution is a circular normal distribution from 0 to 2π, making it useful to extract orientations. The von Mises distribution is modelled with tuning coefficient κ and a preferred orientation $\mu \in [0, 180°]$,

$$f(x; \mu, \kappa) = \frac{e^{\kappa \cos(x-\mu)}}{2\pi I_0(\kappa)} \tag{220}$$

with $I_0(\kappa)$ being the modified Bessel function of order 0. This distribution is used to explore properties of the connectivity profile, which is modulated by the OPM in Fig 48, and is dependent on the connectivity parameters; it was used to visualise the orientation tuning produced by the OPM-modulated connectivity. By choosing $\kappa \in [0.7, 1.2]$, computed as a best fit-value to the connectivity, each orientation's connectivity J_i for $i = \{0°, 45°, 90°, 135°\}$ can then be computed using $\mu = i$. These four sub-population maps are shown in Fig. 48, in comparison to the entire OPM they created from [96]. These sub-population maps look patchy and have a roughly periodic structure, prompting us to try to use patchy connections to create an OPM.

We recreated an orientation preference map using a random field model, as described by Petitot in [91] and defined in Chapter 2 by (9). We used the approach from [96] in reverse and applied the von Mises distribution to this OPM for each orientation layer to reverse engineer this into the four sub-population maps, by choosing $\kappa \in [0.7, 1.2]$, each orientation preference input J_i for $i = \{0°, 45°, 90°, 135°\}$ can then be computed using $\mu = i$. These four sub-population inputs are shown in Fig. 49, in comparison to the entire OPM they were extracted from, using the OPM from Petitot described by (9).

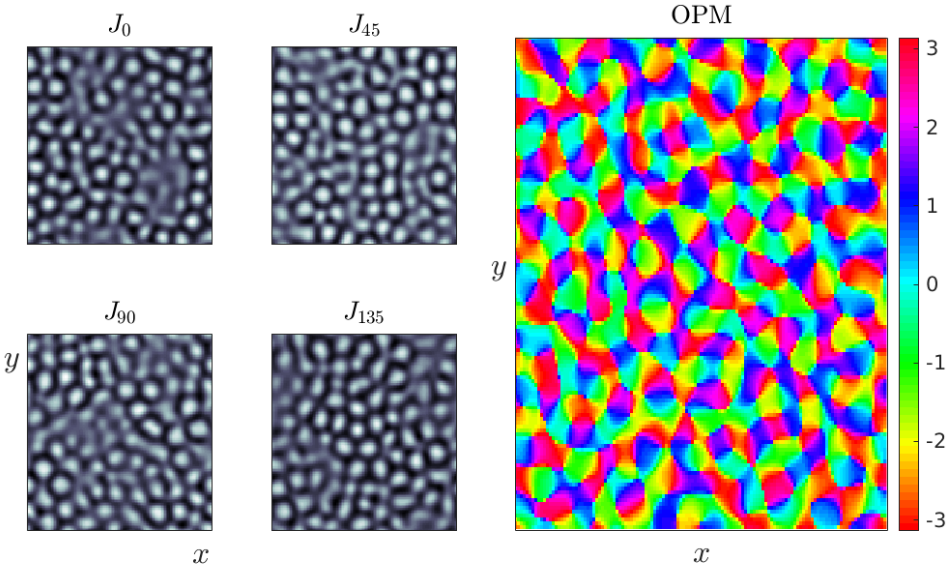

Figure 48.: The four component orientation preference inputs for angles $i = \{0°, 45°, 90°, 135°\}$ with the lighter regions corresponding to higher selectivity for that orientation and darker regions to lower selectivity correspondingly. These are obtained from learned orientation preference (9) (right) by applying the von Mises distribution (220) four times for $u = i$ respectively. Figure reproduced from [96].

7.2.3 *Conversion to One Signal*

Once the activity has been converted to a VSD-like signal, as described in Appendix E, there are now four components of the neural activity, the optical image signal at each of the orientations $i = \{0°, 45°, 90°, 135°\}$, OI_i. The general activation of these four signals can then be computed as,

$$\mathrm{Act}(x,y,t) = \frac{1}{4}\sum_i OI_i(x,y,t), \quad i = \{0°, 45°, 90°, 135°\}. \tag{221}$$

The optical image signal is then normalised by a scaling factor using the max of all of the signals,

$$OI_i = \left(1 - OI_i^{max} + \sum_i \frac{1}{4} OI_i^{max}\right) OI_i \tag{222}$$

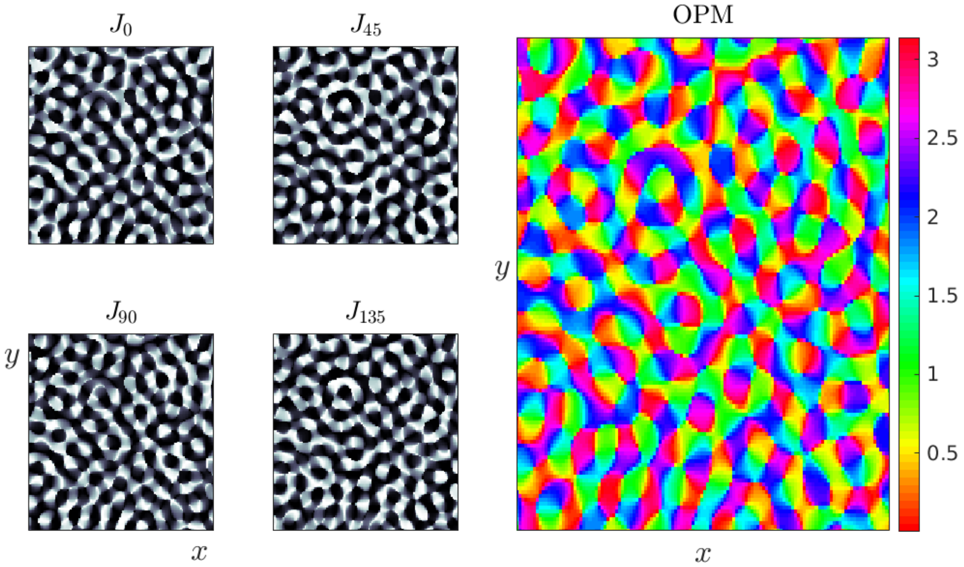

Figure 49.: The four component orientation preference map for angles $i = \{0°, 45°, 90°, 135°\}$ (left) with the lighter regions corresponding to higher selectivity for that orientation and darker regions to lower selectivity correspondingly. These are obtained from the random field model (219) (right) by applying the von Mises distribution (220) four times for $u = i$ respectively.

Difference maps can be computed as the difference between orthogonal optical image signals,

$$D_1(x, y, t) = OI_0(x, y, t) - OI_{90}(x, y, t), \tag{223}$$

$$D_2(x, y, t) = OI_{45}(x, y, t) - OI_{135}(x, y, t). \tag{224}$$

The orientation preference of the optical image signal is the angular coordinate, argument, of the OI signal difference maps, thus computed as,

$$\text{Pref}(x, y, t) = \arctan(D_1(x, y, t), D_2(x, y, t)), \tag{225}$$

and the selectivity strength is the radial coordinate, the magnitude,

$$\text{Sel}(x, y, t) = \sqrt{D_1(x, y, t)^2 + D_2(x, y, t)^2}. \tag{226}$$

This same method will be used for our model to calculate the orientation preference of the layers of activity.

7.2.4 *Summary of Rankin and Chavane Model*

In conclusion, the work of [96] has produced an in depth model that can be manipulated to model an orientation preference map. The results from [96] were reproduced to check the understanding of the model with both the Hebbian-learned orientation weights J_i and also the orientation weights that we generated using (9). By creating an OPM using a different approach, linear stability analysis and pattern formation prediction are able to be performed. This will allow for further mathematical analysis.

7.3 MULTI-LAYERED MODEL WITH HEXAGONAL LATTICE

The orientation preference map can be created using Hebbian-learning as seen in [96] and also using models such as (9). However, they have a similar structure as the patchy connections, as seen in chapter 6 and now with the patchy connectivity model and techniques from chapter 6 and model from [96], we can create a layered model inspired by the work in [96] and analyse the resultant pattern formation using Turing analysis.

We will now introduce a multi-layer two dimensional scalar neural field model, based on the work in chapter 6 and the model from [96],

$$\frac{\partial}{\partial t}u_j(\mathbf{r},t) = -\sum_i \rho_{ij}u_i(\mathbf{r},t) + \int_{\mathbb{R}} w(|\mathbf{r}-\mathbf{r}'|)[1+\epsilon M_j(\mathbf{r}-\mathbf{r}')]f(u_j(\mathbf{r}',t))\,\mathrm{d}\mathbf{r}' \tag{227}$$

for $j = [1,2,3,4]$, where $\epsilon \in \mathbb{R}$ and

$$\begin{aligned}\rho_{ii} &= 1\\ \rho_{ij} &= \rho; \quad i \neq j.\end{aligned}$$

The choice to use four layers is motivated by the work in [96] meaning we are also able to use the same methods to combine the four layers of activity into one for the OPM. Furthermore, the four layers are used to keep the analysis relatively easy to compute; however, this could be extended. The choice of $\rho_{ii} = 1$ is to maintain the standard neural field model for the layer and then $\rho_{ij} = \rho$ for $i \neq j$ allows for the strength of the interaction between the layers to be controlled.

Now, as each layer represents a different orientation, multiple patchy connectivity formulas are required for each layer, otherwise all of the activity would be in the same location for each orientation. Ideally, the patchy connectivity will overlap as little as possible for the four layers. We will achieve this by using the previous model of patchy connectivity and adding parameters to allow the option to rotate, R, or shift, $\mathbf{a}$, the patchy lattice for each layer of the model. Therefore, we require one formula for M_j, the simple model of patchiness as previously seen in chapter 6 with

$$M_j(\mathbf{r}) = \sum_{\mathbf{q}} J^j_{\mathbf{q}} e^{i\mathbf{q}\cdot R_j(\mathbf{r}-\mathbf{a}_j)}, \tag{228}$$

here

$$R_j = \begin{pmatrix} \cos\theta_j & -\sin\theta_j \\ \sin\theta_j & \cos\theta_j \end{pmatrix}, \tag{229}$$

with θ_j being the angle of rotation and $|\mathbf{a}_j| < d$ for each layer $j = [1, 2, 3, 4]$. The Fourier coefficients are given explicitly by,

$$J^j_{\mathbf{q}} = \frac{1}{(2\pi)^2} \int_{\mathbb{R}^2} M_j(\mathbf{r}) e^{-i\mathbf{q}\cdot R_j(\mathbf{r}-\mathbf{a}_j)} \, d\mathbf{r}. \tag{230}$$

In matrix form, we may rewrite (227), using $u = (u_1, u_2, u_3, u_4)$,

$$\frac{\partial}{\partial t} u = -Au + W \otimes f(u); \quad W_j = w[1 + \epsilon M_j] \tag{231}$$

with $W_{ij} = \delta_{ij} W_j$, $A_{ij} = \delta_{ij} + (1 - \delta_{ij})\rho$, and $\otimes$ denotes spatial convolution.

7.3.1 *Turing Analysis*

Following standard Turing Analysis, as seen in chapter 3, we consider the homogeneous steady state with

$$u_0 = (u^0_1, u^0_2, u^0_3, u^0_4), \tag{232}$$

given by

$$Au_0 = \int_{\mathbb{R}} W(\mathbf{r}) \, \mathrm{d}\mathbf{r} \cdot f(u_0). \tag{233}$$

Introduce the 2D Fourier Transform,

$$\widehat{W_j}(\mathbf{k}) = \int_{\mathbb{R}^2} w(|\mathbf{r}|)[1 + \epsilon M_j(\mathbf{r})] \mathrm{e}^{-\mathrm{i}\mathbf{k}\cdot\mathbf{r}} \mathrm{d}\mathbf{r}, \tag{234}$$

then,

$$Au_0 = \widehat{W}(\mathbf{k} = 0) \cdot f(u_0), \tag{235}$$

with $\widehat{W_{ij}} = \delta_{ij}\widehat{W_j}$ and $[f(u_0)]_j = f(u_j^0)$. The Fourier Transform of W_j is,

$$\begin{aligned} \widehat{W}_j(\mathbf{k}) &= \int_{\mathbb{R}^2} w(\mathbf{r}) \mathrm{e}^{-\mathrm{i}\mathbf{k}\cdot\mathbf{r}} \mathrm{d}\mathbf{r} + \epsilon \sum_{\mathbf{q}} J_{\mathbf{q}}^j \int_{\mathbb{R}^2} w(|\mathbf{r}|) \mathrm{e}^{-\mathrm{i}(\mathbf{k}\cdot\mathbf{r} - \mathbf{q}\cdot R_j(\mathbf{r} - \mathbf{a}_j))} \mathrm{d}\mathbf{r} \\ &= \widehat{w}(\mathbf{k}) + \epsilon \sum_{\mathbf{q}} J_{\mathbf{q}}^j \widehat{w}(\mathbf{k} - R_j^T \mathbf{q}) \mathrm{e}^{-\mathrm{i}\mathbf{q}\cdot R_j \mathbf{a}_j}. \end{aligned} \tag{236}$$

Now $\widehat{w}(\mathbf{k}) = \widehat{w}(|\mathbf{k}|)$, so

$$\widehat{W_j}(\mathbf{k}) = \widehat{w}(|\mathbf{k}|) + \epsilon \sum_{\mathbf{q}} J_{\mathbf{q}}^j \widehat{w}(|\mathbf{k} - R_j^T \mathbf{q}|) \mathrm{e}^{-\mathrm{i}\mathbf{q}\cdot R_j \mathbf{a}_j}. \tag{237}$$

Taking the steady state with a small perturbation $u_j = u_j^0 + c_j \mathrm{e}^{\lambda t} \mathrm{e}^{i\mathbf{k}\cdot\mathbf{r}}$, for $|c_j| \ll 1$, to find the eigensystem,

$$(-\lambda I - A + \Gamma \widehat{W}(\mathbf{k}))c = 0, \tag{238}$$

where $\Gamma_{ij} = \delta_{ij} f'(u_j^0)$ and $c = (c_1, c_2, c_3, c_4)$. Therefore, for non-trivial solutions of c, we need

$$|-\lambda I - A + \Gamma \widehat{W}(\mathbf{k})| = 0. \tag{239}$$

We shall take the model for patchiness to be,

$$M_i(\mathbf{r}) = \frac{1}{3}\left[\cos(\mathbf{q}_1 \cdot R_i(\mathbf{r} - \mathbf{a}_i)) + \cos(\mathbf{q}_2 \cdot R_i(\mathbf{r} - \mathbf{a}_i)) + \cos(\mathbf{q}_3 \cdot R_i(\mathbf{r} - \mathbf{a}_i))\right], \tag{240}$$

with hexagonal patchiness where $\mathbf{q}_1, \mathbf{q}_2, \mathbf{q}_3$ are as in (197-198). This can also be written as,

$$M_j(\mathbf{r}) = \frac{1}{6} \sum_{l=1}^{3} \left[\mathrm{e}^{\mathrm{i}\mathbf{q}_l \cdot R_j(\mathbf{r} - \mathbf{a}_j)} + \mathrm{e}^{-\mathrm{i}\mathbf{q}_l \cdot R_j(\mathbf{r} - \mathbf{a}_j)} \right], \tag{241}$$

with Fourier coefficients,

$$J^j_{\mathbf{q}} = \frac{1}{(2\pi)^2}\frac{1}{6}\sum_{l=1}^{3}\int_{\mathbb{R}^2}\left[\mathrm{e}^{\mathrm{i}\mathbf{q}_l\cdot R_j(\mathbf{r}-\mathbf{a}_j)} + \mathrm{e}^{-\mathrm{i}\mathbf{q}_l\cdot R_j(\mathbf{r}-\mathbf{a}_j)}\right]\mathrm{e}^{-\mathrm{i}\mathbf{q}\cdot R_j(\mathbf{r}-\mathbf{a}_j)}\,\mathrm{d}\mathbf{r} \tag{242}$$

$$= \frac{1}{6}\sum_{l=1}^{3}\frac{1}{(2\pi)^2}\int_{\mathbb{R}^2}\left[\mathrm{e}^{-\mathrm{i}(\mathbf{q}-\mathbf{q}_l)\cdot R_j(\mathbf{r}-\mathbf{a}_j)} + \mathrm{e}^{-\mathrm{i}(\mathbf{q}+\mathbf{q}_l)\cdot R_j(\mathbf{r}-\mathbf{a}_j)}\right]\,\mathrm{d}\mathbf{r} \tag{243}$$

$$= \frac{1}{6}\sum_{l=1}^{3}\left[\mathrm{e}^{\mathrm{i}(\mathbf{q}-\mathbf{q}_l)\cdot R_j\mathbf{a}_j}\delta(R_j^T(\mathbf{q}-\mathbf{q}_l)) + \mathrm{e}^{\mathrm{i}(\mathbf{q}+\mathbf{q}_l)\cdot R_j\mathbf{a}_j}\delta(R_j^T(\mathbf{q}+\mathbf{q}_l)\right]. \tag{244}$$

Where we have used the fact that

$$\frac{1}{(2\pi)^2}\int_{\mathbb{R}^2}\mathrm{e}^{-\mathrm{i}(\mathbf{q}-\mathbf{q}_l)\cdot R_j(\mathbf{r}-\mathbf{a}_j)}\mathrm{d}\mathbf{r} = \mathrm{e}^{\mathrm{i}(\mathbf{q}-\mathbf{q}_l)\cdot R_j\mathbf{a}_j}\delta(R_j^T(\mathbf{q}-\mathbf{q}_l)). \tag{245}$$

This gives the Fourier transform of the patchy connectivity as,

$$\widehat{W_j}(\mathbf{k}) = \widehat{w}(|\mathbf{k}|) + \frac{\epsilon}{6}\sum_{l=1}^{3}\left[\mathrm{e}^{-\mathrm{i}\mathbf{q}_l\cdot R_j\mathbf{a}_j}\widehat{w}(|\mathbf{k}-R_j^T\mathbf{q}_l|) + \mathrm{e}^{\mathrm{i}\mathbf{q}_l\cdot R_j\mathbf{a}_j}\widehat{w}(|\mathbf{k}+R_j^T\mathbf{q}_l|)\right], \tag{246}$$

for shifts $\mathbf{a}_j$ and rotations R_j of the patchiness in each layer.

7.3.2 *Steady State*

From the Turing Analysis, we have a steady state (235). Now, we have,

$$\widehat{W_j}(\mathbf{k}=0) = \frac{\epsilon}{6}\sum_{l=1}^{3}\left[\mathrm{e}^{-\mathrm{i}\mathbf{q}_l\cdot R_j\mathbf{a}_j}\widehat{w}(|R_j^T\mathbf{q}_l|) + \mathrm{e}^{\mathrm{i}\mathbf{q}_l\cdot R_j\mathbf{a}_j}\widehat{w}(|R_j^T\mathbf{q}_l|)\right] \tag{247}$$

$$= \frac{\epsilon}{6}\sum_{l=1}^{3}\left[\mathrm{e}^{-\mathrm{i}\mathbf{q}_l\cdot R_j\mathbf{a}_j} + \mathrm{e}^{\mathrm{i}\mathbf{q}_l\cdot R_j\mathbf{a}_j}\right]\widehat{w}(|R_j^T\mathbf{q}_l|) \tag{248}$$

$$= \frac{\epsilon}{3}\sum_{l=1}^{3}\widehat{w}(|R_j^T\mathbf{q}_l|)\cos(\mathbf{q}_l\cdot R_j\mathbf{a}_j). \tag{249}$$

In our case, $\widehat{w}(|R_j^T\mathbf{q}_l|) = \widehat{w}\left(\frac{4\pi}{\sqrt{3}d}\right)$ for all j and l, as $|\mathbf{q}_l| = \frac{4\pi}{\sqrt{3}d}$ and $|R_j^T\mathbf{q}_l| = |\mathbf{q}_l|$.

We have,

$$\widehat{W_1}(\mathbf{k}=0) = \frac{\epsilon}{3}\widehat{w}\left(\frac{4\pi}{\sqrt{3}d}\right)\left[\cos(2\pi) + \cos(-\pi) + \cos(-\pi)\right]$$

$$= -\frac{\epsilon}{3}\widehat{w}\left(\frac{4\pi}{\sqrt{3}d}\right),$$

$$\begin{aligned}\widehat{W_2}(\mathbf{k}=0) &= \frac{\epsilon}{3}\widehat{w}\left(\frac{4\pi}{\sqrt{3}d}\right)\Big[\cos(-\pi)+\cos(2\pi)+\cos(-\pi)\Big] \\ &= -\frac{\epsilon}{3}\widehat{w}\left(\frac{4\pi}{\sqrt{3}d}\right),\end{aligned}$$

$$\begin{aligned}\widehat{W_3}(\mathbf{k}=0) &= \frac{\epsilon}{3}\widehat{w}\left(\frac{4\pi}{\sqrt{3}d}\right)\Big[\cos(-\pi)+\cos(-\pi)+\cos(2\pi)\Big] \\ &= -\frac{\epsilon}{3}\widehat{w}\left(\frac{4\pi}{\sqrt{3}d}\right),\end{aligned}$$

and

$$\begin{aligned}\widehat{W_4}(\mathbf{k}=0) &= \frac{\epsilon}{3}\widehat{w}\left(\frac{4\pi}{\sqrt{3}d}\right)\Big[\cos(0)+\cos(0)+\cos(0)\Big] \\ &= \epsilon\widehat{w}\left(\frac{4\pi}{\sqrt{3}d}\right).\end{aligned}$$

Therefore, for the steady state we need to solve $G(u_0)=0$ where,

$$G(u) = Au - \widehat{W}f(u), \quad u \in \mathbb{R}^4. \tag{250}$$

7.3.3 *Computational Examples*

Firstly, we considered using the shifts $\mathbf{a}_j$ to make $\sum_{j=1}^{4} M_j(\mathbf{r}) = 0$ with no rotation θ_j so that the patchy connections of each layer overlap as little as possible and the inhibitory and excitatory connections cancel each other out for simplicity. However, when we started to explore the simulations, we found that whilst we expected these shifts to ultimately produce accurate looking OPM's, this was not the case. We then considered no shifts $\mathbf{a}_j = 0$ and just rotation R_j. The hexagonal patchy connections has a rotational symmetry of order 6 and therefore rotations of the form, $\theta_j = 2\pi j/3$ or $\theta_j = 2\pi j/4$ would result in two of the profiles to be identical. Therefore, we then tried the orientation of each layer to be $\theta_j = [2\pi/5, 4\pi/5, 6\pi/5, 0]$ and $\mathbf{a}_j = 0$. The patchy connectivity profiles for each of the following computational plots are shown in Fig. 50.

We will now simulate the multi-layered neural field model (227) with

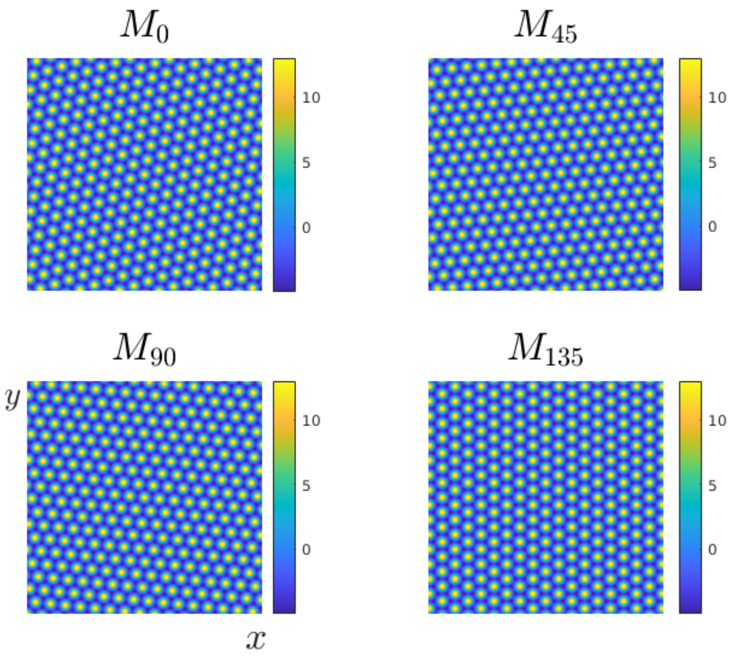

Figure 50.: The choice of patchy connectivity for each layer of the four layer model (227) with the choice of $\theta_j = [2\pi/5, 4\pi/5, 6\pi/5, 0]$ and no shifts, namely $\mathbf{a}_j = 0$, $\forall j$. These are each computed on the domain $[-5\pi, 5\pi] \times [-5\pi, 5\pi]$.

the patchy connections M_j as in Fig. 50. Firstly, we explore the case when $\rho = 0$ to test the theory and code for (227), as this recovers the single layer model that is reproduced four times as there is no connectivity between the layers. Therefore, the four layers of neural activity should be the similar to the activity profiles with patchy hexagonal connectivity seen in Chapter 6. Again, the choice of formula for the connectivity kernel $w(r)$ and firing rate $f(u, \mu, h)$ for this example are (186) and (187) respectively. In general (when $\rho \neq 0$), due to the analysis of the four layer model being more complex, we don't have the same bifurcation calculations as the single layer model and hence have to vary parameters to push the system past bifurcation. The simulation when $\rho = 0$ can be seen in Fig. 52. The code for these computations is provided in Appendix F. The eigenvalues of the system are shown in Fig. 51, this highlights that there are eigenvalues greater than zero to induce pattern formation and the six peaks can be identified due to the patchy hexagonal connectivity.

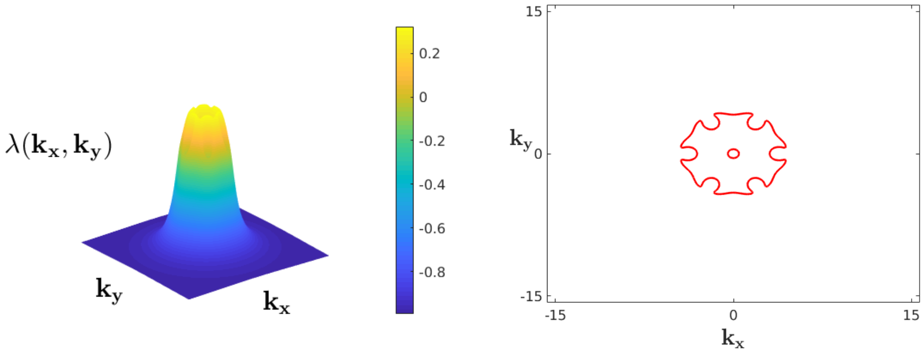

Figure 51.: A computational plot of the eigenvalues of the multi-layer patchy connections model (227) and its zero contour with $\mu = 0.8$, $\epsilon = 12$, $h = 2.1$, $\sigma = 0.6$, $d = 2$, $\rho = 0$ and the patchy connectivity profile is shown in Fig. 50, with the choice of θ_j = $[2\pi/5, 4\pi/5, 6\pi/5, 0]$ and no shifts, namely $\mathbf{a}_j = 0$, $\forall j$. These are computed on the domain $[-5\pi, 5\pi] \times [-5\pi, 5\pi]$.

The resultant neural activity in each layer is shown in Fig. 52. This again shows lines of excitatory and inhibitory cortical activity with similar angles to hexagons, horizontal lines and lines at approximately 60° and 120°. The simulations are started at the steady state u_0 with random noise added and due to being unstable past bifurcation, this results in different patterns of activity with every simulation.

Next, we look at different cases when $\rho \neq 0$ to introduce the connectivity between the layers. For the following plots, the choice of formula for the connectivity kernel $w(r)$ and firing rate $f(u, \mu, h)$ are (186) and (187) respectively. Moreover, the simulations are started at the steady state u_0 with random noise added and due to being unstable past bifurcation, this results in different patterns of activity with every simulation. For the eigenvalues of the system, $\rho \neq 0$ so A is no longer diagonal. Though as ρ is still relatively small and all the other parameters remain the same, the

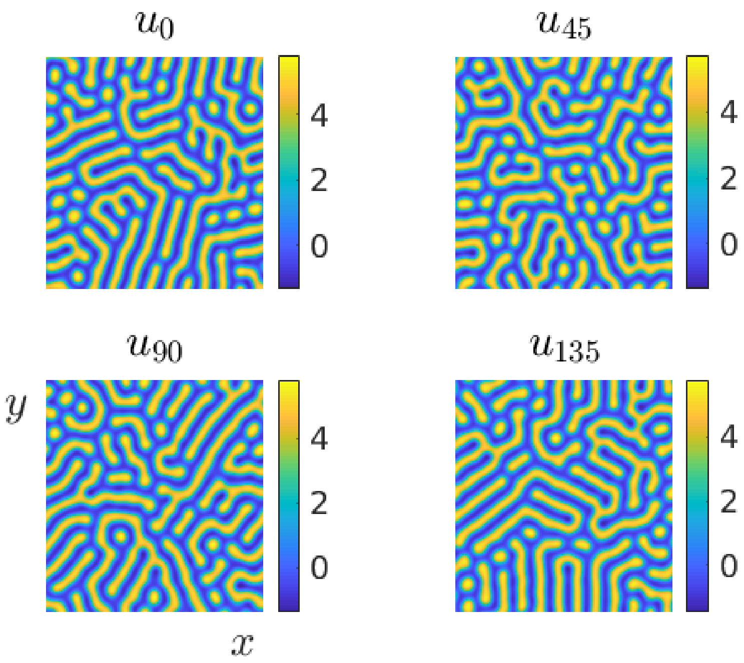

Figure 52.: The neural activity for the four layer patchy connectivity model (227). Computed using the following parameters $\mu = 0.8$, $\epsilon = 12$, $h = 2.1$, $\sigma = 0.6$, $d = 2$, $\rho = 0$ and the patchy connectivity profile is shown in Fig. 50, with the choice of $\theta_j = [2\pi/5, 4\pi/5, 6\pi/5, 0]$ and no shifts, namely $\mathbf{a}_j = 0$, $\forall j$. These are computed on the domain $[-5\pi, 5\pi] \times [-5\pi, 5\pi]$, using the steady state with added random noise as the initial condition for each layer.

spectrum for $\rho = 0.2$ has a similar shape as seen in Fig. 53.

Biologically, there is only weak connection between the layers, so we start at $\rho = 0.01$, Fig. 54. This still looks very similar to $\rho = 0$. To see changes in the patchiness, we look at $\rho = 0.1$ in Fig. 55 and $\rho = 0.2$ in Fig. 56.Activity patterns for increasing ρ show similar features of stripes of activity orientated at 60° and 120° but with decreasing distinction between areas of stripes of each orientation as ρ increases. When using this model to create the OPM, there needs to be the right balance between short and long range connections, as the pinwheels in the OPM need to have a certain density.

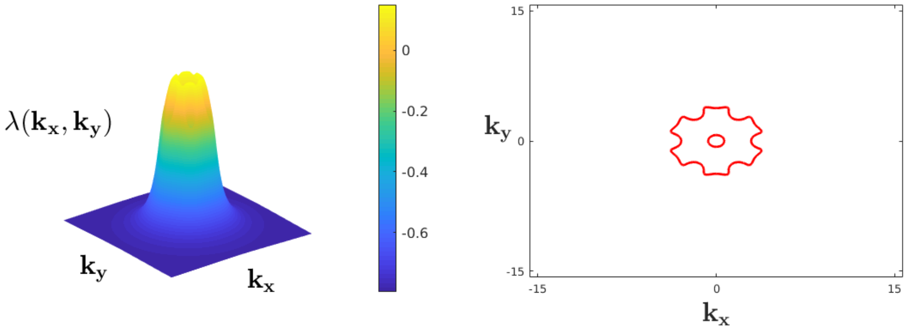

Figure 53.: A computational plot of the eigenvalues of the multi-layer patchy connections model (227) and its zero contour with $\mu = 0.8$, $\epsilon = 12$, $h = 2.1$, $\sigma = 0.6$, $d = 2$, $\rho = 0.2$ and the patchy connectivity profile is shown in Fig. 50, with the choice of $\theta_j = [2\pi/5, 4\pi/5, 6\pi/5, 0]$ and no shifts, namely $\mathbf{a}_j = 0$, $\forall j$. These are computed on the domain $[-5\pi, 5\pi] \times [-5\pi, 5\pi]$.

7.4 ORIENTATION PREFERENCE MAP SIMULATIONS

The methods from [96] to convert four signals of neural activity into one are outlined in section 7.2.3, we will be focusing on using the orientation preference equation (225) to compute the OPM. The code for the activity of the multi-layered patchy neural model being converted to an OPM is provided in Appendix F. Firstly, we compute the OPM using the neural activity with $\rho = 0$ and 0.01 that are presented in Fig. 52 and 54 respectively. The resultant OPMs can be seen in Fig. 57, the neural activity for these plots were highly connected over a long range and this is highlighted with a greater amount of linear regions in the OPM than normally biologically seen. Therefore, we would like to create an OPM from neural activity that has less long range connectivity to highlight the pinwheel structure. The neural activity plots with $\rho = 0.1$ and 0.2 that are presented in Fig. 55 and 56, show a lot of small patches of neural activity and therefore are better suited to create an OPM that has a better pinwheel density. The resultant OPMs for these are seen in Fig. 58 and from visual inspection look a lot

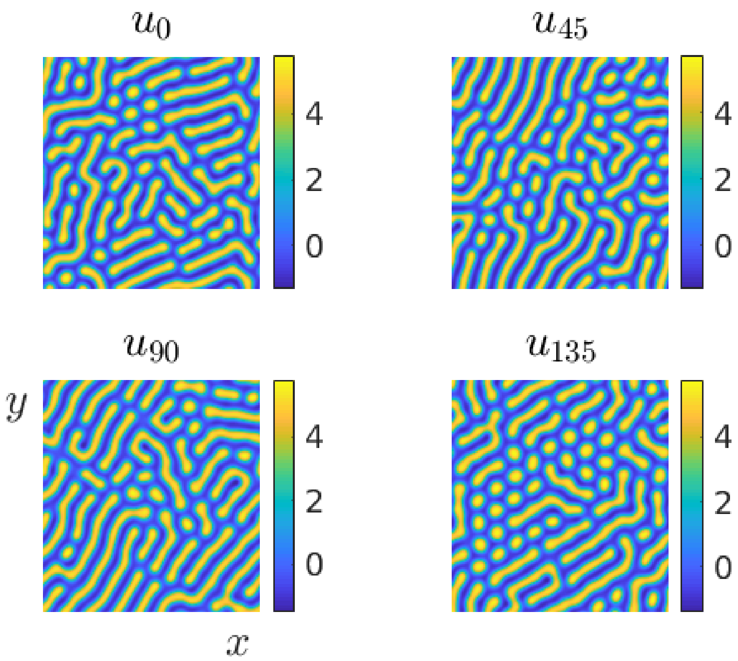

Figure 54.: The neural activity for the four layer patchy connectivity model (227). Computed using the following parameters $\mu = 0.8$, $\epsilon = 12$, $h = 2.1$, $\sigma = 0.6$, $d = 2$, $\rho = 0.01$ and the patchy connectivity profile is shown in Fig. 50, with the choice of $\theta_j = [2\pi/5, 4\pi/5, 6\pi/5, 0]$ and no shifts, namely $\mathbf{a}_j = 0$, $\forall j$. These are computed on the domain $[-5\pi, 5\pi] \times [-5\pi, 5\pi]$, using the steady state with added random noise as the initial condition for each layer.

more like a biological OPM with pinwheel structures and linear regions. The computations were also repeated with the system closer to bifurcation by altering the value of the bifurcation parameter h, using $\rho = 0.2$ and $h = 2.3$. This resulted in the OPM forming similar to the previous example, the pattern formation takes longer to appear but results in the same style of OPM, the neural activity and OPM are shown in Fig. 59. Finally, the computations were repeated with the system far from bifurcation, using $\rho = 0.2$ again and $h = 1.5$. The pattern formation of the neural activity far from bifurcation results in more areas of activity, similar to when ρ is very small or turned off and hence, this again produces an OPM that has

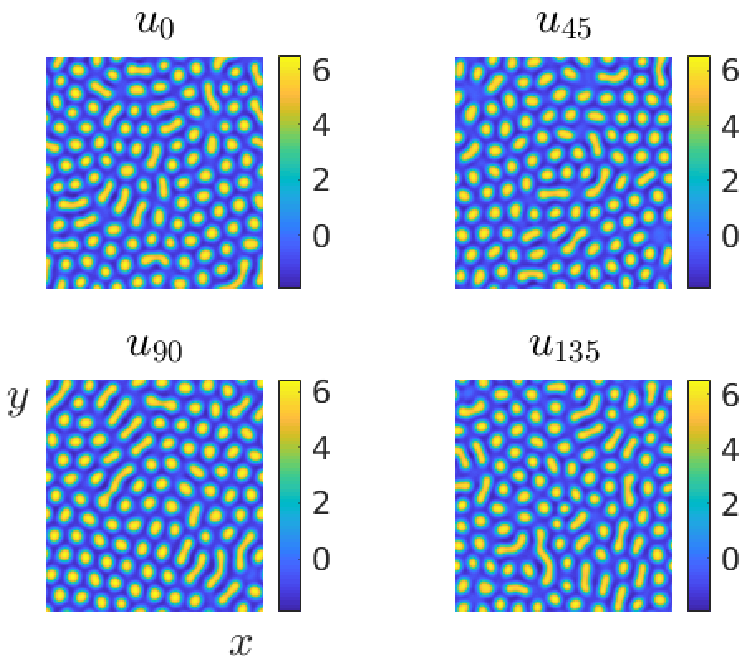

Figure 55.: The neural activity for the four layer patchy connectivity model (227). Computed using the following parameters $\mu = 0.8$, $\epsilon = 12$, $h = 2.1$, $\sigma = 0.6$, $d = 2$, $\rho = 0.1$ and the patchy connectivity profile is shown in Fig. 50, with the choice of θ_j = $[2\pi/5, 4\pi/5, 6\pi/5, 0]$ and no shifts, namely $\mathbf{a}_j = 0$, $\forall j$. These are computed on the domain $[-5\pi, 5\pi] \times [-5\pi, 5\pi]$, using the steady state with added random noise as the initial condition for each layer.

a sparser pinwheel density. The neural activity and OPM for $\rho = 0.2$ and $h = 1.5$, far from bifurcation, is shown in Fig. 60. Therefore, the parameters for the most realistic OPM are $\rho \geq 0.1$ and close to bifurcation, $2 < h < 2.3$.

7.5 SUMMARY

In this chapter, we set out to draw on the patchy connections model we had analysed in the previous chapter, along with the work of a

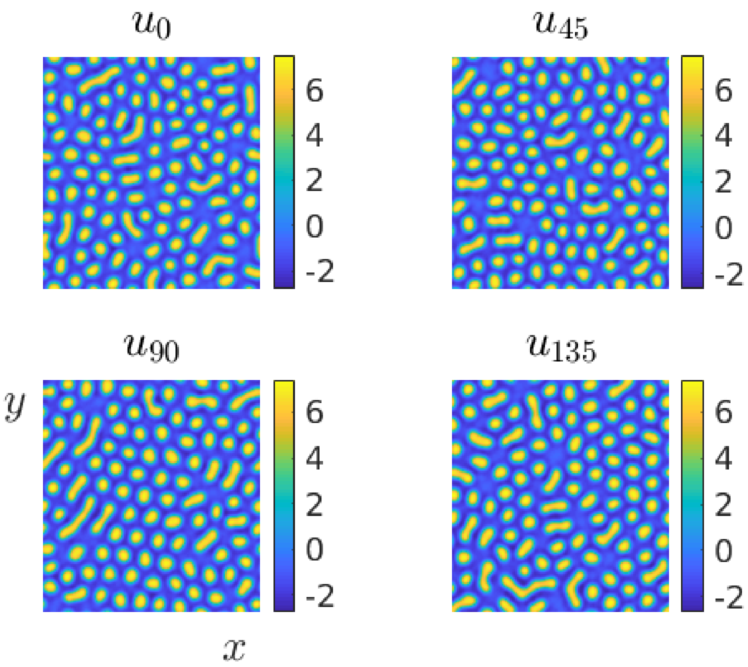

Figure 56.: The neural activity for the four layer patchy connectivity model (227). Computed using the following parameters $\mu = 0.8$, $\epsilon = 12$, $h = 2.1$, $\sigma = 0.6$, $d = 2$, $\rho = 0.2$ and the patchy connectivity profile is shown in Fig. 50, with the choice of $\theta_j = [2\pi/5, 4\pi/5, 6\pi/5, 0]$ and no shifts, namely $\mathbf{a}_j = 0$, $\forall j$. These are computed on the domain $[-5\pi, 5\pi] \times [-5\pi, 5\pi]$, using the steady state with added random noise as the initial condition for each layer.

multi-layered neural field mode by [96], to create our own multi-layered patchy connections model. In turn, we used this model to create an OPM as the structure of an OPM is patchy as well. Having outlined the model of [96] and understood the multi-layered model and also methods used in this paper to combine neural activity for orientation preference; this allowed us to create a multi-layered neural field model for which we performed Turing analysis and which we also computationally simulated. We started with turning off the coupling between the layers to reproduce the patchy connectivity neural activity in four separate layers and confirm our analysis and code. Slowly the connectivity between the layers was turned on to create a patchier neural activity to replicate the OPM pinwheel structure. The patchier activity created an OPM with a higher pinwheel density giving a more biologically sound OPM. The parameter regions in which the OPM can be computed are not tuned and therefore this can be seen as a robust model.

This work has shown a good proof of concept for this model, especially as this is the first known work to extend the patch connectivity model. However, there are limitations to the work. The choice of a Wizard's hat (or Mexican hat) connectivity function for (169), whilst analytically tractable, this is choice is a little limiting and unrealistic. Long-range (beyond a pinwheel's distance away) patchy connections in visual cortex are solely excitatory. But all of the long-range interactions from these choices of connectivity function are through inhibition in the tail of $w(r)$, albeit modulated by M. To extend this work, different choices of connectivity function could be used with excitatory long range connections to create a more realistic model, for example the oscillatory connectivity model from [71]. The change in connectivity may make the analysis either more difficult or unable to be completed so direct simulations and parameter searches may be implemented instead.

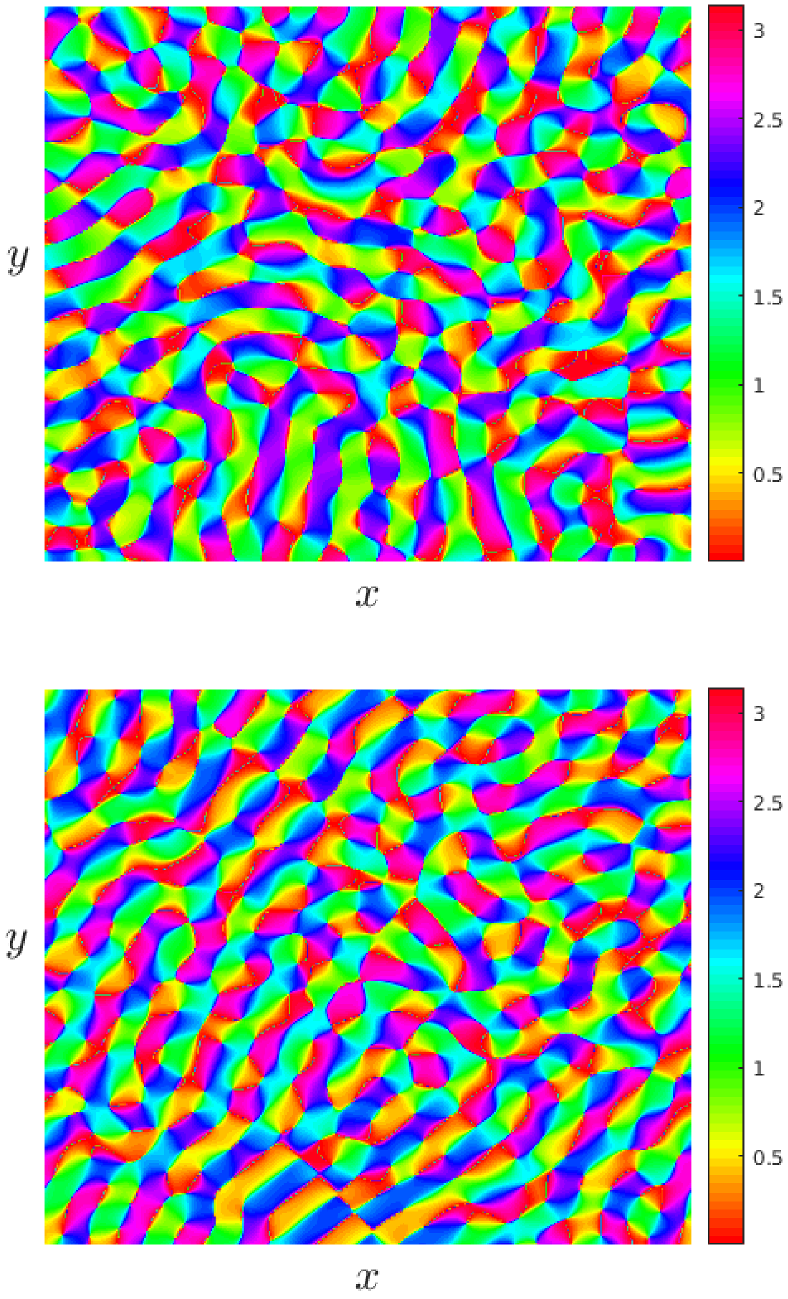

Figure 57.: Orientation preference maps created using the neural activity from the multi-layered patchy connection model (227) for $\rho = 0$ (top) and $\rho = 0.01$ (bottom). Computed using the following parameters $\mu = 0.8$, $\epsilon = 12$, $h = 2.1$, $\sigma = 0.6$, $d = 2$ and the patchy connectivity profile is shown in Fig. 50, with the choice of $\theta_j = [2\pi/5, 4\pi/5, 6\pi/5, 0]$ and no shifts, namely $\mathbf{a}_j = 0$, $\forall j$. These are computed on the domain $[-5\pi, 5\pi] \times [-5\pi, 5\pi]$.

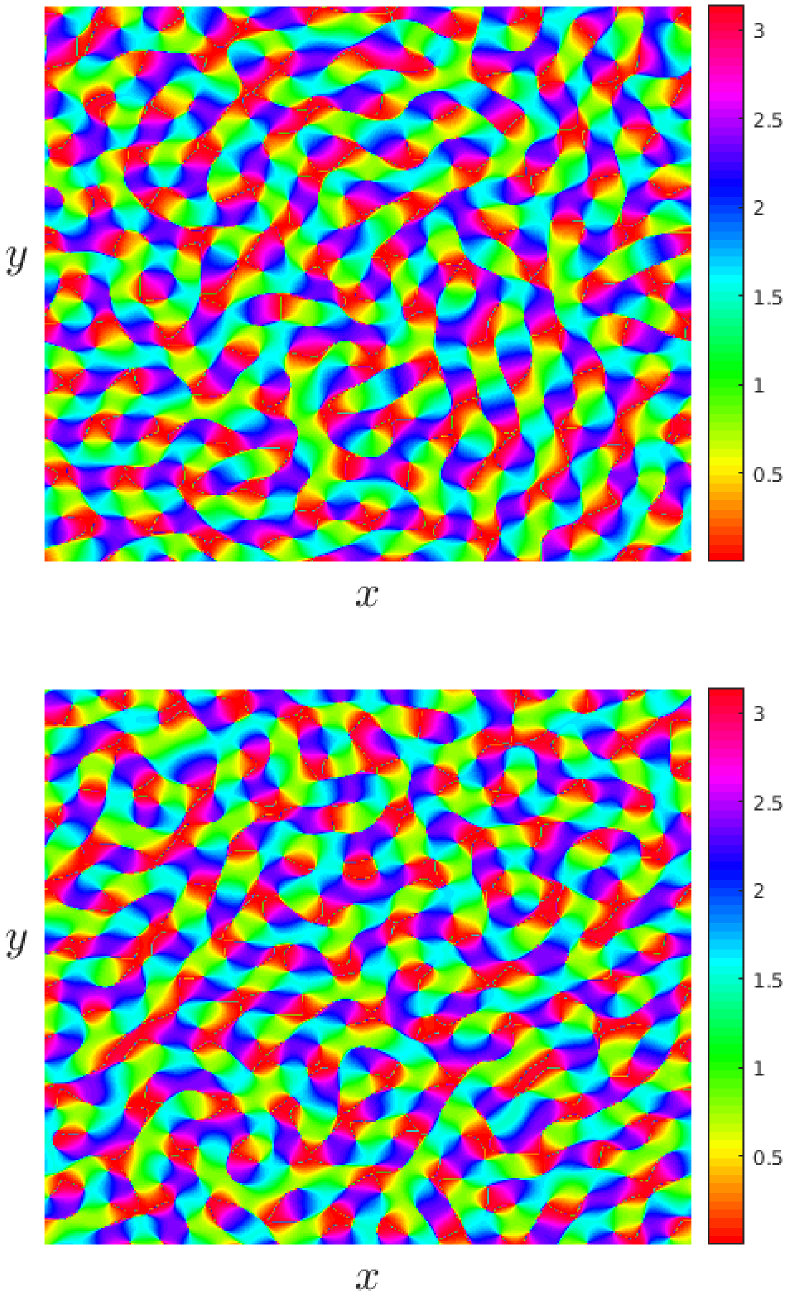

Figure 58.: Orientation preference maps created using the neural activity from the multi-layered patchy connection model (227) for $\rho = 0.1$ (top) and $\rho = 0.2$ (bottom). Computed using the following parameters $\mu = 0.8$, $\epsilon = 12$, $h = 2.1$, $\sigma = 0.6$, $d = 2$ and the patchy connectivity profile is shown in Fig. 50, with the choice of $\theta_j = [2\pi/5, 4\pi/5, 6\pi/5, 0]$ and no shifts, namely $\mathbf{a}_j = 0$, $\forall j$. These are computed on the domain $[-5\pi, 5\pi] \times [-5\pi, 5\pi]$.

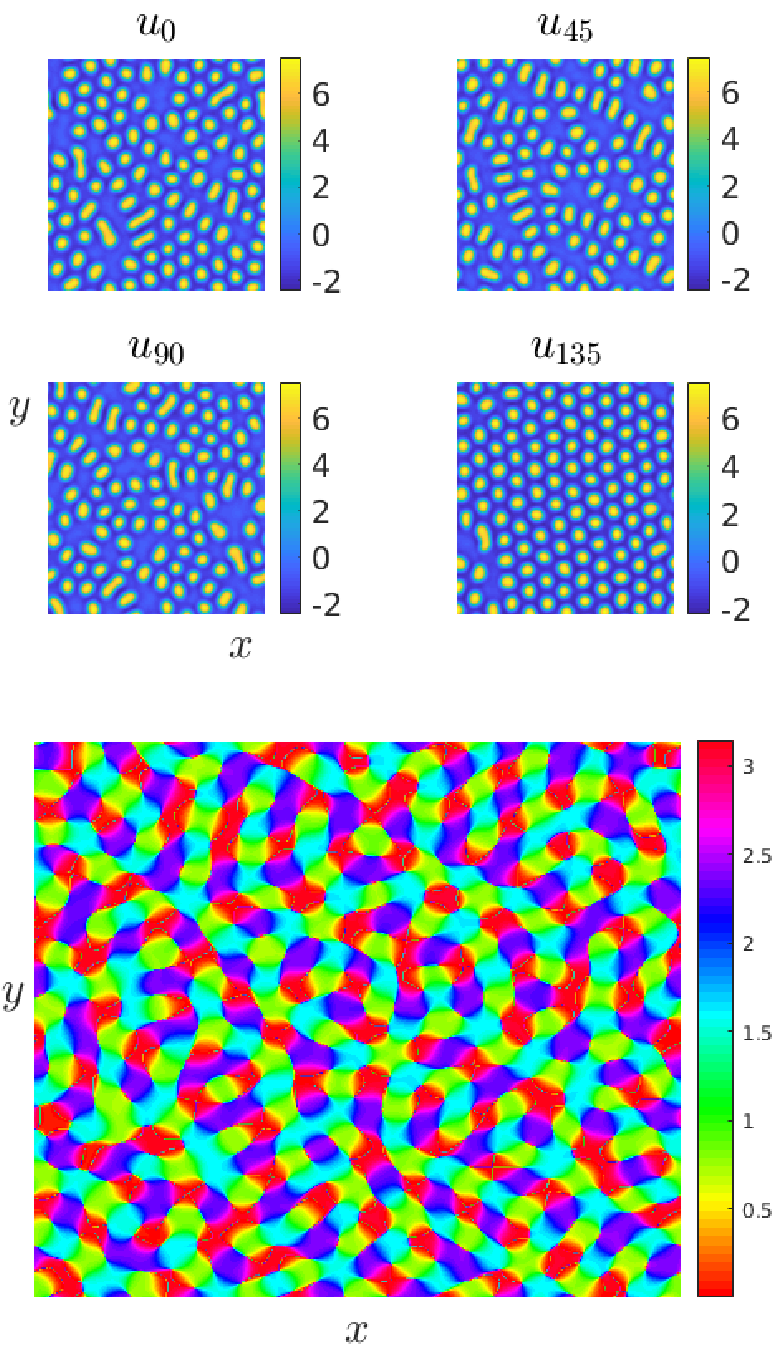

Figure 59.: Neural activity computed by the multi-layered patchy connection model (227) and the resultant orientation preference map for $\rho = 0.2$ and $h = 2.3$, close to bifurcation. Computed using the following parameters $\mu = 0.8$, $\epsilon = 12$, $\sigma = 0.6$, $d = 2$ and the patchy connectivity profile is shown in Fig. 50, with the choice of $\theta_j = [2\pi/5, 4\pi/5, 6\pi/5, 0]$ and no shifts, namely $\mathbf{a}_j = 0$, $\forall j$. These are computed on the domain $[-5\pi, 5\pi] \times [-5\pi, 5\pi]$.

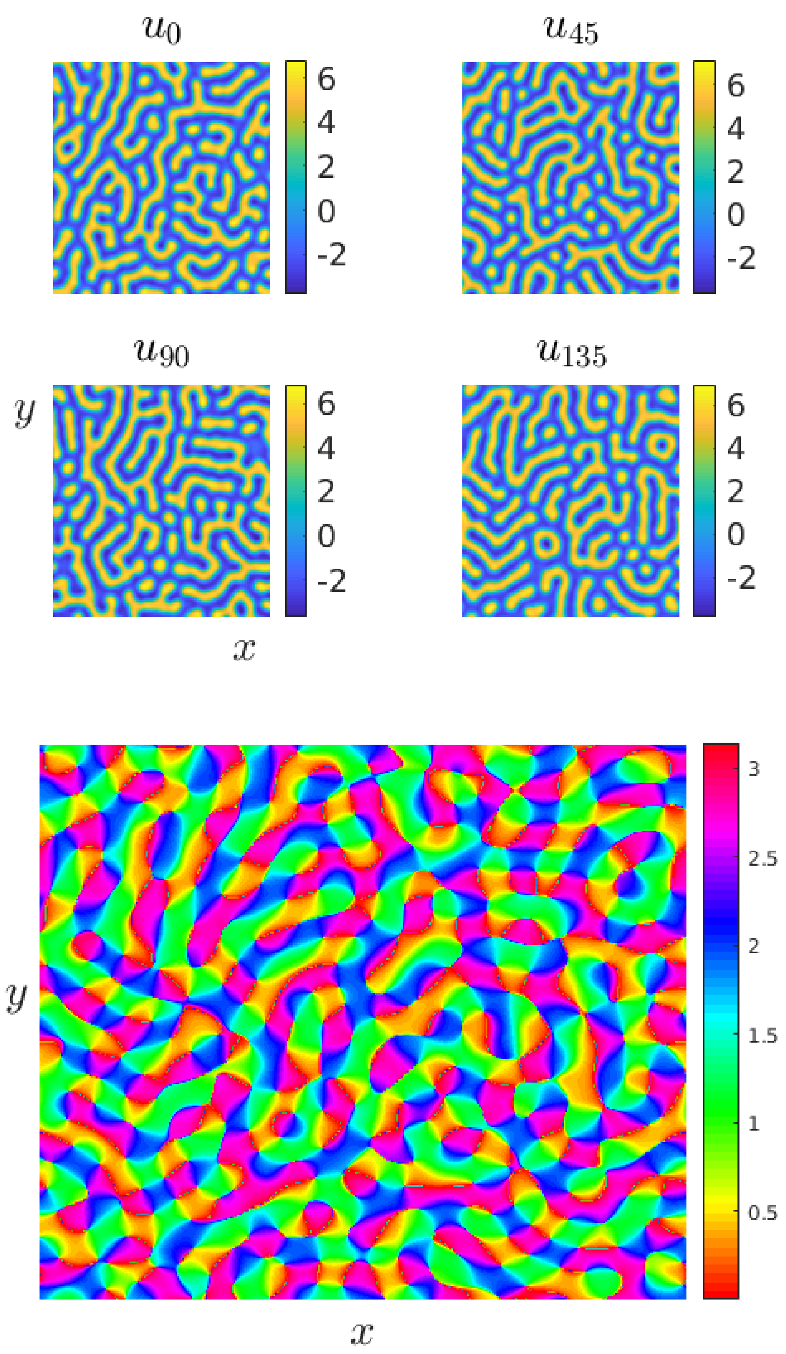

Figure 60.: Neural activity computed by the multi-layered patchy connection model (227) and the resultant orientation preference map for $\rho = 0.2$ and $h = 1.5$, far from bifurcation. Computed using the following parameters $\mu = 0.8$, $\epsilon = 12$, $\sigma = 0.6$, $d = 2$ and the patchy connectivity profile is shown in Fig. 50, with the choice of $\theta_j = [2\pi/5, 4\pi/5, 6\pi/5, 0]$ and no shifts, namely $\mathbf{a}_j = 0$, $\forall j$. These are computed on the domain $[-5\pi, 5\pi] \times [-5\pi, 5\pi]$.

8

CONCLUSION

To conclude the work in this thesis, we first start by reviewing the main results presented. Finally, we provide ideas for future exploration based on this work.

8.1 SUMMARY OF THESIS

There were two main aims of this thesis; the first was to create a neural field model to replicate the phenomena of the hallucinations observed by Billock and Tsou in [10]. The second was to introduce patchy connectivity into a neural field model and generate an orientation preference map.

After an overview of the thesis, we started by exploring the biological background of vision in chapter 2, this was accompanied by an introduction to neural field models, first exploring the standard neural field model and then looking at different approaches to extend it. In chapter 3, we introduced the work of Billock and Tsou [10] on sensory induced hallucinations that observed a counter-intuitive psychophysical phenomena. After explored this psychological study, we then introduced the Swift-Hohenburg equation that could be driven to give an orthogonal response of activity. We wanted to utilize similar analysis techniques used by [81] on the Swift-Hohenburg model with spatial forcing to create our own driven system. This then brought us to the point at which we could introduce a forced neural field model in chapter 4. We analysed this model, firstly in one dimension and then two, by deriving the amplitude equations for pattern formation past bifurcation. This provided us with parameter regimes in which we could position the system to model the induced perpendicular activity seen in the neural activity induced by the psychophysical observations. Whilst the work in chapter 4 provided stationary models of the hallucinations, the observed psychophysical phenomena included movement. We did this by extending the neural field to include adaptation as this allows for travelling waves to form past bifurcation. This made the derivation of amplitude equations more complex, so we only calculated them in one dimension and used this as a starting point for the two dimensional simulations. The numerical simulations of the full nonlinear model were shown to be consistent with the psychophysical observations.

Having concluded the first aim of the thesis in chapter 5, we moved onto the second. In chapter 6, we introduced the concept of patchy connectivity, breaking the homogeneity of the standard model used to create a connectivity profile that is more biologically accurate. After starting with a square lattice, we then changed to a hexagonal one, which again is more in tune with the actual structure of visual cortex. Furthermore, by including a parameter to control the strength of the patchiness, this gave us more control over the model. For all of these versions of the model, we performed Turing analysis and simulate neural activity using the patchy connectivity. The aim of the work in chapter 7 is to define a simple connectivity rule that can lead to spontaneous pattern formation of a realistic orientation preference map via a Turing instability. We reviewed the work performed by Rankin and Chavane in [96] on a multi-layered model with orientation preference which also provides methods for combining multiple layers into one VSD-like signal. After summarising of their work, we used similar principles in our multi-layer model. We performed simulations of the multi-layer model, beyond Turing instability, using different strengths of coupling between layers and using patchy connectivity in preference to the learned connectivity used in [96]. Once the activity of the four layers had been combined into one signal the orientation preference map was generated. This was completed again with different strengths of coupling and also close and far away from bifurcation. The orientation preference map was observed to be biologically plausible for multiple parameters indicating that the model is robust. This completed the second aim of the thesis in creating an orientation preference map from a neural field model.

8.2 DISCUSSION OF EXTENSIONS TO THIS THESIS

The work in this thesis provided interesting results for modelling illusory phenomena and patchy connectivity especially with respect to orientation preference. There are many directions in which this could be extended and we will discuss a few of these in this last section, focusing mainly on other types of illusory phenomena that could be modelled, direct extensions of the generation of the orientation preference map and a transcranial magnetic stimulation experiment that could involve patchy connections.

8.2.1 *Illusory phenomena*

In chapter 4 and 5, we focused on the analysis of simple spatially repetitive and time-independent stimuli. Interestingly, since the work of MacKay in the 1950s, it has been well known that relatively simple patterns of regular stimuli, such as radial lines or concentric rings, are enough to induce illusory motion at right angles to those of the stimulus pattern [80]. Many of these phenomena are amenable to further study using the tools of psychophysics. Even simple variants of such patterns, such as the

Enigma, created by pop-artist Isia Léviant [79], consisting of concentric annuli on top of a pattern of radial spokes, can lead to very striking illusory motion percepts; this illusion is shown in Fig. 61. It is a similar concept to the hallucinations seen by Billock and Tsou in [10] and the work performed on these could be extended to cover this illusion too. Future work could consider input patterns with more spatial structure and explore the conditions for the emergence of global illusory percepts from local interactions, such as the Barber pole, Fig. 62, Rotating snakes, Fig. 63, Café wall, Fig. 64, and Fraser Wilcox spiral, Fig. 65, in which local orientation differences lead to the appearance of the global rotation of contours (see [66] for further examples). All of these illusions are based on similar concepts to the hallucinations we studied and the work presented here could be extended to model these too.

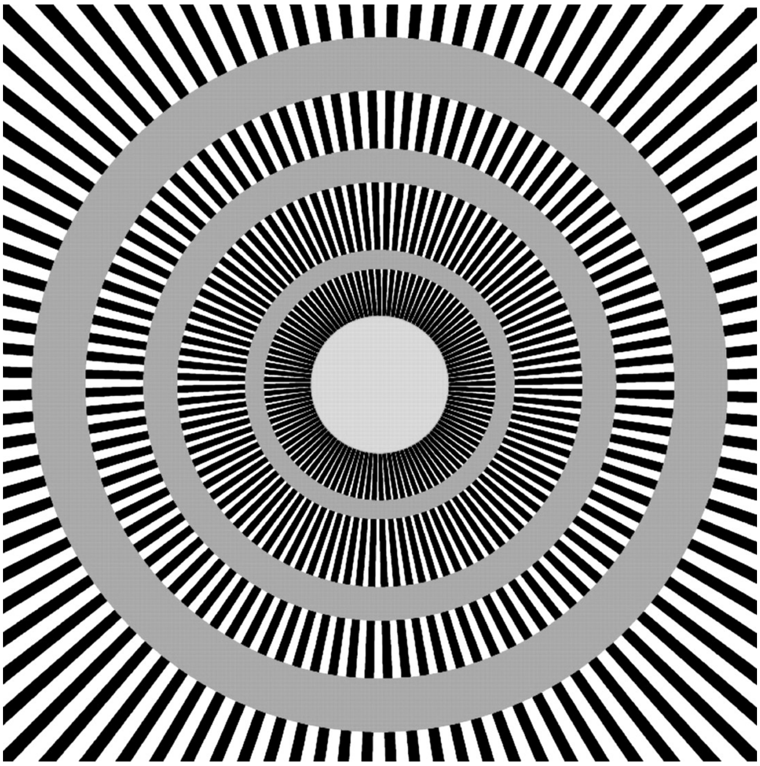

Figure 61.: A gray-scale image based on Enigma adapted from [76], the hallucinatory effect perceived is rotatory movement in the grey circles bound by fan arms. An example of a visual hallucination that could be modelled using an extension of chapter 4 and 5.

Figure 62.: The Barber pole illusion adapted from [66], when moved up and down the stripes appear to move laterally. An example of a visual hallucination that could be modelled using an extension of chapter 4 and 5.

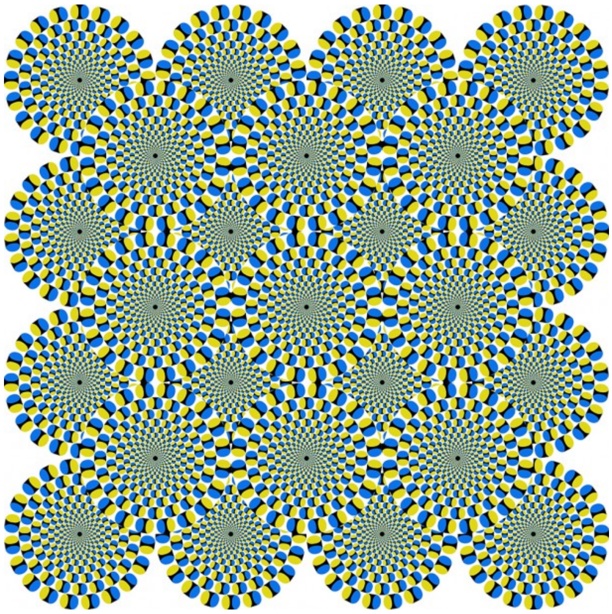

Figure 63.: The rotating snakes illusion adapted from [66], the perception being rotatory movement of the outer parts of the circles in the periphery of the visual field. An example of a visual hallucination that could be modelled using an extension of chapter 4 and 5.

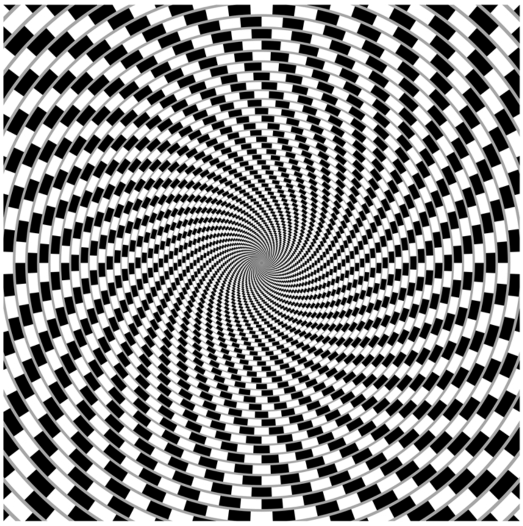

Figure 64.: The Café wall illusion adapted from [66], this illusion is created from superimposing fans and results in grey lines appearing to form spirals. An example of a visual hallucination that could be modelled using an extension of chapter 4 and 5.

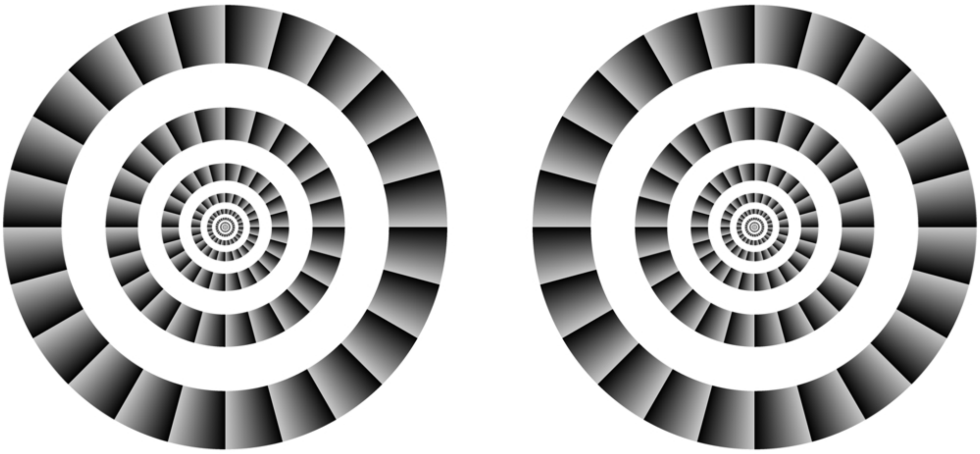

Figure 65.: The Fraiser Wilcox illusion adapted from [66], a combination of spirals and fans to illicit illusory movement. An example of a visual hallucination that could be modelled using an extension of chapter 4 and 5.

Moreover, given that periodic and quasi-crystal patterns in physical (Faraday) systems can be excited by periodic temporal forcing [101], this motivates a further study of associated behavior in neural models. It is known that fullfield flickering visual stimulation in humans can produce geometric hallucinations in the form of radial or spiral arms (and conversely that brain rhythms at the flicker frequency can be enhanced with the presentation of static radial or spiral arms) [83]. Indeed, flicker induced hallucinations have previously been studied from a theoretical perspective in neural fields with time periodic forcing by Rule, Stoffregen, and Ermentrout [102], and it would be very natural to extend the work here to include models of spatio-temporal sensory drive, and in particular to further understand visual hallucinations induced by flicker constrained to a thin annulus centered on the fovea [90]. Another natural extension is to extend very recent work on undriven neural fields that shows how quasi-crystal patterns can arise via a Turing instability [44] to further include spatio-temporal forcing.

8.2.2 *Direct Extensions to the Generation of the Orientation Preference Map*

For the orientation preference generated in chapter 7, we only appraised how realistic they were visually. However, there are methods that one could do to extend this work to confirm whether these are realistic OPM's numerically as well. These methods are seen in [96], which have been taken from the Supplementary Material of [62], here the spectral power as a function of the radial wave number of a synthetic OPM is plotted to show the length scale. Also, properties like pinwheel density, polarity etc which would be important in determining how realistic the OPM plots are. Finally there are also many other parameters that can be explored, for the patchy model that includes ϵ, this had to be made quite large for the same patterns as the previous models to appear. Perhaps, altering other parameters such as d and σ could mean that this does not have to be made quite so large. Furthermore, different choices of connectivity function could be used with excitatory long range connections to create a more realistic model, for example the oscillatory connectivity model from [71]. Finally, we have only considered a four layer model, the work of [56] shows that the neurons responding to a certain orientation preference changed every 10 degrees on average. Therefore, ideally would be modelled as roughly 18 different orientations; however, this may be computationally heavy so the number of layers could be extended incrementally up to 18.

8.2.3 *Transcranial Magnetic Stimulation Effects on the Orientation Preference Map*

Transcranial magnetic stimulation (TMS) is a clinical method that has the ability to modify cortical processing. Unspecific TMS stimulation can result in specific neuronal reorganisation; this includes large-scale remodelling of primary visual cortex (V1), a mature functional architecture that is usually fixed. The cause of the functional changes that are induced by TMS are still quite unknown as the current recording methods such as fMRI, MEG and EEG are either incompatible with the magnetic field required for TMS or do not have the necessary spatiotemporal resolution to be able to show the changes. The work of [69] studies how TMS-induced neuronal plasticity allows temporary orientation specific remodelling of visual cortical maps. The study [69] uses voltage sensitive dye (VSD) to give real-time optical imaging to track the functional changes that occur in the OPM after high frequency TMS is applied to the V1 on a mm^2 scale. This creates a temporary increase in excitability of the cortex which gives a time window of several hours for enhanced plasticity for the architecture of the visual feature maps to be remodelled or trained. The overall outcome of the study shows that if visual stimulation of a single orientation occurs after high frequency TMS, this leads to enlarged imprinting of the chosen stimuli orientation on the OPM in V1.

First, summarising the approach in [69], VSD imaging is used to acquire the OPM before the procedure. The experiment starts with 30 minutes of 10 Hz TMS situated 5 to 10 mm over the occipital cortex. The OPM is then evaluated directly after TMS again. Visual stimulation of prolonged overexposure to a single orientation grating with counterphase flickering occurs for the next 30 minutes. After waiting over 60 minutes from the end of the visual stimulation, to ensure that the adaptation effects stabilise, the OPM is acquired a final time using VSD. This was repeated for 8 different orientations in 22.5° steps. Placebo experiments involving no TMS were also carried out to ensure the results were due to the TMS and not the VSD or visual stimulation alone. The VSD imaging acquired the OPMs by computing the vector sum of the responses at each pixel. Before the experiment the OPMs had a typical layout of regular representation of orientations around pinwheel centres, see left OPMs in Fig. 66. Immediately after the TMS the OPMs show the same structure; however, the reproducibility of the OPM was strongly reduced, with neurons not responding as strongly to their preferred orientation. The excited cortical state with weakened inhibition and decreased orientation selectivity is grounds for the plastic remodelling of the OPM. After the 30 minutes of visual stimulation and at least 60 minutes of waiting for the changes to stabilise, the OPM acquired is dominated by the stimulated orientation. Across all of the experiments, there was a 19.0% increase in the orientation of the stimuli (± 4.0% standard error of the mean). The increase in orientation was from a systematic shift in orientation preference with a larger shift in neighbouring orientation domains of ±45° and is not random. Furthermore, after the remodelling the neurons, especially those with a new orientation preference, show consistent orientation tuning. These results were stable for up to 6 hours after the visual stimulation. The sham experiments showed no change. The experiment was also repeated using 1 Hz TMS; in previous literature this has shown to be dominantly suppressive and therefore should not result in any remodelling, it should in fact stabilise the OPM. There was no shift in the OPM, thus proving that the remodelling is specifically facilitated by high frequency TMS.

There is still debate in the literature on how the TMS induced remodelling of the OPM is facilitated. The first proposal is that it promotes existing essential connectivity by unmasking undeveloped inhibitory connections; the other being that it incorporates plastic changes across thalamic afferents. Therefore, one could use the work in chapter 6 and 7 to try and produce the overexposure results of the TMS experiment by developing plasticity rules that act on the firing threshold, to mimic the known effects of the TMS on excitability. Furthermore, this work could be used to explore how patchy connections between the neurons would be a key principle into how the TMS-remodelling occurs. By changing parameters and completing parameter searches, the parameters required to show the phenomena could be found. By using insight from anatomical behaviour and the behaviour occurring due to TMS, this could decide which parameters are best to change. However, whilst we have some insight, this may not always give the desired results so working with a multitude of different parameter changes could be required to get the best result. Our initial ideas are to change the firing rate threshold of the model both globally and for the individual orientations. From there we could also look at only allowing one orientation in the input and also changing the strength of connectivity to give the model net excitation or for it to be balanced with regards to inhibition and excitation.

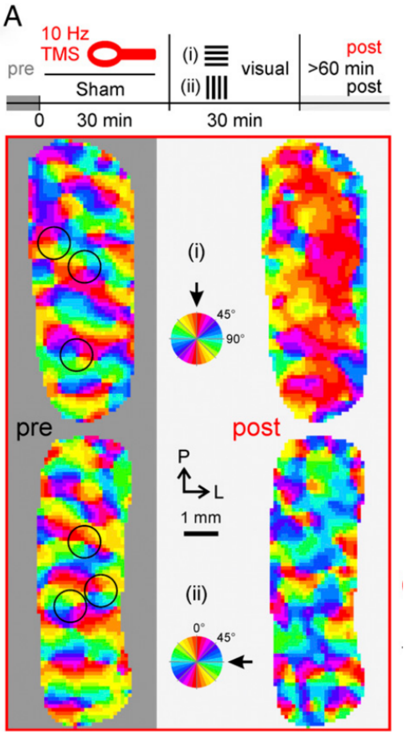

Figure 66.: Remodelling of the orientation preference map after 30 minutes of 10Hz TMS, then passive visual stimulation for 30 minutes. The coloured pixels represent the orientation tuning of the neuron $>$ 60 minutes after the stimulation. The top part of the figure shows the experimental process. Two different orientations are used for the stimulation, i) 0° and ii) 90°. The bottom part shows the orientation preference map averaged over 8-17 trials pre and post experiment. Examples of pinwheel structures are circled in black. The axis is P and L, posterior and lateral. Figure adapted from [69].

A

USEFUL RESULTS AND DERIVATIONS FOR CHAPTER 4

A.1 DERIVATION OF ONE DIMENSIONAL AMPLITUDE EQUATIONS

$$\langle \mathrm{e}^{ik_0x}, \mathcal{L}u_3 \rangle = 0, \tag{251}$$

$$\langle \mathrm{e}^{ik_0x}, \frac{\partial u}{\partial \tau} \rangle = \frac{\partial A}{\partial \tau}, \tag{252}$$

$$\langle \mathrm{e}^{ik_0x}, 2\beta_2 w \otimes u_1 u_2 \rangle = 2\beta_2 \widehat{w}(k_0) d_0 A|A|^2, \tag{253}$$

$$\langle \mathrm{e}^{ik_0x}, \beta_3 w \otimes u_1^3 \rangle = 3\beta_3 \widehat{w}(k_0) A|A|^2, \tag{254}$$

$$\langle \mathrm{e}^{ik_0x}, \delta w \otimes u_1 \rangle = \delta \widehat{w}(k_0) A, \tag{255}$$

$$\langle \mathrm{e}^{ik_0x}, \frac{1}{2}\beta_c W^{xx} \otimes \partial_{\chi\chi} u_1 \rangle = \frac{1}{2}\beta_c \widehat{W}^{xx}(k_0) \frac{\partial^2 A}{\partial \chi^2}, \tag{256}$$

$$\langle \mathrm{e}^{ik_0x}, \beta_2 W^x \otimes \partial_\chi u_1^2 \rangle = 0, \tag{257}$$

$$\langle \mathrm{e}^{ik_0x}, \beta_c W^x \otimes \partial_\chi u_2 \rangle = (1 - \delta_{n,2}) \frac{\overline{\gamma_1}}{2} \beta_c \widehat{W}^x(k_0) \alpha_- \mathrm{e}^{-2ivx} \partial_\chi A^* \delta_{n,2} = 0, \tag{258}$$

$$\langle \mathrm{e}^{ik_0x}, \gamma_2 u_1 \cos k_f x \rangle = \frac{\gamma_2}{2} A^* \mathrm{e}^{-2i\nu x} \delta_{n,2} = \frac{\gamma_2}{2} A^* \mathrm{e}^{-2ic\chi} \delta_{n,2}, \tag{259}$$

$$\begin{aligned} \langle \mathrm{e}^{ik_0x}, \gamma_1 u_2 \cos k_f x \rangle &= (1 - \delta_{n,2}) \left(\frac{\overline{\gamma_1}}{2} \right)^2 \left[(d_+ + d_-) A + \delta_{n,1} d_- A^* \mathrm{e}^{-2i\nu x} \right] \\ &= (1 - \delta_{n,2}) \left(\frac{\overline{\gamma_1}}{2} \right)^2 \left[(d_+ + d_-) A + \delta_{n,1} d_- A^* \mathrm{e}^{-2ic\chi} \right]. \end{aligned} \tag{260}$$

A.2 DERIVATION OF TWO DIMENSIONAL AMPLITUDE EQUATIONS

A.2.1 *Solving the equations*

We note that

$$\langle \mathrm{e}^{i(k_x x + k_y y)}, \mathcal{L}_g u_2 \rangle = 0, \quad \langle \mathrm{e}^{i(k_x x + k_y y)}, \beta_2 w \otimes u_1^2 \rangle = 0, \tag{261}$$

$$\langle \mathrm{e}^{i(k_x x + k_y y)}, \beta_c (W^x \otimes \partial_\chi + W^y \otimes \partial_Y) u_1 \rangle = 0, \tag{262}$$

$$\langle \mathrm{e}^{i(k_x x + k_y y)}, \gamma_1 u_1 \cos k_f x \rangle = \begin{cases} 0 & n \neq 2 \\ \frac{\gamma_1}{2} B^* \mathrm{e}^{-2i\nu_1 x} & n = 2 \end{cases}, \tag{263}$$

and hence the solvability condition is automatically satisfied for all $n \neq 2$ and for $n = 2$ we must set $\gamma_1 = 0$. We write $\gamma_1 = (1 - \delta_{n,2})\overline{\gamma}_1$. We find a particular solution u_2 by assuming that it has the form of $u_1^2 + (1 - \delta_{n,2})\overline{\gamma}_1 u_1 \cos(k_f x)$, substituting into (67) and balancing terms. For our balanced kernel where $\widehat{w}(0) = 0$ we find that the particular solution of u_2, therefore is,

$$\begin{aligned} u_2 = z_1 \big(& A^2 \mathrm{e}^{2i(k_x x + k_y y)} + A^{*2} \mathrm{e}^{-2i(k_x x + k_y y)} + B^2 \mathrm{e}^{2i(k_x x - k_y y)} + B^{*2} \mathrm{e}^{-2i(k_x x - k_y y)} \big) \\ & + z_2 \left(AB \mathrm{e}^{2ik_x x} + A^* B^* \mathrm{e}^{-2ik_x x} \right) + z_3 \left(AB^* \mathrm{e}^{2ik_y y} + A^* B \mathrm{e}^{-2ik_y y} \right) \\ & + \frac{\overline{\gamma_1}}{2} (1 - \delta_{n,2}) \Big[z_+ \Big(A \mathrm{e}^{i(k_x x + k_y y + k_f x)} + B \mathrm{e}^{i(k_x x - k_y y + k_f x)} \\ & \qquad + A^* \mathrm{e}^{-i(k_x x + k_y y + k_f x)} + B^* \mathrm{e}^{-i(k_x x - k_y y + k_f x)} \Big) \\ & \qquad + z_- \Big(A \mathrm{e}^{i(k_x x + k_y y - k_f x)} + B \mathrm{e}^{i(k_x x - k_y y - k f_x)} \\ & \qquad\qquad + A^* \mathrm{e}^{-i(k_x x + k_y y - k_f x)} + B^* \mathrm{e}^{-i(k_x x - k_y y - k_f x)} \Big) \Big], \end{aligned} \tag{264}$$

where

$$z_1 = \frac{\beta_2 \widehat{w}(2k_0)}{1 - \beta_c \widehat{w}(2k_0)}, \quad z_2 = \frac{2\beta_2 \widehat{w}(2k_x)}{1 - \beta_c \widehat{w}(2k_x)}, \quad z_3 = \frac{2\beta_2 \widehat{w}(2k_y)}{1 - \beta_c \widehat{w}(2k_y)},$$

$$k_\pm = \sqrt{(k_x \pm k_f)^2 + k_y^2}, \quad z_\pm = \frac{1}{1 - \beta_c \widehat{w}(k_\pm)}.$$

We now use this in the solvability conditions for u_3 where we find the following projections:

$$\langle \mathrm{e}^{i(k_x x+k_y y)}, \mathscr{L}u_3\rangle = 0, \tag{265}$$

$$\langle \mathrm{e}^{i(k_x x+k_y y)}, \frac{\partial u}{\partial \tau}\rangle = \frac{\partial A}{\partial \tau}, \tag{266}$$

$$\langle \mathrm{e}^{i(k_x x+k_y y)}, \delta w \otimes u_1\rangle = \delta \widehat{w}(k_0)A, \tag{267}$$

$$\langle \mathrm{e}^{i(k_x x+k_y y)}, 2\beta_2 w \otimes u_1 u_2\rangle = 2\beta_2 \widehat{w}(k_0)[z_1|A|^2A + (z_2+z_3)|B|^2A], \tag{268}$$

$$\langle \mathrm{e}^{i(k_x x+k_y y)}, \beta_3 w \otimes u_1^3\rangle = 3\beta_3 \widehat{w}(k_0)\left[|A|^2A + 2|B|^2A\right], \tag{269}$$

$$\langle \mathrm{e}^{i(k_x x+k_y y)}, \frac{1}{2}\beta_c W^{xx} \otimes \partial_{\chi\chi} u_1\rangle = -\frac{1}{2}\beta_c \widehat{w}''(k_0)\frac{\partial^2 A}{\partial \chi^2}, \tag{270}$$

$$\langle \mathrm{e}^{i(k_x x+k_y y)}, \frac{1}{2}\beta_c W^{yy} \otimes \partial_{\mathrm{YY}} u_1\rangle = -\frac{1}{2}\beta_c \widehat{w}''(k_0)\frac{\partial^2 A}{\partial \mathrm{Y}^2}, \tag{271}$$

$$\langle \mathrm{e}^{i(k_x x+k_y y)}, \gamma_2 u_1 \cos k_f x\rangle = \frac{\gamma_2}{2}B^*\mathrm{e}^{-2i\nu_1 x}\delta_{n,2}, \tag{272}$$

$$\langle \mathrm{e}^{i(k_x x+k_y y)}, \overline{\gamma_1}(1-\delta_{n,2})u_2 \cos k_f x\rangle = \left(\frac{\overline{\gamma_1}}{2}\right)^2 (1-\delta_{n,2})\left[(z_+ + z_-)A + z_- B^*\mathrm{e}^{-2i\nu_1 x}\delta_{n,1}\right]. \tag{273}$$

and similarly for the other mode.

Therefore, with the scaling $\nu_1 = \epsilon c_1$, so $\mathrm{e}^{-2i\nu_1 x} = \mathrm{e}^{-2ic_1\chi}$, the projections give the evolution of the amplitude as,

$$\frac{\partial A}{\partial \tau} = \widehat{w}(k_0)\left(\delta A - \Phi_1|A|^2A - \Phi_2|B|^2A\right) - \frac{\beta_c}{2}\widehat{w}''(k_0)\left(\frac{\partial^2 A}{\partial \chi^2} + \frac{\partial^2 A}{\partial \mathrm{Y}^2}\right) + \frac{\gamma_2}{2}B^*\mathrm{e}^{-2ic_1 x}\delta_{n,2} + \left(\frac{\overline{\gamma_1}}{2}\right)^2 (1-\delta_{n,2})\left[(z_+ + z_-)A + z_- B^*\mathrm{e}^{-2i\nu_1 x}\delta_{n,1}\right], \tag{274}$$

and

$$\frac{\partial B}{\partial \tau} = \widehat{w}(k_0)\left(\delta B - \Phi_1|B|^2B - \Phi_2|A|^2B\right) - \frac{\beta_c}{2}\widehat{w}''(k_0)\left(\frac{\partial^2 B}{\partial \chi^2} + \frac{\partial^2 B}{\partial \mathrm{Y}^2}\right) + \frac{\gamma_2}{2}A^*\mathrm{e}^{-2ic_1 x}\delta_{n,2} + \left(\frac{\overline{\gamma_1}}{2}\right)^2 (1-\delta_{n,2})\left[(z_+ + z_-)B + z_- A^*\mathrm{e}^{-2i\nu_1 x}\delta_{n,1}\right], \tag{275}$$

where

$$\Phi_1 = -2\beta_2 z_1 - 3\beta_3 \text{ and } \Phi_2 = -2\beta_2(z_2+z_3) - 6\beta_3. \tag{276}$$

These now needs to be rescaled back to the original time and space variables. We take,

$$a = \epsilon A e^{ic_1 X}, \quad b = \epsilon B e^{ic_1 X} b, \tag{277}$$

and

$$\frac{\partial}{\partial \tau} = \frac{1}{\epsilon^2}\frac{\partial}{\partial t}, \quad \frac{\partial}{\partial \chi} = \frac{1}{\epsilon}\frac{\partial}{\partial x}, \quad \frac{\partial}{\partial \chi^2} = \frac{1}{\epsilon^2}\frac{\partial}{\partial x^2}, \quad \frac{\partial}{\partial \mathrm{Y}} = \frac{1}{\epsilon}\frac{\partial}{\partial y},$$

$$\text{and} \quad \frac{\partial}{\partial \mathrm{Y}^2} = \frac{1}{\epsilon^2}\frac{\partial}{\partial y^2}. \tag{278}$$

This rescaling gives the amplitude equations (97 - 98).

B

USEFUL RESULTS AND DERIVATIONS FOR CHAPTER 5

B.1 FORCED ADAPTATION MODEL IN ONE DIMENSION

The hierarchy consists of equations of the form $\mathcal{L}_g u_\alpha = g_\alpha(u_1, \ldots, u_\alpha)$ for the linear operator $\mathcal{L}_g = -\frac{\partial}{\partial t} - 1 + \beta_c w \otimes -g\eta *$. The adjoint of this operator is $\mathcal{L}_g^\dagger = \frac{\partial}{\partial t} - 1 + \beta_c w \otimes -g\eta_- *$ where $\eta_-(t) = \eta(-t)$. For all $u \in \ker \mathcal{L}_g^\dagger$ then $\langle u, g_\alpha \rangle = \langle u, \mathcal{L}_g u_\alpha \rangle = \langle \mathcal{L}_g^\dagger u, u_\alpha \rangle = 0$. It is straightforward to establish that $\ker \mathcal{L}_g^\dagger = \ker \mathcal{L}_g$ so that the set of solvability conditions are $\langle \mathrm{e}^{\pm i(k_0 x \pm \omega_c t)}, g_\alpha \rangle = 0$. By using the Fredholm Alternative, equation (151) gives,

$$\langle \mathrm{e}^{i(k_0 x + \omega_c t)}, \mathscr{L}_g u_2 \rangle = 0, \tag{279}$$

$$\langle \mathrm{e}^{i(k_0 x + \omega_c t)}, \beta_2 w \otimes u_1^2 \rangle = 0, \tag{280}$$

$$\langle \mathrm{e}^{i(k_0 + \omega_c t)}, \beta_c (W^x \otimes \partial_\chi) u_1 \rangle = 0, \tag{281}$$

$$\langle \mathrm{e}^{i(k_0 x + \omega_c t)}, \gamma_1 u_1 \cos k_f x \rangle = \begin{cases} 0 & n \neq 2 \\ \frac{\gamma_1}{2} B^* \mathrm{e}^{-2i\nu x} & n = 2 \end{cases} \tag{282}$$

and similarly for the other mode.

The particular solution of u_2, therefore is,

$$
\begin{aligned}
u_2 = 2\zeta_0 \left(|A|^2 + |B|^2\right) + \zeta_1 \big(A^2 \mathrm{e}^{2i(k_0 x + \omega_c t)} + B^{*2} \mathrm{e}^{-2i(k_c x - \omega_c t)}\big) \\
+ \zeta_2 \left(AB\mathrm{e}^{2ik_c x}\right) + \zeta_3 \left(AB^* \mathrm{e}^{2i\omega_c t}\right) \\
+ (1 - \delta_{n,2}) \frac{\gamma_1}{2} \left[\zeta_4 \left(A_1 \mathrm{e}^{i(k_c x + \omega_c t + k_f x)} + B^* \mathrm{e}^{-i(k_c x - \omega_c t - k_f x)}\right)\right. \\
\left. + \zeta_5 \left(A\mathrm{e}^{i(k_c x + \omega_c t - k_f x)} + B^* \mathrm{e}^{-i(k_c x - \omega_c t + k_f x)}\right)\right] + \text{c.c.}, \quad (283)
\end{aligned}
$$

where

$$
\begin{aligned}
\zeta_0 &= \frac{\beta_2 \widehat{w}(0)}{1 - \beta_c \widehat{w}(0) + g\widetilde{\eta}(0)}, \\
\zeta_1 &= \frac{\beta_2 \widehat{w}(2k_0)}{1 + 2i\omega_c - \beta_c \widehat{w}(2k_0) + g\widetilde{\eta}(2i\omega_c)}, \\
\zeta_2 &= \frac{2\beta_2 \widehat{w}(2k_0)}{1 - \beta_c \widehat{w}(2k_0) + g\widetilde{\eta}(0)}, \\
\zeta_3 &= \frac{2\beta_2 \widehat{w}(0)}{1 + 2i\omega_c - \beta_c \widehat{w}(0) + g\widetilde{\eta}(2i\omega_c)}, \\
\zeta_4 &= \frac{1}{1 + i\omega_c - \beta_c \widehat{w}\left(k_0 + k_f\right) + g\widetilde{\eta}\left(i\omega_c\right)} \\
\zeta_5 &= \frac{1}{1 + i\omega_c - \beta_c \widehat{w}\left(k_0 - k_f\right) + g\widetilde{\eta}\left(i\omega_c\right)}.
\end{aligned}
$$

However, we note that $\widehat{w}(0) = 0$ so this gives $\zeta_0 = \zeta_3 = 0$. Also note that $\widetilde{\eta}(0) = 1$.

Equation (153) gives the derivation of the amplitude equation by using the Fredholm Alternative again,

$$\langle \mathrm{e}^{i(k_0 x+\omega_c t)}, \mathscr{L} u_3 \rangle = 0, \tag{284}$$

$$\langle \mathrm{e}^{i(k_0 x+\omega_c t)}, \frac{\partial u_1}{\partial \tau} \rangle = \frac{\partial A}{\partial \tau}, \tag{285}$$

$$\langle \mathrm{e}^{i(k_0 x+\omega_c t)}, 2\beta_2 w \otimes u_1 u_2 \rangle = 2\beta_2 \widehat{w}(k_0)[(2\zeta_0+\zeta_1)|A|^2 + (\zeta_0+\zeta_2+\zeta_3)|AB|^2]A, \tag{286}$$

$$\langle \mathrm{e}^{i(k_0 x+\omega_c t)}, \beta_3 w \otimes u_1^3 \rangle = \beta_3 \widehat{w}(k_0) \left[3|A|^2 + 6|B|^2\right] A, \tag{287}$$

$$\langle \mathrm{e}^{i(k_c x+\omega_c t)}, \delta w \otimes u_1 \rangle = \delta \widehat{w}(k_0) A, \tag{288}$$

$$\langle \mathrm{e}^{i(k_0 x+\omega_c t)}, \frac{1}{2}\beta_c W^{xx} \otimes \partial_{\chi\chi} u_1 \rangle = \frac{1}{2}\beta_c \widehat{W}^{xx}(k_0) \frac{\partial^2 A}{\partial \chi^2}, \tag{289}$$

$$\langle \mathrm{e}^{i(k_0 x+\omega_c t)}, g\eta^t * u_1 \rangle = g \frac{\partial A}{\partial \tau} \widetilde{\eta}'(i\omega_c), \tag{290}$$

$$\langle \mathrm{e}^{i(k_0 x+\omega_c t)}, \gamma_2 u_1 \cos k_f x \rangle = \frac{\gamma_2}{2} B^* \mathrm{e}^{-2ivx} \delta_{n,2}, \tag{291}$$

$$\langle \mathrm{e}^{i(k_0 x+\omega_c t)}, \gamma_1 u_2 \cos k_f x \rangle = \left(\frac{\overline{\gamma}_1}{2}\right)^2 (1-\delta_{n,2}) \left[(\zeta_4+\zeta_5)A + \zeta_5 B^* \mathrm{e}^{-2ivx} \delta_{n,1}\right]. \tag{292}$$

and similarly for the other mode.

Here, we note that

$$\widetilde{\eta}^t(\lambda) = -\int_0^\infty t\eta(t)\mathrm{e}^{-\lambda t}\mathrm{d}t = \frac{\mathrm{d}}{\mathrm{d}\lambda}\int_0^\infty \eta(t)\mathrm{e}^{-\lambda t}\mathrm{d}t = \frac{\mathrm{d}}{\mathrm{d}\lambda}\widetilde{\eta}(\lambda) = \frac{-\tau_a}{(1+\lambda\tau_a)^2}. \tag{293}$$

We also have the scaling $v = \epsilon c$ so $\mathrm{e}^{-2ivx} = \mathrm{e}^{-2ic\chi}$. The projections give the evolution of the amplitude A as

$$\begin{aligned}\left(1+g\widetilde{\eta}'(i\omega_c)\right)\frac{\partial A}{\partial \tau} &= \widehat{w}(k_0)\left(\delta - \Phi_1|A|^2 - \Phi_2|B|^2\right)A \\ &\quad - \frac{\beta_c}{2}\widehat{w}''(k_0)\frac{\partial^2 A}{\partial \chi^2} + \frac{\gamma_2}{2}B^*\mathrm{e}^{-2ic\chi}\delta_{n,2} \\ &\quad + \left(\frac{\overline{\gamma}_1}{2}\right)^2(1-\delta_{n,2})\left[(\zeta_4+\zeta_5)A + \zeta_5 B^*\mathrm{e}^{-2ic\chi}\delta_{n,1}\right],\end{aligned} \tag{294}$$

where

$$\Phi_1 = -3\beta_3 - 2\beta_2\left[2\zeta_0 + \zeta_1\right] = -3\beta_3 - 2\beta_2\zeta_1,$$
$$\Phi_2 = -6\beta_3 - 2\beta_2\left[2\zeta_0 + \zeta_2 + \zeta_3\right] = -6\beta_3 - 2\beta_2\zeta_2.$$

and we note that $\widetilde{\eta}'(-i\omega_c) = (\widetilde{\eta}'(i\omega_c))^*$. Similarly, by considering the projections $\langle \mathrm{e}^{i(k_0-\omega_c t)}, \cdot \rangle$, we obtain the evolution of the amplitude B as

$$\begin{aligned}\left(1 + g\widetilde{\eta}'(-i\omega_c)\right)\frac{\partial B}{\partial \tau} = \widehat{w}(k_0)&\left(\delta - \Phi_1^*|B|^2 - \Phi_2^*|A|^2\right)B \\ &- \frac{\beta_c}{2}\widehat{w}''(k_0)\frac{\partial^2 B}{\partial \chi^2} + \frac{\gamma_2}{2}A^*\mathrm{e}^{-2ic\chi}\delta_{n,2} \\ &+ \left(\frac{\overline{\gamma}_1}{2}\right)^2(1-\delta_{n,2})\left[(\zeta_4^* + \zeta_5^*)B + \zeta_5^* A^*\mathrm{e}^{-2ic\chi}\delta_{n,1}\right]. \quad (295)\end{aligned}$$

These now need to be rescaled back to the original time and space variables. Note that away from the bifurcation the solution will have a (temporal) frequency $\omega = \omega_c + \xi$ where ξ is a frequency detuning parameter which we can assume is order ϵ^2. Recall also that we also have the spatial frequency detuning parameter $v_1 = k_x - k_f/n$. When we rescale back to the original length and timescales we also let $a = \epsilon A \mathrm{e}^{ic_1\chi}\mathrm{e}^{i\xi_1 t}$ and $b = \epsilon B \mathrm{e}^{ic_1\chi}\mathrm{e}^{i\xi_2 t}$ where $\xi_1 = -\xi$ and $\xi_2 = \xi$. Upon rescaling

$$\frac{\partial A}{\partial \tau} \to \frac{\mathrm{e}^{-iv_1 x}}{\epsilon^3}\frac{\partial}{\partial t}\left(a\mathrm{e}^{-i\xi_1 t}\right) = \frac{\mathrm{e}^{-iv_1 x}\mathrm{e}^{-i\xi_1 t}}{\epsilon^3}\left(\frac{\partial a}{\partial t} - i\xi_1 a\right), \quad (296)$$

and similarly for the other mode. The parameters ξ_1 and ξ_2 can be removed from the amplitude equations by noting that the factor outside the bracket in (296) is also a factor on the right hand side of the rescaled amplitude equation and by making a transformation $a \to a\mathrm{e}^{i\xi_1 t}$ and $b \to b\mathrm{e}^{i\xi_2 t}$. The transformation removes the imaginary term inside the bracket and is equivalent to changing the carrier wave frequency to $\omega = \omega_c + \xi$. This rescaling gives the amplitude equations (156) and (157).

C

TOOLS FOR CODING

The numerical simulations were performed in the plane by discretising in space on a regular square mesh, and solving the resultant set of ordinary differential equations using Matlab's in-built ode45 algorithm to evolve the system forward in time. We use the Fast Fourier Transform Method to numerically solving the model, and this provides substantial computational speed-up over quadrature-based numerical methods for calculating $w \otimes f(u)$. This is also the method used in work of [29, 30, 72]. We are able to use this method as the integral, $\int_{\Omega} w(|\mathbf{r} - \mathbf{r}'|) f(u(\mathbf{r}', t))\, \mathrm{d}\mathbf{r}'$, has a convolution structure and can be written as the inverse Fourier Transform of $\widehat{w} \times \widehat{f}$ to give a solution of the integral.The discrete Fourier Transform, Y, of a m by n matrix is,

$$Y_{p+1,q+1} = \sum_{j=0}^{m-1} \sum_{k=0}^{n-1} \omega_m^{jp} \omega_n^{kq} X_{j+1,k+1} \tag{297}$$

where ω_m and ω_n are the complex roots of unity, $\omega_m = \mathrm{e}^{-2\pi i/m}$ and $\omega_n = \mathrm{e}^{-2\pi i/n}$. The discrete inverse Fourier Transform, X, of a m by n matrix Y is,

$$X_{p,q} = \frac{1}{m} \sum_{j=1}^{m} \frac{1}{n} \sum_{k=1}^{n} \omega_m^{jp} \omega_n^{kq} Y_{j,k}. \tag{298}$$

D

CODE FOR PATCHY CONNECTIONS

The following Matlab code follows the model and analysis in section 6.3. The code produced the figures highlighting the results of the Turing analysis and also the figure showing the resulting activity for the neural field model with square patchy connections.

```
d = 2; P.d = d;
mu = 11; P.mu = mu;

sigma = 0.6; A = 1/sigma^2;
w = @(r) A.*exp(-r./sigma)-exp(-r);

q1 = (2.*pi./P.d);  q2 = q1;
M = @(X,Y) 1/2*(cos(q1.*X)+cos(q2.*Y));
wp = @(X,Y) w(sqrt(X.^2+Y.^2)).*M(X,Y);
wHat = @(k) 2.*pi.*(A./(sigma.*(sigma.^(-2)+k.^2).^(3/2))
- 1./((1+k.^2).^(3/2)));
wpHat = @(k1,k2) (wHat(sqrt((k1-q1).^2+k2.^2))
+ wHat(sqrt((k1+q1).^2+k2.^2)) + wHat(sqrt(k1.^2+(k2-q2).^2))
+ wHat(sqrt(k1.^2+(k2+q2).^2)))/4;
dwHat = @(k) 6*pi*k*(1/((1+k^2)^(5/2))
- A/(sigma*(sigma^(-2)+k^2)^(5/2)));

DwpHat = @(k) [1/4.*(dwHat(sqrt((k(1)-q1)^2+k(2)^2))
```

```
*(k(1)-2*pi/d)/(sqrt((k(1)-q1)^2+k(2)^2))
+ dwHat(sqrt((k(1)+q1)^2+k(2)^2))*(k(1)+2*pi/d)/
(sqrt((k(1)+q1)^2+k(2)^2))
+ dwHat(sqrt((k(2)-q2)^2+k(1)^2))*k(1)/(sqrt((k(2)-q2)^2+k(1)^2))
+ dwHat(sqrt((k(2)+q2)^2+k(1)^2))*k(1)/(sqrt((k(2)+q2)^2+k(1)^2))),
1/4.*(dwHat(sqrt((k(2)-q2)^2+k(1)^2))*(k(2)-2*pi/d)/
(sqrt((k(2)-q2)^2+k(1)^2))
+ dwHat(sqrt((k(2)+q2)^2+k(1)^2))*(k(2)+2*pi/d)/
(sqrt((k(2)+q2)^2+k(1)^2))
+ dwHat(sqrt((k(1)-q1)^2+k(2)^2))*k(2)/(sqrt((k(1)-q1)^2+k(2)^2))
+ dwHat(sqrt((k(1)+q1)^2+k(2)^2))*k(2)/(sqrt((k(1)+q1)^2+k(2)^2)))];

kc = [2,0];
kc = fsolve(DwpHat,kc);
kc1 = kc(1); kc2 = kc(2);

P.wHatd = wHat(2*pi/d);
P.wpHatMax = wpHat(kc(1),kc(2));

h = linspace(-0.5,1,1000); u0 = linspace(-0.5,1,1000);
bif1 = @(u0,h) u0 - f(u0,P.mu,h)*P.wHatd;
bif2 = @(u0,h) -1+fd(u0,P.mu,h)*P.wpHatMax;

x = [0.1, 0.3];
x = fsolve(@(x) BifurcationCondition(x,P),x);
u0 = x(1);P.h = x(2);

[U0, H] = meshgrid(u0,h);
figure(1); hold on
contour(U0,H,bif1(U0,H), [0 0], 'r-', 'linewidth', 2)
contour(U0,H,bif2(U0,H), [0 0], 'g-', 'linewidth', 2)
```

```
plot(u0,P.h,'bo','MarkerSize',10)
hold off

kx = linspace(-5*pi,5*pi,200); ky = linspace(-5*pi,5*pi,200);
[Kx, Ky] = meshgrid(kx,ky);
P.h = P.h*0.95;

figure(2); hold on
surf(Kx,Ky,wpHat(Kx,Ky)), view(3)
plot3(kc(1),kc(2),wpHat(kc(1),kc(2)),'r.','MarkerSize',30);
sheet = surf(Kx,Ky,0*Kx+1/fd(u0,P.mu,P.h),'FaceAlpha',0.5);
set(sheet, 'cdata',zeros(200)); shading interp;view(3);
hold off

P.Lx = 5*pi; P.Ly = 5*pi; P.N=2^9;
x = linspace(-P.Lx,P.Lx,P.N); y = linspace(-P.Ly,P.Ly,P.N);
[X,Y] = meshgrid(x,y); R = sqrt(X.^2+Y.^2);
U0 = u0*ones(P.N)+0.1*rand(P.N,P.N);
tspan = linspace(0,150,151);
P.wHat = real(fft2(wp(X,Y)));
[t,u] = ode45(@RHS,tspan,U0,[],P);

figure(3)
for i = 1:length(t)
surf(X,Y,reshape(u(i,:),[P.N,P.N]));
shading interp; colorbar; view(2);
drawnow;
end

function BifCondition = BifurcationCondition(x, P)
u0 = x(1); h = x(2);
```

```
BifCondition = [u0 - f(u0,P.mu,h)*P.wHatd;
-1+fd(u0,P.mu,h)*P.wpHatMax];
end

function fr = f(u,mu,h)
fr = 1./(1+exp(-mu*(u-h)));
end

function frd = fd(u,mu,h)
frd = mu*f(u,mu,h).*(1-f(u,mu,h));
end

function NF = RHS(t,u,P)
u = reshape(u,P.N,P.N);
fHat = fft2(f(u,P.mu,P.h));
psi = (2.*P.Lx/P.N)*(2.*P.Ly/P.N)
.*ifftshift(real(ifft2(fHat.*P.wHat)));
NF = -u + psi; NF = NF(:);
end
```

This Matlab code was very similarly reproduced for the hexagonal lattice and the hexagonal lattice with ϵ. These models require for the basis vectors and the M, wpHat and dwHat equations to be altered; see section 6.4 and section 6.5 for the relevant versions of the equations.

E

RANKIN AND CHAVANE LAYERED MODEL

E.1 CONNECTIVITY

The connectivity for the Rankin and Chavane model is made up of three different types of neuron connections, local excitation, lateral excitation and inhibition. These are separated in peaks of excitation by Λ, the hyper column separation, taking $\Lambda = 2\pi$. The model is written using radial coordinates $r = \sqrt{x^2 + y^2}$, $x, y \in \mathbb{R}$.

Peaks of excitatory connections are centered at distances $\{0, \Lambda, 2\Lambda\}$ and decay within an exponential envelope

$$\chi(r, \zeta) = \mathrm{e}^{\frac{r}{\zeta}}, \tag{299}$$

where $\zeta = 0.625\Lambda$. This is used in defining the lateral excitation connectivity profile.

Rankin and Chavane define a radially shifted Gaussian that is maximal at radius $r = r_0$ and decays with spatial scale σ to define the bumps at Λ and 2Λ,

$$h(r, r_0, \sigma) = \mathrm{e}^{\left(-\frac{(r-r_0)^2}{2\sigma^2}\right)}. \tag{300}$$

The connectivity components are,

$$w_{\mathrm{I}}(r) = g(r, RW_{\mathrm{in}}), \tag{301}$$

$$w_{\mathrm{E}}^{\mathrm{loc}}(r) = h(r, 0, RW_{\mathrm{ex}}), \tag{302}$$

and

$$w_{\mathrm{E}}^{\mathrm{lat}}(r) = \chi(\Lambda, \zeta) h(r, \Lambda, RW_{\mathrm{ex}}) + \chi(2\Lambda, \zeta) h(r, 2\Lambda, RW_{\mathrm{ex}}), \tag{303}$$

where $RW_{\mathrm{in}} = 0.55\Lambda$ and RW_{ex} is a free parameter in [0.1,0.4].

Furthermore, to normalise the connectivity profile, a coefficient B_{E} needs to be found such that,

$$\int_{\Omega} B_{\mathrm{E}} w_{\mathrm{E}}(r) = B_{\mathrm{E}} \int_{\Omega} w_{\mathrm{E}}^{\mathrm{loc}}(r) + w_{\mathrm{E}}^{\mathrm{lat}}(r) = 1. \tag{304}$$

To do this we need to use the zero-mode of the Fourier Transform of $h(r, r_0, \sigma)$. This can be calculated as,

$$H(0, r_0, \sigma) = 2\pi\sigma^2 \mathrm{e}^{-\frac{r_0^2}{2\sigma^2}} + \pi\sigma r_0 \sqrt{2\pi} \left(1 + \mathrm{erf}\frac{r_0^2}{2\sigma^2}\right). \tag{305}$$

Therefore,

$$B_{\mathrm{E}} = 1 / \left[2\pi RW_{\mathrm{ex}}^2 + \chi(\Lambda, \zeta) H(0, \Lambda, RW_{\mathrm{ex}}) + \chi(2\Lambda, \zeta) H(0, 2\Lambda, RW_{\mathrm{ex}})\right]. \tag{306}$$

The complete connectivity function is,

$$w(r) = P\left[B_{\mathrm{E}}\left(w_{\mathrm{E}}^{\mathrm{loc}}(r) + w_{\mathrm{E}}^{\mathrm{lat}}(r)\right) + (C-1) w_{\mathrm{I}}(r)\right], \tag{307}$$

where P is the largest Fourier mode of w. Here, C is the global balance between inhibition and excitation. When $C = 0$, they are balanced, when C is negative/positive this gives net inhibition/excitation. We choose $C = \pm 0.4$ depending on the type of connectivity required as this is large enough to give excitatory/inhibitory connectivity but when C is larger then localised patterns of activity are more likely to destabilise and hence spread across the cortex.

Two coefficients required for (214 - 215) are,

$$g_{\mathrm{ex}} = B_{\mathrm{E}} P \text{ and } g_{\mathrm{in}} = P(C-1), \tag{308}$$

thus, giving a normalised connectivity profile.

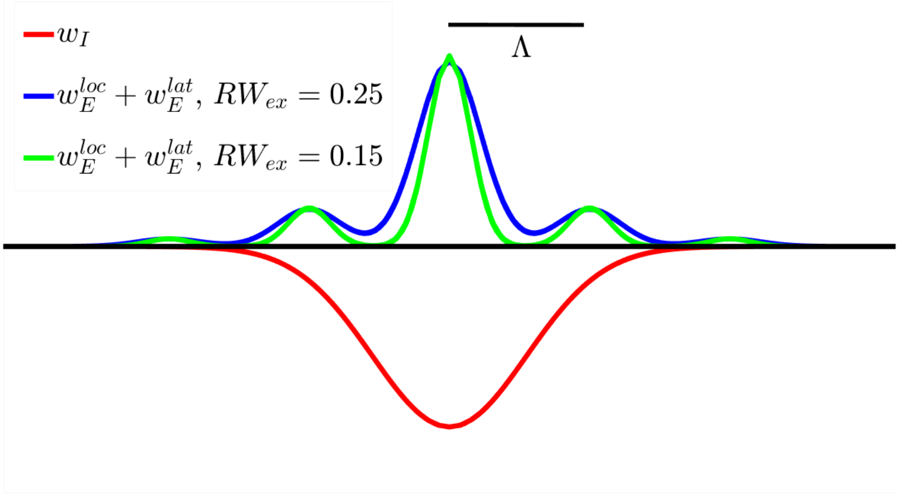

Figure 67.: Cross-section of the connectivity profiles for excitation and inhibition. There are regular peaks in excitation, Λ-distance, black bar, from the origin; the width controlled byRW_{ex}. Figure redrawn from [96].

E.2 FIRING RATE AND INPUT

The firing rate function, S is given by the sigmoid,

$$S(u, \mu, \theta) = \frac{1}{1 + e^{-\mu u + \theta}} - \frac{1}{1 + e^{\theta}}, \qquad \theta, \mu > 0, \tag{309}$$

where μ is the steepness of the slope and θ is the threshold. The firing rate relates to the input strengths k_1 and k_2. These are set so that $\mu k_1 > \theta$ so that the sub-population with the same orientation is above threshold and that $\mu k_2 < \theta$ so that the other sub-populations are below threshold. Therefore, the only neurons that are firing are those responding to that orientation.

The radial inputs $I_j(r)$ are,

$$I_j(r) = \begin{cases} 1, & r < 0.7\Lambda, \\ h(r, 0.725\Lambda, 0.3\Lambda), & r \geq 0.7\Lambda, \end{cases} \tag{310}$$

There is a linear ramp up of amplitude of the input from 0 to 1 over $t \in [20, 120]$ ms using $(t - 20)/120$ for the required time points meaning that the input strength is greatest at the end of the simulation.

E.3 CONVERSION TO VSD LIKE SIGNAL

There are four solutions, one for each of the four orientations over the entire domain. To combine these, in [96] a VSD-like signal is computed and then the orientation preference, activation and selectivity can be computed from this.

Firstly the sub-population membrane potential u_i for each orientation is computed. The pre-synaptic firing rate is then convolved with a connectivity profile to give a postsynaptic population response. The optical image (OI) signal is the postsynaptic response convolved with a 2D Gaussian distribution with spatial decay rate σ,

$$g(r, \sigma) = A(\sigma) \mathrm{e}^{\left(\frac{r^2}{2\sigma^2}\right)}, \tag{311}$$

where $A(\sigma) = 1/(2\pi\sigma^2)$ normalises the area under the curve. Therefore, the OI signal for each orientation is

$$\begin{aligned} OI(x, y, t) = (\sum_i S(u_i(x, y, t)) \overset{(x,y)}{\otimes} \Big[& w_{\mathrm{E}}^{\mathrm{loc}}(x, y) - p_{\mathrm{I}} w_{\mathrm{I}}(x, y) \\ & + (1 - \mathrm{e}^{-t/\tau_{\mathrm{lat}}}) w_{\mathrm{E}}^{\mathrm{lat}}(x, y)(1 + \beta_{\mathrm{rec}} J_i) \Big]) \otimes g(x, y, \sigma_{\mathrm{OI}}) \end{aligned} \tag{312}$$

where $p_{\mathrm{I}} = 0.177$ and $\sigma_{\mathrm{OI}} = 0.075\Lambda$ for $i = \{0°, 45°, 90°, 135°\}$. The assumption that the activity from long range connection will propagate across the cortex instantaneously is not biologically correct. To incorporate this but not have to include delays in the original model, as this extremely computationally heavy, but still have a slower temporal scale for the long range connections, the parameter $\tau_{\mathrm{lat}} = 240$ms is introduced. This transforms the four activities which include the four orientations that are linked, to give only an optical image signal for each orientation OI_0, OI_{45}, OI_{90} and OI_{135}.

E.4 PARAMETERS

A table of all the parameter values used in the model,

Parameter	Value
Λ	2π
β_{rec}	0.6
C	-0.4
RW_{ex}	0.225Λ
P	58.82
L	30
t	550 ms
θ	5.6
μ	2.3

Parameter	Value
β_{inp}	0.25
k_1	2.8
ρ_{ij}	0.2
τ	10 ms
RW_{in}	0.55Λ
ζ	0.625Λ
p_{I}	0.177
σ_{OI}	0.075Λ
τ_{lat}	240 ms

F

CODE FOR MULTI LAYERED PATCHY CONNECTIONS MODEL

The following Matlab code realises the multi layered patchy connection model (227) and Turing analysis. The code produces the figures highlighting the results of the Turing analysis and also the figure showing the resulting activity for the neural field model with hexagonal patchy connections.

```
function Patchy(rho, epsilon, mu0, h)

% Define w
sigma = 0.6; A = 1/sigma^2;
w = @(r) A.*exp(-r./sigma)-exp(-r);
wHat = @(k) 2.*pi.*(A./(sigma.*(sigma.^(-2)+k.^2).^(3/2))
- 1./((1+k.^2).^(3/2)));

% Define parameters
d = 2; P.d = d;
P.rho1 = rho; P.rho2 = rho; P.rho3 = rho; P.rho4 = rho;
P.HSSw = wHat(4*pi/(sqrt(3)*d));
P.h = [h h h h]; P.mu = mu0;

% Define basis vectors and shifts
```

```
q = [1 -0.5 -0.5 0; 0 sqrt(3)/2 -sqrt(3)/2 0] ;
q = q.*(4*pi/(sqrt(3)*d));

%% Compute grid
P.N=2^9; L =4*pi;
x = linspace(-L,L,P.N); y = x; [X,Y] = meshgrid(x,y);
P.Lx = L; P.Ly = L; P.X = X; P.Y = Y;

%% Define patchy equation eq 38
a = [0 0 0 0]; epsilon = [epsilon epsilon epsilon epsilon];
theta = [2*pi/5 4*pi/5 6*pi/5 0];
M = @(X,Y,i) 1/3*(cos(q(1,1).*(cos(theta(i)).*(X-a(i).*q(1,i))
-sin(theta(i)).*(Y-a(i).*q(2,i)))+q(2,1).*(sin(theta(i)).*(X-a(i)
.*q(1,i))+cos(theta(i)).*(Y-a(i).*q(2,i))))+cos(q(1,2).*(cos(theta(i))
.*(X-a(i).*q(1,i)) - sin(theta(i)).*(Y-a(i).*q(2,i)))
+q(2,2).*(sin(theta(i)).*(X-a(i).*q(1,i)) +cos(theta(i)).*(Y-a(i)
.*q(2,i)))) +cos(q(1,3).*(cos(theta(i)).*(X-a(i).*q(1,i))
- sin(theta(i)).*(Y-a(i).*q(2,i)))+q(2,3).*(sin(theta(i)).*(X-a(i)
.*q(1,i))+cos(theta(i)).*(Y-a(i).*q(2,i)))));
J = @(X,Y,i) 1+epsilon(i)*M(X,Y,i);
wp = @(X,Y,i) w(sqrt(X.^2+Y.^2)).*J(X,Y,i);

figure;
subplot(2,2,1); surf(X,Y,J(X,Y,1)); shading interp; view(2); colorbar;
subplot(2,2,2); surf(X,Y,J(X,Y,2)); shading interp; view(2); colorbar;
subplot(2,2,3); surf(X,Y,J(X,Y,3)); shading interp; view(2); colorbar;
subplot(2,2,4); surf(X,Y,J(X,Y,4)); shading interp; view(2); colorbar;

%Define WpHat
Sum = @(k1,k2,i) 0;
for l = 1:3
```

```
    term = @(k1,k2,i) exp(-1i*(q(1,l)*a(i)*q(1,i) + q(2,l)*a(i)*q(2,i)))
    .*wHat(sqrt((k1-q(1,l)).^2+(k2-q(2,l)).^2)) + exp(1i*(q(1,l)
    *a(i)*q(1,i) + q(2,l)*a(i)*q(2,i))).*wHat(sqrt((k1+q(1,l)).^2
    +(k2+q(2,l)).^2));
    Sum = @(k1,k2,i) Sum(k1,k2,i) + term(k1,k2,i);
end
WpHat = @(k1,k2,i) wHat(sqrt(k1.^2+k2.^2)) + epsilon(i)/6.*Sum(k1,k2,i);

%% Solve for u0
U0 = [1 1 1 1];
U = fsolve(@(x) SteadyStateCondition(x,P),U0)

u0_1 = U(1); u0_2 = U(2); u0_3 = U(3); u0_4 = U(4);

%% Eigenvalues and plot eq 42
matrix = @(k1,k2)
         [-1+fd(u0_1,P,1).*WpHat(k1,k2,1) -P.rho2 -P.rho3 -P.rho4;...
          -P.rho1 -1+fd(u0_2,P,2).*WpHat(k1,k2,2) -P.rho3 -P.rho4;...
          -P.rho1 -P.rho2 -1+fd(u0_3,P,3).*WpHat(k1,k2,3) -P.rho4;...
          -P.rho1 -P.rho2 -P.rho3 -1+fd(u0_4,P,4).*WpHat(k1,k2,4)];

k1 = linspace(-P.Lx,P.Lx,2^9); k2 = linspace(-P.Ly,P.Ly,2^9);
alleigs = [];

for i=1:length(k2)
    allk1eigs = [];
    for j = 1:length(k1)
        myeigs = eig(matrix(k1(j),k2(i)));
        allk1eigs=[allk1eigs max(real(myeigs))];
    end
    alleigs = [alleigs; allk1eigs];
```

```
end

%% Compute NF equation
noise = 0.1*rand(P.N);
U0_1 = u0_1*ones(P.N)+noise; U0_2 = u0_2*ones(P.N)+noise;
U0_3 = u0_3*ones(P.N)+noise; U0_4 = u0_4*ones(P.N)+noise;
U0 = [U0_1(:); U0_2(:); U0_3(:); U0_4(:)];

T = 1000; tsave = T/10+1; tspan = linspace(0,T,tsave);

P.wHat1 = (fft2(wp(X,Y,1))); P.wHat2 = (fft2(wp(X,Y,2)));
P.wHat3 = (fft2(wp(X,Y,3))); P.wHat4 = (fft2(wp(X,Y,4)));

[t,u] = ode45(@RHS,tspan,U0,[],P);

%% Plots
Idx1=1:P.N*P.N; Idx2=P.N*P.N+1:2*P.N*P.N;
Idx3=2*P.N*P.N+1:3*P.N*P.N; Idx4=3*P.N*P.N+1:4*P.N*P.N;
figure;
 for i=1:tsave
     U1=reshape(u(i,Idx1),P.N,P.N);
     U2=reshape(u(i,Idx2),P.N,P.N);
     U3=reshape(u(i,Idx3),P.N,P.N);
     U4=reshape(u(i,Idx4),P.N,P.N);

     subplot(2,2,1)
     surf(X,Y,U1); shading interp; view(2); colorbar;
     subplot(2,2,2)
     surf(X,Y,U2); shading interp; view(2); colorbar;
     subplot(2,2,3)
     surf(X,Y,U3); shading interp;  view(2); colorbar;
```

```
     subplot(2,2,4)
     surf(X,Y,U4); shading interp;  view(2); colorbar;
     drawnow;
 end

figure;
surf(k1,k2,real(alleigs)); shading interp;
figure;
contour(k1,k2,real(alleigs), [0 0], 'r-', 'linewidth', 2);

%% Change to OPM
maxAct = max(u(tsave,:));
uend = u(tsave,:)/maxAct;

U1final=reshape(uend(Idx1),P.N,P.N);
U2final=reshape(uend(Idx2),P.N,P.N);
U3final=reshape(uend(Idx3),P.N,P.N);
U4final=reshape(uend(Idx4),P.N,P.N);

Act = (U1final + U2final + U3final + U4final)./4;

maxUfinal = [max(uend(Idx1)) max(uend(Idx2))
             max(uend(Idx3)) max(uend(Idx4))];

scalefac1 = 1+mean(maxUfinal)-maxUfinal(1);
scalefac2 = 1+mean(maxUfinal)-maxUfinal(2);
scalefac3 = 1+mean(maxUfinal)-maxUfinal(3);
scalefac4 = 1+mean(maxUfinal)-maxUfinal(4);

U1scale = U1final.*scalefac1; U2scale = U2final.*scalefac2;
U3scale = U3final.*scalefac3; U4scale = U4final.*scalefac4;
```

```
D1 = U1scale - U3scale; D2 = U2scale - U4scale;
Pref=atan2(D2,D1);
figure;
surf(X,Y,Pref); shading interp; colormap hsv; view(2);

end

function SteadyState = SteadyStateCondition(U, P)

u0_1 = U(1); u0_2 = U(2); u0_3 = U(3); u0_4 = U(4);
SteadyState =  [u0_1+P.rho2*u0_2+P.rho3*u0_3+P.rho4*u0_4
- P.epsilon1*P.HSSw*f(u0_1,P,1);...
u0_2+P.rho1*u0_1+P.rho3*u0_3+P.rho4*u0_4
- P.epsilon2*P.HSSw*f(u0_2,P,2);...
u0_3+P.rho1*u0_1+P.rho2*u0_2+P.rho4*u0_4
- P.epsilon3*P.HSSw*f(u0_3,P,3);...
u0_4+P.rho1*u0_1+P.rho2*u0_2+P.rho3*u0_3
- P.epsilon4*P.HSSw*f(u0_4,P,4)];

end

function fr = f(u,P,i)
        fr = 1./(1+exp(-P.mu*(u-P.h(i))));
end



function frd = fd(u,P,i)
        frd = P.mu*f(u,P,i).*(1-f(u,P,i));
end

function NF = RHS(t,u,P)
```

```
    Idx1 = 1:P.N*P.N;             u1 = reshape(u(Idx1),P.N,P.N);
    Idx2 = P.N*P.N+1:2*P.N*P.N;   u2 = reshape(u(Idx2),P.N,P.N);
    Idx3 = 2*P.N*P.N+1:3*P.N*P.N; u3 = reshape(u(Idx3),P.N,P.N);
    Idx4 = 3*P.N*P.N+1:4*P.N*P.N; u4 = reshape(u(Idx4),P.N,P.N);

    fHat1 = fft2(f(u1,P,1)); fHat2 = fft2(f(u2,P,2));
    fHat3 = fft2(f(u3,P,3)); fHat4 = fft2(f(u4,P,4));

    F1 = -u1 - P.rho2.*u2 - P.rho3.*u3 - P.rho4.*u4 + (2.*P.Lx/P.N)
    *(2.*P.Ly/P.N).*ifftshift(real(ifft2(fHat1.*P.wHat1)));
    F2 = -u2 - P.rho1.*u1 - P.rho3.*u3 - P.rho4.*u4 + (2.*P.Lx/P.N)
    *(2.*P.Ly/P.N).*ifftshift(real(ifft2(fHat2.*P.wHat2)));
    F3 = -u3 - P.rho1.*u1 - P.rho2.*u2 - P.rho4.*u4 + (2.*P.Lx/P.N)
    *(2.*P.Ly/P.N).*ifftshift(real(ifft2(fHat3.*P.wHat3)));
    F4 = -u4 - P.rho1.*u1 - P.rho2.*u2 - P.rho3.*u3 + (2.*P.Lx/P.N)
    *(2.*P.Ly/P.N).*ifftshift(real(ifft2(fHat4.*P.wHat4)));

    NF = [F1(:); F2(:); F3(:); F4(:)];
end
```

BIBLIOGRAPHY

[1] S. Amari. Dynamics of pattern formation in lateral-inhibition type neural fields. *Biological Cybernetics*, 27(2):77–87, 06 1977.

[2] T. I. Baker and J. D. Cowan. Spontaneous pattern formation and pinning in the primary visual cortex. *Journal of Physiology-Paris*, 103(1):52–68, 2009. Neuromathematics of Vision.

[3] M. Balasubramanian, J. Polimeni, and E. L. Schwartz. The V1-V2-V3 complex: Quasiconformal dipole maps in primate striate and extra-striate cortex. *Neural Networks*, 15(10):1157–1163, 2002.

[4] N. Barbosa, L. Rosa, A. Menezes, J. Reis, A. Facure, and D. Braz. Assessment of ocular beta radiation dose distribution due to 106ru/106rh brachytherapy applicators using mcnpx monte carlo code. *International Journal of Cancer Therapy and Oncology*, 3:12, 05 2014.

[5] J. Beatty. *Principles of behavioral neuroscience*. Brown and Benchmark Publishers, 1995.

[6] W. H. Beaudot and K. T. Mullen. Orientation selectivity in luminance and color vision assessed using 2-d band-pass filtered spatial noise. *Vision Research*, 45(6):687–696, 2005.

[7] S. Behnke. *Neurobiological Background*, pages 17–33. Springer Berlin Heidelberg, 2003.

[8] R. Ben-Yishai, R. L. Bar-Or, and H. Sompolinsky. Theory of orientation tuning in visual cortex. *Proceedings of the National Academy of Sciences, USA*, 92:3844–3848, 1995.

[9] R. L. Beurle. Properties of a mass of cells capable of regenerating pulses. *Philosophical Transactions of the Royal Society of London B: Biological Sciences*, 240(669):55–94, 1956.

[10] V. A. Billock and B. H. Tsou. Neural interactions between flicker-induced self-organized visual hallucinations and physical stimuli. *Proceedings of the National Academy of Sciences*, 104(20):8490–8495, 2007.

[11] G. Blasdel. Orientation selectivity, preference, and continuity in monkey striate cortex. *Journal of Neuroscience*, 12(8):3139–3161, 1992.

[12] G. G. Blasdel and D. Campbell. Functional retinotopy of monkey visual cortex. *Journal of Neuroscience*, 21(20):8286–8301, 2001.

[13] G. G. Blasdel and G. Salama. Voltage-sensitive dyes reveal a modular organization in monkey striate cortex. *Nature*, 321(6070):579–585, 1986.

[14] T. Bonhoeffer and A. Grinvald. Iso-orientation domains in cat visual cortex are arranged in pinwheel-like patterns. *Nature*, 353(6343):429–431, 1991.

[15] W. H. Bosking, Y. Zhang, B. Schofield, and D. Fitzpatrick. Orientation selectivity and the arrangement of horizontal connections in tree shrew striate cortex. *The Journal of Neuroscience*, 17(6):2112–2127, 1997.

[16] P. L. Boyland. Bifurcations of circle maps: Arnol'd tongues, bistability and rotation intervals. *Communications in Mathematical Physics*, 106:353–381, 1986.

[17] P. C. Bressloff. Travelling fronts and wave propagation failure in an inhomogeneous neural network. *Physica D*, 155:83–100, 2001.

[18] P. C. Bressloff. Spatially periodic modulation of cortical patterns by long-range horizontal connections. *Physica D*, 185:131–157, 2003.

[19] P. C. Bressloff. Spatiotemporal dynamics of continuum neural fields. *Journal of Physics A: Mathematical and Theoretical*, 45(3), 2012.

[20] P. C. Bressloff and J. D. Cowan. Amplitude equation approach to contextual effects in visual cortex. *Neural Computation*, 14:493–525, 2002.

[21] P. C. Bressloff, J. D. Cowan, M. Golubitsky, P. J. Thomas, and M. C. Wiener. Geometric visual hallucinations, Euclidean symmetry and the functional architecture of striate cortex. *Philosophical Transactions of the Royal Society B: Biological Sciences*, 356(1407):299–330, 2001.

[22] P. C. Bressloff, S. E. Folias, A. Prat, and Y.-X. Li. Oscillatory waves in inhomogeneous neural media. *Physical Review Letters*, 91:178101, Oct 2003.

[23] P. C. Bressloff and M. Webber. Neural field model of binocular rivalry waves. *Journal of Computational Neuroscience*, 32:233–252, 2012.

[24] M. Camperi and X.-J. Wang. A model of visuospatial short-term memory in prefrontal cortex: Recurrent network and cellular bistability. *Journal of Computational Neuroscience*, 5:383–405, 1998.

[25] G. Citti and A. Sarti. *Neuromathematics of Vision*, volume 10. Springer, 01 2010.

[26] S. Coombes. Waves, bumps and patterns in neural field theories. *Biological Cybernetics*, 93:91–108, 2005.

[27] S. Coombes, P. Beim Graben, R. Potthast, and J. Wright. *Neural Fields: Theory and Applications*. Springer, 07 2014.

[28] S. Coombes and M. R. Owen. Bumps, breathers, and waves in a neural network with spike frequency adaptation. *Physical Review Letters*, 94:148102, 2005.

[29] S. Coombes, H. Schmidt, and D. Avitabile. Spots: Breathing, drifting and scattering in a neural field model. *Neural Fields: Theory and Applications*, 9783642545931:187–211, 2014.

[30] S. Coombes, H. Schmidt, and I. Bojak. Interface dynamics in planar neural field models. *Journal of Mathematical Neuroscience*, 2(1):1–46, 2012.

[31] M. C. Cross and P. C. Hohenberg. Pattern formation outside of equilibrium. *Reviews of Modern Physics*, 65:851–1111, 2003.

[32] R. Curtu and B. Ermentrout. Pattern formation in a network of excitatory and inhibitory cells with adaptation. *Society for Industrial and Applied Mathematics*, 3:191–231, 01 2004.

[33] D. Debanne, E. Campanac, A. Bialowas, E. Carlier, and G. Alcaraz. Axon physiology. *Physiological reviews*, 91(2):555–602, 2011.

[34] S. O. Dumoulin and B. A. Wandell. Population receptive field estimates in human visual cortex. *NeuroImage*, 39(2):647–60, 2008.

[35] M. Dybowski. Conditions for the appearance of hypnagogic visions. *Kwartalnik Psychologiczny*, 11:68–94, 1939.

[36] B. Ermentrout. Simulating, analyzing, and animating dynamical systems: A guide to xppaut for researchers and students. *Applied Mechanics Reviews*, 56, 07 2003.

[37] G. B. Ermentrout. Neural networks as spatio-temporal pattern-forming systems. *Reports on Progress in Physics*, 61:353–430, 1998.

[38] G. B. Ermentrout and J. D. Cowan. A mathematical theory of visual hallucination patterns. *Biological Cybernetics*, 34(3):137–150, 1979.

[39] J. Ferreira and M. Castelo-Branco. *3D structure and motion multimodal perception (State-of-the-Art Report)*. Institute of Systems and Robotics

and Institute of Biomedical Research in Light and Image, University of Coimbra. (Bayesian Approach to Cognitive Systems (BACS) European Project), 2007.

[40] S. E. Folias and P. C. Bressloff. Breathing Pulses in an Excitatory Neural Network. *SIAM Journal on Applied Dynamical Systems*, 3(3):378–407, 2004.

[41] I. Fredholm. Sur une classe d'équations fonctionnelles. *Acta Mathematica*, 27:365 – 390, 1903.

[42] A. Garliauskas. The visual cortex modeling by the hexagonal topology. *Neurocomputing*, 38-40:1229–1238, 2001.

[43] M. A. Geise. *Neural Field Theory for Motion Perception*. Kluwer Academic, Dordrecht, 1999.

[44] A. Gökçe, D. Avitabile, and S. Coombes. Quasicrystal patterns in a neural field model. *Physical Review Research*, 2:013234, 2020.

[45] H. Greenside and M. Cross. *Pattern Formation and Dynamics in Nonequilibrium Systems*. Cambridge University Press, 2009.

[46] A. Grinvald, E. Lieke, R. D. Frostig, C. D. Gilbert, and T. N. Wiesel. Functional architecture of cortex revealed by optical imaging of intrinsic signals. *Nature*, 324(6095):361–364, 1986.

[47] S. Hagen. The mind's eye. *Rochester Review*, 74(4):32–37, 2012.

[48] D. Hansel and H. Sompolinsky. Modeling feature selectivity in local cortical circuits. *Methods in neuronal modeling : from synapses to networks*, 01 1989.

[49] H. Helmholtz. *Physiological Optics*, volume 2. Rochester, NY: Optical Society of America, 1924.

[50] J. C. Horton. Cytochrome oxidase patches: a new cytoarchitectonic feature of monkey visual cortex. *Philosophical transactions of the Royal Society of London. Series B, Biological sciences*, 304(1119):199–253, 1984.

[51] R. Hoyle. *Pattern Formation: An Introduction to Methods*. Cambridge University Press, 2006.

[52] W. Huang, C. Troy, Q. Yang, H. Ma, C. R. Laing, S. J. Schiff, and J. Wu. Spiral waves in disinhibited mammalian neocortex. *Journal of Neuroscience*, 24:9897–9902, 2004.

[53] D. Hubel. *Eye, Brain, and Vision*. Scientific American Library series. Scientific American Library, 1988.

[54] D. Hubel and T. Wiesel. Receptive fields, binocular interaction and functional architecture in the cat's visual cortex. *Journal of Physiology*, 160(1):106–154.2, 1962.

[55] D. Hubel and T. Wiesel. Receptive field and functional architechture in two nonstriate visual areas (18 and 19) of the cat. *Journal of Neurophysiology*, 28:229–289, 1965.

[56] D. Hubel and T. Wiesel. Functional architecture of macaque monkey visual cortex. *Proceedings of the Royal Society, London [B],*, 198(1130):1–59, 1977.

[57] A. Hutt, M. Bestehorn, and T. Wennekers. Pattern formation in intracortical neuronal fields. *Network: Computation in Neural Systems*, 14(2):351–368, 2003. PMID: 12790189.

[58] V. Jirsa and H. Haken. A derivation of a macroscopic field theory of the brain from the quasi-microscopic neural dynamics. *Physica D: Nonlinear Phenomena*, 99(4):503–526, 1997.

[59] A. Johnston. A spatial property of the retino-cortical mapping. *Spatial Vision*, 1(4):319–331, 1986.

[60] A. Johnston. The geometry of the topographic map in striate cortex. *Vision Research*, 29(11):1493–1500, 1989.

[61] M. Joukal. Anatomy of the human visual pathway. In *Homonymous visual field defects*, pages 1–16. Springer, 2017.

[62] M. Kaschube, M. Schnabel, S. Löwel, D. M. Coppola, L. E. White, and F. Wolf. Universality in the evolution of orientation columns in the visual cortex. *Science*, 330(6007):1113–1116, 2010.

[63] W. Keil, M. Kaschube, M. Schnabel, Z. F. Kisvarday, S. Löwel, D. M. Coppola, L. E. White, and F. Wolf. Response to comment on universality in the evolution of orientation columns in the visual cortex. *Science*, 336(6080):413–413, 2012.

[64] T. Kenet, D. Bibitchkov, M. Tsodyks, A. Grinvald, and A. Arieli. Spontaneously emerging cortical representations of visual attributes. *Nature*, 425(6961):954–956, 2003.

[65] Z. P. Kilpatrick and P. C. Bressloff. Effects of synaptic depression and adaptation on spatiotemporal dynamics of an excitatory neuronal network. *Physica D*, 239:547–60, 2010.

[66] A. Kitaoka. *Akiyoshi's Illusion Pages*. `http://www.ritsumei.ac.jp/~akitaoka/index-e.html`. Accessed: 02/05/2022.

[67] H. Kluver. *Mescal, and Mechanisms of hallucinations.* University of Chicago Press, 1966.

[68] S. M. Kosslyn. *Image and Brain*. Cambridge, MA: MIT Press, 1994.

[69] V. Kozyrev, R. Staadt, U. T. Eysel, and D. Jancke. TMS-induced neuronal plasticity enables targeted remodeling of visual cortical maps. *Proceedings of the National Academy of Sciences*, 115(25):6476–6481, 2018.

[70] A. E. Krill, H. J. Alpert, and A. M. Ostfield. Effects of a hallucinogenic agent in totally blind subjects. *Archives of Ophthalmology.*, 69:180–185, 1963.

[71] C. R. Laing and A. Longtin. Dynamics of deterministic and stochastic paired excitatory—inhibitory delayed feedback. *Neural Computation*, 15(12):2779–2822, 12 2003.

[72] C. R. Laing and W. C. Troy. PDE Methods for Nonlocal Models. *SIAM Journal on Applied Dynamical Systems*, 2(3):487–516, 2003.

[73] C. R. Laing, W. C. Troy, B. Gutkin, and G. B. Ermentrout. Multiple bumps in a neuronal model of working memory. *SIAM Journal on Applied Mathematics*, 63:62–97, 2002.

[74] T. S. Lee, D. Mumford, R. Romero, and V. a. Lamme. The role of the primary visual cortex in higher level vision. *Vision Research*, 38(15-16):2429–2454, 1998.

[75] S. LeVay and S. B. Nelson. Columnar organization of the visual cortex. In A. G. Leventhal, editor, *The Neural Basis of Visual Function*, pages 266–315, Boca Raton, 1991. CRC Press.

[76] I. Leviant. Does brain-power make Enigma spin? *Proceedings of the Royal Society of London. Series B: Biological Sciences*, 263(1373):997–1001, 1996.

[77] D. J. T. Liley, P. J. Cadusch, and M. P. Dafilis. A spatially continuous mean field theory of electrocortical activity. *Network*, 13:67–113, 2002.

[78] M. Livingstone and D. Hubel. Specificity of intrinsic connections in primate primary visual cortex. *Journal of Neuroscience*, 4(11):2830–2835, 1984.

[79] I. Léviant. Illusory motion within still pictures: The l-effect. *Leonardo*, 15(3):222–223, 1982.

[80] D. M. MacKay. Moving Visual Images Produced by Regular Stationary Patterns. *Nature*, 180:849–850, 1957.

[81] R. Manor, A. Hagberg, and E. Meron. Wavenumber locking and pattern formation in spatially forced systems. *New Journal of Physics*, 11(6):63016, 2009.

[82] Y. Mau, L. Haim, A. Hagberg, and E. Meron. Competing resonances in spatially forced pattern-forming systems. *Physical Review E*, 88(3):1–9, 2013.

[83] F. Mauro, A. Raffone, and R. VanRullen. A bidirectional link between brain oscillations and geometric patterns. *Journal of Neuroscience*, 35:7921–7926, 2015.

[84] J. D. Murray. *Mathematical Biology*, volume 1 and 2. Berlin: Springer, 2002.

[85] R. Nicks, A. Cocks, D. Avitabile, A. Johnston, and S. Coombes. Understanding Sensory Induced Hallucinations : From Neural Fields to Amplitude Equations. *SIAM Journal on Applied Dynamical Systems*, 20(4):1683–1714, 2021.

[86] P. L. Nunez. The brain wave equation: a model for the EEG. *Mathematical Biosciences*, 21(3-4):279–297, 1974.

[87] P. L. Nunez. *Neocortical Dynamics and Human EEG Rhythms*. Oxford University Press, New York, 1995.

[88] G. Oster. Phosphenes. *Scientific American*, 222:83–87, 1970.

[89] S.-B. Paik and D. Ringach. Retinal origin of orientation maps in visual cortex. *Nature neuroscience*, 14:919–25, 05 2011.

[90] J. Pearson, R. Chiou, S. Rogers, M. Wicken, S. Heitmann, and B. Ermentrout. Sensory dynamics of visual hallucinations in the normal population. *eLife*, 5:e17072, 2016.

[91] J. Petitot. The neurogeometry of pinwheels as a sub-Riemannian contact structure. *Journal of Physiology Paris*, 97(2-3):265–309, 2003.

[92] J. Petitot. *Elements of Neurogeometry: Functional Architectures of Vision*, volume 1. Springer, 2017.

[93] R. Philips, M. Sur, and V. Chakravarthy. The influence of astrocytes on the width of orientation hypercolumns in visual cortex: A computational perspective. *PLoS Computational Biology*, 13(10), 10 2017.

[94] D. Pinto and G. B. Ermentrout. Spatially structured activity in synaptically coupled neuronal networks: I. travelling fronts and pulses. *SIAM Journal on Applied Mathematics*, 62:206–225, 2001.

[95] J. E. Purkinje. *Opera Omnia*, volume 1. Prague: Society for Czech Physicians, 1918.

[96] J. Rankin and F. Chavane. Neural field model to reconcile structure with function in primary visual cortex. *PLOS Computational Biology*, 13(10):1–30, 2017.

[97] J. Rankin, A. I. Meso, G. S. Masson, O. Fuageras, and P. Kornprobst. Bifurcation study of a neural field competition model with an application to perceptual switching in motion integration. *Journal of Computational Neuroscience*, 36:193–213, 2014.

[98] K. A. Richardson, S. J. Schiff, and B. J. Gluckman. Control of traveling waves in the mammalian cortex. *Physical Review Letters*, 94:028103, 2005.

[99] P. A. Robinson, C. J. Rennie, J. J. Wright, H. Bahramali, E. Gordon, and D. I. Rowe. Prediction of electroencephalographic spectra from neurophysiology. *Physical Review E*, 63:021903, 2001.

[100] A. Romagnoni, J. Ribot, D. Bennequin, and J. Touboul. Parsimony, exhaustivity and balanced detection in neocortex. *PLOS Computational Biology*, 11(11):e1004623, Nov 2015.

[101] A. M. Rucklidge and M. Silber. Quasipatterns in parametrically forced systems. *Physical Review E*, 75:055203, 2007.

[102] M. Rule, M. Stoffregen, and B. Ermentrout. A model for the origin and properties of flicker-induced geometric phosphenes. *PLOS Computational Biology*, 7:1–14, 2011.

[103] I. Rümeysa, S. Seda, and F. Sevmez. The inventor of electroencephalography (EEG): Hans. *Child's Nervous System*, 2020.

[104] M. M. Schira, C. W. Tyler, B. Spehar, and M. Breakspear. Modeling magnification and anisotropy in the primate foveal confluence. *PLoS Computational Biology*, 6(1):1–10, 2010.

[105] M. Schottdorf, W. Keil, D. Coppola, L. White, and F. Wolf. Random wiring, ganglion cell mosaics, and the functional architecture of the visual cortex. *PLOS Computational Biology*, 11, 10 2015.

[106] E. Schwartz. Spatial mapping in the primate sensory projection: Analytic structure and relevance to perception. *Biological cybernetics*, 25:181–94, 03 1977.

[107] E. L. Schwartz. Computational anatomy and functional architecture of striate cortex: A spatial mapping approach to perceptual coding. *Vision Research*, 20(8):645–669, 1980.

[108] R. K. Siegel. Hallucinations. *Scientific American*, 237:132–140, 1977.

[109] L. C. Sincich and J. C. Horton. Divided by cytochrome oxidase: A map of the projections from v1 to v2 in macaques. *Science*, 295(5560):1734–1737, 2002.

[110] J. R. Smythies. The stroboscopic patterns. iii. further experiments and discussion. *British Journal of Psychology*, 51:247–255, 1960.

[111] D. C. Somers, S. Nelson, and M. Sur. An emergent model of orientation selectivity in cat visual cortical simple cells. *Journal of Neuroscience*, 15:5448–5465, 1995.

[112] J.-L. R. Stevens, J. S. Law, J. Antolík, and J. A. Bednar. Mechanisms for stable, robust, and adaptive development of orientation maps in the primary visual cortex. *Journal of Neuroscience*, 33(40):15747–15766, 2013.

[113] M. L. Steyn-Ross, D. A. Steyn-Ross, J. W. Sleigh, and D. R. Whiting. Theoretical predictions for spatial covariance of the electroencephalographic signal during the anesthetic-induced phase transition: Increased correlation length and emergence of spatial self-organization. *Physical Review E*, 68:021902, 2003.

[114] J. Swift and P. C. Hohenberg. Hydrodynamic fluctuations at the convective instability. *Physical Review A*, 15:319–328, Jan 1977.

[115] N. V. Swindale. The development of topography in the visual cortex: a review of models. *Network*, 7:161–274, 1996.

[116] P. Tass. Oscillatory cortical activity during visual hallucinations. *Journal of Biological Physics*, 23:21–66, 03 1997.

[117] P. Tass. Oscillatory cortical activity during visual hallucinations. *Journal of Biological Physics*, 23:21–66, 2007.

[118] R. B. Tootell, M. S. Silverman, E. Switkes, and R. L. De Valois. Deoxyglucose analysis of retinotopic organization in primate striate cortex. *Science*, 218(4575):902–904, 1982.

[119] R. B. Tootell, E. Switkes, M. S. Silverman, and S. L. Hamilton. Functional anatomy of macaque striate cortex. II. Retinotopic organization. *Journal of Neuroscience*, 8(5):1531–1568, 1988.

[120] A. M. Turing. The chemical basis of morphogenesis. *Philosophical Transactions of the Royal Society of London B*, 237:32–72, 1952.

[121] C. W. Tyler. Do grating stimuli interact with the hyper- column spacing in the cortex? *Investigative Ophthalmology and Visual Sciences*, 222(254), 1982.

[122] N. A. Venkov, S. Coombes, and P. C Matthews. Dynamic instabilities in scalar neural field equations with space-dependent delays. *Physica D*, 232:1–15, 08 207.

[123] B. A. Wandell, S. O. Dumoulin, and A. A. Brewer. Visual field maps in human cortex. *Neuron*, 56(2):366–83, 2007.

[124] M. A. Webber and P. C. Bressloff. The effects of noise on binocular rivalry waves: A stochastic neural field model. *Journal of Statistical Mechanics*, 3:P03001, 2013.

[125] H. Wilson and J. Cowan. A mathematical theory of the functional dynamics of cortical and thalamic nervous tissue. *Kybernetik*, 13:55–80, 10 1973.

[126] H. R. Wilson and J. D. Cowan. Excitatory and inhibitory interactions in localized populations of model neurons. *Biophysical Journal*, 12:1–24, 1972.

[127] W. D. Winters, L. J. West, and R. K. Siegel. *Hallucinations : behavior, experience, and theory*. New York : John Wiley, 1975.

[128] F. Wolf. Symmetry, multistability, and long-range interactions in brain development. *Phys. Rev. Lett.*, 95:208701, Nov 2005.

[129] J. J. Wright and P. D. Bourke. On the dynamics of cortical development: synchrony and synaptic self-organization. *Frontiers in Computational Neuroscience*, 7(4), 2013.

[130] N. H. Yabuta and E. M. Callaway. Cytochrome-oxidase blobs and intrinsic horizontal connections of layer 2/3 pyramidal neurons in primate v1. *Visual Neuroscience*, 15(6):1007–1027, 1998.

[131] K. Zhang. Representation of spatial orientation by the intrinsic dynamics of the head-direction cell ensemble: A theory. *Journal of Neuroscience*, 16:2112–2126, 1996.